Development of a Single-Degree-of-Freedom Algorithm for the Analysis of Buried Composite Pipes Subjected to Internal Dynamic Pressure

by

Dustin Price Sadler

A thesis submitted to the Graduate Faculty of
Auburn University
in partial fulfillment of the
requirements for the Degree of
Master of Science

Auburn, Alabama
December 12, 2011

Approved by

James S. Davidson, Chair, Associate Professor of Civil Engineering
Hassan H. Abbas, Assistant Professor of Civil Engineering
Mary L. Hughes, Lecturer of Civil Engineering

Abstract

The overall objective of this research project was to develop a practical engineering methodology for the analysis of underground composite pipes subjected to internal dynamic loading. The need for this analytical methodology has been emphasized by events such as accidental gas line explosions that have resulted in extensive property damage and injuries, and the detonation of explosive devices placed in drainage culverts to harm vehicle occupants on the roadway above the pipe. The loading was considered to be sufficient to rupture the pipe and cause significant acceleration of the ground surface. The analytical tool developed is intended to aid in the design of high-strength composite pipes that can resist internal high-order explosions.

Static models of composite pipes were developed using Abaqus finite element (FE) software with shell elements formulated for analyzing composite materials. The finite element results were used to establish "effective" nonlinear stress-strain relationships for each type of pipe considered, which varied by fiber type, fiber stacking sequence, and pipe diameter and thickness. The generalized stress-strain relationships were then used to compute pressure-displacement relationships based upon fundamental thin-walled pipe mechanics theory. A dynamic analysis approach was then implemented, based upon a single-degree-of-freedom (SDOF) model in which the resistance was represented by the nonlinear pressure-displacement relationship of the pipe and the mass was represented by a soil prism mobilized by the dynamic loading plus the weight of any

objects positioned above the pipe. In order to solve the equations of motion, algorithms were programmed in a user-friendly worksheet format that utilized the central difference method to advance the solution with time.

Time domain displacement, velocity, and acceleration response curves were generated for a wide range of input parameters. From these results, general trends and conclusions were drawn toward identifying the parameters that most affect the blast resistance of buried composite pipes. Finally, the implementation of the methodology was illustrated using two design scenarios.

Acknowledgments

I would like to dedicate my thesis to my father Jerry Sadler, whom I lost in the midst of this research. I cannot express how thankful I am for all his guidance, love, and support in my life. I wish he could see this today, but I know he is now in a better place.

I would also like to thank Dr. James Davidson, whose patience, guidance, and wisdom not only tremendously helped me complete my thesis, but also provided me with a better understanding of structural engineering and new insight into blast engineering. I would like to thank Dr. Jun Suk Kang, who generated many finite element models and helped me with understanding the static analysis portion of the project. Thanks to Michael Newberry for his assistance with generating the blast load approximations. Also, I would like to thank the Auburn University Civil Engineering faculty and the research sponsor for the financial assistance and resources I was provided the last couple of years.

I am tremendously thankful to my mother Judy Sadler for her encouragement, love, and inspiration throughout this process. I would not be where I am without her guidance from the day I was born. Many thanks also to the rest of my family for their love and support, as well as my friends and the Auburn family.

Most importantly, I would like to thank the Lord for the opportunity to write this thesis and for the many blessings I have received along the way, including my academic success thus far. All things are possible through Him, and all praise and glory are to Him for this work and any future endeavors.

Table of Contents

List of Tables

List of Figures

Chapter 1

Research Introduction

1.1 Project Background

Buried pipes are used for various industrial applications, such as water supply, gas supply, oil supply, drainage, and irrigation (Olarewaju et al. 2011). Unfortunately, though, their serviceability is often jeopardized due to internal blast loads from incidents such as gas line explosions, steam explosions, petrochemical explosions, detonation of improvised explosive devices, etc., which may cause catastrophic collateral damage to above-ground resources and harm people at ground level. Furthermore, since many of these pipes are buried beneath roadways, the safety of vehicle occupants is of major concern.

As a recent example, an explosion occurred on September 9, 2010, when a natural gas pipeline exploded in a suburb of San Francisco, California. Witnesses reported that the blast created "a wall of fire more than 1000 feet high." This explosion and fire destroyed nearby houses, being fed by the ruptured gas line as clouds of smoke spread into the sky (Figure 1.1) (Rose 2010). Seven people were killed, dozens of others were injured, and 37 homes were destroyed from the explosion (Hoeffel et al. 2010).

Figure 1.1: 2010 gas line explosion near San Francisco, California (Rose 2010)

In addition to gas line explosions, there has been a recent surge in criminal activity involving placement and detonation of improvised explosive devices (IEDs) within underground roadway culverts. The explosive device is often strategically placed within a culvert, directly underneath a roadway, so as to be detonated when a vehicle travels overhead; thus, the safety of its occupants is at major risk, and much attention must be paid to this problem.

For example, in the first two days of August, 2009, nine soldiers were killed from IED attacks in Afghanistan, and more than 60 percent of North Atlantic Treaty Organization (NATO) and American soldier casualties in July of that year were related to roadside IED attacks (Oppel 2009). Additionally, on October 15, 2009, four more American soldiers were killed when their patrol vehicle was hit by an IED in southern

Afghanistan (Otterman 2009).

Because of these aforementioned issues, an urgent requirement to reinforce and analyze buried pipes subjected to extremely high magnitude, short duration internal pressure loads has spawned. At the core of this analysis is an understanding of the dynamic behavior of an underground pipe and its surrounding environment when subjected to blast loading, and using this knowledge to determine which methods demonstrate the most effectiveness in mitigating damage against these high internal pressure loads.

Since existing underground culverts are typically designed only to resist static loading conditions, primarily gravity loads from the surrounding soil and the overlaying pavement and roadway vehicles, techniques must be developed to provide resistance to the culverts subjected to dynamic impulse loads. This presents a challenge since the structural response differs significantly as it is subjected to an extremely high load in a small localized area, within just a fraction of a second. A sudden expansion of energy from the blast source produces significant fragmentation of the structure, as well as "breaching" of the energy through the soil and pavement directly above, which ultimately leads to casualties among vehicle occupants traveling the roadway.

Over the past few decades, innovative techniques have been developed to retrofit existing roadway culverts and sewer pipes without excavating or removing the existing pipes. The most prominent approaches include: flowable grout sliplining, cured-in-place pipe (CIPP) installation, and in-situ cement mortar lining. While all of these techniques have been successfully demonstrated, they all have limitations, such as cost, hydraulic capacity reduction, extensive labor and equipment requirements, etc.

These typical roadway culvert rehabilitation methods would not provide significant resistance to an internal explosion. Cured-in-place pipe approaches do have the potential to use high-strength fiber composite materials to substantially increase internal pressure resistance. Therefore, analytical research efforts presented herein are applicable to the analyses of composite pipes and liners that can be installed using cured-in-place pipe approaches.

1.2 Objective

The overall objective of this research effort was to develop an engineering methodology for the analysis of underground composite pipes subjected to short duration internal dynamic pressure loads and to demonstrate its applicability.

1.3 Scope and Methodology

After an extensive review of technical literature related to blast loading and composite pipes, finite element (FE) models were developed using Abaqus to determine the nonlinear resistance functions of the composite pipes, varying several material and geometric parameters. The material parameters varied by fiber type and fiber stacking sequence, and the geometric parameters varied by pipe diameter and wall thickness. After generating these models and obtaining "effective" stress-strain relationships, spreadsheets were used to compute nonlinear pressure-displacement curves in a step-wise fashion, using basic thin-walled pipe mechanics calculations.

A single-degree-of-freedom (SDOF) algorithm was developed in a spreadsheet based on central difference methodology, and this was used to compute several dynamic

response curves in order to determine which combination of system parameters provided the most blast resistance for the composite pipes. Several system parameters were varied, including the following: resistance parameters just mentioned in regard to the composite pipe; mass parameters including soil cover depth, soil cohesion angle, soil type, and additional mass above the pipe; and impulsive loading.

1.4 Report Organization

This report consists of five chapters. Chapter 1 provides a research introduction by describing the project background, objectives, research plan, and report organization. Chapter 2 provides a technical review of literature relevant to the project. Chapter 3 consists of a description of the static analysis of the composite pipes using finite element modeling to determine their nonlinear resistances to internal pressure loading. Chapter 4 describes the development of a SDOF algorithm and its implementation in determining the dynamic response prediction of an underground culvert system. Finally, Chapter 5 closes the report by providing conclusions and recommendations for future analyses of underground composite pipes subjected to internal dynamic pressure.

Chapter 2

Literature Review

2.1 Introduction

Research on the mitigation of blast effects started during World War II due to explosions occurring on various structures during warfare. Primarily, those studies dealt with the manner in which structures responded to extremely high blast loads from nuclear weapons. Soon thereafter, the decades of the Cold War led to further evaluation of blast resistance methods. Again, much attention was given to the effects of nuclear weapons, as the United States civil defense focused a great amount of their efforts on developing protective methods for existing buildings subjected to the thermal radiation and loads from nuclear explosions. More recently, terrorist attacks such as the bombing of the Alfred P. Murrah Federal Building in Oklahoma City in 1995 and the plane crashes into the World Trade Center towers on September 11, 2001, have ultimately led to the implementation of the blast mitigation technologies developed during those previous wars into various construction and engineering entities. Finally, all of the extensive research conducted since World War II has provided a large contribution to the area of structural dynamics (Alkhrdaji 2006; Biggs 1964; Longinow 2003).

2.2 Sources of Blast Loads

Explosive materials can be classified into two main categories: commercial and military. Included in the category of commercial explosives are trinitrotoluene (TNT), dynamite, and ammonium nitrate and other chemicals. Military explosives consist of cased explosives designed for a specific method of delivery, such as bombs, bullets, and mortar shells; explosives used for demolition such as uncased plastic explosives; and low explosives such as propellants. Additionally, there are many other low explosives that are capable of exploding but do not primarily pose a threat to society in an explosive manner, including propane, gasoline, natural gas, and other chemicals (Longinow 2003).

Typically, peak pressure and impulse (area under the pressure-time curve of a blast load) are used as quantitative measures of an explosive material's loading effects. In order to better understand the physical effectiveness of their explosions, though, many high explosives are compared to TNT by using an equivalency factor. The equivalency factor is the ratio of the heat of detonation of the explosive in question to that of TNT, and it can be multiplied by the weight of that explosive to give an equivalent weight of TNT, as shown in the following equation:

$$W_E = \left(\frac{H_{EXP}^d}{H_{TNT}^d} \right) \cdot W_{EXP} \tag{2-1}$$

where W_E is the equivalent weight of TNT, H_{EXP}^d is the heat of detonation of the explosive, H_{TNT}^d is the heat of detonation of TNT, and W_{EXP} is the weight of the explosive.

Furthermore, since experiments have shown that blast parameters of high explosives confined within steel casing significantly differ from those of bare charges, an equivalent weight of bare charge can be computed as follows:

$$W' = \left(0.2 + \frac{0.8}{1 + \frac{m_c}{W}} \right) \cdot W \tag{2-2}$$

where *W'* is the equivalent weight of bare charge, *W* is the weight of the charge inside the casing, and m_c is the weight of the casing (USACE PDC 2008).

2.3 Phenomena of an Explosion

In an explosion, energy is released as either detonation from high explosives such as C4 or TNT, or deflagration from the rapid burning of low explosives such as dust and vapor clouds. The reaction process of detonation occurs at or above the speed of sound, whereas the reaction process of deflagration occurs below the speed of sound.

A detonation causes a shock wave, which propagates spherically outward from the source and causes an instantaneous rise to peak pressure. A deflagration causes a pressure wave, which also causes a sudden rise to peak pressure, only at a more gradual rate and to a lower peak pressure than that of a detonation.

Although both types of pressure are of tremendous magnitude, and occur over very small fractions of a second, more attention is usually paid to detonations since the instantaneous and intense pressure from a shock wave can cause much more damage to a structural component (USACE PDC 2008). Furthermore, military and terrorist applications often depend on the tremendous shattering power and high rate detonations from high explosives (Longinow 2003).

2.3.1 Components of an Explosive Device

There are three main components of an explosive device: the primer, the booster, and the main bulk of the explosive. The primer consists of less than one gram of a high explosive that is very sensitive to shock and heat and is easily detonated by a small application of heat such as a spark. The booster, usually only of a few pounds in weight, is less sensitive to shock and heat, and it serves as an intermediary component between the other two components, often being initiated by the primer and subsequently initiating the main bulk of the explosive itself. Finally, the main bulk, which may account for up to 99% of the explosive in weight, is initiated by a compression wave arriving from the booster. If compression is not sufficient to cause detonation, it continues to propagate as a wave through the main bulk of the explosive; on the other hand, if the compression wave is sufficient to cause detonation, a very rapid chemical reaction occurs in a zone known as the detonation wave. This detonation wave then propagates faster than the speed of sound through the explosive, following the compression wave (Longinow 2003).

2.3.2 Confined vs. Unconfined Charge

If the charge is unconfined—i.e., there is nothing between the explosive and air—the gases produced from the detonation expand at high temperature, velocity, and pressure, creating a well-defined boundary between the air and the zone of hot gases, behind which the temperature and pressure very rapidly decrease toward the interior of the explosive as the expansion rate of this zone continually decreases. Subsequently, this gives rise to a sharp and discontinuous rise in pressure, known as a shock wave, which propagates from the zone and through the air surrounding the explosion.

In contrast, if the charge is confined—e.g., by the steel case of a bomb—high pressure from the gases expands the metal case, causing it to flow plastically until it ultimately ruptures. This results in fragments travelling at an extremely high speed. Since the acceleration of these fragments requires a significant amount of energy, much of the detonation energy is taken away from the explosive. Thus, there is less pressure and energy associated with a confined explosive than with an unconfined explosive (Longinow 2003).

2.4 Blast Loading Overview

Very generally, a blast can be defined simply as a violent gust of wind. More specifically, though, a blast represents the effects or accompaniment of such a gust, produced by some source of energy, or "charge," in the vicinity of a sudden expansion, or "explosion." As mentioned previously, a shock wave is accompanied by a sudden increase in ambient atmospheric pressure (overpressure) followed by a monotonic decrease in pressure below the local atmospheric pressure (suction). Temperature and density associated with the shock wave also dramatically increase and decrease in a similar manner (Tedesco et al. 1999).

Figure 2.1 shows an idealized time-history shape of a blast load, or the "pressure pulse," produced by a shock front from an unconfined charge at an open point in air (i.e., not in contact with any surface). In open air, the shock wave propagates spherically away from the initial centralized bursting point, commonly known as "ground zero." As shown in the figure, it is evident that the pressure increases instantaneously at this point, and then decreases nonlinearly as the shock front progresses beyond the point, until it drops

below ambient atmospheric pressure into a negative phase. The figure shows the idealized shapes of the positive and negative phases. The area under the pressure-time curve represents the impulse of the blast (USACE PDC 2008).

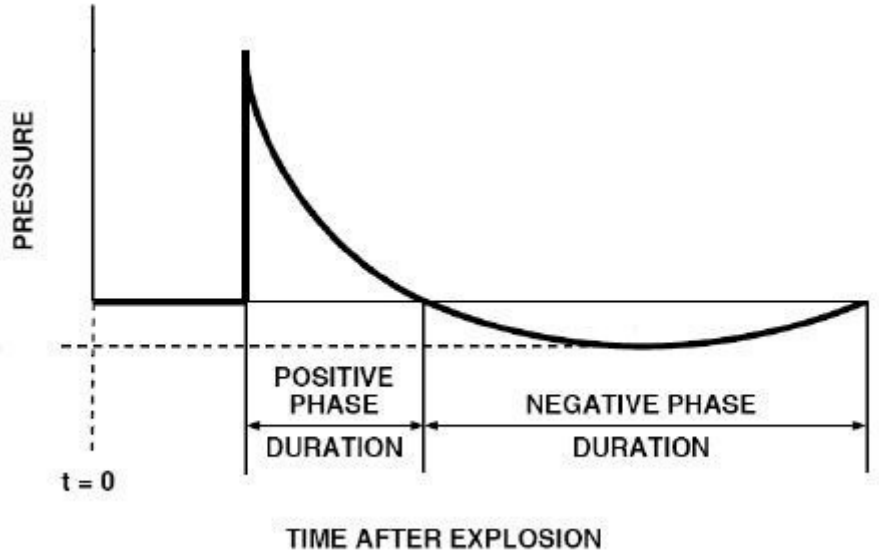

Figure 2.1: Idealized pressure-time history of an explosion in free air (USACE PDC 2008)

2.5 Blast Loading from an Internal Explosion

An internal explosion produces two types of pressure loads: shock and quasi-static gas pressure. Shock pressure results from the initial shock wave coming directly from the charge and from shock waves reflected from other surfaces. Gas pressure results from the heat and products of the explosion being confined by the surrounding structure. Although this gas pressure initially increases relatively quickly to a peak value, it then decreases much slower and ultimately has a longer duration than the shock pressure, as shown in Figure 2.2. Also shown in the figure are the approximate equations for the

shock and gas impulses. Even though the peak pressure from the shock wave is generally much higher than that of the quasi-static gas pressure, the gas pressure could have a higher impulse; therefore, both the shock and gas pressure loadings should be considered when analyzing the blast effects of an internal explosion.

The rate of decay of the gas pressure depends on the extent of confinement the structure has on the gases, which can be categorized into three classes of confinement: fully vented, partially confined, and fully confined (USACE PDC 2008). An explosion is considered fully vented when gas can be released through openings before significant gas pressure and impulse can develop. It is considered partially confined when gas is not released through openings quickly enough to prevent relatively long gas pressure loads and significant impulse to develop. Finally, it is considered fully confined when the structure totally encloses the products of explosion, as in a solid hardened structure, thereby resulting in a very long duration of gas pressure accumulation and a very significant impulse (Longinow 2003).

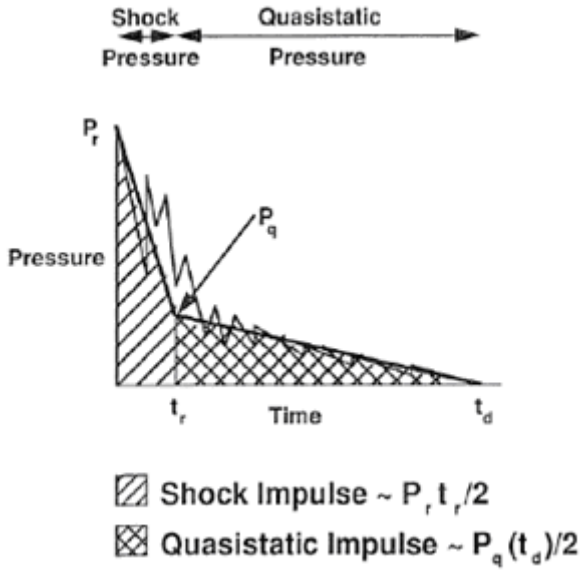

Figure 2.2: Blast loading from an internal explosion (USACE PDC 2008)

2.6 Composite Pipes

In its most general definition, a "composite" material consists of "two or more dissimilar materials which when combined are stronger than the individual materials" (Laney 2002). Thus, "composite" pipes may exist as pipes with reinforcing fibers embedded within a resin matrix, as steel pipes with composite reinforcement wrapped around the outside, as steel pipes with a composite reinforcement lined internally, as plastic liners with reinforcing wrap around the outside, etc. All of these pipes are considered composites in various high-pressure applications such as the chemical, oilfield, natural gas, and water industries, in addition to explosion mitigation applications (Laney 2002).

Of primary focus in this research, though, is the thermosetting resin composite, which is defined as "a combination of a reinforcement fiber in a thermoset polymer resin matrix, where the reinforcement has an aspect ratio that enables the transfer of loads between fibers, and the fibers are chemically bonded to the resin matrix" (Laney 2002). This composition gives composite pipes good structural characteristics such as resistance to cathodic and chemical corrosion, flexibility, high strength, and light weight. (In fact, they have a higher strength-to-weight ratio than steel.) Since the reinforcing material can be broadly manipulated in terms of its type, amount, and arrangement, composite pipes are often ideal for a wide variety of high-pressure applications (Laney 2002).

As a composite pipe is subjected to extremely high internal dynamic pressure, it receives a tremendous amount of energy. Most of it is conveyed through the material of the pipe at the direct location of impact; however, some of the energy dissipates outwardly and along the fiber strands. Therefore, it is important to select an appropriate

material so that, when the explosive material hits the composite pipe, the energy is dissipated from the impact point and over a large area, without much damage to the surrounding area. Primary focus on this research project has been aimed toward a composite pipe consisting of fibers impregnated within a resin matrix. This combination results in a strong composite material that is light-weight and corrosion-resistant.

2.6.1 Design Flexibility of Composite Pipes

Composite materials have a tremendous advantage structurally because of how their main two components—the fibers and the matrix resin—complement one another (Composites One 2005). Fibers are the main source of reinforcement and strength for the composite, whereas the matrix resin "glues" together the fibers and transfers the stresses between them (NPTEL 2006).

Although glass fibers are high in strength, they tend to behave in a very brittle manner and are therefore vulnerable to damage. On the contrary, as shown in Figure 2.3, the matrix resin tends to be weaker but much more ductile, thereby giving the composite more toughness and ultimately energy absorption capacity.

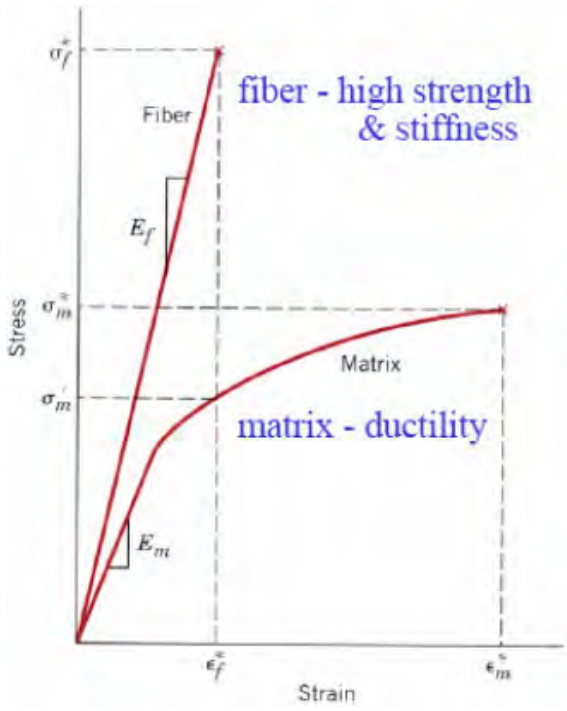

Figure 2.3: Stress-strain curves of fiber and matrix resin (adapted from NPTEL 2006)

Combining the fiber and matrix resin results in a much more useful material than either one of those components acting alone. Ultimately, composites can be designed to meet certain product requirements that other materials cannot meet, by using the correct type and ratio of fiber and matrix resin along with a good manufacturing process (Composites One 2005).

2.6.2 Fibers

As shown in Figure 2.3, the strength of a composite material comes from the thin, stiff fibers set within the matrix resin. These fibers carry the imposing load, while the matrix resin spreads the load over the composite. By choosing the correct make-up, such

as type of fiber, sizing chemistry, and filament diameter, various desired material properties can be attained (Composites One 2005).

The common fiber-reinforcing agents are described in the following subsections. The main four types of fiber material are glass, carbon (or graphite), aramid, and ultra high molecular weight polyethylene (UHMWPE). Figure 2.4 shows a sample of each kind of fiber.

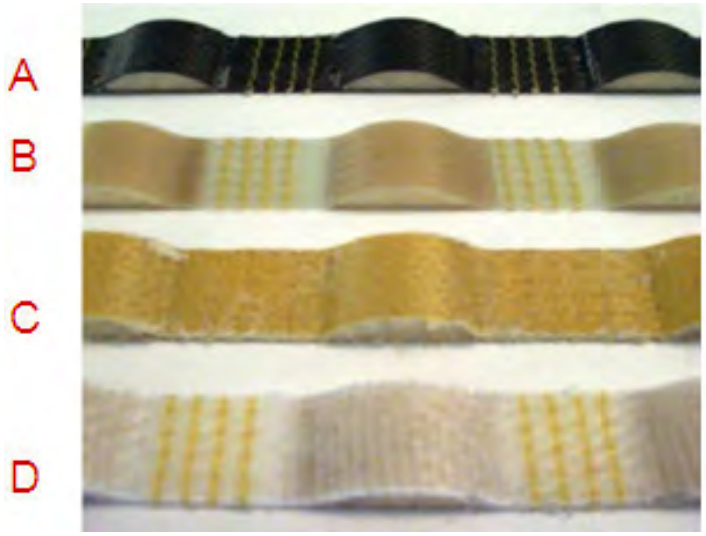

Figure 2.4: Test specimen samples of carbon (A), glass (B), aramid (C), and UHMWPE (D) fibers (Whitman and Saponara 2007)

2.6.2.1 Glass Fibers

Fibers can be produced from silica-based glass, which contains many metal oxides. These fibers offer high thermal, impact, and chemical resistance; tensile strength; and insulating properties (Composites One 2005). The main two types of glass fibers are known as E-glass and S-glass.

E-glass, named for its excellence as an "electrical" insulator, is presently the most popular and least expensive type of fiber—it accounts for over 90% of glass fiber-reinforcement applications and usually costs between $0.50 and $5 per pound (Composites World 2002a). It is made from molten glass, spun into individual fibers, and contains aluminum, calcium, and boron in its make-up. In original form, individual E-glass fibers have very high strength values; however, much strength is lost when they are sized, processed, and woven. Since the fibers are subjected to much less manipulation in unidirectional form, E-glass holds its greatest advantage in this direction. Overall, though, E-glass is an excellent choice of fiber with a high strength and low cost.

S-glass, or high-"strength" glass, is a glass fiber of higher quality, originally created for highly technical applications (Baltic Yachts Americas 2006). While S-glass has much higher strength values than E-glass (40 to 70% stronger) and is more corrosion-resistant, it tends to be more expensive (Composites World 2002a).

2.6.2.2 Carbon Fibers

Fibers made from carbon have higher tensile strength and stiffness values than those made from glass, and are more light-weight; however, they are much more expensive. Prices range from around $7 per pound to as high as $100 per pound, depending on the application (Composites World 2002a). Therefore, they are typically only selected by customers willing to pay a premium, and only used for highly technical applications that require excellent material properties. Instead of using carbon by itself, though, a hybrid fiber is a sensible alternative; by combining the expensive carbon fiber

with a glass fiber, overall performance is improved without as much expense (Composites One 2005).

Carbon fiber is composed of 80 to 90% carbon, and it is created by heating organic precursors, such as polyacrylonitrile, rayon, or pitch, to a temperature of approximately 1800°F while under tension. It is typically categorized according to its modulus: low or standard, intermediate, high, and ultra-high. The fiber comes in "tow" form, which is a bundle of untwisted filaments. For example, the "12K tow" form has 12,000 filaments (Composites World 2002a). Each single filament of carbon is essentially a thin tube having a diameter of 5 to 8 micrometers. The original carbon fibers, T300 and AS4 carbon, have diameters of approximately 7 to 8 micrometers, whereas newer carbon fibers, such as IM6 carbon, are somewhat smaller, at diameters of approximately 5 micrometers (KAYA Archery 2011).

2.6.2.3 Aramid Fibers

Aramid, most commonly available under Dupont's brand name "Kevlar," is a multi-filament synthetic fiber that has very high tensile strength and high ductility (Baltic Yachts Americas 2006). An aromatic polyamide that is known for its excellent flexibility and impact resistance, it is usually reserved for applications such as ballistic or impact containment/protection. While less stiff and brittle than carbon, aramid is stiffer and more light-weight than glass. However, it is also more expensive than glass, with costs ranging between $12 per pound to $30 per pound (Composites World 2002a).

Kevlar is commonly available in various grades, with two of the popular ones being Kevlar 29 and Kevlar 49. Kevlar 29 is the original type of Kevlar, and is commonly

used in ballistic applications, ropes, cables, protective gloves and helmets, tires, automotive hoses, and vehicular armoring. Kevlar 49 is a high-modulus form, commonly used in fiber optic cables, textiles, plastic reinforcement, ropes, and composites for marine and aerospace applications (DuPont 2011).

Table 2.1 shows a comparison of the material properties between Kevlar 29 and Kevlar 49. While both grades have the same density, Kevlar 49 has the higher tensile modulus and strength, but Kevlar 29 shows more ductility. The modulus and strength of Kevlar 29 is similar to that of E-glass and S-glass, but its density is almost half as much. Furthermore, Kevlar 49 has higher modulus and strength than glass with half as much weight. Thus, Kevlar would be a good substitute for glass if less weight is desired. However, due to Kevlar's high cost, it is often too expensive an alternative (About.com 2011a).

Table 2.1: Material properties of Kevlar 29 and Kevlar 49
(adapted from About.com 2011a)

Grade	Density (pcf)	Tensile Modulus (ksi)	Tensile Strength (ksi)	Elongation (%)
29	89.9	12038.1	522.1	4.0
49	89.9	18999.9	594.7	2.8

2.6.2.4 UHMWPE Fibers

Ultra-high molecular weight polyethylene (UHMWPE), also commonly known as high-performance polyethylene (HPPE), is a subset of the thermoplastic polyethylene. A popular brand is DSM's Dyneema. It has an extremely high molecular weight (as indicated by its name), and it has very long polyethylene chains, making the material very

tough and giving it the highest impact strength among all thermoplastics. Also, it is very light-weight considering its high performance, with a strength-to-weight ratio approximately 40% higher than aramid (BPM 2010).

2.6.2.5 Fiber Selection

Glass, carbon, and aramid tend to be the most commonly used fibers (Composites World 2002a). For a particular application, the most appropriate fiber may depend on various factors, such as strength, stiffness, ductility, corrosion resistance, thermal properties, type of manufacturing process, availability, and fiber cost. The graph of Figure 2.5 illustrates how the strength, stiffness, and ductility differ for each type of fiber. Dyneema shows the greatest combination of strength and ductility; however, it is very costly. In Chapter 3, various fiber types will be used in a composite pipe finite element model so they can be compared in terms of resistance to internal pressure loading.

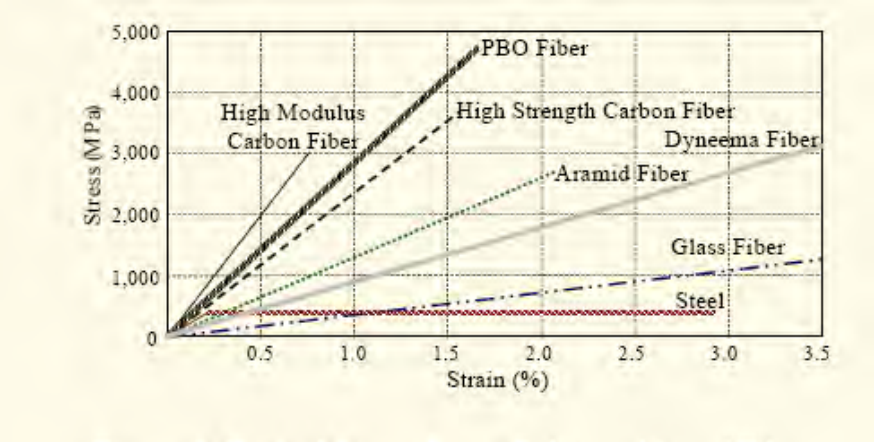

Figure 2.5: Stress-strain curves of various materials (IIFC 2005)

2.6.2.6 Fiber Orientation

Since it is important that the high energy from an explosive source be quickly dissipated from a local impact point to a large area of the composite material, the orientation of the fibers plays an important role in mitigating damage to the surrounding environment. A better "lay-up" pattern of fibers allows energy to flow faster from the central impact point, thereby spreading more energy over a large area and thus allowing less shock energy concentrated at the point of impact.

To obtain high impact resistance, fibers of a single layer laid parallel to one another is the dominant orientation pattern used. Then, the next layer is laid at right angles to the first layer, and so on. This is the most effective arrangement of fibers for allowing the energy to quickly and efficiently dissipate from the point of impact (Ashley 2007).

2.6.3 Matrix Resins

The matrix resin is a very important component of a fiber-reinforced composite material because it binds the fibers together, and ultimately protects them from the impact and the environment. When composites are reinforced continuously by the fibers, the fiber properties dominate the composite but are enhanced by the resin. Particularly, the ductility is an important property of the resin since the glass fibers behave in such a brittle manner (Composites One 2005).

As shown in Figure 2.6, three main types of matrix resins are commonly used with continuous fiber reinforcement: polyester, vinyl ester, and epoxy resins.

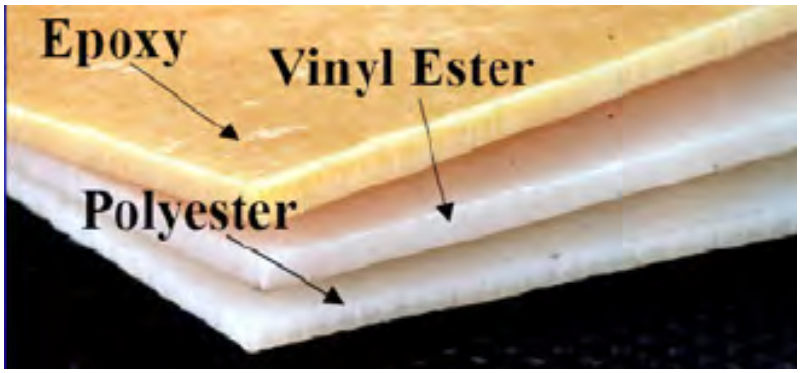

Figure 2.6: Samples of epoxy, vinyl ester, and polyester (NASTT 2005)

2.6.3.1 Polyester Resins

Polyester resins come in two forms: orthophthalic and isophthalic. Orthophthalic polyester is inexpensive and easy to handle, and has mediocre strength values. However, its ductility is poor, having an elongation to break of only 1.6%. Isophthalic polyester is a higher quality polyester, with much greater strength values and ductility (5% elongation to break). However, it must be cured very carefully for the required strength to be met (Baltic Yachts Americas 2006).

Overall, polyester provides the most economical matrix resin system. Also, due to its great chemical resistance, it is the most commonly used resin in municipal sewer and storm water line systems (CIPP Corporation 2011).

2.6.3.2 Vinyl Ester Resins

Vinyl ester costs more than polyester, but is still very easy to use and used in many of the same applications. Its ductility is approximately the same as the isophthalic polyester (4.9% elongation to break), but its process of curing is very sensitive to

temperature. The laminate must be cured under high temperature (post-cured) to ensure it reaches its potential strength values (Baltic Yachts Americas 2006).

Vinyl esters also provide excellent chemical resistance and fatigue resistance, and are great for applications involving high temperatures. They are most commonly used in sewer system applications that use aggressive additives, systems with high corrosive environments or high service temperatures such as special waste or industrial applications, and pressure applications due to their great fatigue resistance (CIPP Corporation 2011).

2.6.3.3 Epoxy Resins

Although it is the most expensive resin and not as easy to use, epoxy is known for its high performance capability and various advantages it holds over the other resins. Specifically, it has the highest ductility (5.7% elongation to break), which is a very important property for a resin, and is the most light-weight among the resin types (Baltic Yachts Americas 2006). Additionally, it has very high tensile strength, toughness, and corrosion resistance, as well as low shrinkage during the curing process. Applications for epoxy include potable water, pressure pipe, industrial, and high temperature systems (Hu et al. 2006).

2.6.3.4 Resin Selection

Ultimately, epoxy was chosen as the resin to be tested in the field, and thus it was chosen as the sole resin for all finite element models in Chapter 3. Although not most economical, it holds many advantages over the other resins. The graphs in Figure 2.7

summarize how epoxy is superior in terms of tensile strength and stiffness, and Figure 2.8 shows how it is superior in terms of ductility.

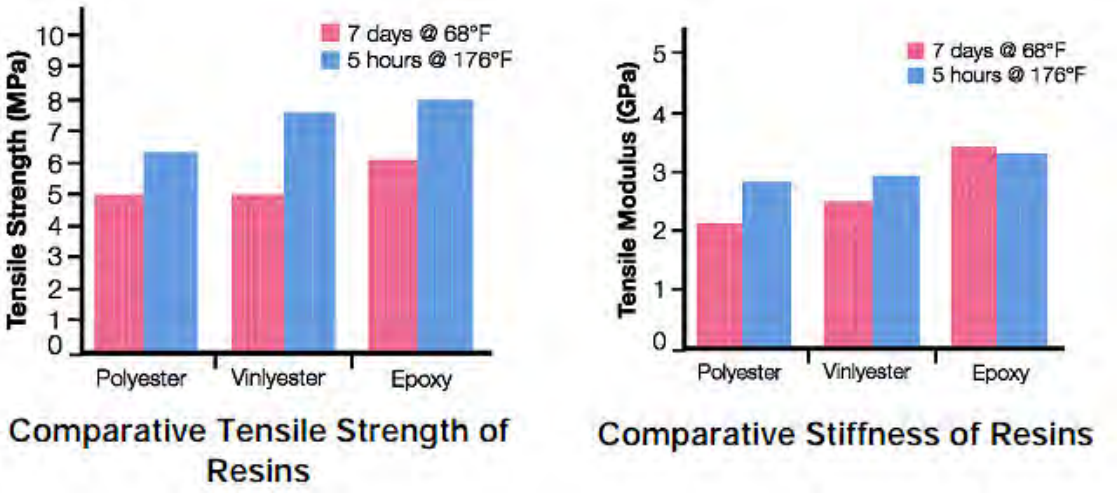

Figure 2.7: Epoxy's advantages in tensile strength and stiffness (adapted from SP Systems 2010)

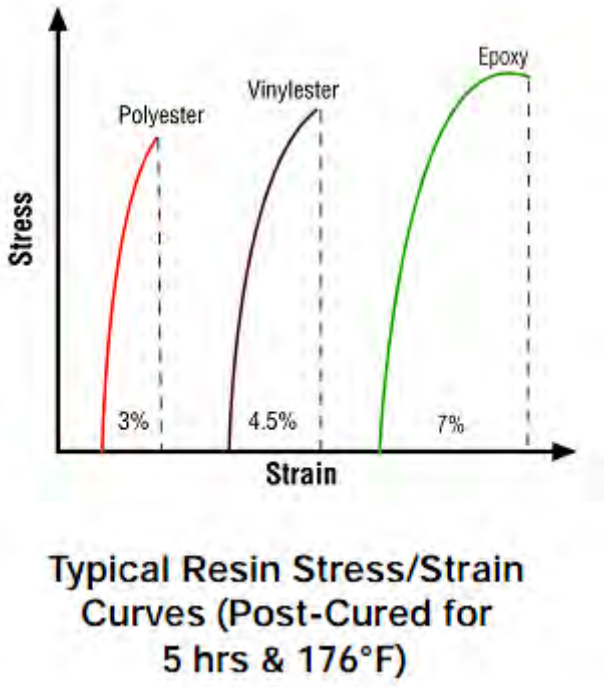

Figure 2.8: Epoxy's advantage in elongation to break (adapted from SP Systems 2010)

2.6.4 Composite Pipes Manufactured for High-Pressure Applications

Various brands of fiber-reinforced composite pipes are manufactured for high-pressure applications. The following paragraphs describe the manufacturing of composite pipes by two companies: NCF Industries, Inc., and PurePipe Composite Manufacturing.

Norman C. Fawley of NCF Industries developed a technique for pre-curing composite sleeves for the repair of high-pressure pipes in the gas pipeline industry. Known as "Clock Spring," it involves impregnating eight layers of 12-inch-wide, continuous unidirectional E-glass fibers with polyester resin, shaped around circular mandrels. The composite coils are then oven-cured at 250°F for at least 12 hours, resulting in a 70% fiber volume by weight. This approach is only designed to have circumferential strength, without much resistance provided in the axial direction. The typical tensile strength of the composite in the circumferential direction is approximately 90 ksi. Long-term stress rupture tests show that this repair method can last up to 50 years. Major oil companies such as Amoco, Chevron, Conoco, and Exxon have used this technique for offshore pipelines (Composites World 2002b).

PurePipe offers three different variations of their composite pipes manufactured for high-pressure water applications: a discontinuous helical filament wound without sand, a centrifugally cast reinforced plastic mortar, and a continuous filament wound with sand.

In the discontinuous helical filament wound without sand, reinforcing fibers are laid in the circumferential and longitudinal directions. Consisting of 65% glass fibers and 35% resin, this composition offers high pressure resistance, stiffness, corrosion

resistance, and flexibility, and is considered as PurePipe's best quality of fiber-reinforced composite pipe.

In the centrifugally cast reinforced plastic mortar, the fibers are chopped and randomly arranged. Consisting of 15% glass fibers, 20% resin, and 65% sand, this option provides high stiffness but low pressure resistance.

Finally, in the continuous filament wound with sand, the fibers are laid at an 88-degree angle, slightly less than the circumferential angle of 90 degrees. Chopped fibers are also laid in the longitudinal direction. Capable of handling higher internal pressures than the other two types, this composition consists of 25% glass fibers, 25% resin, and 50% sand.

Figure 2.9 shows a summary of the compositions of the three types of composite pipes manufactured by PurePipe (PurePipe Composite Manufacturing 2011).

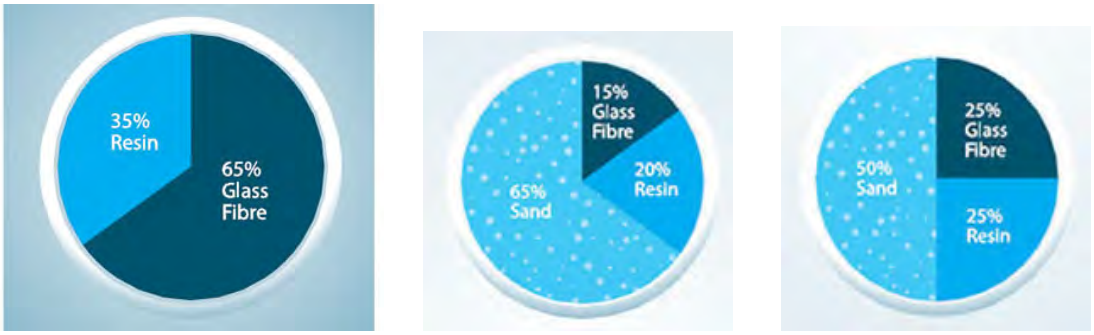

(a) (b) (c)

Figure 2.9: (a) Discontinuous helical filament wound without sand; (b) centrifugally cast reinforced plastic mortar; (c) continuous filament wound with sand (adapted from PurePipe Composite Manufacturing 2011)

2.6.5 Resistance of Composite Pipes

In a study performed by Onder et al. (2008), the resistance of composite pipes subjected to pure internal pressure was investigated. The finite element (FE) method, analytical theory, and experimental procedures were used to determine the effects of angle-ply orientations and filament winding angles on the maximum bursting pressure of composite pressure vessels. (The filament winding technique is discussed later in this chapter, and the FE method and angle-ply orientations are discussed in further detail in Chapter 3.)

The composite pipes consisted of four plies of E-glass fibers and epoxy resin, and the plies were oriented symmetrically and antisymmetrically at angles of 45°, 55°, 60°, 75°, and 88°. Experimentation was performed using a hydraulic pressure testing machine (Figure 2.10) on a pressure vessel specimen. Results from those experiments were compared to analytical results, as well as finite element results from ANSYS 10.0 software based on Tsai-Wu failure criterion and maximum stress and strain failure theory. The results are presented in Figures 2.11 through 2.13.

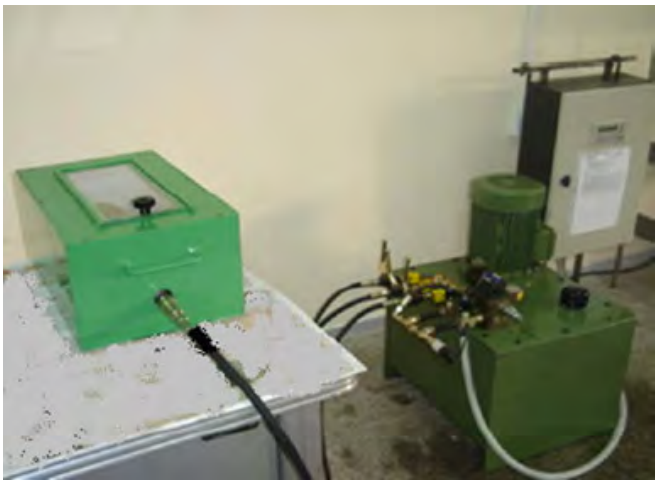

Figure 2.10: Hydraulic pressure testing machine (Onder et al. 2008)

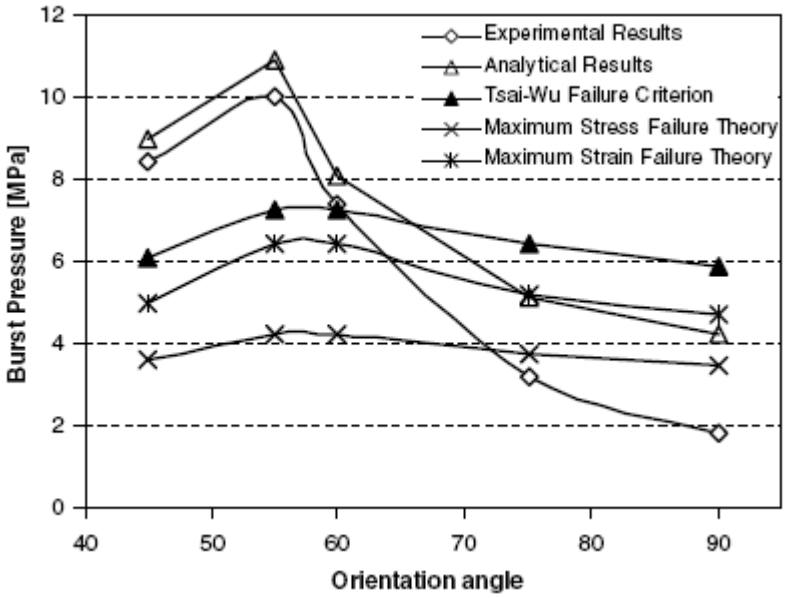

Figure 2.11: Effect of orientation angle on bursting pressure for symmetric orientation (Onder et al. 2008)

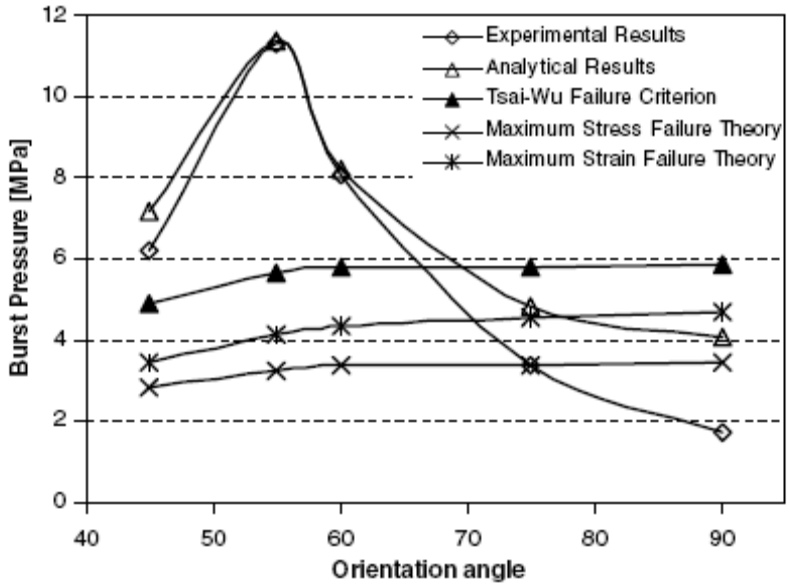

Figure 2.12: Effect of orientation angle on bursting pressure for antisymmetric orientation (Onder et al. 2008)

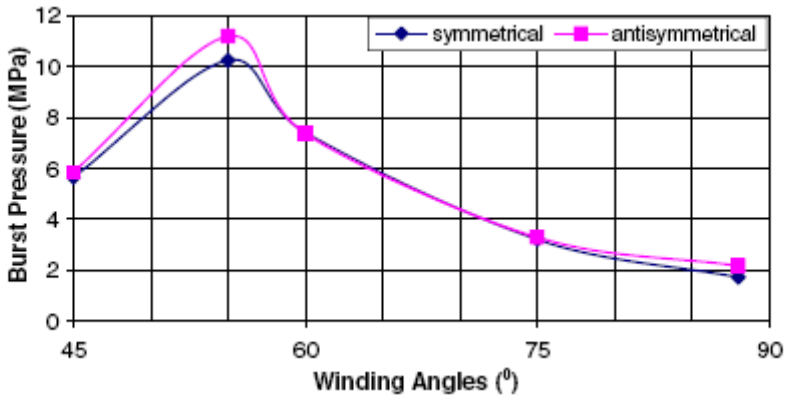

Figure 2.13: Effect of filament winding angle on bursting pressure (Onder et al. 2008)

As shown in the figures, the experimental and analytical solutions closely match, yielding an optimal angle-ply orientation of approximately 55° for both the symmetric and antisymmetric cases, and an optimal filament winding angle also of approximately 55°. The peak bursting pressure is in the range of 10 to 12 MPa at this angle, which is equivalent to approximately 1450 to 1740 psi. It should be noted, though, that the finite element results are not close to the experimental and analytical results because the FE method produces first-ply failure of the composite pressure pipes (Onder et al. 2008).

In another experiment, Al-Sulaiman et al. (2010) studied the effects of weathering on filament-wound glass fiber-reinforced composite pipes used for crude oil transportation. Testing was performed to determine the bursting resistance of composite pipes consisting of E-glass fibers and epoxy or vinyl ester resins. Subjected to various weathering conditions, experimental results showed peak bursting pressures in the range of approximately 3000 to 5000 psi for the pipes with vinyl ester resin, and peak bursting pressures in the range of approximately 5000 to 5500 for the pipes with epoxy resin.

2.6.6 High Strain-Rate Effects in Composite Pipes

Internal dynamic impulsive loading imposes high loading rates, or strain rates, on fiber-reinforced composite pipes, and composite materials are known to exhibit an increase in strength as the strain rate increases. A "high" strain rate typically ranges from 10 to 10,000 s^{-1}, and strain rate effects should be appropriately implemented into composite material modeling. Typically, the yield strength is increased by a dynamic increase factor (DIF), which is the ratio of its strength at a particular high strain rate to its static strength, and is usually expressed in terms of strain rate (Tedesco et al. 1999).

For a fiber-reinforced composite, information on strain-rate data remains an ongoing research task due to the multiphase characteristics of the material. Specifically, limited information is available on the rate dependency of the fiber phase due to difficulties in testing of filaments and fiber bundles. Complex interaction occurs between the fibers and the resin matrix, and it has been observed that the failure mode of the composite changes with increased rate of loading. Further research and experimentation must be performed to develop a better understanding of the damage mechanisms for specified rates of loading.

One rate-dependent model has been developed for a composite material reinforced with AS4 carbon, which covers strain rates from 0.000001 to 1000 s^{-1}. The stress in the direction of loading is determined by the following equation:

$$\sigma_x = \sigma_x^* \left[1 + C \ln\left(\frac{\dot{\varepsilon}_x}{\dot{\varepsilon}_x^*} \right) \right] \tag{2-3}$$

where $\dot{\varepsilon}_x$ is the strain rate in the direction of loading; σ_x^* and $\dot{\varepsilon}_x^*$ are the reference stress and strain rate, respectively, in that direction; and C is an experimental constant (Sierakowski 1997).

In another study, Deshpande (2006) investigated the tensile properties of glass and carbon fiber-reinforced composites subjected to high strain-rate testing. From testing data collected, it is evident that the failure strength of the composite increases with increasing strain rate to a certain point. The failure strain, however, does not follow this trend; instead, it does not vary significantly, and actually initially decreases slightly with increasing strain rate. Table 2.2 shows test data collected for a carbon-reinforced composite, with fibers aligned in the 0° direction. As shown in the table, the failure stress increases significantly with increasing strain rate (with exception of the strain rate of 92.2 s^{-1}).

Table 2.2: Test data collected for carbon-reinforced composite at 0° fiber orientation (adapted from Deshpande 2006)

Average Strain Rate (s^{-1})	Failure Strain	Failure Stress (psi)
0.000415	0.0146	107,935
0.146	0.0124	115,104
1.7225	0.012	118,085
57.0393	0.0121	179,144
92.2193	0.0121	87,679
98.482	0.012	118,886

Various high strain-rate tests exist for fiber-reinforced composites. Examples of such tests include the Hopkinson pressure bar test, the expanding ring test, and the flyer plate test. The applicable strain rates for these three tests are 100 to 10,000 s^{-1}; 10,000 s^{-1}; and 100,000 s^{-1} and higher, respectively.

First, the Hopkinson pressure bar test is a very popular test for high strain-rate evaluation. A cylindrical projectile collides into a loading block, causing a tensile elastic loading wave to propagate down the loading bar to the specimen and output bar (Figure 2.14) (Hamouda and Hashmi 1998).

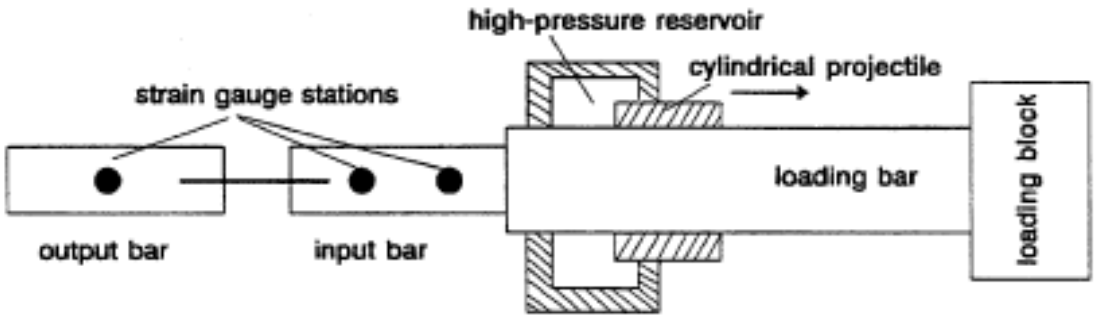

Figure 2.14: Hopkinson pressure bar test (Hamouda and Hashmi 1998)

Second, the expanding ring test involves a short-duration impulsive radial load being applied to a thin ring. Using a cylindrical ring made of steel, it initially expands as it leaves a driver, and then continues to expand from its own inertia. This test may, perhaps, be most appropriate for the composite pipe since it is circular in shape (Figure 2.15).

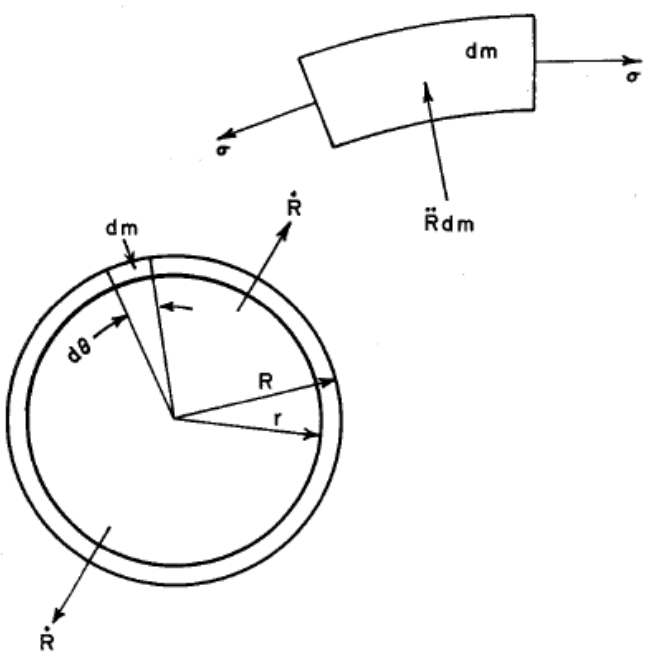

Figure 2.15: Expanding ring test (adapted from Chaturvedi and Sierakowski 1997)

The hoop stress can be solved for by the following equation:

$$\sigma = -\rho \frac{(R_0^2 - r_0^2)}{2(R - r)} \frac{Z_0}{Z} \ddot{R} \tag{5-1}$$

where ρ is the mass density in lb·s^2/in^4, R is the final external radius in inches, R_0 is the initial external radius in inches, r is the final internal radius in inches, r_0 is the initial internal radius in inches, Z is the final axial length of the cylindrical ring in inches, Z_0 is the initial axial length of the cylindrical ring in inches, and $\ddot{R}$ is the deceleration of the ring in in/s^2.

Third, the flyer plate test involves the projection of a flyer plate consisting of one material into a target of another type of material. Some launching devices include magnetic-driven propulsive devices, gas guns, exploding foil, and explosive discharge (Chaturvedi and Sierakowski 1997).

2.7 Culverts

As described in Chapter 1, an underground roadway culvert is a category of buried pipe structure that is of interest. A culvert is essentially a pipe that transports water from one side of the roadway to the other side. In regard analyses and modeling performed, explained in further detail later, various parameters had to be considered, such as pipe shape, material type, dimensions, wall thickness, density, and depth of soil cover.

The shape of a culvert may be circular, elliptical, arching, square, or rectangular (Figure 2.16), and its material may consist of concrete (Figure 2.17) (reinforced or prestressed), metal (Figure 2.18) (corrugated steel or corrugated aluminum), or thermoplastic (Figure 2.19) (polyvinyl chloride (PVC) or high-density polyethylene (HDPE)).

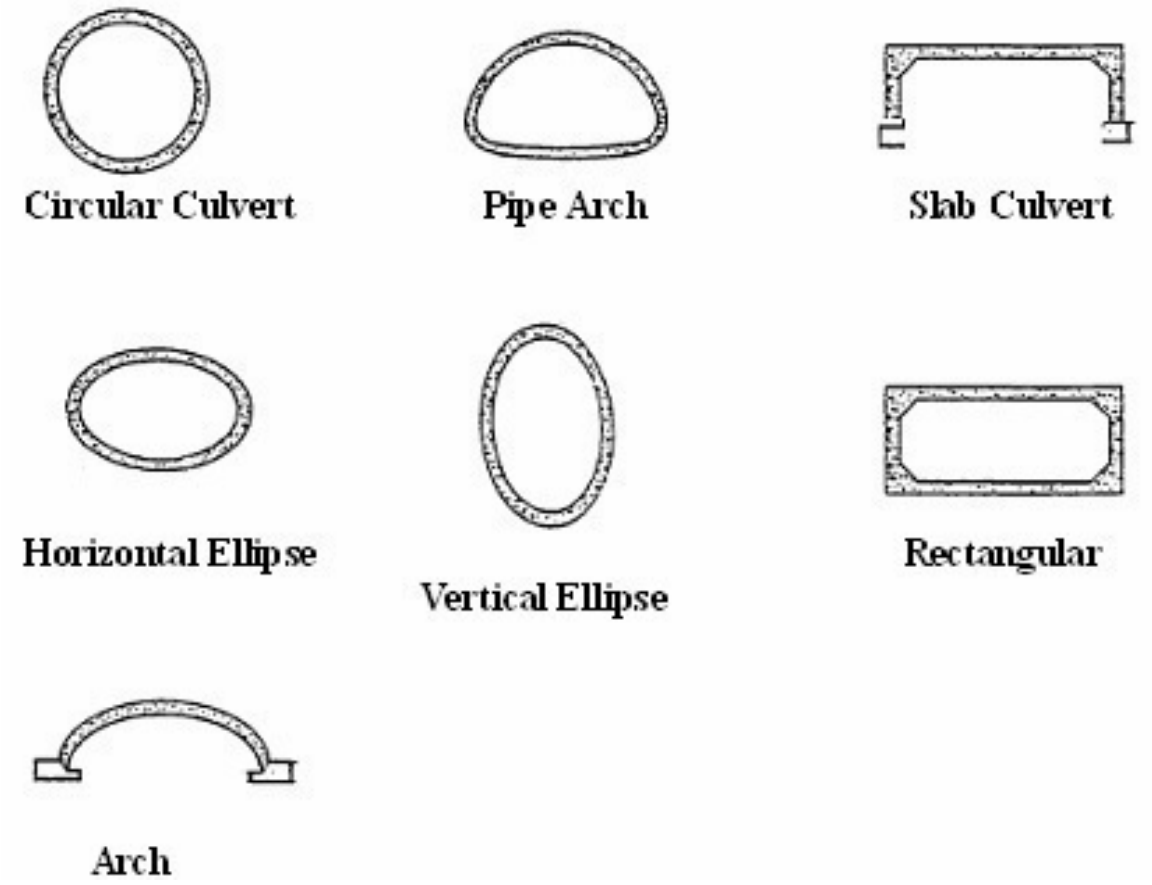

Figure 2.16: Culvert shapes

Figure 2.17: Concrete culvert pipes

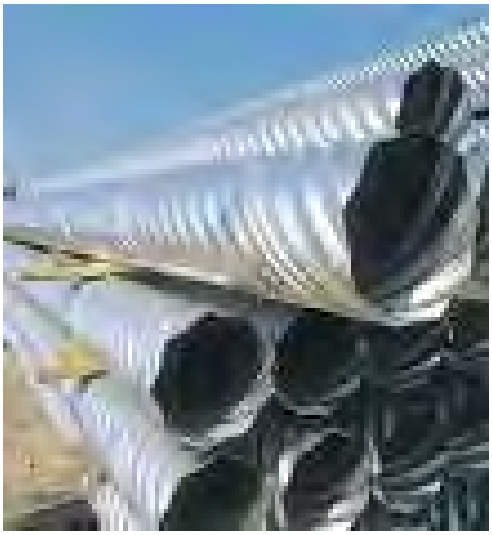

Figure 2.18: Metal culvert pipes

Figure 2.19: Thermoplastic culvert pipes

As shown in Figure 2.20, culverts are buried below the roadway, aligned so that water can easily flow with minimum impedance, and so that access can be provided to homes, farms, and commercial developments. They are generally open at both ends and must withstand significant traffic loads (PPI 2011).

Figure 2.20: Underground roadway drainage culvert (COH 2011)

2.8 Fiber-Reinforced Composite Liners

As mentioned in Chapter 1, the CIPP retrofitting approach involves installation of a composite liner within existing roadway culverts to increase their pressure resistance. Fabrication of a glass fiber-reinforced composite liner typically is performed by using a filament winding approach. This involves immersing a roving of glass fibers into the resin. Then, it is continuously and spirally wound onto a rotational mandrel, as shown in Figure 2.21 (Gilgwang Greentech 2004).

Figure 2.21: Fabrication of glass fiber-reinforced composite liner (Gilgwang Greentech 2004)

The CIPP lining process involves inverting or pulling the resin-saturated, fiber-reinforced composite tube into the host culvert, inflating it, and then heating it with hot water or steam in order to cure the resin. Since minimal digging is involved, this is considered a "trenchless" rehabilitation method, making it easier and more environmentally friendly than traditional "dig-and-replace" rehabilitation methods (API 2010). Once it is completely inserted into the culvert, the resin is "cured in place" by hot water, steam, ambient curing, or ultraviolet light, thereby forming a replacement pipe that is seamless, tight-fitting, and corrosion-resistant (Insituform 2011).

Chapter 3

Finite Element Modeling and Static Analysis of Composite Pipes

3.1 Overview

At the heart of this research study is the development of a single-degree-of-freedom algorithm that analyzes the dynamic behavior of underground composite pipes subjected to short duration internal dynamic pressure. The algorithm involves a nonlinear dynamic time-stepping numerical evaluation that will be explained further in Chapter 4. Along with defining the system's mass and dynamic loading, a nonlinear resistance function must be defined for the composite pipe in order to properly implement the numerical formulas of the algorithm.

Because of the complexity involved with such a structure behaving nonlinearly, a finite element model is a very useful tool for performing structural analyses. Then, if select models are validated by testing results, more models can be created to reduce additional costs, time, and labor associated with further testing.

Although the system experiences dynamic loading and, therefore, its dynamic response should be evaluated numerically, a static analysis must first be performed in order to completely understand its resistance mechanism. At the core of this analysis are "effective" stress-strain relationships of the material (to be explained further later in the chapter) and relationships between applied internal pressure and radial displacement of the pipe. These relationships define how the composite pipe responds with respect to

various geometries and material types, and the pressure-displacement relationships are ultimately the source of the resistance data necessary to perform a dynamic analysis on the entire underground composite pipe system.

The finite element models for this research project were developed using Abaqus. Abaqus is a general purpose finite element software, well known for its ability to address complex systems involving nonlinear structural behavior. The following sections explain in further detail the parameters involved in establishing the models, the respective responses of those models, static analyses performed based on those responses, and interpretations of the results.

3.2 Developing the Finite Element Model

Developing the finite element model involved the following: specifying the unit system, selecting the element type, specifying various material properties and the stacking sequence of the composite laminates, setting up the correct geometry, meshing the finite elements together, specifying boundary conditions, and applying the loading. These procedures are explained in further detail in the subsections that follow.

3.2.1 Unit System

The U.S. customary unit system was used for all finite element modeling and results. Table 3.1 shows the unit used for each type of measurement.

Table 3.1: Units of measurement for finite element modeling and associated results

Measurement	Unit
Distance	inch (in)
Force	pound (lb)
Internal pressure	pound per square inch (psi)
Radial displacement	inch (in)
Effective stress	pound per square inch (psi)
Effective strain	inch per inch (in/in) (unitless)
Toughness modulus	pound per square inch (psi)

3.2.2 Selection of Element Type

Figure 3.1 shows various families of elements that are typically used in finite element modeling. The type of element selected for this research was the four-node shell element, labeled as the "S4" element in Abaqus, which allows finite membrane deformations and is suitable for nonlinear geometric analysis (SIMULIA 2009). A shell element has a very small thickness compared to its other dimensions, and it has curvature along its plane (unlike a plate element, which is completely flat) (Chen 1997). Its four nodes are located at the corners, each having six degrees of freedom—a translational and rotational degree of freedom along each of the three axes. Figure 3.2 shows a general four-node shell element (Austin 1996).

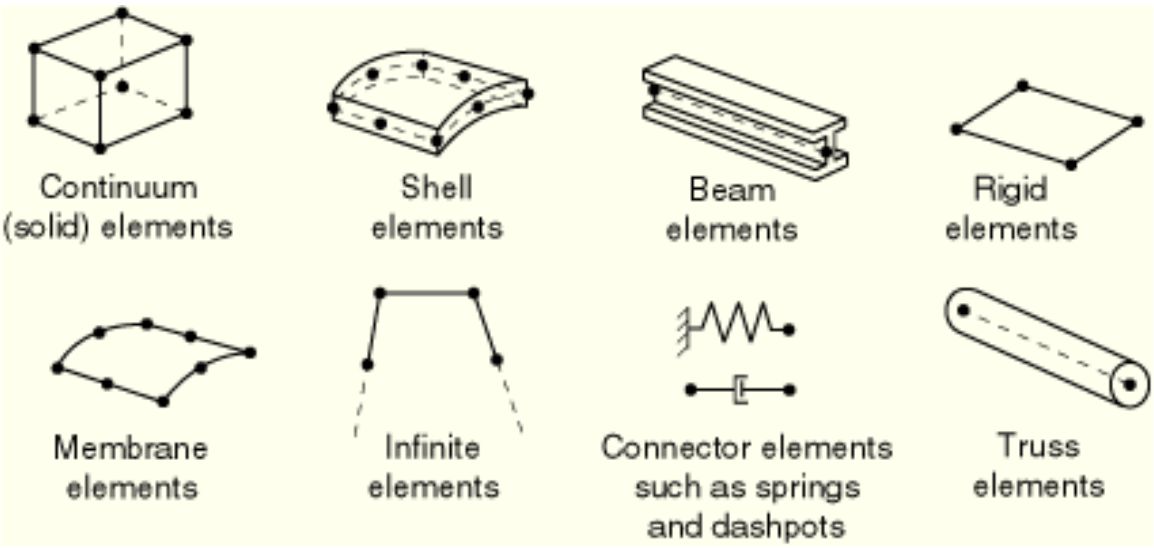

Figure 3.1: Some examples of finite element families (SIMULIA 2009)

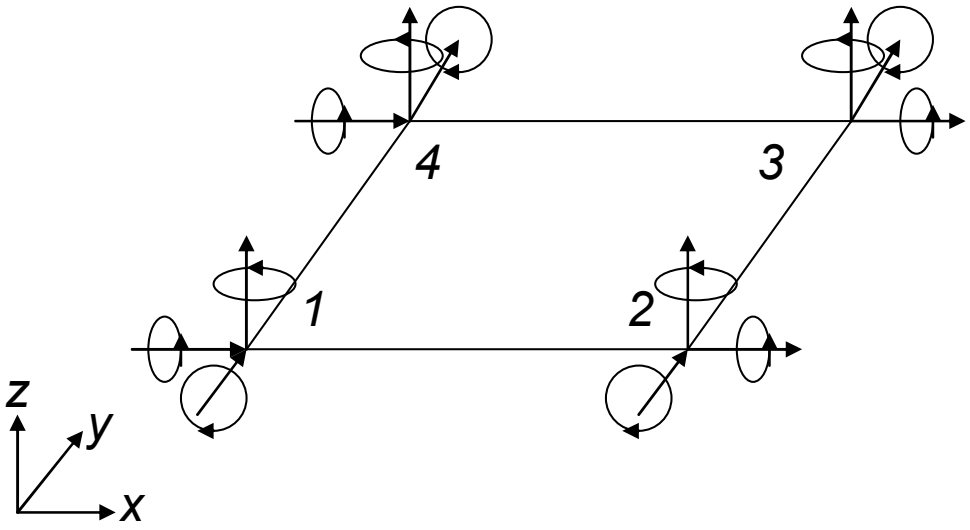

Figure 3.2: Four-node shell element

3.2.3 Specifying Material Properties and Laminate Stacking Sequence

To truly idealize the composite pipe, a layered section had to be created, thereby graphically representing the composite plies, or laminates, stacked on top of one another, as shown in Figure 3.3. This required various material parameters, such as the ply thickness, the number of plies, the orientation of the fibers and their stacking sequence, and the anisotropic properties shown in Table 3.2. These properties differed based on the type of fiber-resin combination selected for the composite pipe. Appendix A provides the specific values used for these properties (About.com 2011b).

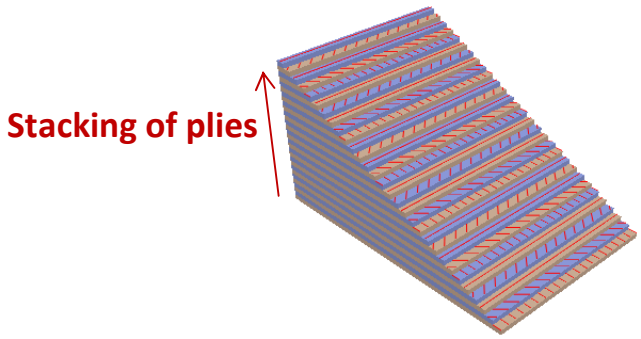

Figure 3.3: Visualization of laminate stacking within composite pipe

Table 3.2: Anisotropic material properties used for finite element models

Nomenclature	Description
E_1	Longitudinal modulus
E_2, E_3	Transverse modulus
F_{1t}	Longitudinal yield strength
F_{2t}, F_{3t}	Transverse yield strength
F_6	In-plane shear strength
G_{12}, G_{13}, G_{23}	In-plane shear modulus
ν_{12}, ν_{13}, ν_{23}	Poisson's ratio

Ply thicknesses ranged from 0.01 to 0.05 inches, and the number of plies used was 20, 50, or 100, depending on the ply thickness chosen and the total wall thickness desired.

Composites respond differently, depending on the orientation of the laminate stacking (Figure 3.4). The laminates were stacked at different fiber alignment angles, and it is important to understand which types of loading can be carried, as well as how material properties vary, with respect to the fiber alignment angles. With respect to the longitudinal axis of the pipe, the 0-degree alignment of fibers carries pure longitudinal loading, the 45-degree alignment carries pure shear loading, and the 90-degree alignment carries pure transverse loading. Regarding material properties, elastic moduli are highest at 0 and 90 degrees and lowest at 45 degrees, but the shear modulus is highest at 45 degrees and lowest at 0 and 90 degrees. Figure 3.5 shows how the tensile strength decreases as the fiber angle increases, with the 0-degree alignment being the strongest and the 90-degree alignment being the weakest (Askeland and Phule 2003).

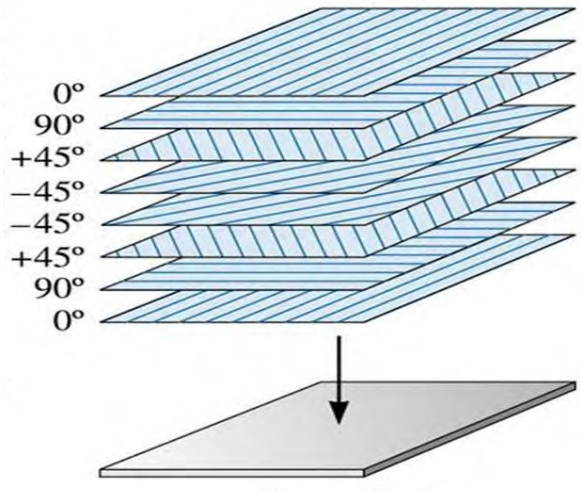

Figure 3.4: Stacking of laminates within a composite
(adapted from Askeland and Phule 2003)

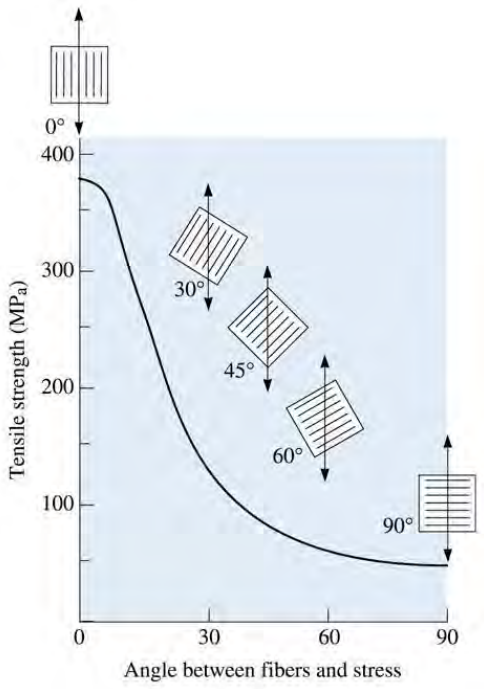

Figure 3.5: Dependence of tensile strength on fiber orientation angle (Askeland and Phule 2003)

Various stacking sequences are commonly used for composites. In this research project, the following stacking sequences were used: [0/90/0], [0/45/90], [0/30/60/90], and [+45/-45] degrees. Later sections explain how the stacking sequences affected the response of the pipe with respect to stress-strain and pressure-displacement relationships.

3.2.4 Setting up Geometry and Meshing

A model of the composite pipe was created by setting up its geometry, and then meshing was performed automatically by the FE software so that the composite pipe could be broken up into small discrete shell elements (Figure 3.6). Through the meshing process, these finite elements are arranged so that they are mathematically linked together, allowing stresses, strains, and displacements to be solved for. Symmetry was

used in creating in order to reduce the model size and computational requirements; hence, only half the pipe is shown in the figure although the full 360 degrees of the pipe was simulated. As will be shown later, the use of symmetry results in reaction forces that act as circumferential forces on the pipe wall.

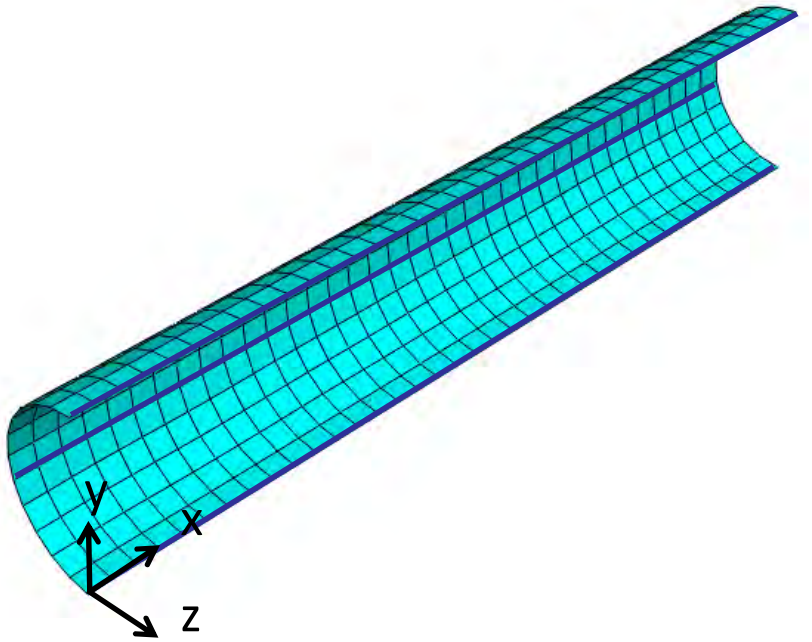

Figure 3.6: Meshed cross-section of composite pipe

3.2.5 Specifying Boundary Conditions

The boundary conditions were applied to the structure by constraining translations and rotations at three separate locations (*A*, *B*, and *C*) along a semi-circular cross section of the pipe, as well as at the two longitudinal ends of the pipe (Figure 3.7).

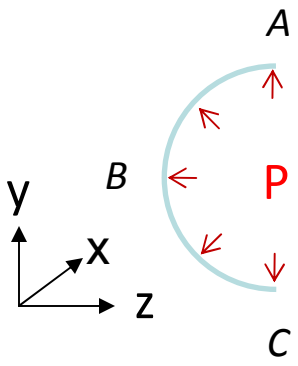

(a)

	A & C	B	Ends
X-displacement			X
Y-displacement		X	
Z-displacement	X		
X-rotation	X	X	
Y-rotation	X		
Z-rotation			

(b)

Figure 3.7: (a) Free body diagram of pipe, showing uniformly applied pressure *P*; (b) table showing which displacements were constrained in FE model

3.2.6 Application of Loading

Loading was incorporated into the model by applying a uniform static pressure load along the interior of the pipe, increasing the pressure incrementally until numerical convergence, which theoretically represents failure (bursting) of the pipe. This incremental procedure is discussed further in the following section.

3.3 Nonlinear Static Analysis Results

The initial goal of performing a nonlinear static analysis on the finite element pipe model was to determine its pressure-displacement history, as well as to record the reaction (circumferential) forces at points *A* and *C* at each loading step. To compute these values, the Riks method was used due to its common application for predicting unstable, geometrically nonlinear collapse of structures having nonlinear materials and boundary conditions.

In the case of a fiber-reinforced pipe subjected to internal pressure loading, its failure may consist of instability due to large deflections, and softening or rupture of its material; therefore, a nonlinear incremental analysis was performed by solving for the nonlinear equilibrium path using the Riks method. This method provides a solution regardless of whether the structure responds in a stable or unstable manner. The internal pressure is increased incrementally within the structure until it becomes unstable. After providing an initial internal pressure load, subsequent iterations and loading increments are automatically computed by the FE software. After each loading increment, the structure's stiffness matrix is adjusted to account for geometric changes due to deformations of the structure and its stress-strain levels. Thus, since both material and geometric nonlinearity of the structure are accounted for, the Riks method provides an accurate solution for the capacity of a fiber-reinforced pipe (SIMULIA 2009).

3.4 Effective Stress and Strain

"Effective" stress-strain relationships were determined by analyzing the response of the pipe to the applied internal pressure. Once the finite element model was run, a radial displacement and circumferential forces were output at each loading step. Figure 3.8 shows a basic free body diagram of the composite pipe in its undeformed position, at initial diameter D with pressure P applied along the interior of the wall, and in its deformed position, a radial distance Δ away from the undeformed position. Because of the internal pressure forces and symmetric boundary conditions being applied, a resulting circumferential reaction force F acts at points A and C. Essentially, the finite element analysis provided the F and Δ values, in pound and inch units, respectively.

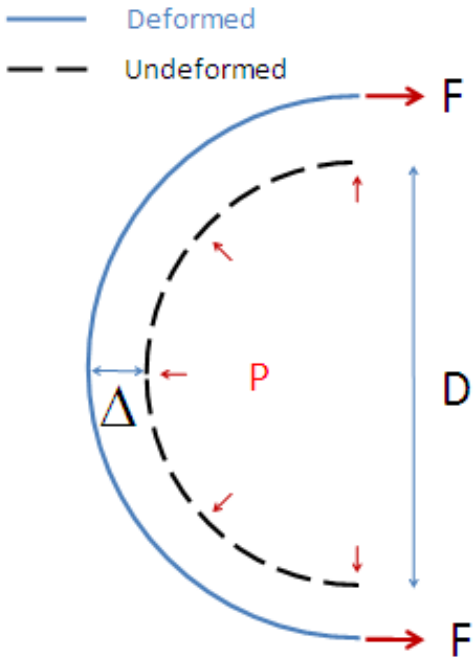

Figure 3.8: Composite pipe with loading and displacement shown, in its deformed and undeformed shape

The effective stress is simply the force F divided by the area A. The effective strain is the change in circumference divided by the initial circumference.

The cross-sectional area A over which the force F acts is the wall thickness t times the longitudinal length l of the pipe over which the pressure is applied, so the effective stress σ is ultimately calculated as

$$\sigma = \frac{F}{l \cdot t} \tag{3-1}$$

The change in circumference is the initial circumference C_0 subtracted from the final circumference C_f. Thus, the computation of effective strain ε is

$$\varepsilon = \frac{C_f - C_0}{C_0} = \frac{\pi(D + 2\Delta) - \pi \cdot D}{\pi \cdot D} = \frac{2\Delta}{D} \tag{3-2}$$

or, in terms of the pipe's radius r,

$$\varepsilon = \frac{\Delta}{r} \tag{3-3}$$

3.5 Internal Pressure and Radial Displacement

Once an effective stress-strain relationship is known, theoretical values of internal pressure and radial displacement of the pipe can be determined. In order to determine the internal pressure, one must understand the relationship between this pressure and the stress in the circumferential (or "hoop") direction of the pipe. This is a basic concept in the subject of mechanics of materials concerning the behavior of cylindrical pressure vessels—the relationship is ultimately derived using equilibrium of forces along the pipe wall. Once the internal pressure is determined, the radial displacement can be derived using the tangent modulus.

In the study of engineering mechanics, circular cylinders are typically divided into two categories: *thin-walled* and *thick-walled*. The general threshold dividing the two types of wall classifications is the ratio between the diameter (or radius) and the wall thickness. Typically, if this diameter-to-thickness ratio is greater than 10, the cylinder is considered thin-walled. If it is less than or equal to 10, it is considered thick-walled. For the applications of this research project, various diameter-thickness combinations were analyzed, but the smallest ratio was 14.2 (diameter of 8 inches and a wall thickness of 9/16 of an inch); therefore, all pipes analyzed henceforth can be considered thin-walled (Ugural and Fenster 1981).

Considering a closed-ended, thin-walled cylindrical pressure vessel with wall thickness t, radius r, and internal pressure P, a stress element on its wall is shown in Figure 3.9. The normal stress component σ_h represents the stress in the hoop direction,

and the normal stress component σ_l represents the stress in the longitudinal direction. Because of the axisymmetry of the pressure vessel, shear stress is not present, so only these normal stresses are accounted for, and they therefore act as *principal* stresses. If the vessel is cut across the cylinder, as shown in Figure 3.10, equilibrium of forces gives

$$\sigma_l \cdot t \cdot 2\pi \cdot r = P \cdot \pi \cdot r^2 \tag{3-4}$$

From this equation, the longitudinal stress can be solved for:

$$\sigma_l = \frac{P \cdot r}{2t} \tag{3-5}$$

(eFunda 2011).

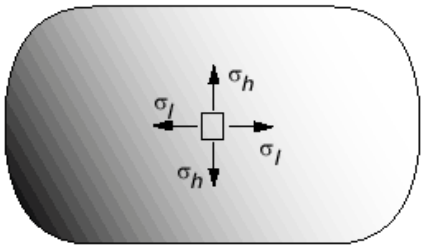

Figure 3.9: Stress components on wall of thin-walled pressure vessel (eFunda 2011)

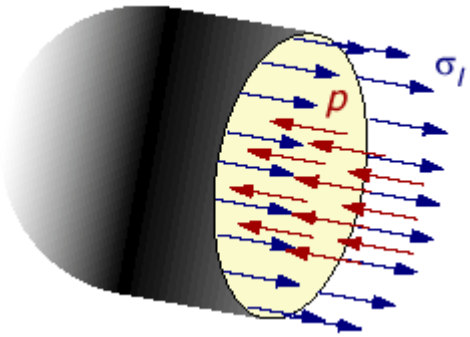

Figure 3.10: Free body diagram of stresses acting in longitudinal direction (eFunda 2011)

However, for the purpose of this research project, it should be recognized that an underground composite pipe is not necessarily representative of a closed-ended vessel. Instead, it often acts as an open-ended cylinder. It will be assumed henceforth that the pipe contains open ends and is therefore not subjected to any axial load; thus, the longitudinal stress is actually zero:

$$\sigma_l = 0 \tag{3-6}$$

(Ugural and Fenster 1981).

From this point, focus is paid solely to the hoop stress that acts in the circumferential direction of the pipe wall. If the vessel is cut along the longitudinal direction, as shown in Figure 3.11, equilibrium of forces gives

$$2 \cdot \sigma_h \cdot t \cdot dx = P \cdot 2 \cdot r \cdot dx \tag{3-7}$$

where *dx* represents a differential slice along the longitudinal length of the pipe. From this equation, the hoop stress can be solved for:

$$\sigma_h = \frac{P \cdot r}{t} \tag{3-8}$$

From this equation, the internal pressure can be solved for:

$$P = \frac{\sigma_h \cdot t}{r} \tag{3-9}$$

(eFunda 2011).

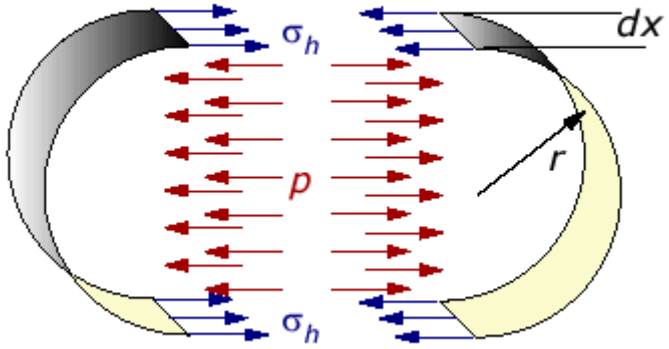

Figure 3.11: Free body diagram of stresses acting in circumferential direction (eFunda 2011)

Having established a relationship between internal pressure and stress, the radial displacement can now be solved for using the tangent modulus E_t; the strain is proportional to the stress by this modulus at each loading increment. Furthermore, recall that the effective strain is the radial displacement divided by the radius. Thus,

$$\sigma_h = E_t \varepsilon_h = E_t \left(\frac{\Delta}{r} \right) \tag{3-10}$$

at each loading increment. Then, knowing the expression for stress in terms of internal pressure, the radial displacement is solved for as follows:

$$\Delta = \frac{r}{E_t} \cdot \sigma_h = \frac{r}{E_t} \cdot \left(\frac{P \cdot r}{t} \right) = \frac{P \cdot r^2}{t \cdot E_t} \tag{3-11}$$

This equation provides a direct relationship between radial displacement and internal pressure.

Overall, the finite element model produces a displacement and circumferential forces at points *A* and *C* of the pipe for each increment of internally applied pressure. Using these values, the effective stress-strain data is determined as explained in Section

3.4. Then, the theoretical values of internal pressure and radial displacement can be solved for using Equations 3-9 and 3-11.

Finally, it is important to note the purpose of using the effective stress-strain approach in determining the pressure-displacement relationship of the composite pipe. The following reasons give credence to this approach:

- With the pressure-displacement relationship determined, a nonlinear resistance function has been established for implementation into the single-degree-of-freedom model, which will be explained in further detail in Chapter 4.
- Once an effective stress-strain relationship has been determined for a particular type of composite material and fiber stacking sequence, that relationship can be applied to a pipe of any diameter and thickness.
- The effective stress-strain approach facilitates a convenient method to compare different composite materials and fiber stacking sequences.

3.6 Development of Static Analysis Spreadsheets

With a comprehensive understanding of the mechanics of a composite pipe subjected to internal pressure, spreadsheets were generated to produce graphical results of stress-strain behavior and pressure-displacement relationships, in order to determine how various parameters, such as types of composite material, ply thicknesses, numbers of plies, wall thicknesses, pipe diameters, and fiber stacking sequences, affect the resistance

of the pipe. Furthermore, from effective stress-strain curves, toughness moduli were calculated, which are also important values used to measure the impact resistance of the pipe material. Figure 3.12 shows a flowchart that was developed before creating the spreadsheet. These steps are explained in further detail in the paragraphs that follow.

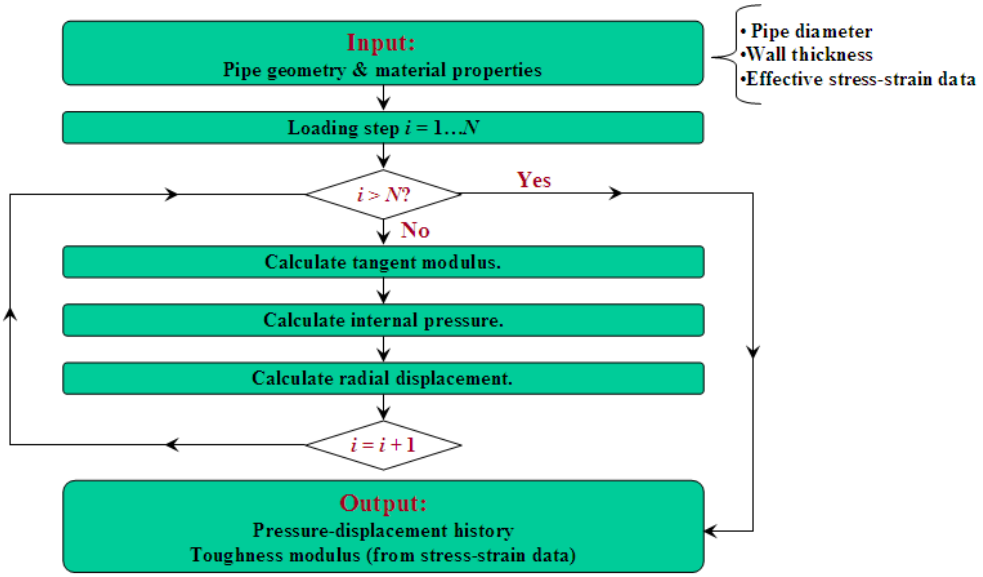

Figure 3.12: Flowchart for static analysis spreadsheet

As mentioned previously, the primary results output by the finite element model were the radial displacements and the circumferential forces of the pipe, both recorded at each loading step of internal pressure, from $i = 1$ to the number of loading steps N. These values were used to calculate the effective stress and effective strain using Equations 3-1 and 3-3, respectively. Thus, for each loading step i, the incremental effective stress was calculated as $\sigma_i = F_i/(l \times t)$, and the incremental effective strain was calculated as $\varepsilon_i = \Delta_i/r$.

Once an effective stress-strain history was obtained, the static analysis spreadsheet could be created. The spreadsheet was organized by input and output values.

Input values include the effective stress-strain history, including its graphical representation; the pipe diameter (specifically, the initial outer diameter); and the pipe's wall thickness. The type of composite material, the stacking sequence (fiber degree orientation), and the number of loading steps were shown for informative purposes. Figure 3.13 shows a snapshot of the input portion of the spreadsheet.

Input:

Pipe material	E-glass/UV	
Fiber degree orientation	45/-45	
Pipe diameter (D)	8	in
Wall thickness (t)	0.28125	in
Loading steps (N)	55	

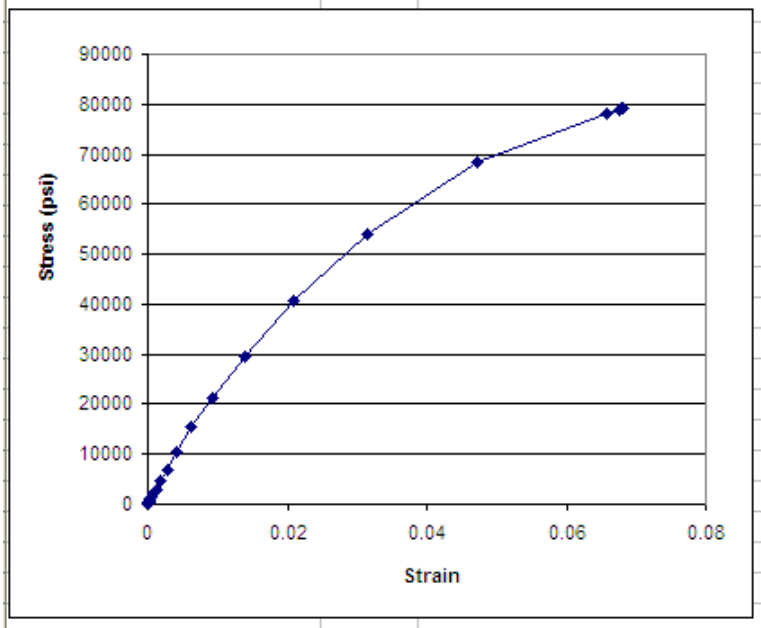

Input Stress-Strain Values		
i	ε_i	σ_i (psi)
0	0	0
1	3.7E-11	9.2E-05
2	7.39E-11	0.000184
3	1.29E-10	0.000322
4	2.12E-10	0.000529
5	3.37E-10	0.00084
6	5.24E-10	0.001306
7	8.05E-10	0.002005
8	1.23E-09	0.003053
9	1.86E-09	0.004626
10	2.8E-09	0.006985
11	4.23E-09	0.010524
12	6.36E-09	0.015832
13	9.55E-09	0.023795
14	1.43E-08	0.035738
15	2.15E-08	0.053652
16	3.23E-08	0.080523
17	4.85E-08	0.12083
18	7.28E-08	0.18125
19	1.09E-07	0.271964
20	1.64E-07	0.408036
21	2.46E-07	0.612143
22	3.69E-07	0.918214
23	5.53E-07	1.377321
24	8.29E-07	2.066071
25	1.24E-06	3.098214
26	1.87E-06	4.648214
27	2.8E-06	6.973214
28	4.2E-06	10.45893
29	6.3E-06	15.68929

Figure 3.13: Input portion of static analysis spreadsheet

Output values include the inner radius, outer radius, average radius r, toughness modulus U_t, and the following values for each loading step i = 1 to N: tangent modulus E_{ti}, internal pressure P_i, and radial displacement Δ_i.

The average radius r is simply the average of the radii at the inner and outer edges of the pipe wall a and b, respectively (Equation 3-12). The incremental tangent modulus E_{ti} was calculated on the spreadsheet using Equation 3-13, and the incremental internal pressure P_i and radial displacement Δ_i were calculated using Equations 3-14 and 3-15, respectively, based off Equations 3-9 and 3-11, respectively.

$$r = \frac{a+b}{2} \tag{3-12}$$

$$E_{ti} = \frac{\sigma_i - \sigma_{i-1}}{\varepsilon_i - \varepsilon_{i-1}} \tag{3-13}$$

$$P_i = \frac{t \cdot \sigma_i}{r} \tag{3-14}$$

$$\Delta_i = \Delta_{i-1} + \frac{(P_i - P_{i-1}) \cdot r^2}{t \cdot E_{ti}} \tag{3-15}$$

An "effective" toughness modulus U_t was calculated by integrating the stress-strain curve (Figure 3.14):

$$U_t = \int_0^{\varepsilon_N} \sigma_i d\varepsilon_i \tag{3-16}$$

A value is shown at each loading step, corresponding to the area calculation at that particular increment. However, only the final number, at the last loading step, is the actual toughness modulus. The modulus of toughness represents the total strain energy capacity of the composite material. Its units are pounds per square inch since it actually measures the energy absorbed (pound-inches) per unit volume of material (cubic inches).

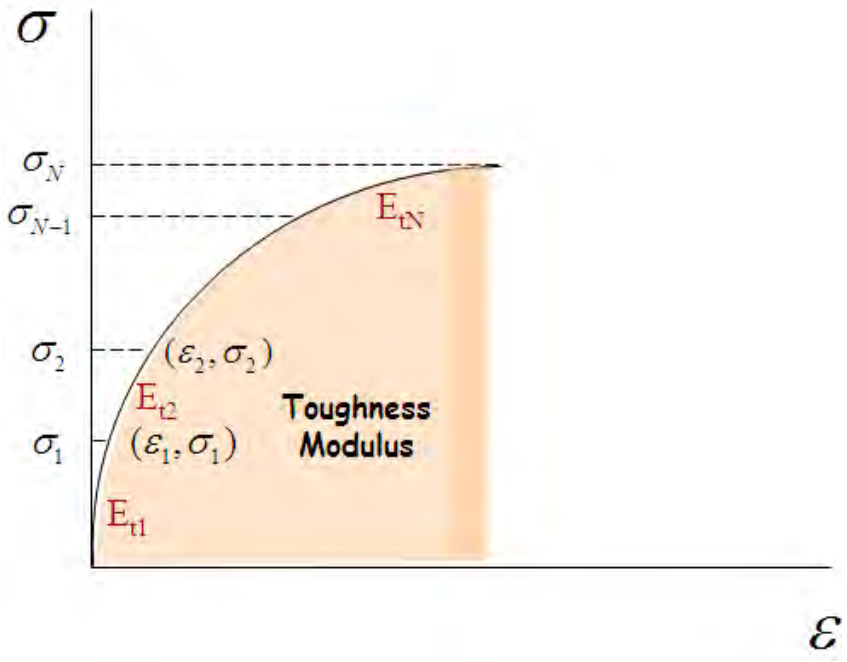

Figure 3.14: Stress-strain curve with toughness modulus shaded

Pipes with high energy absorption capacity will have high toughness moduli, so this is a good value to use as a numerical index for comparison of impact resistance among the pipes. The toughness modulus also shows the importance of the effective stress-strain curve. Not only is the data input to determine the pressure-displacement relationship; it is used to determine the energy capacity of the pipe.

Finally, the pressure-displacement curve was also plotted on the spreadsheet. Figure 3.15 shows a snapshot of the output portion of the spreadsheet.

Output:

Inner radius (a)	3.71875	in
Outer radius (b)	4	in
Average radius (r)	3.85938	in

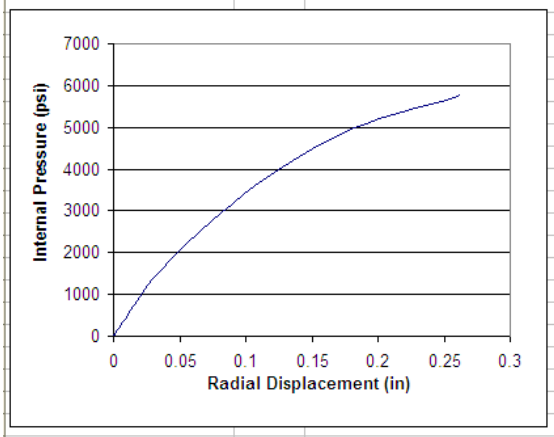

Output Values				
i	E_i (psi)	P_i (psi)	Δ_i (in)	*Toughness Modulus* (psi)
0	0	0	0	0
1	2490987	6.71E-06	1.42614E-10	1.70071E-15
2	2490626	1.34E-05	2.85237E-10	6.80304E-15
3	2491237	2.35E-05	4.99162E-10	2.08343E-14
4	2490915	3.86E-05	8.2005E-10	5.62317E-14
5	2490915	6.12E-05	1.30138E-09	1.41615E-13
6	2490980	9.52E-05	2.02337E-09	3.42337E-13
7	2491059	1.46E-04	3.10641E-09	8.06904E-13
8	2490688	2.23E-04	4.73092E-09	1.87151E-12
9	2491162	3.37E-04	7.16763E-09	4.29587E-12
10	2491006	5.09E-04	1.08227E-08	9.79426E-12
11	2490636	7.67E-04	1.63059E-08	2.22324E-11
12	2491158	1.15E-03	2.45292E-08	5.03113E-11
13	2491062	1.73E-03	3.68657E-08	1.13645E-10
14	2490949	2.60E-03	5.53695E-08	2.56358E-10
15	2490949	3.91E-03	8.31251E-08	5.77791E-10
16	2490632	5.87E-03	1.24764E-07	1.3016E-09
17	2491171	8.81E-03	1.87209E-07	2.93055E-09
18	2489222	1.32E-02	2.80885E-07	6.59667E-09
19	2491466	1.98E-02	4.21405E-07	1.48474E-08
20	2491580	2.97E-02	6.32175E-07	3.34157E-08
21	2491542	4.46E-02	9.48335E-07	7.52022E-08
22	2490866	6.69E-02	1.42257E-06	1.69225E-07
23	2490748	1.00E-01	2.13394E-06	3.80788E-07
24	2491184	1.51E-01	3.20097E-06	8.56794E-07
25	2488740	2.26E-01	4.80154E-06	1.92767E-06
26	2491661	3.39E-01	7.20237E-06	4.3371E-06
27	2491828	5.08E-01	1.08034E-05	9.75879E-06

Figure 3.15: Output portion of static analysis spreadsheet

3.7 Results from Finite Element Modeling and Static Analysis Spreadsheets

Several models were developed, and the results associated with internal pressure, radial displacement, effective stress, and effective strain are given in the subsections that follow. A comparison is first shown between the pressure-displacement curve recorded by the finite element model and the one developed theoretically with the spreadsheet, in order to validate the output of the spreadsheet. Once validated, the spreadsheet was used to make several comparisons to determine which material and geometric parameters are most effective in terms of internal pressure resistance, ductility, and energy absorption capacity.

3.7.1 Validation of Static Analysis Spreadsheet

Figure 3.16 shows the pressure-displacement history of one of the finite element models. This particular model consisted of an E-glass/epoxy pipe with a diameter of 8 inches and wall thickness of 9/16 of an inch. Models were run at fiber stacking sequences of [0/90/0] and [+45/-45] degrees.

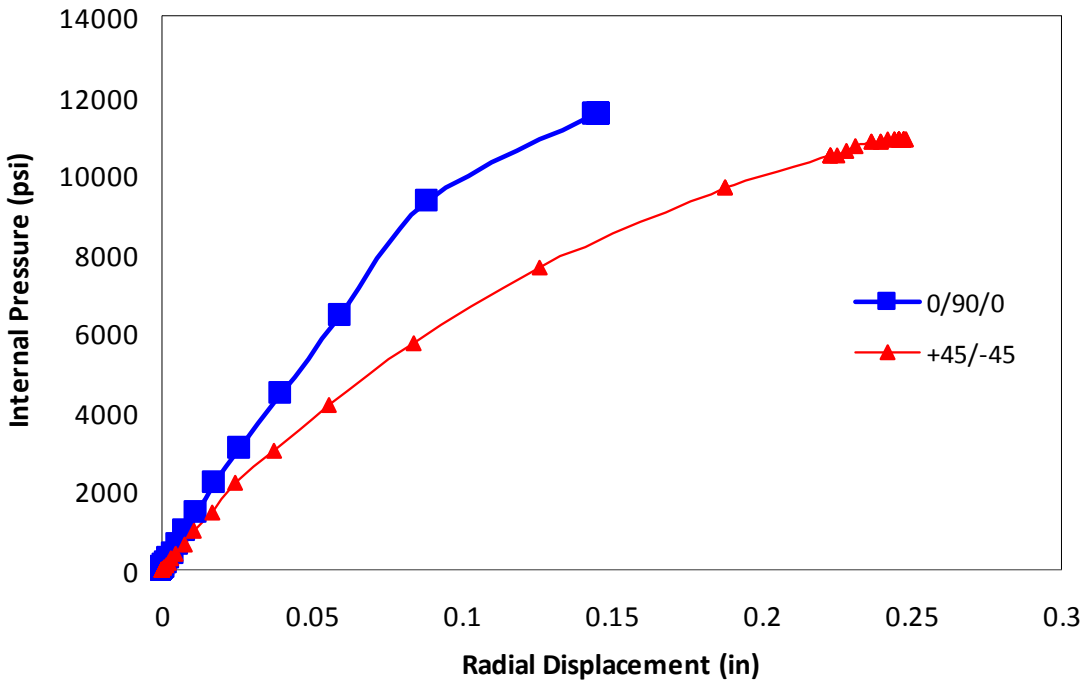

Figure 3.16: Pressure-displacement history for E-glass/epoxy at 8-inch diameter and 9/16-inch wall thickness

Figure 3.17 shows the resulting effective stress-strain history of both fiber stacking sequences. Once this data was input into the static analysis spreadsheet, the resulting pressure-displacement curves shown in Figure 3.18 were generated based off the methods of Section 3.6.

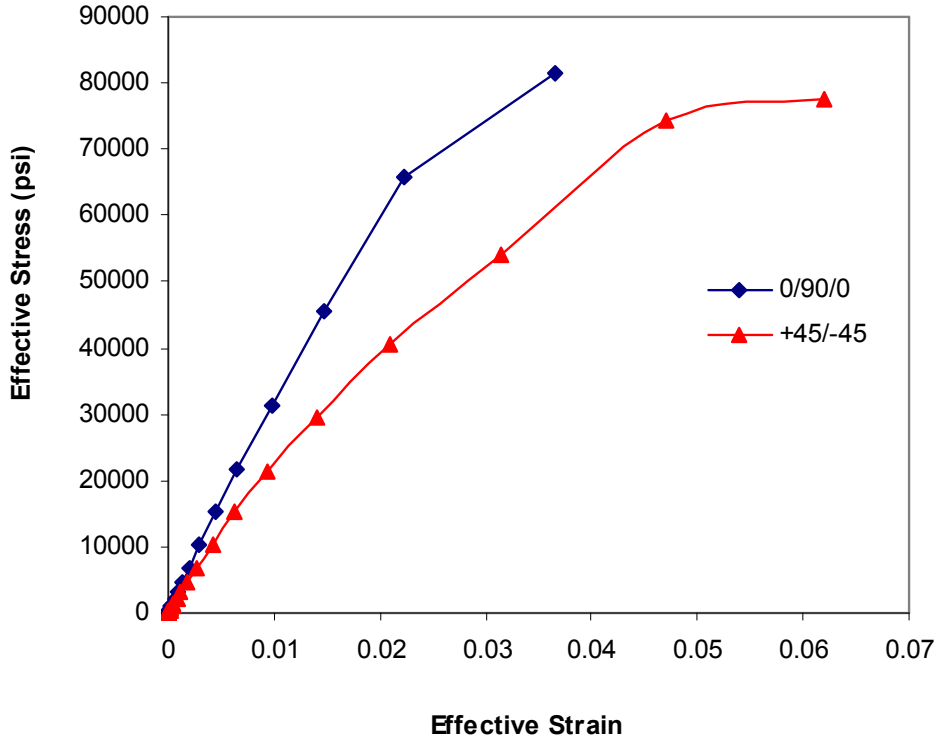

Figure 3.17: Resulting effective stress-strain curve from FE model

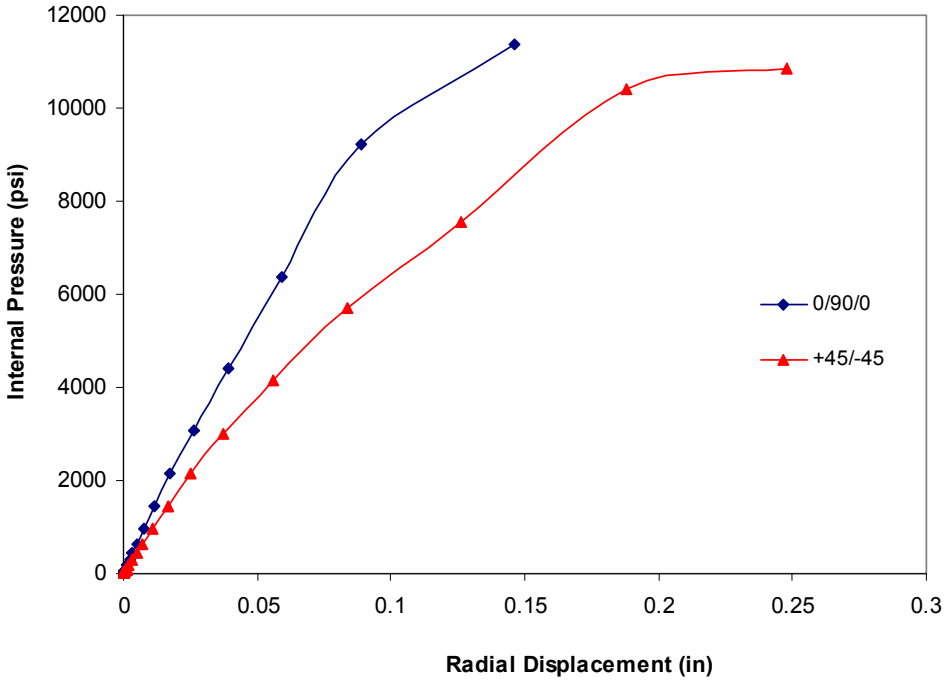

Figure 3.18: Pressure-displacement history output from spreadsheet

Comparing the graphs of Figures 3.16 and 3.18, it is apparent that both pressure-displacement relationships output by the spreadsheet closely match those generated by the finite element model. Furthermore, Table 3.3 shows a numerical comparison of the internal pressure at rupture of the pipe material for both stacking sequences; likewise, Table 3.4 shows a comparison of the radial displacements at rupture.

Table 3.3: Internal pressure comparison of E-glass/epoxy pipe at rupture

Stacking Sequence (deg)	FE Model (psi)	Spreadsheet (psi)	% Error
0/90/0	11500	11383.75	1.0
+45/-45	10900	10867.25	0.3

Table 3.4: Radial displacement comparison of E-glass/epoxy pipe at rupture

Stacking Sequence (deg)	FE Model (in)	Spreadsheet (in)	% Error
0/90/0	0.146	0.146	0.0
+45/-45	0.248	0.248	0.0

The results of Table 3.3 indicate that the internal pressure values computed by the spreadsheet match those of the finite element model very closely; the range of errors is only 0.3% to 1.0%. The results of Table 3.4 show that the radial displacement values are identical for both the spreadsheet and finite element model. Since these values are so close, it has been shown that the static analysis spreadsheet coding was implemented correctly; thus, it could be used for further analyses.

3.7.2 Effects of Ply Lay-up Parameters

Several finite element models were developed to represent S-glass pipes with a diameter of 48 inches and fiber stacking sequence of [0/45/90]°. Parameters were varied according to the following cases:

1. Ply thickness, keeping the number of plies constant at 50
2. Number of plies, keeping the ply thickness constant at 0.01 inches
3. Ply thickness and number of plies, keeping the total wall thickness constant at 1 inch

For Case 1, Figure 3.19 shows the pressure-displacement history recorded from the finite element model, and Figure 3.20 shows the resulting effective stress-strain curve. Likewise, Figures 3.21 and 3.22, respectively, show the same for Case 2, and Figures 3.23 and 3.24, respectively, show the same for Case 3.

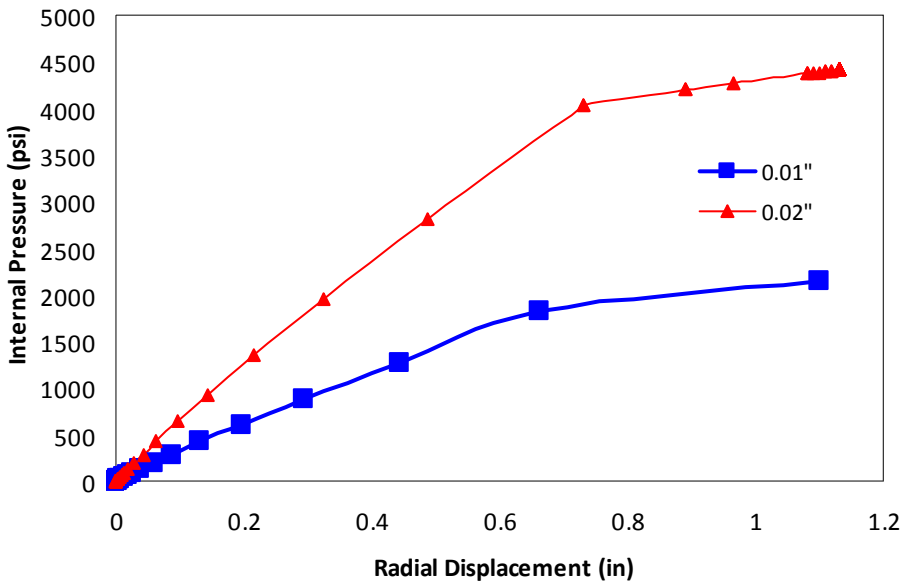

Figure 3.19: Pressure-displacement history of FE model for Case 1

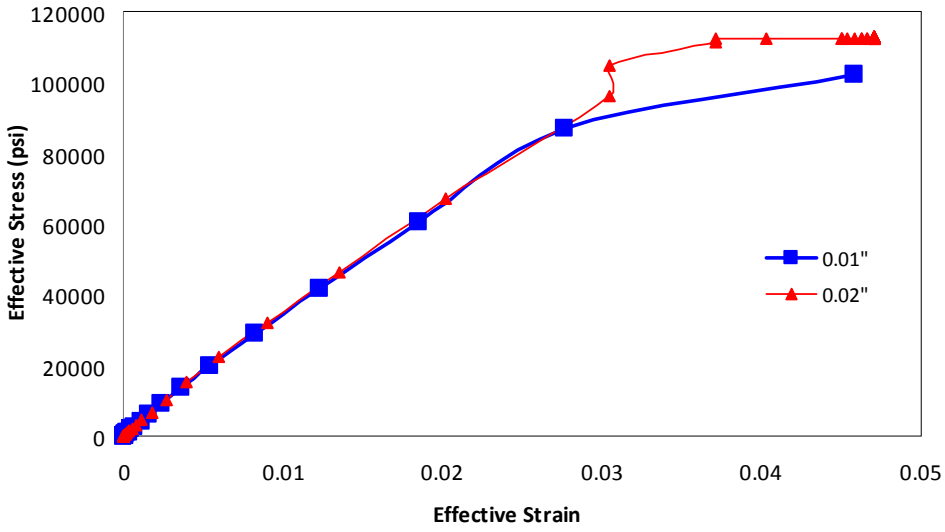

Figure 3.20: Effective stress-strain curves for Case 1

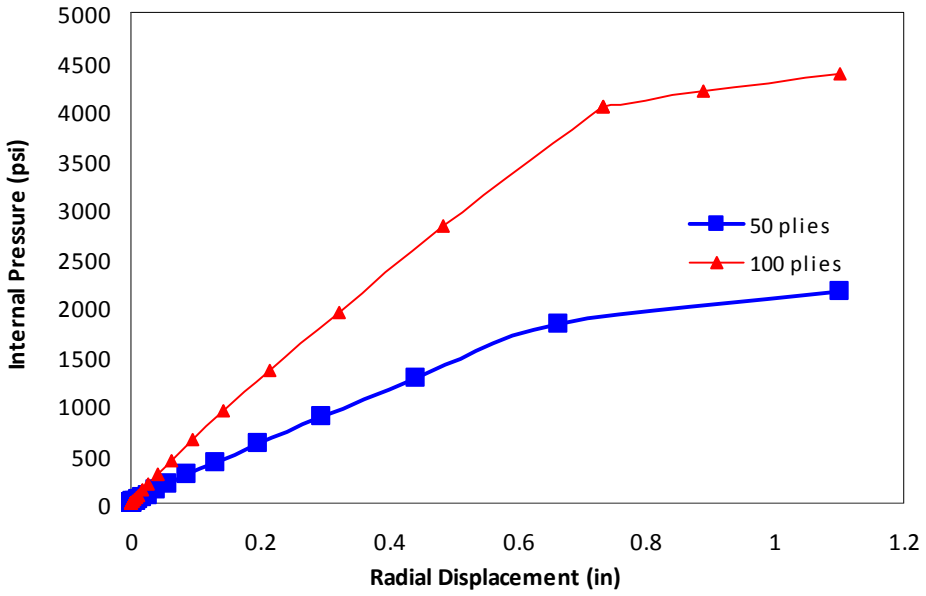

Figure 3.21: Pressure-displacement history of FE model for Case 2

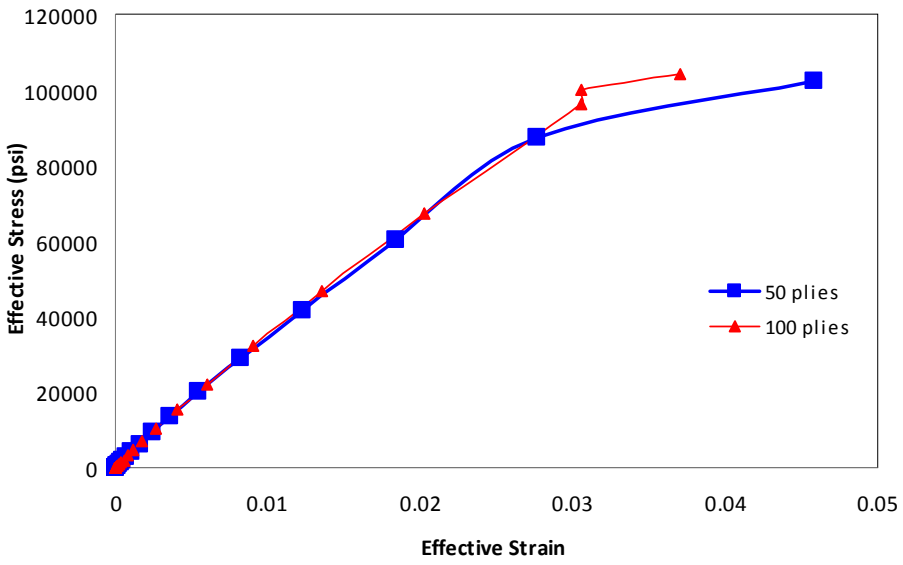

Figure 3.22: Effective stress-strain curves for Case 2

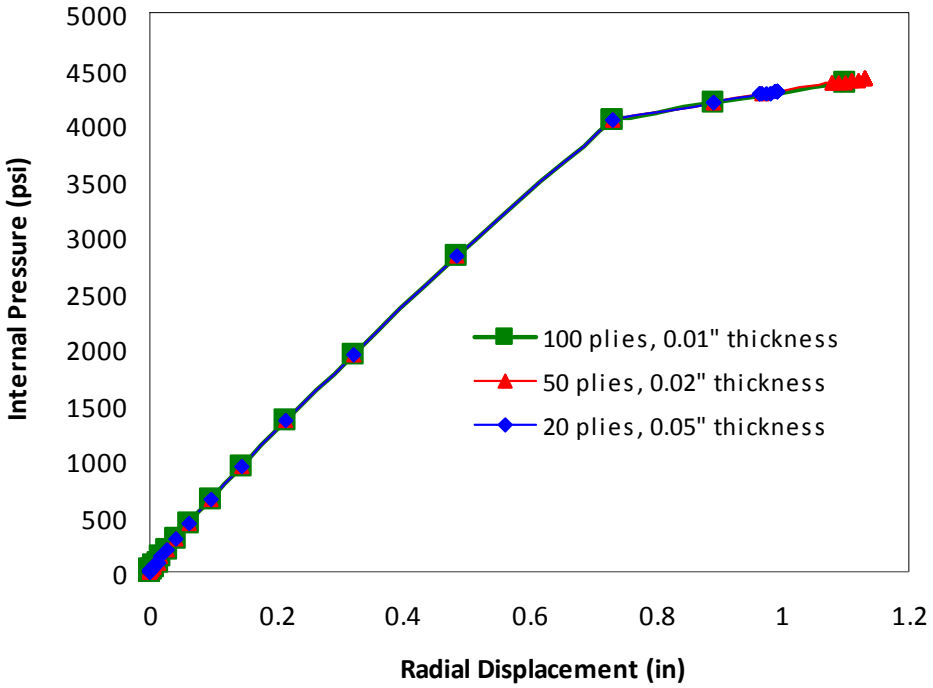

Figure 3.23: Pressure-displacement history of FE model for Case 3

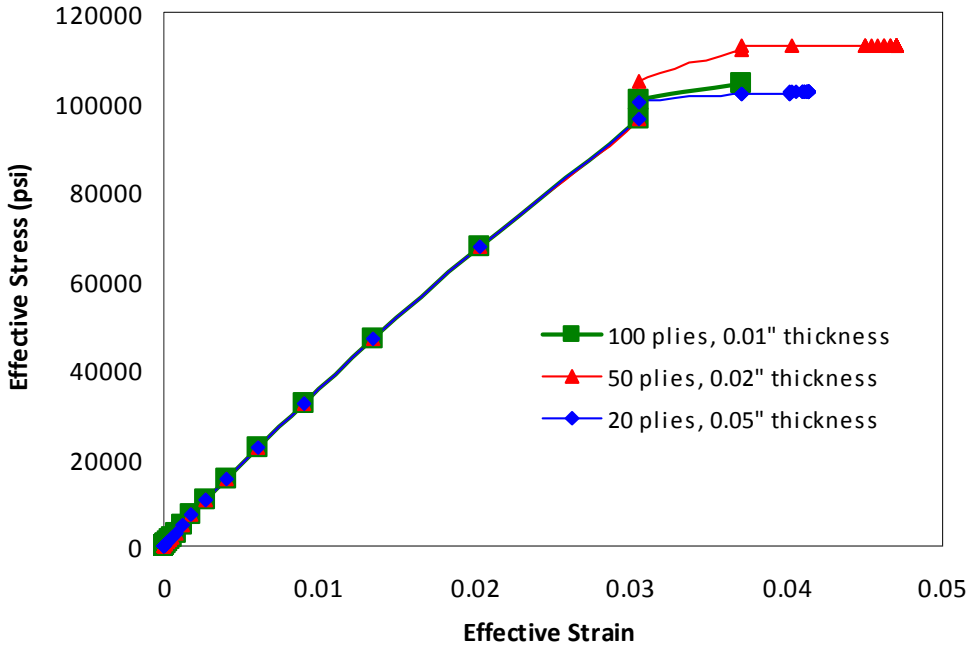

Figure 3.24: Effective stress-strain curves for Case 3

Looking at the results from Case 1 (Figure 3.19), the larger ply thickness (0.02 inches) provides much more resistance but the same ductility as the smaller ply thickness. Similarly, for Case 2 (Figure 3.21), the larger number of plies (100) provides much more resistance but the same ductility as the smaller number of plies (50).

Case 3 shows that the total wall thickness is ultimately the parameter that affects the resistance of the pipe. Figure 3.23 proves this, showing that the resistance and ductility both match up well for all three variations in ply thickness and number of plies while the wall thickness was held constant at 1 inch. Hence, it was determined that no further attention be paid to the variation in ply thickness nor the number of plies, but only on the total wall thickness. A ply thickness of 0.01 inches was typically used henceforth for the purpose of consistency. Furthermore, the wall thicknesses used were sometimes

only fractions of an inch, so using a ply thickness of 0.01 inches allowed the total wall thickness to be divided into an even number of plies.

3.7.3 Effects of Material Parameters

Several more finite element models were run, and static analyses were performed on those models to determine how the fiber stacking sequences and the types of fiber material compared. The comparison of fiber stacking sequences is classified as Case 4, and the comparison of fiber types is classified as Case 5.

For the Case 4 models, the fiber stacking sequences were varied as the following parameters were held constant: composite material of E-glass/epoxy, pipe diameter of 48 inches, and wall thickness of 1 inch. Once the pressure-displacement history was recorded from the finite element analysis for each stacking sequence, the effective stress-strain data was computed. This data was then input into the static analysis spreadsheets, generating the curves shown in Figure 3.25. With the effective stress-strain data input into the spreadsheets, the resulting pressure-displacement curves shown in Figure 3.26 were generated based off the methods of Section 3.6. With these curves generated, the toughness moduli could be calculated to provide a numerical comparison of the energy required to burst the pipe. The toughness moduli comparison is shown in Figure 3.27.

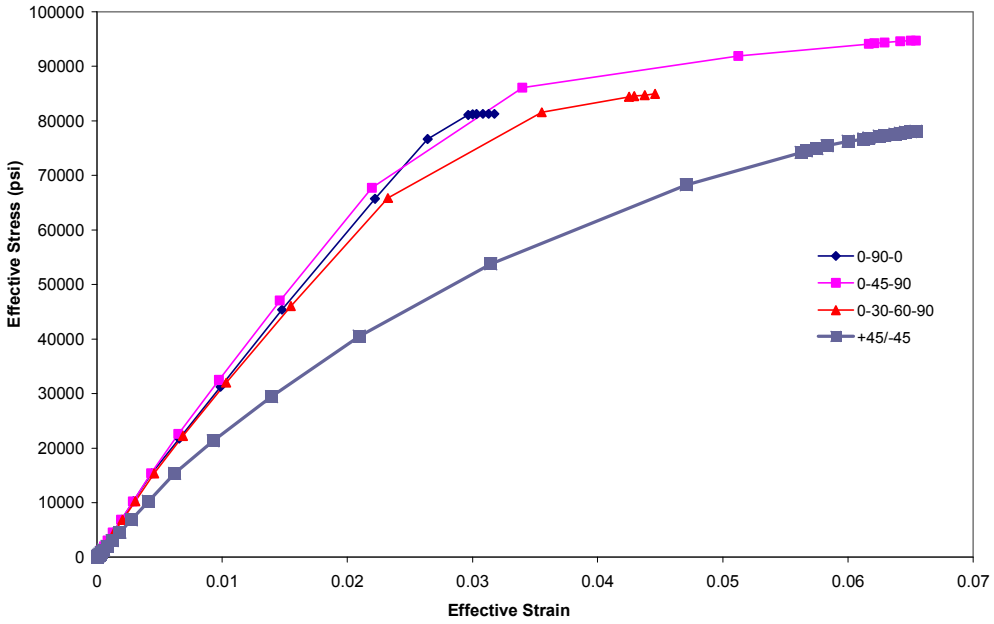

Figure 3.25: Effective stress-strain curves for Case 4

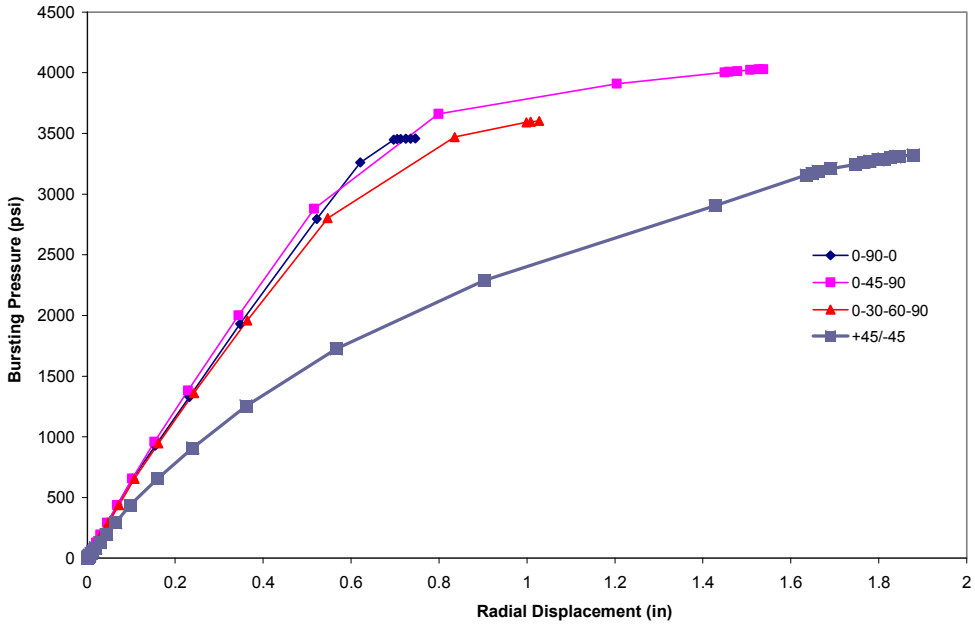

Figure 3.26: Pressure-displacement curves for Case 4

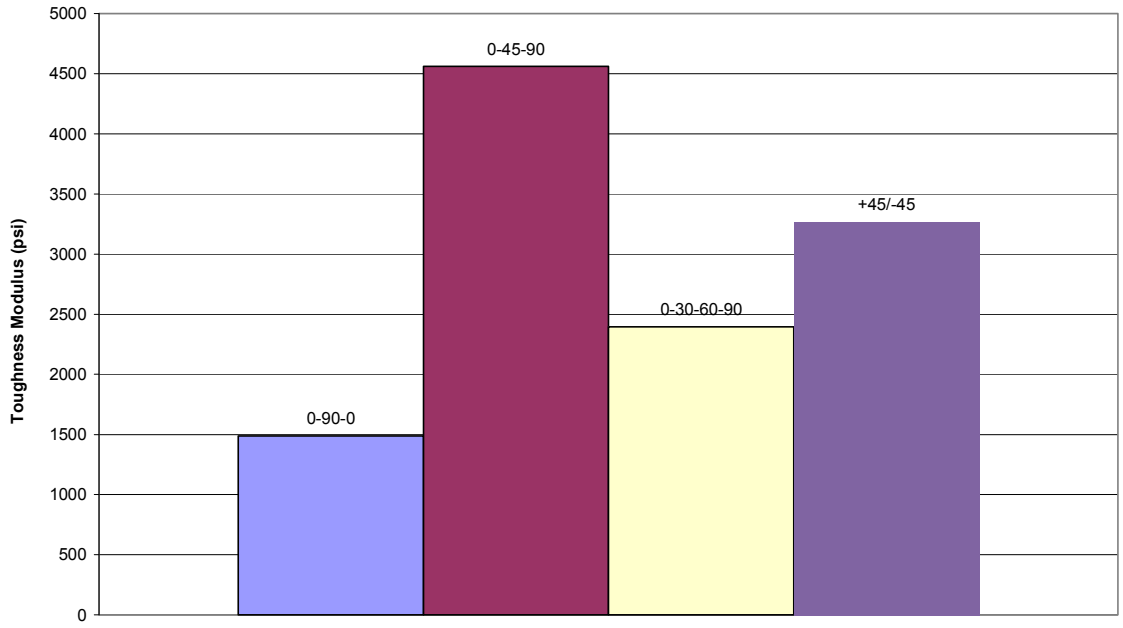

Figure 3.27: Comparison of toughness moduli for Case 4

As shown in Figure 3.26, the [0/45/90]° fiber stacking sequence has the highest impact resistance, but the [+45/-45]° fiber stacking sequence has the highest ductility. Therefore, the toughness modulus becomes a very useful tool for determining which fiber stacking sequence best resists internal pressure loading since it indicates which one absorbs the most strain energy. Figure 3.27 shows that fiber stacking sequence to be [0/45/90]°.

For Case 5, a model was created for each of the following fibers: E-glass, S-glass, AS carbon, IM6 carbon, T300 carbon, and Kevlar 49. The following parameters were held constant: resin of epoxy, pipe diameter of 48 inches, wall thickness of 1 inch, and fiber stacking sequence of [0/45/90]°. Just like Case 4, the effective stress-strain data was calculated and input into the spreadsheet (Figure 3.28). Then, the pressure-displacement

curves and toughness moduli were output, as shown in Figures 3.29 and 3.30, respectively.

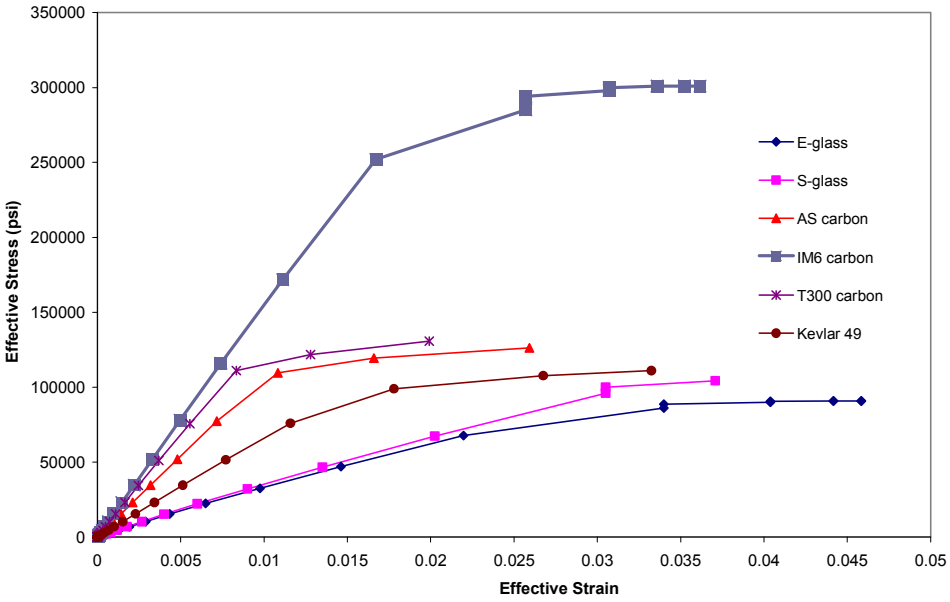

Figure 3.28: Effective stress-strain curves for Case 5

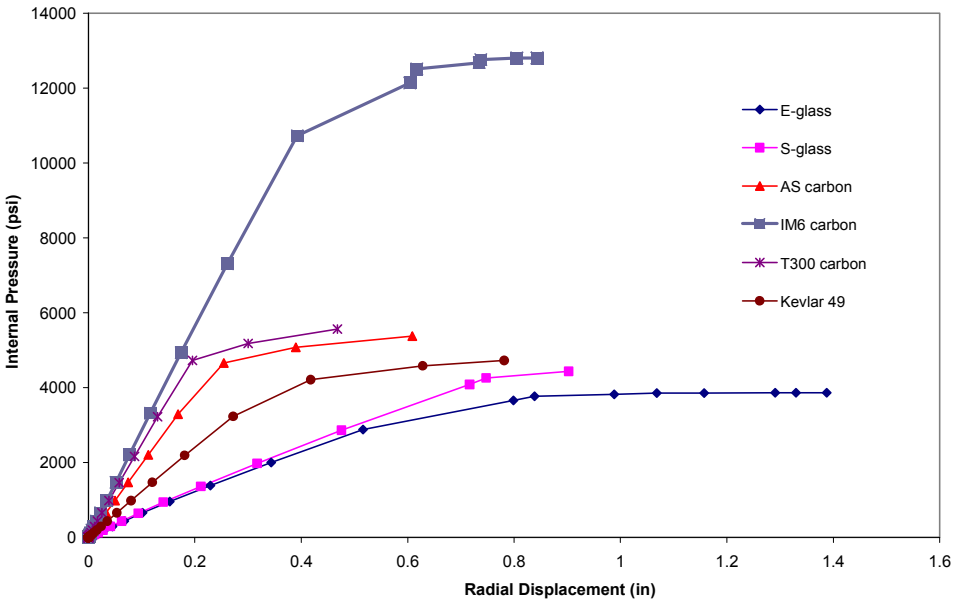

Figure 3.29: Pressure-displacement curves for Case 5

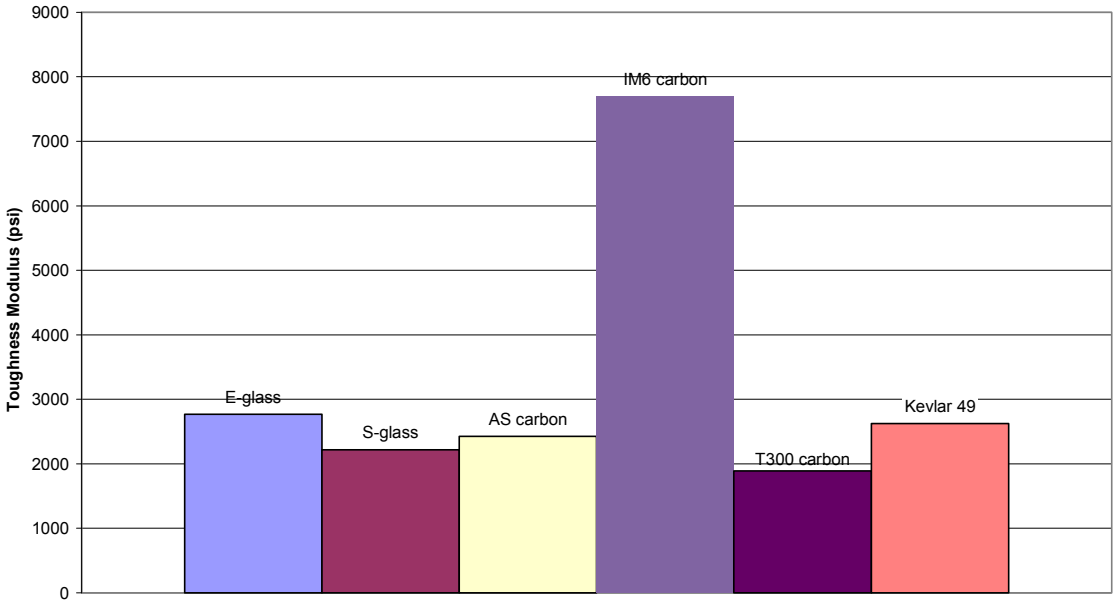

Figure 3.30: Comparison of toughness moduli for Case 5

As shown in Figure 3.29, IM6 carbon has the highest strength; however, E-glass shows the most ductility. The toughness modulus ultimately proves, though, that the IM6 carbon fiber performs the best in terms of energy capacity.

3.7.4 Effects of Geometric Parameters

The next set of models was created in order to analyze the geometric parameters—i.e., pipe diameter (or radius) and wall thickness. The comparison of pipe diameters is classified as Case 6, and the comparison of wall thicknesses is classified as Case 7.

For Case 6, the pipe diameters were varied as the rest of the parameters were held constant. The material used was S-glass/epoxy, the fiber stacking sequence was [0/45/90]°, and the wall thickness was 1 inch. Figure 3.31 shows the effective stress-

strain curve that was calculated based off the pressure-displacement history recorded from the finite element analysis; the same effective stress-strain data was used for each diameter and for each thickness, so this curve represents the stress-strain data used for each pipe in both Case 6 and Case 7. Once input into the spreadsheet, the pressure-displacement curves were generated as shown in Figure 3.32. Since the stress-strain data did not differ, it is not necessary to calculate and compare the toughness modulus for each of the three diameters.

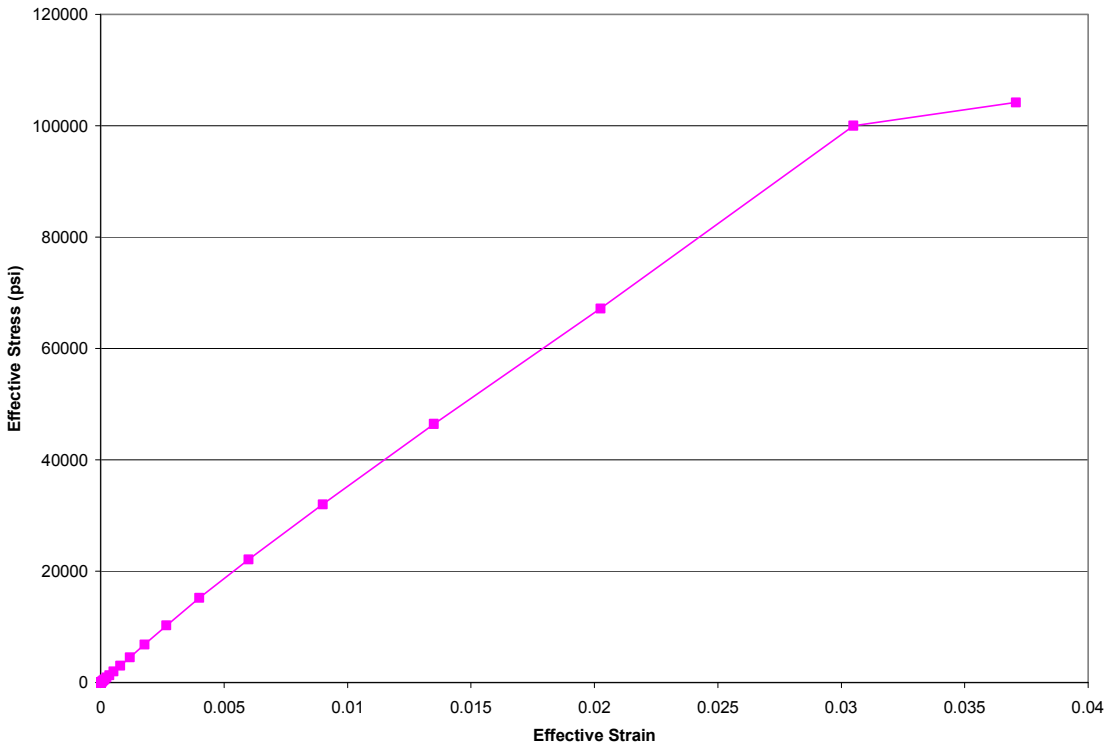

Figure 3.31: Effective stress-strain curve for Case 6 and Case 7

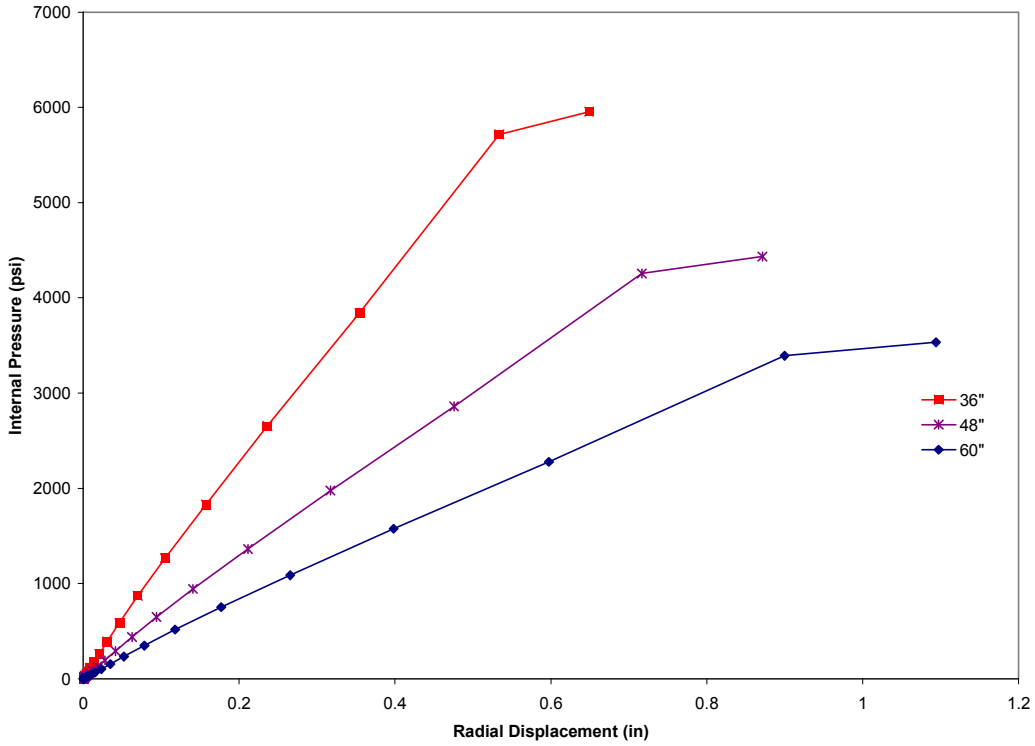

Figure 3.32: Pressure-displacement curves for Case 6

As shown by Figure 3.32, the bursting strength decreases as the diameter increases, whereas the ductility increases. This is understandable since the internal pressure and radial displacement are based off Equations 3-9 and 3-11, respectively; thus, with the thickness held constant, the pressure and ductility simply become inversely and directly proportional, respectively, to the radius at a given stress value.

For Case 7, which is very similar to Case 6, the pipe thicknesses were varied as all other parameters were held constant. Again, the material used was S-glass/epoxy, and the fiber stacking sequence was [0/45/90]°. Additionally, the pipe diameter was held constant at 48 inches. Figure 3.33 shows the resulting pressure-displacement curves for Case 6.

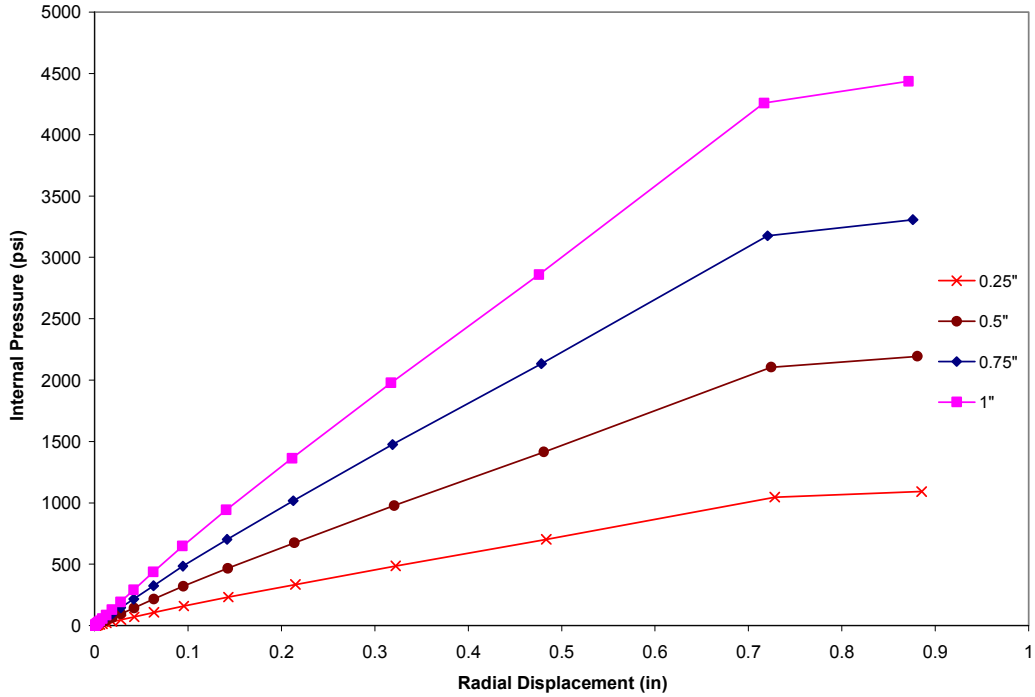

Figure 3.33: Pressure-displacement curves for Case 7

As shown by Figure 3.33, as the wall thickness increases, the bursting strength increases, but the ductility slightly decreases. Again, just as in Case 6, this is understandable because the internal pressure and radial displacement are based off Equations 3-9 and 3-11, respectively. In this case, though, the radius rather than the thickness is held constant in the equation; thus, the pressure becomes directly proportional to the thickness at a given stress value, but the ductility becomes inversely proportional to the thickness.

Ultimately, the important concept in regard to pipe geometry effects is how the internal pressure is related to the thickness-to-radius (t/r) ratio. If Equation 3-9 is followed correctly, the internal pressure is just the stress factored by this ratio; thus, the pressure should follow a linear relationship with the effective stress. Figures 3.34 and

3.35 demonstrate this relationship. Figure 3.34 shows the bursting pressure versus thickness-to-radius ratio for each pipe diameter used in Case 6, and Figure 3.35 shows those values for each wall thickness used in Case 7. Both figures ultimately show that, as this ratio increases, the bursting pressure of the pipe increases.

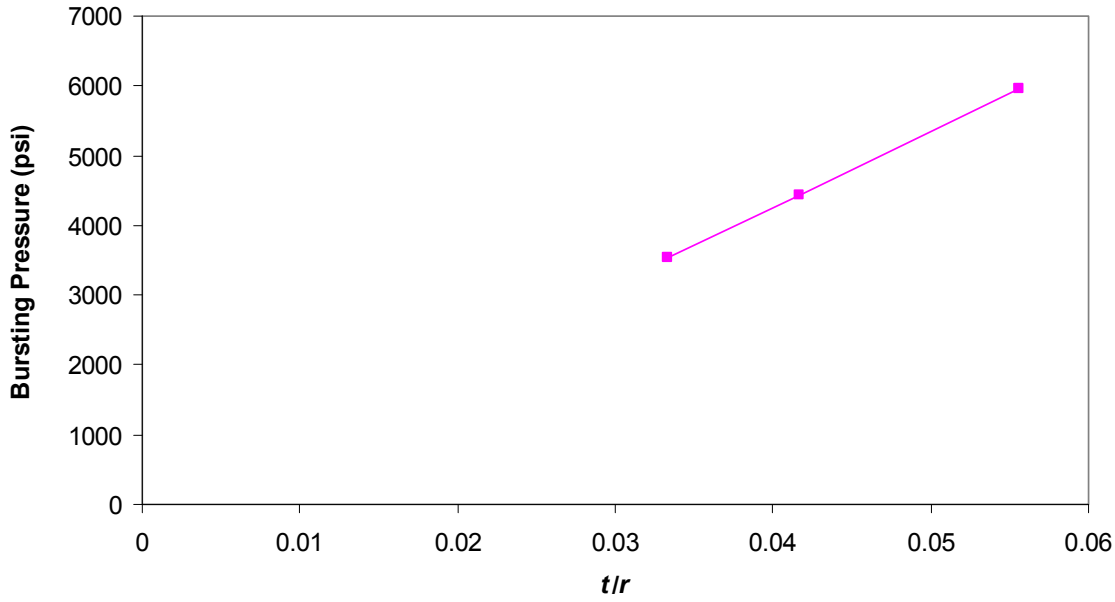

Figure 3.34: Linear relationship between bursting pressure and *t*/*r* ratio (Case 6)

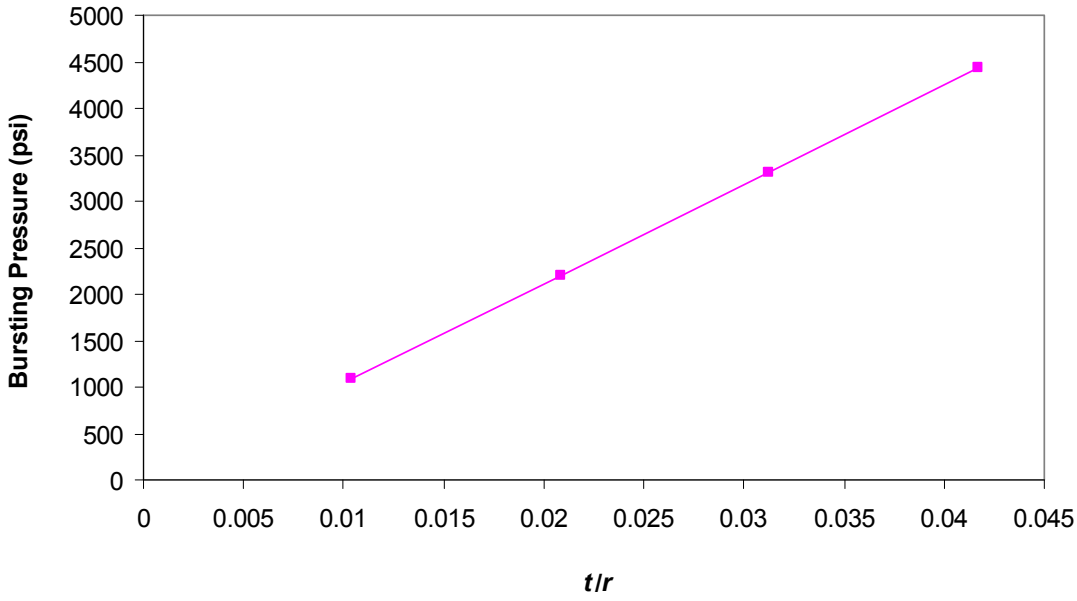

Figure 3.35: Linear relationship between bursting pressure and *t*/*r* ratio (Case 7)

3.7.5 Final Observations of Results

Reviewing the results of Cases 1 through 7, the following observations were made:

- Regardless of the density of plies used throughout the pipe wall, the total wall thickness is the parameter that most affects the pipe's resistance to internal pressure.
- The [0/45/90]° fiber stacking sequence is the most effective one in terms of strength, but the [+45/-45]° fiber stacking sequence offers the most ductility. However, the toughness modulus ultimately indicates that [0/45/90]° is the fiber stacking sequence that provides the most energy absorption capacity within the pipe.

- IM6 carbon is the most effective type of fiber in terms of strength, but E-glass offers the most ductility. However, the toughness modulus ultimately indicates that IM6 carbon is the fiber that provides the most energy absorption capacity within the pipe.
- The internal pressure follows a simple linear relationship with respect to the thickness-to-radius ratio, increasing as t/r increases.

The overall objectives of the static analysis performed on the composite pipes were the following: to create a tool that could take any stress-strain data and output a pressure-displacement relationship and an energy capacity, to determine how material and geometric parameters of the pipe affect its resistance to internal pressure, and to determine the resistance values necessary to perform a dynamic numerical evaluation on the underground composite pipe system subjected to short-term blast loading.

The tool created was the static analysis spreadsheet. Its usefulness was demonstrated in Section 3.7.1, and the material and geometric effects were summarized in the previous sections. Ultimately, the pressure-displacement relationships will be used as resistance data for the central difference method of dynamic numerical evaluation, explained further in Chapter 4.

Finally, before transitioning into the dynamic analysis of the underground composite pipe, though, it should be noted how other approaches could have been used in the static analysis. This is explained further in the following section.

3.8 Alternate Approaches to Static Analysis

In the nonlinear engineering analysis of cylindrical pipes subjected to internal pressure, it is essential to understand the relationship between stresses and strains under the condition of elasticity and under that of plasticity. If a relationship exists between stress and strain in which the unloading path completely coincides with the original loading path, the material is considered to be in a condition of *elasticity*. Although often defined by a completely linear stress-strain curve, the response can be nonlinear for an elastic material, as shown in Figure 3.36 (a). On the other hand, if the unloading path does not return along the original loading path (path *AB* in Figure 3.36 (b)), the material behaves *inelastically*, and the term *plasticity* is used to describe this type of behavior, which retains a permanent strain upon unloading (Boresi and Schmidt 2003).

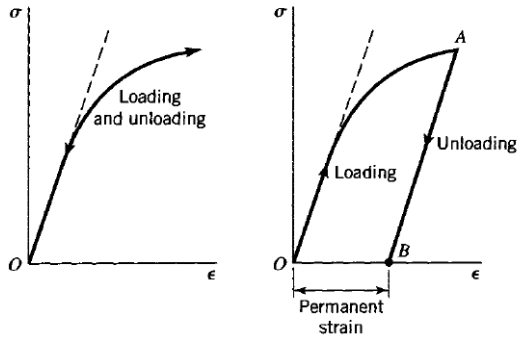

(a) (b)

Figure 3.36: (a) Nonlinear elastic response; (b) plastic response (Boresi and Schmidt 2003)

3.8.1 Elastic Condition

Earlier in the chapter, formulas from the elastic condition were used while deriving the pressure-displacement relationship, using the elastic tangent modulus E_t.

Although this modulus relates stress and strain in a linear fashion, a single value (i.e., simply E) was not used for the entire curve; instead, it was calculated incrementally along the nonlinear effective stress-strain curve. Thus, the effective stress-strain curve essentially behaved like the nonlinear elastic curve in Figure 3.36 (a).

Recalling that the relationship between internal pressure and radial displacement was derived based on pipes classified as *thin-walled*, in which the diameter-to-thickness ratio is greater than 10, it should be explained how the static analysis could be performed to account for *thick-walled* pipes.

Unlike thin-walled pipes, the hoop stress in thick-walled pipes cannot be considered constant throughout the thickness of the pipe. Instead, it varies according to its position r between the inner radius a and outer radius b (Figure 3.37). Considering only internal pressure P acting on the pipe, the hoop stress σ_h is given by the equation

$$\sigma_h = \frac{a^2 P}{b^2 - a^2}\left(1 + \frac{b^2}{r^2}\right) \tag{3-17}$$

(Ugural and Fenster 1981).

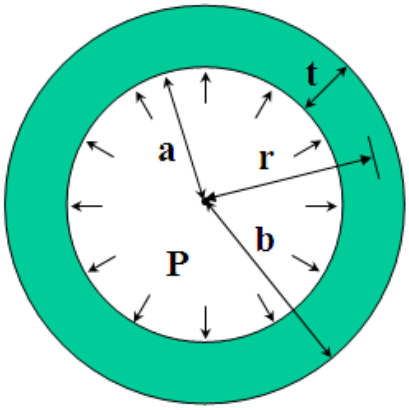

Figure 3.37: Thick-walled pipe subjected to internal pressure P, having inner radius a, outer radius b, radial coordinate r, and wall thickness t

Substituting a for r in Equation 3-17 gives the hoop stress at the inner surface of the wall, simplified as

$$\sigma_h^a = \left(\frac{a^2 + b^2}{b^2 - a^2} \right) P \tag{3-18}$$

Similarly, substituting b for r in Equation 3-17 gives the hoop stress at the outer surface of the wall, simplified as

$$\sigma_h^b = \left(\frac{2a^2}{b^2 - a^2} \right) P \tag{3-19}$$

Finally, since the static analysis methodology must solve for the internal pressure at each increment i, Equations 3-17 through 3-19 can be adjusted to solve for the incremental pressure P_i at each incremental stress σ_i. First, Equation 3-20 gives the general equation for pressure at any position r along the wall thickness.

$$P = \left(\frac{b^2 - a^2}{a^2 \left(1 + \frac{b^2}{r^2} \right)} \right) \sigma \tag{3-20}$$

Next, Equations 3-21 through 3-23 give the actual equations for incremental internal pressure P_i that could be for thick-walled pipes. Equation 3-21 gives the equation for any radial position r along the wall thickness, Equation 3-22 gives the equation at the inner surface of the wall ($r = a$), and Equation 3-23 gives the equation at the outer surface of the wall ($r = b$):

$$P_i = \left(\frac{b^2 - a^2}{a^2 \left(1 + \frac{b^2}{r^2} \right)} \right) \sigma_i \tag{3-21}$$

$$P_i^a = \left(\frac{b^2 - a^2}{a^2 + b^2} \right) \sigma_i \tag{3-22}$$

$$P_i^b = \left(\frac{b^2 - a^2}{2a^2} \right) \sigma_i \tag{3-23}$$

Now that expressions have been derived for the internal pressure, the radial displacement can be solved. Considering only internal pressure acting on a thick-walled cylinder, the radial displacement Δ in the elastic condition is given by

$$\Delta = \frac{(1-\upsilon)}{E} \cdot \frac{a^2 P}{(b^2 - a^2)} r + \frac{(1+\upsilon)}{E} \cdot \frac{a^2 b^2 P}{(b^2 - a^2) r} \tag{3-24}$$

where υ is Poisson's ratio (Ugural and Fenster 1981).

Equation 3-25 gives the actual equation for the incremental radial displacement Δ_i that could be used, for any radial position r within the pipe wall:

$$\Delta_i = \Delta_{i-1} + \frac{(1-\upsilon)}{E_i} \cdot \frac{a^2 (P_i - P_{i-1})}{(b^2 - a^2)} r + \frac{(1+\upsilon)}{E_i} \cdot \frac{a^2 b^2 (P_i - P_{i-1})}{(b^2 - a^2) r} \tag{3-25}$$

Finally, Equations 3-26 and 3-27 give the equations for incremental radial displacement at the inner surface ($r = a$) and outer surface ($r = b$) of the wall, respectively:

$$\Delta_i^a = \Delta_{i-1}^a + \frac{(1-\upsilon)}{E_i} \cdot \frac{a^3 (P_i - P_{i-1})}{(b^2 - a^2)} + \frac{(1+\upsilon)}{E_i} \cdot \frac{a b^2 (P_i - P_{i-1})}{(b^2 - a^2)} \tag{3-26}$$

$$\Delta_i^b = \Delta_{i-1}^b + 2 \cdot \frac{a^2 b (P_i - P_{i-1})}{E_i (b^2 - a^2)} \tag{3-27}$$

3.8.2 Plastic Condition

To analyze a cylindrical pipe that ultimately reaches a condition of plasticity under increasing internal pressure loading, its nonlinear stress-strain curve must be analyzed at three phases, from its stress-free state to a point of full plasticity:

- The *elastic* phase, in which the entire pipe cross-section is in the elastic range and the pressure increases to the point of initial yielding
- The *elastic-plastic* phase, in which the pressure is increased beyond initial yielding and an outer elastic zone surrounds an inner plastic zone that outwardly spreads from the inner wall surface to the elastic-plastic boundary (at $r = c$) until it reaches the outer wall surface (Figure 3.38)
- The *fully plastic* phase, in which the elastic zone has completely vanished and the plastic zone covers the entire pipe cross-section

(Chen and Han 1988).

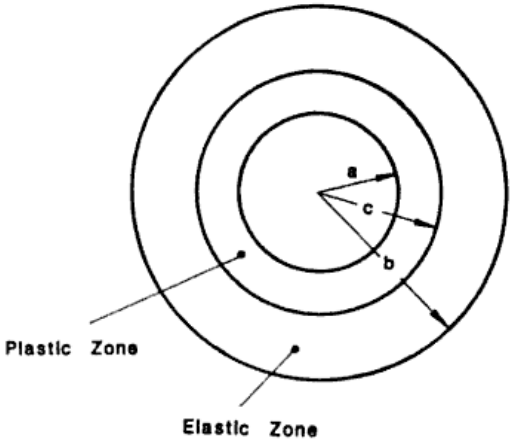

Figure 3.38: Plastic zone and elastic zone within a cylindrical pipe wall, having inner radius *a*, outer radius *b*, and elastic-plastic boundary *c* (Chen and Han 1988)

According to Chen and Han (1988), in the elastic-plastic phase, the radial displacement is controlled by the outer elastic zone and is of the same magnitude as in the elastic phase. Once fully plastic, however, the pipe expands by plastic deformation,

which consists of displacements that are much larger than those of the elastic phase, and continues at a constant plastic pressure until the pipe ultimately bursts.

In the elastic phase, clearly the equations in Section 3.8.1 (if thick-walled) or Section 3.6 (if thin-walled) suffice for determining the internal pressure and radial displacement. The limit of this phase occurs when yielding is reached at the inner surface of the wall. At this point, the maximum elastic pressure P_e, derived using the Tresca yield criterion, is given by

$$P_e = \left(\frac{b^2 - a^2}{2b^2} \right) \sigma_0 \tag{3-28}$$

where σ_0 is the uniaxial yield stress.

In the elastic-plastic phase of the stress-strain curve, the internal pressure is given by

$$P = \left(\frac{b^2 - c^2}{2b^2} + \ln \frac{c}{a} \right) \sigma_0 \tag{3-29}$$

The expression for internal pressure is now dependent on c, rather than σ and r as it was before. Thus, for this to be calculated incrementally, σ_0 would have to be a known constant, and c_i would have to be input incrementally in the elastic-plastic phase:

$$P_i = \left(\frac{b^2 - c_i^{\,2}}{2b^2} + \ln \frac{c_i}{a} \right) \sigma_0 \tag{3-30}$$

Regarding the radial displacement at this phase, since the expansion of the inner plastic zone is controlled by the elastic deformation of the surrounding elastic zone as previously mentioned, Equation 3-24 can be used with some modification, replacing P with P_e (defined in Equation 3-28) and replacing a with c. This results in the equation

$$\Delta = \frac{c^2 \sigma_0 r}{2E(b^2 - c^2)}\left(1 - \frac{c^2}{b^2}\right)\left[(1-\upsilon) + (1+\upsilon)\frac{b^2}{r^2}\right] \tag{3-31}$$

For this to be calculated incrementally, the displacement becomes a function of the elastic-plastic boundary c_i at each incremental step as it moves from the inner radius a to the outer radius b:

$$\Delta_i = \Delta_{i-1} + \frac{{c_i}^2 \sigma_0 r}{2E(b^2 - {c_i}^2)}\left(1 - \frac{{c_i}^2}{b^2}\right)\left[(1-\upsilon) + (1+\upsilon)\frac{b^2}{r^2}\right] \tag{3-32}$$

Since this is calculated beyond the elastic range, E can no longer be used incrementally; instead, it is a constant in the equation, so the average modulus of elasticity for the stress-strain data up to the yielding point can be used. Also, it is important to note that r now varies between c and b, rather than between a and b.

Substituting c_i for r and then b for r in Equation 3-32 gives the radial displacement at the elastic-plastic boundary and the outer edge, respectively:

$$\Delta_i^c = \Delta_{i-1}^c + \frac{{c_i}^3 \sigma_0}{2E(b^2 - {c_i}^2)}\left(1 - \frac{{c_i}^2}{b^2}\right)\left[(1-\upsilon) + (1+\upsilon)\frac{b^2}{{c_i}^2}\right] \tag{3-33}$$

$$\Delta_i^b = \Delta_{i-1}^b + \frac{{c_i}^2 \sigma_0 b}{E(b^2 - {c_i}^2)}\left(1 - \frac{{c_i}^2}{b^2}\right) \tag{3-34}$$

Finally, at the fully plastic phase, the elastic-plastic boundary reaches the outer edge of the wall, and the internal pressure at this point can be determined by solving Equation 3-29 at $c = b$. This *plastic collapse pressure* becomes simply

$$P = \left(\ln\frac{b}{a}\right)\sigma_0 \tag{3-35}$$

At this phase, plastic expansion occurs at this constant pressure until the pipe bursts (Chen and Han 1988).

3.8.3 Final Remarks

Reviewing the various procedures involved in determining the internal pressure and radial displacements, they are fairly straightforward in the elastic condition (for both the thin-walled and thick-walled cases), but they become somewhat more complex in the plastic condition. In this condition, the equations eventually become functions of the transitioning elastic-plastic boundary within the wall of the pipe, rather than functions of the increments of stress and strain, and the uniaxial yield stress must also be known. Because this information was not available, those equations could ultimately not be followed in the development of the static analysis methodology.

Nonetheless, a comparison was made between the bursting pressure that would be obtained at various stress values for the existing elastic thin-walled condition, the elastic thick-walled condition (evaluated at the mid-point of the wall thickness), and the plastic condition (using the ultimate effective stress value as σ_0). Using a pipe having an outer diameter of 48 inches and wall thickness of 2 inches, Figure 3.39 shows the graphical results of the internal pressure at bursting point versus the ultimate effective stress.

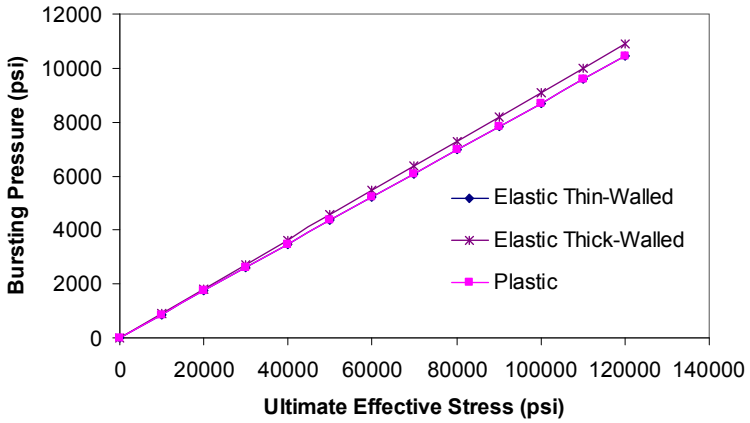

Figure 3.39: Comparison of bursting pressures

From Figure 3.39, it is evident that the results are very similar. At an ultimate effective stress value of 100,000 psi, for example, the elastic thin-walled, elastic thick-walled, and plastic bursting pressures are 8696 psi, 9100 psi, and 8701 psi, respectively. Thus, the elastic thick-walled and plastic conditions only varied 4.65% and 0.06%, respectively, from the elastic thin-walled condition.

Moreover, for the composite pipe subjected to internal pressure, it was assumed that no unloading occurred, so it was unknown whether the structure actually behaved elastically or inelastically. Thus, since final bursting pressure results closely match, either condition could be used.

In conclusion, because of the lack of a true value for the uniaxial yield stress σ_0, and because the difference in results is negligible, the plastic condition was not used. Furthermore, the elastic thin-walled condition was used over the thick-walled condition because all of the pipes analyzed were, in fact, thin-walled pipes. Had it been necessary to analyze thick-walled pipes, the procedures of Section 3.8.1 could have been used without much difficulty.

If the true value of σ_0 is known from experimentation, the pipes can be analyzed in the plastic condition. In order to do so properly, though, the internal pressure and radial displacement must become functions of a transitioning elastic-plastic boundary, and a constant value of E must be used once in that elastic-plastic phase. Judgment must be made as to whether the complexity involved in this process is worth accounting for such a small difference in results.

Finally, it appeared that the elastic thin-walled condition was appropriate for the purposes of this research project, since ultimately the static analyses were primarily

performed for composite material comparison purposes. Since that objective was achieved, dynamic analyses could be performed on the entire system; this research is explained further in Chapter 4.

Chapter 4

Single-Degree-of-Freedom Numerical Evaluation and Dynamic Response of Structural System

4.1 Overview

One of the most useful approaches for predicting the dynamic behavior of a SDOF structural system is to perform a piecewise numerical evaluation of its motion characteristics—i.e., its displacement, velocity, and acceleration—over time. Various numerical procedures exist, but focus will be paid to the central difference method, which is based on a finite difference approximation of the velocity and acceleration of the system. Perhaps the simplest and most common numerical method for nonlinear systems, the central difference method is an *explicit* approximation, meaning the dynamic response at a future time step $i + 1$ is determined by equilibrium of the equation of motion at the current time step i, rather than being determined *implicitly* by equilibrium at the future time step $i + 1$ (Chopra 2007).

This chapter will focus on the development and interpretation of a SDOF model that uses the central difference method to predict the blast response characteristics of an underground composite pipe subjected to short-duration, high internal pressure loading. After field test validation, the model can then be quickly reproduced to account for different structural characteristics—such as pipe diameters, composite materials, soil

depths, etc.—and different impulsive loadings, thereby reducing costs, time, and labor associated with further testing.

It is important to note, though, that the SDOF model was established for the purpose of proposing an approximate approach for performing engineering analyses. Its development, therefore, involves several assumptions and limitations that are discussed further throughout the chapter.

The subsequent sections of the chapter explain in further detail the following: the primary components of the structural system; SDOF methodology; development of the SDOF model; implementation of the model for various nonlinear resistances, pipe geometries, composite materials, and impulsive loadings; analyses based on dynamic response predictions of those models; interpretations of those results; and implementation of the SDOF model for a couple of design examples. Additionally, since the model developed is only a framework for predicting the actual blast response of an underground pipe, it will be discussed how the model should be further refined to account for such issues as a more realistic representation of nonlinear resistance and high strain-rate effects. Finally, it will be discussed how the dynamic response predictions can be used to address, most importantly, the concern of vehicle occupant safety.

4.2 Components of Structural System

The structural system of interest is an underground composite pipe, which supports soil and an additional source of mass above it, and is subjected to short duration, high internal dynamic pressure. Figure 4.1 shows a basic illustration of these

components. The dynamic behavior of each of these in response to blast loading within the pipe will be covered more in depth throughout the remainder of the chapter.

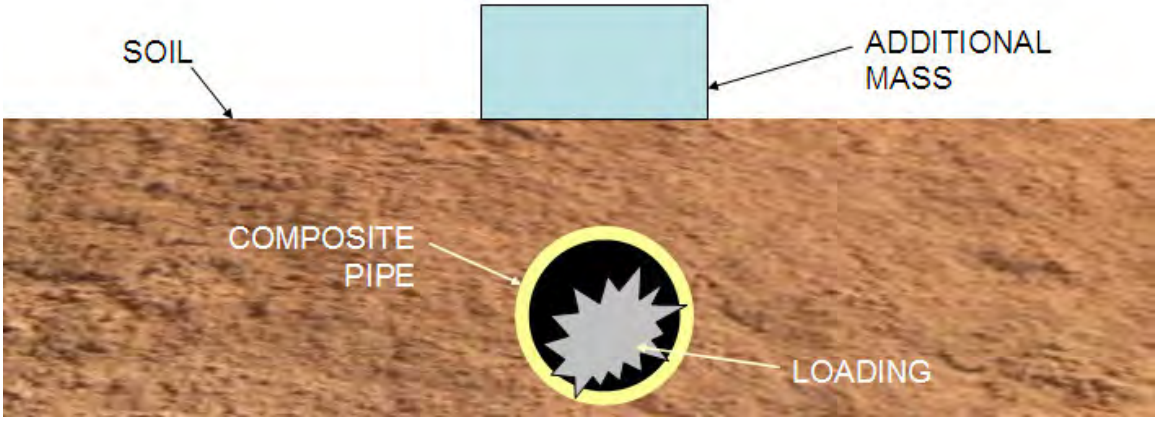

Figure 4.1: Components of underground composite pipe structural system

4.3 SDOF Methodology

The number of degrees of freedom of a structural system is defined by the number of independent displacements in which all of its masses are free to move relative to their original position. Although all structures realistically possess infinite degrees of freedom, dynamic analysis is greatly simplified if the structural system can be reasonably idealized into one in which its mass moves with a single degree of freedom.

An idealized SDOF system consists of three separate components of force defined by its inertial, energy dissipating, and resistance properties: the mass component, damping component, and elastic or inelastic stiffness component, respectively. Once the structure is subjected to a form of dynamic excitation, its response can be predicted based on equilibrium of forces, known as the SDOF equation of motion (Chopra 2007).

4.3.1 SDOF Equation of Motion

The SDOF equation of motion can be derived from Newton's second law of motion:

$$\sum F = m\ddot{u} \tag{4-1}$$

where F represents the forces acting on the mass m of the structure, and $\ddot{u}$ is the acceleration of the mass over time. The forces on the left side of the equation consist of the external force p at time t ($p(t)$), the damping force f_D, and the resisting force f_S. Thus, we now have

$$p(t) - f_D - f_S = m\ddot{u} \tag{4-2}$$

The damping force and resisting force are defined by Equations 4-3 and 4-4, respectively:

$$f_D = c\dot{u} \tag{4-3}$$

$$f_S = ku \tag{4-4}$$

where c is the viscous damping coefficient, k is the linear elastic stiffness, and $\dot{u}$ and u are the velocity and displacement, respectively, of the mass over time. It is important to note that this resistance relationship applies to *linear* systems only. It will be discussed later how to account for nonlinearity.

Equation 4-2 can be rearranged to solve for the external force. Substituting Equations 4-3 and 4-4 for the damping and resisting forces, respectively, yields

$$m\ddot{u} + c\dot{u} + ku = p(t) \tag{4-5}$$

This is the SDOF equation that is the basis for solving the dynamic response of a linear elastic system. Since the underground composite pipe system actually behaves nonlinearly, though, the resistance component of this equation must be modified accordingly.

Figure 4.2 shows an idealized mass-damper-spring system that is often used as a classic representation of a structure governed by the linear elastic SDOF equation of motion. (The spring represents the resisting force.)

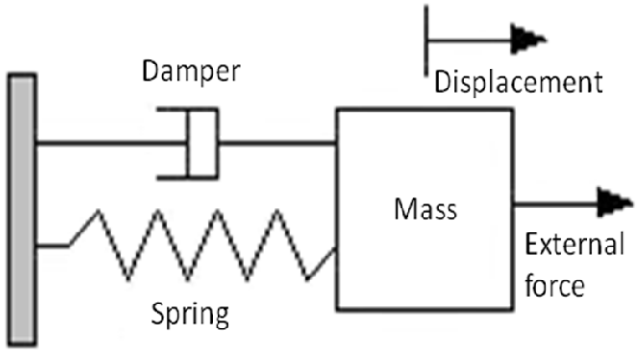

Figure 4.2: Idealized mass-damper-spring system (Ashhab 2004)

Overall, it can be seen that the SDOF equation of motion consists of four primary components of input: mass, damping, resistance, and loading history. With knowledge of these, the displacement, velocity, and acceleration can be output over time. For the purpose of this research project, damping is neglected due to the negligible amount of energy dissipated from such short duration dynamic loading, as will be discussed later in the chapter; the resistance data is provided by static analysis of the composite pipe, as discussed in Chapter 3; the mass is determined from the weight of the soil and any other mass overlaying the pipe; and the loading history consists of a very high peak pressure over a very short time duration, known as *impulsive* loading (although the SDOF model can be run under any type of dynamic loading, as discussed later in the chapter). Details of each of these components will be explained in the development of the SDOF model throughout the chapter.

Ultimately, the only practical way to solve for the dynamic response of the underground composite pipe system is to use numerical time-stepping techniques that follow Equation 4-5. Thus, the central difference method will be used as the basis of the SDOF model. Before explaining the central difference method (Section 4.3.6), however, it is important to understand the concepts of nonlinear dynamic analysis, impulsive loading, damping effects, and numerical time-stepping evaluation in regard to the SDOF system being studied—these are the subjects of the following four sections, respectively (Chopra 2007).

4.3.2 Nonlinear Dynamic Analysis

Nonlinear dynamic analysis may consist of any combination of material nonlinearity, geometric nonlinearity, and contact problems.

Structural systems having only material nonlinearity are the most common ones analyzed. The nonlinear effect in this case stems from the nonlinear stress-strain relation of the resisting material.

Geometric nonlinearity exists in structural systems that experience large displacements, large rotations, and either large or small strains. Equilibrium equations are formulated with respect to the changing geometry. The material stress-strain relation can be either linear or nonlinear.

Contact problems involve boundary conditions that change during the motion of the structural system (Tedesco et al. 1999). This type of nonlinearity will be explained in more detail later in the chapter.

For the underground composite pipe system under study, the composite pipe material is the source of material nonlinearity, as its effective stress-strain curves developed in Chapter 3 are nonlinear. Also, both geometric and material nonlinearity were accounted for when using the Riks method to calculate the load-displacement history. As mentioned in Chapter 3, the structure's stiffness matrix is adjusted at each loading increment to account for geometric deformations and the composite material's nonlinear stress-strain relationship.

Simply taking into account material and geometric nonlinearity, then, the SDOF equation of motion, Equation 4-5, should be modified for the underground composite pipe system. Excluding the linear elastic stiffness constant k, the SDOF equation of motion now becomes

$$m\ddot{u} + c\dot{u} + f_S(u) = p(t) \tag{4-6}$$

This is the SDOF equation of motion that is the basis for performing *nonlinear* numerical evaluation of the dynamic response of the underground composite pipe system. From this equation, it can be seen that, rather than using a constant linear coefficient k, a resistance function f_S is needed instead; its value will vary nonlinearly depending on the displacement u (Figure 4.3).

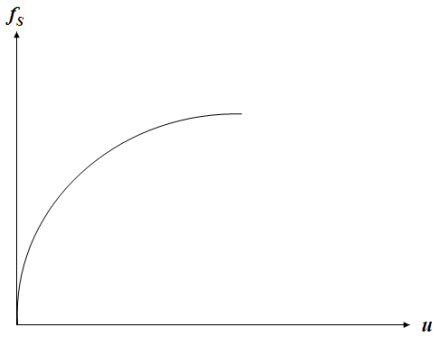

Figure 4.3: Nonlinear resistance function

4.3.3 Impulsive Loading

Various forms of dynamic excitation are classified in the study of structural dynamics, such as harmonic or periodic forces, step forces, linearly increasing or decreasing (ramp) forces, etc. (Figure 4.4). However, of interest for blast analysis are *impulsive* excitations. This class of forces essentially consists of a single, very large pulse over a very short duration of time relative to the natural vibration period of the structure. Its curve may take partial form of any of the previously mentioned forces. For instance, it may actually be a periodic force, but the force abruptly ends very quickly once it falls to zero pressure, rather than continuing cyclically over time (Chopra 2007).

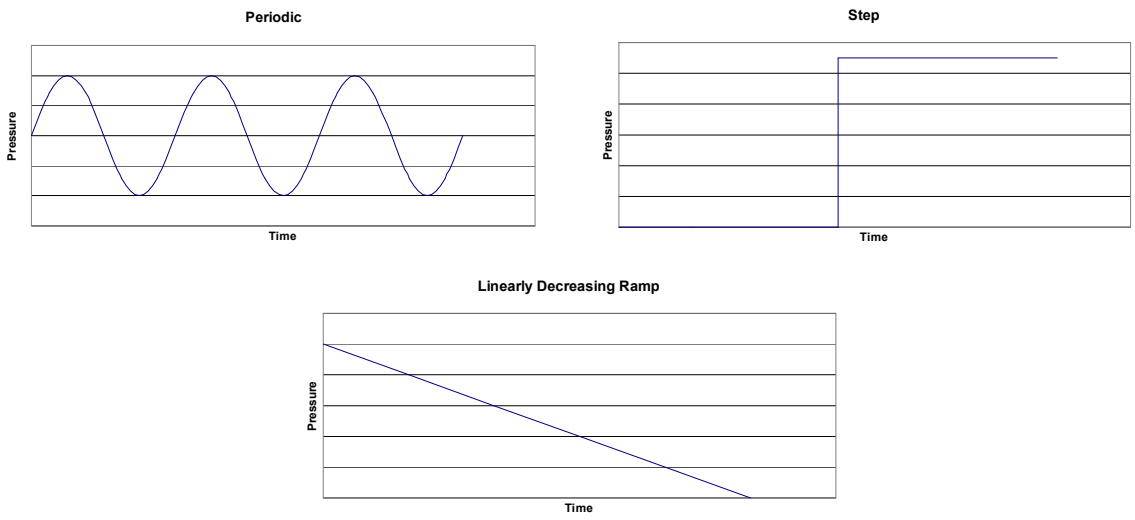

Figure 4.4: Various forms of dynamic excitation

It was explained in Chapter 2 that the pressure pulse from a blast in open air shows an instantaneous increase to a peak pressure, followed by a nonlinear decrease in pressure until it drops below the ambient atmospheric pressure and into a negative phase (Figure 2.1). Recall that the impulse is simply the area under the pressure-time curve.

In the case of a buried composite pipe subjected to internal blast loading, though, the negative phase does not apply since there is no suction. Suction occurs in cases of large blasts detonated externally to the structure. Furthermore, even when negative-phase loading does occur, it is often neglected because it is not as well understood as the positive phase due to a lack of sufficient data, since only the positive phase load has been measured in many tests. Moreover, this approach acts more conservatively since it gives a structural response similar to or slightly higher than the true blast load (USACE PDC 2008).

When only positive-phase loading is taken into account, it is often simplified to the shape of a right triangle as shown in Figure 4.5, having equal impulse and peak

pressure as the actual positive phase curve, but a shorter duration t_d than the actual positive phase duration (USACE PDC 2008).

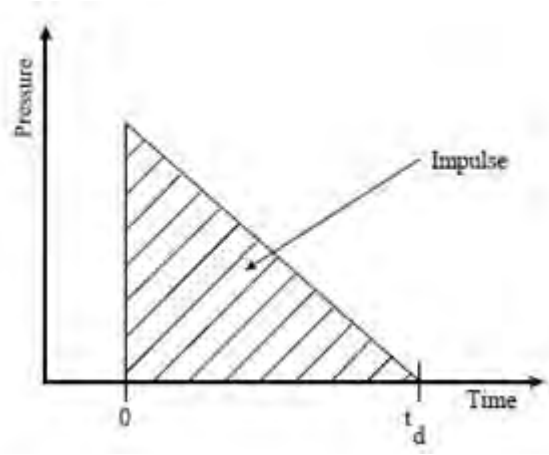

Figure 4.5: Simplified pressure-time history for a positive phase blast load (adapted from USACE PDC 2008)

It is apparent from Figure 4.4 that the simplified impulsive loading fits the form of a linearly decreasing ramp force. A force of this form varies over time as

$$p(t) = p_0 - \frac{t}{t_d} p_0 \tag{4-7}$$

where p_0 is the peak pressure and t_d is the pulse duration.

If the pulse duration is shorter than half the natural period of the system, the maximum response occurs after its pulse phase. For a system with linear elastic stiffness, the natural period T_n is given by

$$T_n = 2\pi\sqrt{\frac{m}{k}} \tag{4-8}$$

(Although this research involves nonlinear resistance as explained previously, and thus the natural period obviously actually varies, the resistance can be thought of as a

simplified linear elastic form for the purpose of the current discussion.) At such a short pulse duration, the maximum deformation u_0 is proportional to the impulse I:

$$u_0 = \left(\frac{2\pi}{k \cdot T_n} \right) I \tag{4-9}$$

For the simplified right triangular impulsive loading, the impulse is simply

$$I = \frac{p_0 t_d}{2} \tag{4-10}$$

Substituting this into Equation 4-9, the maximum deformation becomes

$$u_0 = \left(\frac{p_0 \pi}{k} \right) \frac{t_d}{T_n} \tag{4-11}$$

Equation 4-9 shows that the maximum deformation is ultimately controlled by the area under the pressure-time curve, and Equation 4-11 implies that it varies linearly with t_d/T_n if the loading is simplified as shown in Figure 4.5 (Chopra 2007).

4.3.4 Effects of Damping

According to Chopra (2007), for a structural system imposed to an impulsive excitation, the effect of damping is usually not very influential on its dynamic response unless it is highly damped. The energy dissipated is very small in systems subjected to such loading. It is conservative, but not overly conservative, to neglect damping when approximating the dynamic response of impulsively loaded structures.

Tedesco (1999) reaffirms this by stating that damping effects are negligible under impulsive loading and, thus, damping may be omitted when calculating dynamic response. Furthermore, the impulsive loading is often very extreme for internal blast loading, so an approach is desired that yields reasonably accurate results when a pipe

bursts; however, there is no way to accurately quantify damping in such a scenario. Therefore, although some of the equations involved in the development of the numerical SDOF model include the damping coefficient c, this coefficient will always be given a value of zero henceforth.

4.3.5 Numerical Time-Stepping Evaluation

To solve for the analytical solution of Equation 4-6, a numerical time-stepping technique is necessary, in which the equation will be solved at discrete steps, $i = 0$ to N, subjected to the initial conditions

$$u_0 = u(0) \tag{4-12}$$

$$\dot{u}_0 = \dot{u}(0) \tag{4-13}$$

The time and the applied force are given by sets of discrete values t_i and $p_i = p(t_i)$, respectively. The difference between successive time instants is the incremental time interval

$$\Delta t_i = t_{i+1} - t_i \tag{4-14}$$

It is more commonly known simply as the *time step*, and will be taken as constant henceforth ($\Delta t = \Delta t_i$).

The response values are denoted as u_i, $\dot{u}_i$, and $\ddot{u}_i$ for the displacement, velocity, and acceleration, respectively, at each time instant t_i. These values must satisfy Equation 4-6 for each increment i. Thus, the governing incremental SDOF equation of motion becomes

$$m\ddot{u}_i + c\dot{u}_i + (f_S)_i = p_i \tag{4-15}$$

where $(f_S)_i = f_S(u_i)$. Numerical procedures allow the responses u_{i+1}, $\dot{u}_{i+1}$, and $\ddot{u}_{i+1}$ to be determined at time $i + 1$:

$$m\ddot{u}_{i+1} + c\dot{u}_{i+1} + (f_S)_{i+1} = p_{i+1} \tag{4-16}$$

For $i = 0$ to N, numerical time-stepping evaluation thus gives the response values at each time increment $i = 1$ to $N + 1$, provided the initial conditions of Equations 4-12 and 4-13 are given.

Numerical time-stepping evaluation is an approximate technique that must meet three general requirements: convergence, stability, and accuracy. *Convergence* implies that the procedure must approach the exact solution as the time step decreases (approaching $\Delta t = 0$), *stability* requires the numerical solution to be stable in spite of numerical rounding errors, and *accuracy* means that the procedure must produce results that are very close to the exact responses (Chopra 2007).

4.3.6 Central Difference Method

The central difference method is a numerical integration technique that is based on an incremental approximation of the first and second derivatives of displacement with respect to time—i.e., the velocity and acceleration. These central difference approximations are expressed at time i as

$$\dot{u}_i = \frac{u_{i+1} - u_{i-1}}{2\Delta t} \tag{4-17}$$

$$\ddot{u}_i = \frac{u_{i+1} - 2u_i + u_{i-1}}{(\Delta t)^2} \tag{4-18}$$

Substituting these equations into the nonlinear, incremental SDOF equation of motion, Equation 4-15, yields

$$m\frac{u_{i+1}-2u_i+u_{i-1}}{(\Delta t)^2}+c\frac{u_{i+1}-u_{i-1}}{2\Delta t}+(f_S)_i=p_i \tag{4-19}$$

Since u_i and $u_{i\text{-}1}$ are known from using the procedure at previous time steps, u_{i+1} is the desired value for which to solve. Thus, Equation 4-19 is rearranged so that u_{i+1} can more conveniently be solved for:

$$\left[\frac{m}{(\Delta t)^2}+\frac{c}{2\Delta t}\right]u_{i+1}=p_i-\left[\frac{m}{(\Delta t)^2}-\frac{c}{2\Delta t}\right]u_{i-1}+\frac{2m}{(\Delta t)^2}u_i-(f_S)_i \tag{4-20}$$

or

$$\hat{k}u_{i+1}=\hat{p}_i \tag{4-21}$$

where

$$\hat{k}=\frac{m}{(\Delta t)^2}+\frac{c}{2\Delta t} \tag{4-22}$$

and

$$\hat{p}_i=p_i-\left[\frac{m}{(\Delta t)^2}-\frac{c}{2\Delta t}\right]u_{i-1}+\frac{2m}{(\Delta t)^2}u_i-(f_S)_i \tag{4-23}$$

Now, Equation 4-21 is rearranged to solve for u_{i+1}:

$$u_{i+1}=\frac{\hat{p}_i}{\hat{k}} \tag{4-24}$$

Recalling from the beginning of the chapter that the central difference method acts *explicitly*, this equation proves that statement, since the solution at time $i + 1$ is found based upon the equilibrium conditions at time i (rather than at time $i + 1$).

Before fully implementing the central difference method, two more initial calculations must be performed: $u_{\text{-}1}$ and $\ddot{u}_0$. The initial acceleration $\ddot{u}_0$ can be determined

by substituting $i = 0$ into the incremental equilibrium equation, Equation 4-15, and solving for $\ddot{u}_0$:

$$\ddot{u}_0 = \frac{p_0 - c\dot{u}_0 - (f_S)_0}{m} \tag{4-25}$$

This is easily calculated using the constants c and m, and the initial values p_0, $\dot{u}_0$, and $(f_S)_0$. The initial force is given from the pressure-time history, and the initial velocity is given from Equation 4-13. The initial resistance is always zero since it acts *explicitly*; therefore, it is calculated based only on the response at time i, rather than $i + 1$.

The displacement u_{-1} must be known since, as can be seen from Equations 4-23 and 4-24, calculation of u_1 requires $\hat{p}_0$, and calculation of $\hat{p}_0$ requires u_0 and u_{-1}. The initial displacement u_0 is always given. To derive an expression for u_{-1}, though, Equations 4-17 and 4-18 are first expressed at $i = 0$:

$$\dot{u}_0 = \frac{u_1 - u_{-1}}{2\Delta t} \tag{4-26}$$

$$\ddot{u}_0 = \frac{u_1 - 2u_0 + u_{-1}}{(\Delta t)^2} \tag{4-27}$$

Solving for u_1 in Equation 4-26 and substituting it into Equation 4-27 yields the expression for u_{-1}:

$$u_{-1} = u_0 - \Delta t(\dot{u}_0) + \frac{(\Delta t)^2}{2}\ddot{u}_0 \tag{4-28}$$

To summarize, given the initial displacement and velocity from Equations 4-12 and 4-13, respectively, as well as a constant time step, a pressure-time history following that time step, a nonlinear resistance function with respect to displacement, the mass, and the damping coefficient, a constant value for $\hat{k}$ and an incremental value for $\hat{p}_i$ can be

determined, which ultimately yield the displacement u_{i+1} from Equation 4-24. Once this displacement is known, the velocity and acceleration at time $i + 1$ can be determined from Equations 4-17 and 4-18, respectively.

Recall from the end of Section 4.3.5 that the requirements of convergence, stability, and accuracy must be met for a numerical time-stepping method to be useful. For the central difference method, convergence and accuracy can only be validated by actually knowing the exact results based upon test results. Thus, only the issue of *stability* is discussed at this point.

A *conditional* stability requirement for the central difference method is that the time step must be small enough so that

$$\Delta t < \frac{T_n}{\pi} \tag{4-29}$$

Recall that T_n is the natural period of the structural system. For a SDOF system, however, the time step must be smaller for adequate accuracy in the response values. Thus, a maximum requirement of one-tenth of the natural period will be used for the time step in the development of the SDOF model:

$$\Delta t < 0.1T_n \tag{4-30}$$

A time step greater than this may yield meaningless response values because of numerical round-off errors (Chopra 2007).

4.4 Development of SDOF Model

Simply stated, a SDOF model was developed for the purpose of predicting the blast response of an underground composite pipe system with an additional mass above it. Figure 4.6 shows a flowchart used in developing the model. The following subsections

will explain the unit system; the components necessary for numerical evaluation, such as mass, resistance, time step, and loading history; and finally the compilation of these components into the central difference method and implementation of its formulas into a spreadsheet.

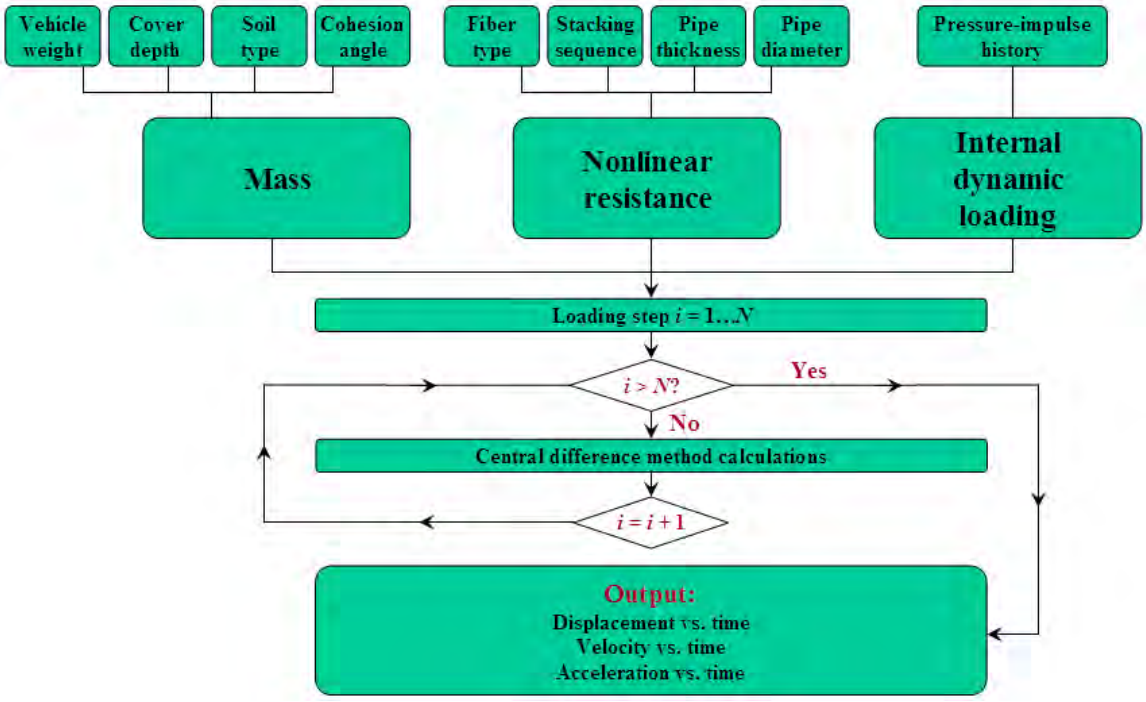

Figure 4.6: Flowchart for SDOF model

4.4.1 Unit System

The U.S. customary unit system was used for all calculations and results associated with the SDOF model. Table 4.1 shows the unit used for each type of measurement.

Table 4.1: Units of measurement for SDOF model

Measurement	Unit
Weight	pound (lb)
Material density	pound per cubic foot (pcf)
Mass	pound-second squared per inch (lb-s^2/in)
Geometric dimensioning	inch (in)
Cross-sectional area	square inch (in^2)
Soil cohesion angle	degree (°)
Damping coefficient	pound-second per inch (lb-s/in)
Time	second (s) or millisecond (ms)
Displacement	inch (in)
Velocity	inch per second (in/s)
Acceleration	inch per second squared (in/s^2)
Internal pressure / resisting force	pound per square inch (psi)
Internal loading	pound (lb)
Explosive density	pound per cubic inch (pci)

4.4.2 Mass

The mass of the entire structural system is an important parameter for central difference method calculations. For the SDOF model, it was calculated by adding the weights of each significant component of the system, and then dividing this by the acceleration due to gravity of 386.4 in/s^2.

Primarily, the soil and any additional mass above the pipe contribute to the overall mass that should be considered. The composite pipe contributes mass, but because its weight varies depending on the material type (e.g., E-glass/epoxy or carbon/epoxy), and because its weight is negligible compared to the soil and other mass, the mass of the pipe is neglected.

The parameters used to calculate the weight of the soil were the soil density (depending on soil type), cohesion angle, and cover depth. Figure 4.7 illustrates the cohesion angle and cover depth, as well as the boundary of the soil mass considered for

the structural system. As seen in the figure, the cohesion angle represents the angle between the mass boundary and a horizontal projection from mid-height of the pipe, and the boundary of the soil mass follows the dashed line along this angle to the top of the soil. (It is important to note, though, that the cohesion angle factors into only the mass, not the resistance, portion of the system.) The cover depth is simply the distance from the top soil surface to the top of the pipe.

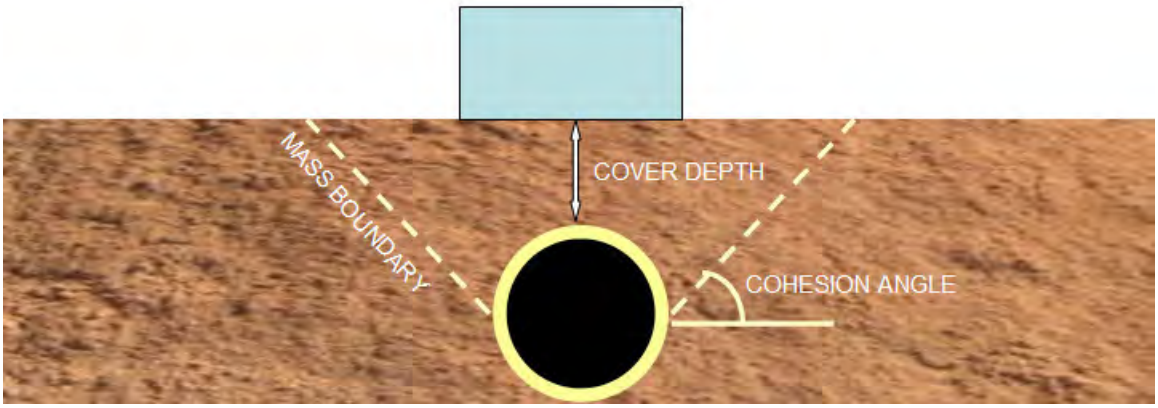

Figure 4.7: Soil dimensions and mass boundary

To calculate the total weight of the soil, the density is simply multiplied by the total volume. Due to the symmetrically propagating pattern of blast waves, it was decided to treat the volume of the soil as a truncated cone (Figure 4.8). Thus, with soil density ρ and cover depth h, the total weight of the soil is

$$w_{soil} = \rho \cdot \frac{\pi}{12} \cdot h \cdot (b_1^2 + b_2^2 + b_1 b_2) \tag{4-31}$$

where b_1 and b_2 are the top and bottom diameters, respectively. The bottom diameter b_2 is equivalent to the outer diameter of the composite pipe, and the top diameter b_1 can be determined based on the cohesion angle and cover depth.

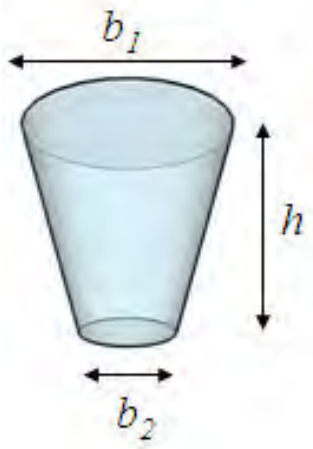

Figure 4.8: Truncated cone used for calculation of soil volume (Nova Scotia DOE 2011)

Calculation of the weight of additional mass depends on what mass is positioned above the pipe. This may consist of any combination of a vehicle, roadway pavement, concrete barriers, a building, a human, etc.

The contributing weight of the soil and additional mass were added together to obtain the total weight of the system. Figure 4.9 shows an example spreadsheet that was created to calculate the total weight. The total mass m of the system will be calculated in the SDOF model by dividing this total weight w by the acceleration due to gravity g:

$$m = \frac{w}{g} \tag{4-32}$$

System	Long. length at top of pipe	52	in
	Long. length at road level	76	in
Soil	Density	120	pcf
	Cohesion angle	45	°
	Cover depth	12	in
	SOIL WT	2712.242	lbs
Additional Mass	Mass 1	2600	lbs
	Mass 2	0	lbs
	Mass 3	0	lbs
	ADDITIONAL MASS WT	2600	lbs
	TOTAL WEIGHT =	5312.2	lbs

Figure 4.9: Example calculation of total weight of structural system

4.4.3 Resistance

As explained in Section 4.3.2, material and geometric nonlinearity must be accounted for in order to properly perform the nonlinear dynamic analysis. These nonlinearities exist in the resistance of the structure, ultimately stemming from the nonlinear stress-strain relation of the composite material as determined from finite element modeling in Chapter 3. From the incremental nonlinear SDOF equation of motion, Equation 4-15, the resisting force $(f_S)_i$ must be expressed in terms of the displacement u_i at time i. Since the composite pipe acts as the resisting mechanism for the underground composite pipe system, the pressure-displacement curves computed in Chapter 3, which are generated directly from the effective stress-strain data, will be used as the actual numerical data of the nonlinear resistance function. Figure 4.10 shows an

example of the nonlinear resistance curve. The internal pressure represent $(f_S)_i$, and the radial displacement represents u_i.

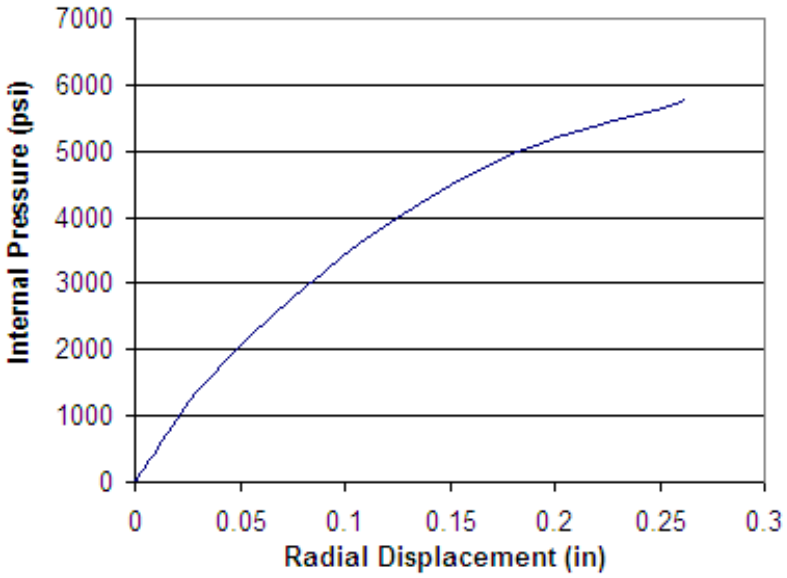

Figure 4.10: Example of nonlinear resistance curve used in SDOF model

The SDOF model extracts the displacement u_i at the current time i, and then searches for it within the nonlinear resistance curve data. Once it finds that displacement, it obtains the internal pressure P_i at that point and the resisting force at time i is computed as

$$(f_S)_i = P_i \cdot A \tag{4-33}$$

where A is the cross-sectional area subjected to internal pressure. If an exact match for the displacement u_i is not found within the composite's nonlinear resistance data, the pressure is interpolated between the displacement points that are just below and above u_i, unless, however, u_i exceeds the maximum radial displacement of the composite's data; in

this case, the composite pipe is resisting no more, and the resisting force simply becomes zero.

The area subjected to internal pressure is constant within the SDOF model, and it is calculated as

$$A = [\pi(D_o - 2T)] \times D_o \tag{4-34}$$

where T is the wall thickness of the composite pipe and D_o is its outer diameter. This is simply the internal circumference multiplied by a longitudinal length of pipe equivalent to the pipe's outer diameter. A longitudinal length equivalent to the pipe's outer diameter is used since this is approximately equal to the longitudinal length along the bottom of the soil volume.

4.4.4 Time Step

Recalling from Section 4.3.6 that the time step cannot exceed one-tenth of the natural period of the structural system (Equation 4-30), a conditional programming statement was created within the SDOF model to account for this upper limit. It is required by the user to input the pressure-time data in equal time step intervals. Therefore, a formula could be created to test whether the difference between the times at simply the first two loading increments is less than one-tenth of the natural period. If it is, calculation of the time step is calculated as the difference between those two times, and this value is used throughout the central difference method computations at every loading increment; if not, though, an error message is displayed instead of calculating the time step, indicating to the user that the time step is too large. This ultimately results in errors for the central difference calculations at every loading increment. Thus, in order for the

SDOF model to run successfully, a sufficiently small time step with respect to the total load duration must be used.

4.4.5 Loading History

As just mentioned, the pressure-time data must be input into the SDOF model at equal time increments. The loading history is input as a simplified triangular impulse load, as explained in Section 4.3.3 (Figure 4.5). It is important to emphasize, though, that this type of loading is not a requirement for the central difference computations, and the SDOF model can actually be run under any form of dynamic loading.

The pressure-time histories of structures subjected to internal explosions can be extremely complicated. Figure 4.11 shows an example loading history from an 18-inch-diameter sphere of explosive material within a 48-inch diameter pipe. The impulse was calculated as the integral of the pressure-time curve. Appendix B shows a figure of the underground composite pipe model, with the location of the center of gravity of the explosive source and the location of the "target" at which the pressure-time data was recorded.

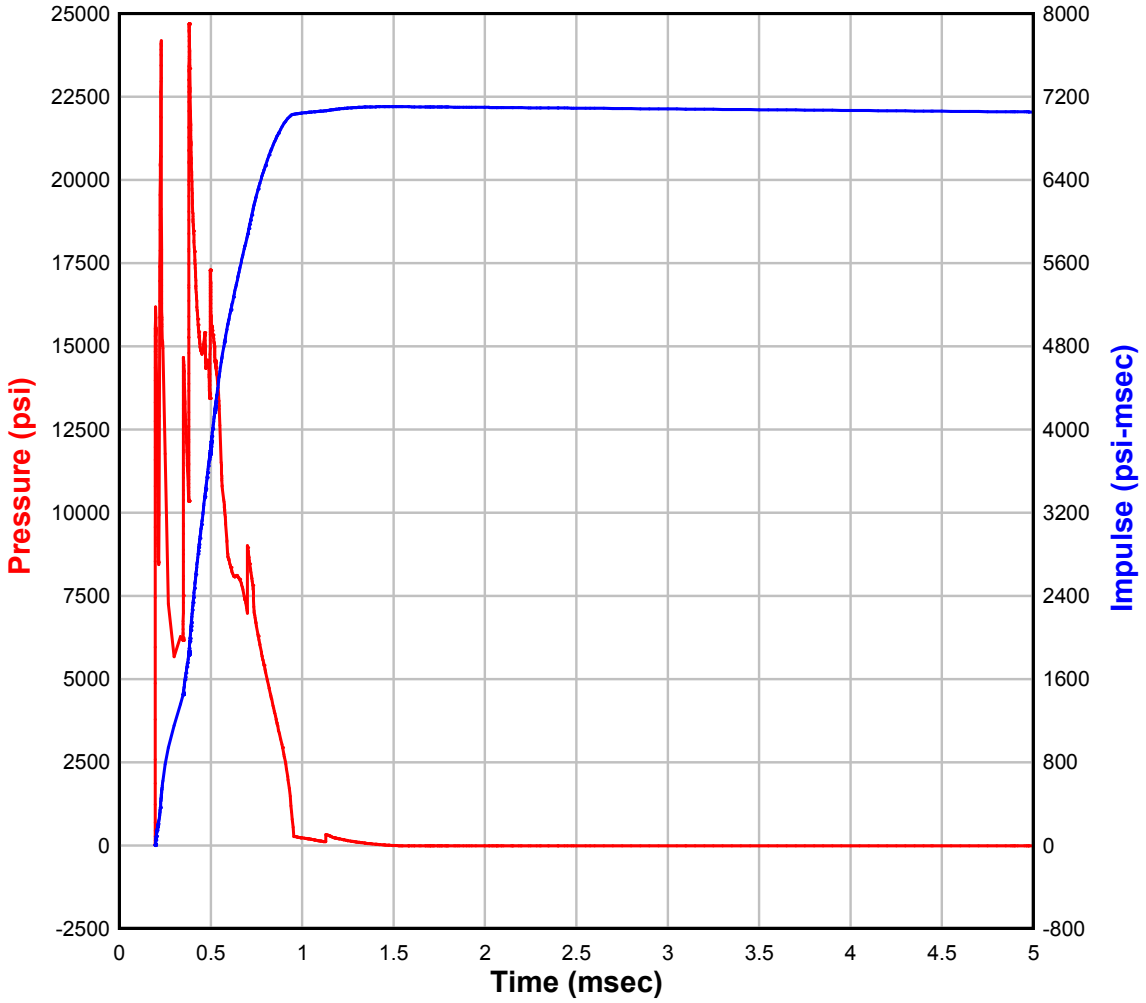

Figure 4.11: Example pressure-time history with calculated impulse curve

The weight of explosive material used was determined based on its density and its spherical diameter. Generally, two diameters of explosive material were used for each pipe diameter—one equivalent to one-fourth the pipe diameter and the other equivalent to half the pipe diameter. Thus, multiplying its density by its spherical volume, the total weight of explosive material could be determined. The density of explosive material used in forthcoming calculations was 0.056 pci, which is similar to TNT (Agrawal and Hodgson 2007).

Appendix B shows the original pressure-time history curves for all the examples generated within this chapter. Sixteen different pressure-time curves were generated, and special nomenclature is used to label each curve. Table 4.2 lists the labels and their respective loading sphere diameters and pipe diameters. Refer to Appendix B for the pressure-impulse histories of these loadings.

Table 4.2: Internal pressure loading labels

Label	Loading Sphere Diameter (in)	Pipe Diameter (in)
HE-1	8	16
HE-2	4	16
HE-3	12	24
HE-4	6	24
HE-5	18	36
HE-6	9	36
HE-7	24	48
HE-8	12	48
HE-9	30	60
HE-10	15	60
HE-11	8	24
HE-12	8	36
HE-13	8	48
HE-14	18	48
HE-15	18	60
HE-16	24	60

For each load case, the peak pressure and impulse were obtained from the loading history graph, and these numbers were used to simplify the graph into the triangular impulsive loading shape of Figure 4.5. Knowing these two values, the total pulse duration t_d was determined based on the area of a triangle. The data was then modified so that the peak pressure occurred at $t = 0$ seconds, decreasing linearly until dropping to 0 psi at time t_d. This impulsive loading was then divided into increments small enough to meet the

maximum time step requirement of one-tenth the natural period of the structure; generally, division into about 100 time steps was well sufficient to meet the requirement. (Each simplified pressure-time history has a load duration of only a few milliseconds, so the time steps are thus only a few microseconds long.)

The loading curve was then extended at zero pressure for an amount of time (keeping the same constant time step) long enough to adequately calculate the dynamic response curves (displacement, velocity, and acceleration over time). This will be explained further in Section 4.5.

4.4.6 Implementation of Central Difference Method Formulas

Table 4.3 summarizes the procedure followed in Section 4.3.6 for the central difference method. These steps were used to create a spreadsheet, which acts as the *SDOF model*. The spreadsheet outputs the displacement, velocity, and acceleration over time (Chopra 2007).

Table 4.3: Central difference method steps followed in development of SDOF model (adapted from Chopra 2007)

	Step	Equation
Initial calculations	1	$\ddot{u}_0 = \frac{p_0 - c\dot{u}_0 - (f_S)_0}{m}$
	2	$u_{-1} = u_0 - \Delta t(\dot{u}_0) + \frac{(\Delta t)^2}{2}\ddot{u}_0$
	3	$\hat{k} = \frac{m}{(\Delta t)^2} + \frac{c}{2\Delta t}$
	4	$a = \frac{m}{(\Delta t)^2} - \frac{c}{2\Delta t}$
	5	$b = -\frac{2m}{(\Delta t)^2}$
Incremental calculations	6	$\hat{p}_i = p_i - au_{i-1} - bu_i - (f_S)_i$
	7	$u_{i+1} = \frac{\hat{p}_i}{\hat{k}}$
	8	$\dot{u}_i = \frac{u_{i+1} - u_{i-1}}{2\Delta t}$
	9	$\ddot{u}_i = \frac{u_{i+1} - 2u_i + u_{i-1}}{(\Delta t)^2}$
Repetition	10	Repeat equation in Steps 1 through 9 for the next time step.

Figures 4.12(a)-4.12(c) show example snapshots of the SDOF model. All input information is highlighted in yellow, and all output is in green. The total weight value is obtained from a separate spreadsheet (Figure 4.9), following the methods of Section 4.4.2.

CENTRAL DIFFERENCE METHOD FOR SDOF NONLINEAR SYSTEM
(resistance provided by composite pipe)

Chopra (2007)

Weight	w (lb)	5312.2
Gravity acc.	g (in/s^2)	386.4
Pipe outer diam.	D_o (in)	48
Pipe thickness	T (in)	1
Area	A (in^2)	6936.64

Mass	m (lb*s^2/in)	13.75
Damping coefficient	c (lb*s/in)	0
Time step	Δt (s)	5.74899E-06
Initial displacement	u_0 (in)	0
Initial velocity	u'_0 (in/s)	0

Initial acc.	u''_0 (in/s^2)	12462500.52
	u_{-1} (in)	0.000205948
	k^ (lb/in)	4.15966E+11
	a (lb/in)	4.15966E+11
	b (lb/in)	-8.31932E+11

Liner material

E-glass/epoxy, [0/90/0] deg

INPUT

RESULTS

i = 0, 1, 2, ... N

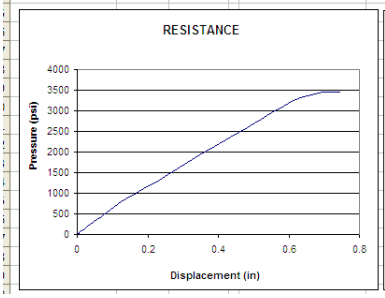

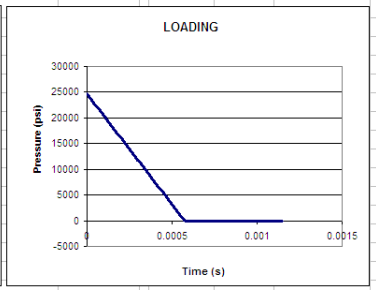

RESISTANCE Displacement Δ_i (in)	RESISTANCE Pressure P_i (psi)	LOADING Time t_i (s)	LOADING Pressure P_i (psi)	Lo p_i (
0	0	0	24700	171334
2.06604E-09	1.32E-05	5.74899E-06	24453	16962
4.13208E-09	2.63E-05	1.1498E-05	24206	16790
7.23604E-09	4.61E-05	1.7247E-05	23959	16619
1.18479E-08	7.57E-05	2.2996E-05	23712	16448
1.88979E-08	0.00012	2.8745E-05	23465	16276
2.9375E-08	0.000187	3.44939E-05	23218	16105
4.50417E-08	0.000287	4.02429E-05	22971	15934
6.86396E-08	0.000437	4.59919E-05	22724	15762
1.03792E-07	0.000662	5.17409E-05	22477	15591
1.56667E-07	0.000999	5.74899E-05	22230	15420
2.36958E-07	0.001505	6.32389E-05	21983	15248
3.55438E-07	0.002264	6.89879E-05	21736	15077
5.34625E-07	0.003403	7.47369E-05	21489	14906
8.02917E-07	0.005111	8.04859E-05	21242	14734
1.20438E-06	0.007672	8.62349E-05	20995	14563
1.81146E-06	0.011515	9.19838E-05	20748	14392
2.71229E-06	0.017281	9.77328E-05	20501	14220
4.07333E-06	0.025928	0.000103482	20254	14049
0.00000611	0.038894	0.000109231	20007	13878
0.000009165	0.05834	0.00011498	19760	13706
1.37083E-05	0.087532	0.000120729	19513	13535
2.06604E-05	0.131319	0.000126478	19266	13364
3.09417E-05	0.196979	0.000132227	19019	13192
4.64125E-05	0.295447	0.000137976	18772	13021

(a)

Load p_i (lb)	Resistance $(f_s)_i$ (lb)	u_{i-1} (in)	p^$_i$ (lb)	u_{i+1} (in)	Displacement u_i (in)	Velocity u'_i (in/s)	Acceleration u''_i (in/s^2)
71334923.5	0	2.06E-04	8.57E+07	2.06E-04	0.00E+00	0.00	12462500.52
69621574.3	9092.418514	0.00E+00	3.41E+08	8.20E-04	2.06E-04	71.29	12337214.16
167908225	36166.45133	2.06E-04	7.64E+08	1.84E-03	8.20E-04	141.85	12210619.85
66194875.8	81207.99105	8.20E-04	1.35E+09	3.25E-03	1.84E-03	211.68	12082718.63
64481526.6	143757.4607	1.84E-03	2.11E+09	5.07E-03	3.25E-03	280.77	11953543.92
62768177.3	223679.5999	3.25E-03	3.02E+09	7.27E-03	5.07E-03	349.12	11823105.57
61054828.1	320807.5384	5.07E-03	4.10E+09	9.86E-03	7.27E-03	416.71	11691415.70
59341478.9	435297.6031	7.27E-03	5.34E+09	1.28E-02	9.86E-03	483.54	11558462.96
57628129.6	567774.8756	9.86E-03	6.73E+09	1.62E-02	1.28E-02	549.61	11424201.87
55914780.4	714514.2364	1.28E-02	8.28E+09	1.99E-02	1.62E-02	614.89	11288903.39
54201431.2	876868.202	1.62E-02	9.98E+09	2.40E-02	1.99E-02	679.40	11152469.14
52488081.9	1058528.606	1.99E-02	1.18E+10	2.84E-02	2.40E-02	743.12	11014630.58
50774732.7	1256812.786	2.40E-02	1.38E+10	3.33E-02	2.84E-02	806.04	10875582.85
49061383.4	1469816.884	2.84E-02	1.60E+10	3.84E-02	3.33E-02	868.17	10735464.42
47348034.2	1697535.148	3.33E-02	1.83E+10	4.39E-02	3.84E-02	929.48	10594275.73
145634685	1940680.683	3.84E-02	2.07E+10	4.98E-02	4.39E-02	989.98	10451964.88
43921335.7	2199098.814	4.39E-02	2.33E+10	5.60E-02	4.98E-02	1049.65	10308543.15
42207986.5	2472555.512	4.98E-02	2.60E+10	6.26E-02	5.60E-02	1108.50	10164027.55
40494637.3	2760817.285	5.60E-02	2.89E+10	6.94E-02	6.26E-02	1166.51	10018435.06
138781288	3063860.037	6.26E-02	3.19E+10	7.66E-02	6.94E-02	1223.69	9871767.43
37067938.8	3382818.876	6.94E-02	3.50E+10	8.41E-02	7.66E-02	1280.02	9723942.11
35354589.6	3716018.759	7.66E-02	3.83E+10	9.20E-02	8.41E-02	1335.49	9575080.92
33641240.3	4063241.676	8.41E-02	4.16E+10	1.00E-01	9.20E-02	1390.11	9425199.74
31927891.1	4424268.119	9.20E-02	4.52E+10	1.09E-01	1.00E-01	1443.86	9274314.52

(b)

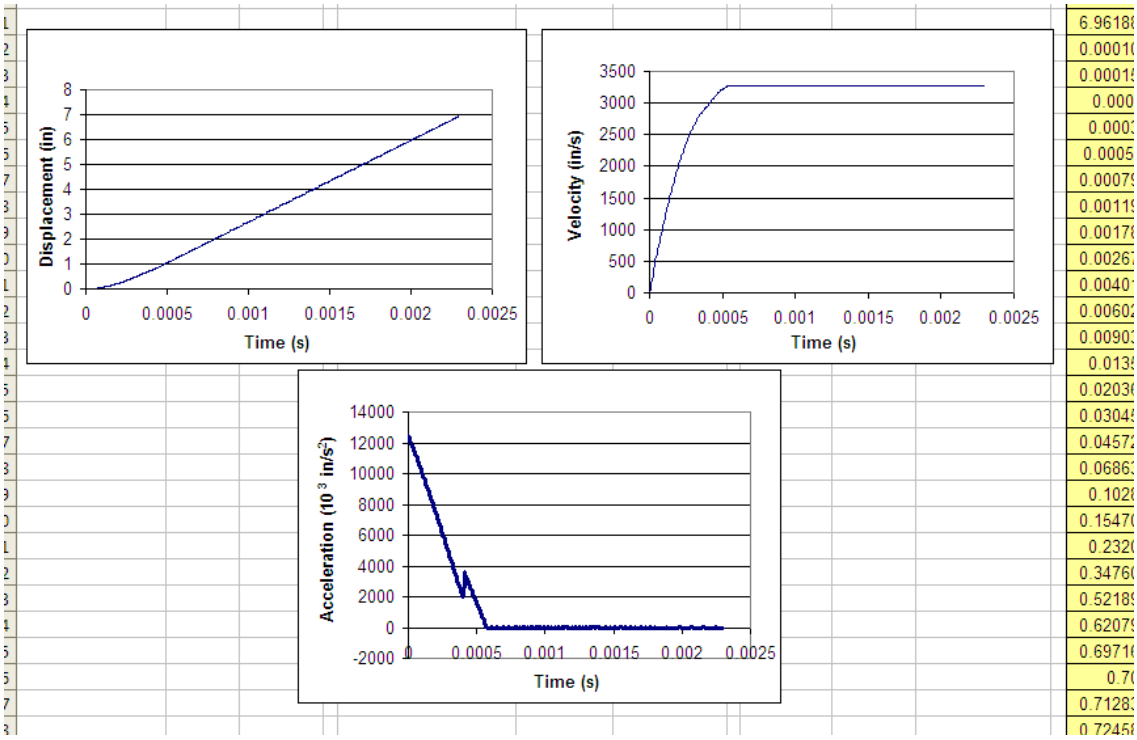

(c)

Figure 4.12: (a) Top-left portion of SDOF model; (b) top-right portion of SDOF model; (c) bottom-left portion of SDOF model

4.5 SDOF Model Runs and Results/Comparisons

With the SDOF model fully developed, several runs were generated, and the results associated with displacement, velocity, and acceleration over time are given in the subsections that follow. These results are affected by several factors, such as the composite type, pipe geometry, cover depth, soil density and cohesion angle, additional mass, and weight of explosive loading, so comparisons were made to demonstrate the system's response to each of these, in order to illustrate trends and determine which models are theoretically most effective in terms of mitigating damage to the additional mass aboveground.

In many of the examples, several parameters are held constant when their effects are not being analyzed. For example, per a published CIPP design specification, the soil density is generally held constant at 120 pcf (Baton Rouge City-Parrish DPW 2010). Also, the additional mass weight is generally held to the weight of one axle of a Humvee vehicle. Hence, from this point forward, the additional mass will sometimes be referred to simply as a vehicle.

According to AM General (2011), a Humvee can weigh from 5200 to 6400 pounds, so a weight of 5200 pounds can be used as a conservative approach. To be even more conservative, though, since it is unknown exactly what portion of the moving vehicle will be directly subjected to the blast loading, only the weight from one axle (two wheels) will usually be accounted for—i.e., half of its total weight, or 2600 pounds.

Results and comparisons of the system parameters are divided into the following subsections as follows: composite material effects, geometric effects, soil effects, additional mass effects, and loading effects.

4.5.1 Composite Material Effects

Several SDOF models were generated to show how the resistance from the composite pipe affects the dynamic behavior of the system. As mentioned earlier in this chapter, nonlinear resistance functions were computed by static analyses on the composite pipes. Thus, the nonlinear resistance data used in the model depends on the fiber type and ply stacking sequence.

Case 1 is used as designation for the models generated to show the effects of the following fiber types: E-glass, S-glass, AS carbon, IM6 carbon, T300 carbon, and Kevlar

49. Varying the fiber type in this way, the following parameters were held constant: resin of epoxy, ply stacking sequence of [0/90/0]°, outer pipe diameter of 48 inches, pipe thickness of 1 inch, soil cover depth of 12 inches, soil density of 120 pcf, cohesion angle of 45°, vehicle weight of 2600 lbs, and impulsive loading HE-14.

Case 2 is similar to Case 1; only, the fiber type is held constant as E-glass, and the ply stacking sequence varies as [0/90/0]°, [0/45/90]°, and [0/30/60/90]°.

Figure 4.13 shows one of the nonlinear resistance curves—the one for E-glass at [0/90/0]°. Since the fiber type and stacking sequence vary, this curve is different for each model generated in both Case 1 and Case 2. Since the composite pipe resistance curves were already shown in Chapter 3, no other composite pipe resistance curves will be shown in this chapter beyond Figure 4.13.

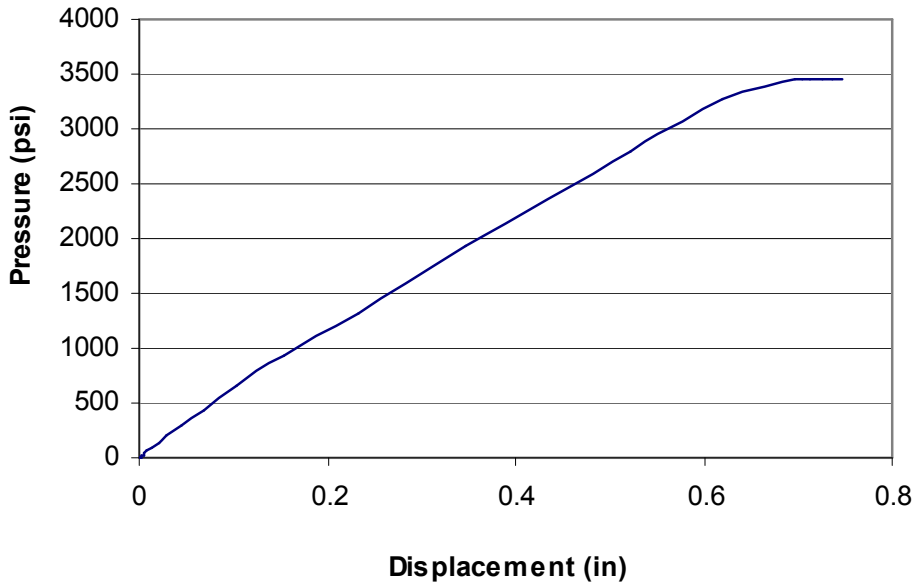

Figure 4.13: Nonlinear resistance curve for E-glass/epoxy at [0/90/0]°

Figure 4.14 shows the impulsive loading history modified from HE-14. This curve is the same for all the models generated in both Case 1 and Case 2, with the exception of some being extended slightly longer at 0-psi pressure to better show the dynamic response graphs. As mentioned in Section 4.4.5, this curve is a simplification of the original pressure-time history curve. Since all the loading history curves generated for all the SDOF models in this chapter look similar to the one in Figure 4.14, only differing by peak pressure and time duration in some cases, no other loading history curves will be shown beyond Figure 4.14.

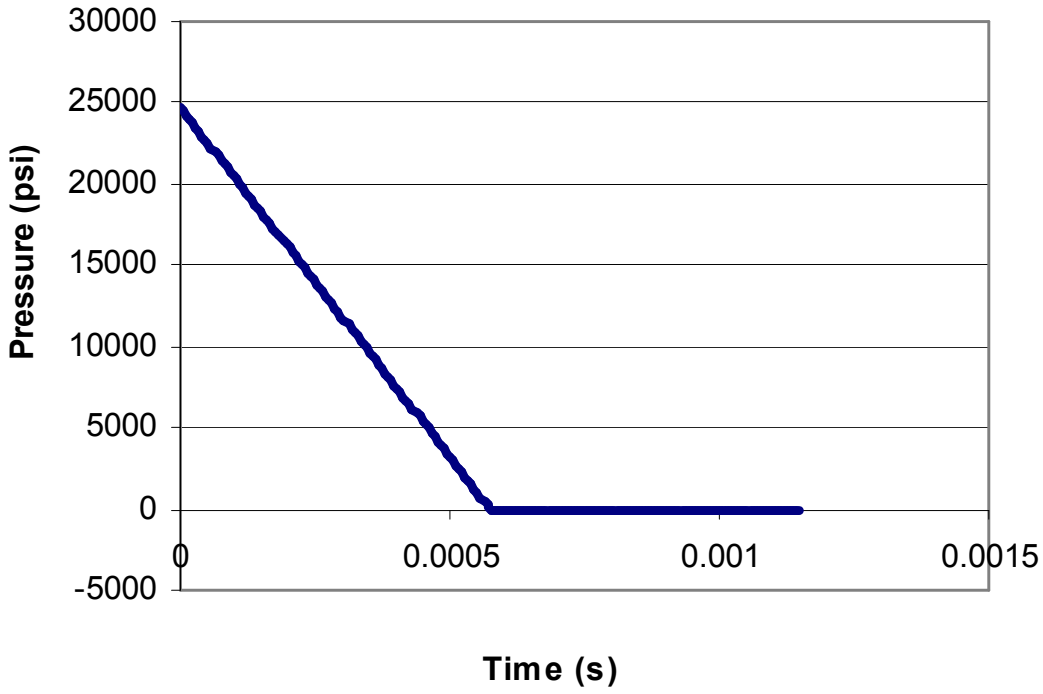

Figure 4.14: Impulsive loading history from HE-14

Figures 4.15 through 4.20 show the displacement, velocity, and acceleration over time for each of the fiber types in Case 1, and Figures 4.21 through 4.23 show them for each of the stacking sequences in Case 2.

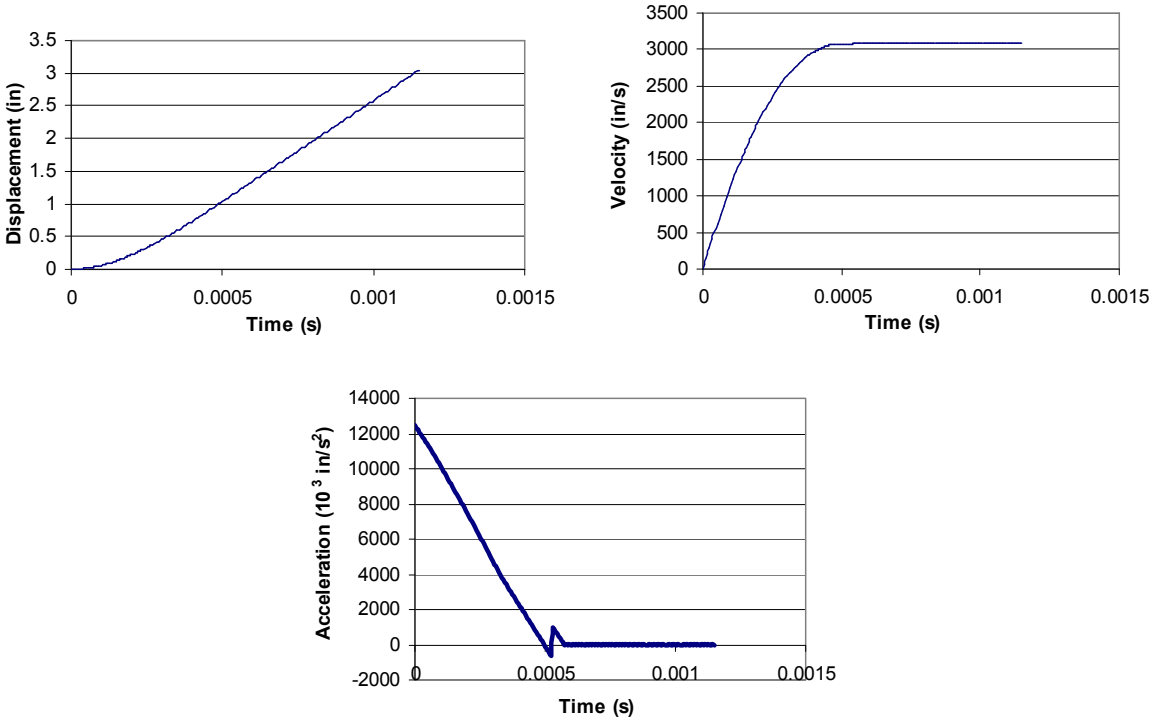

Figure 4.15: Case 1 dynamic response curves for E-glass

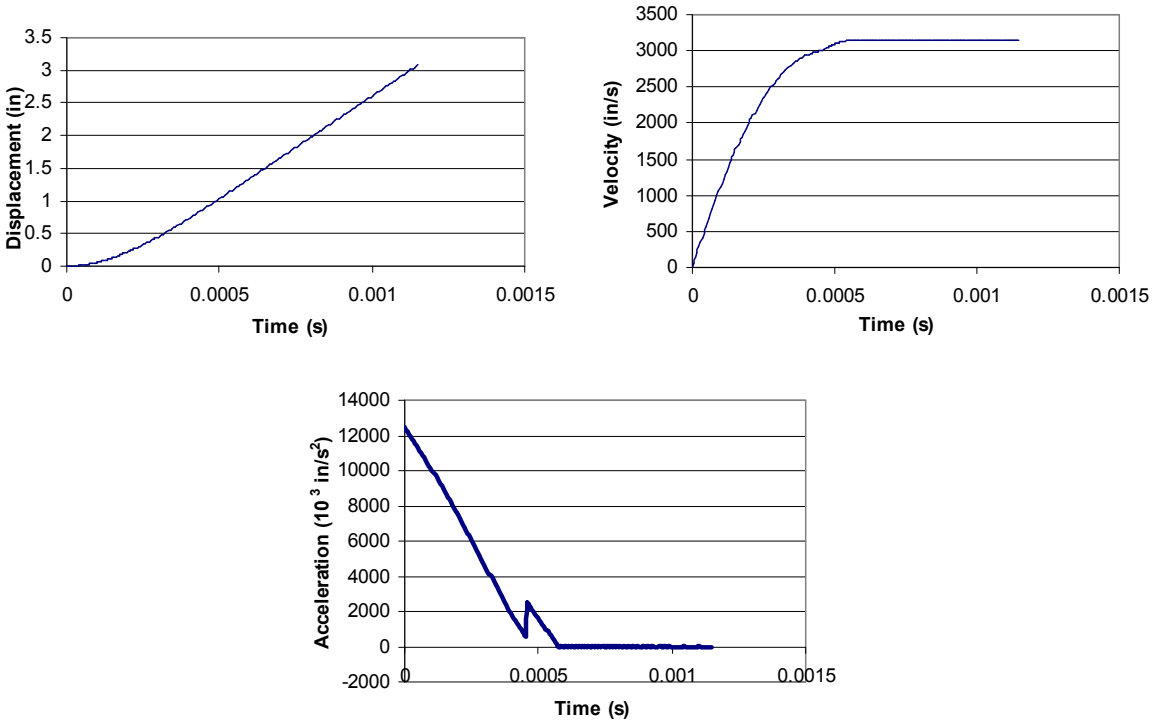

Figure 4.16: Case 1 dynamic response curves for S-glass

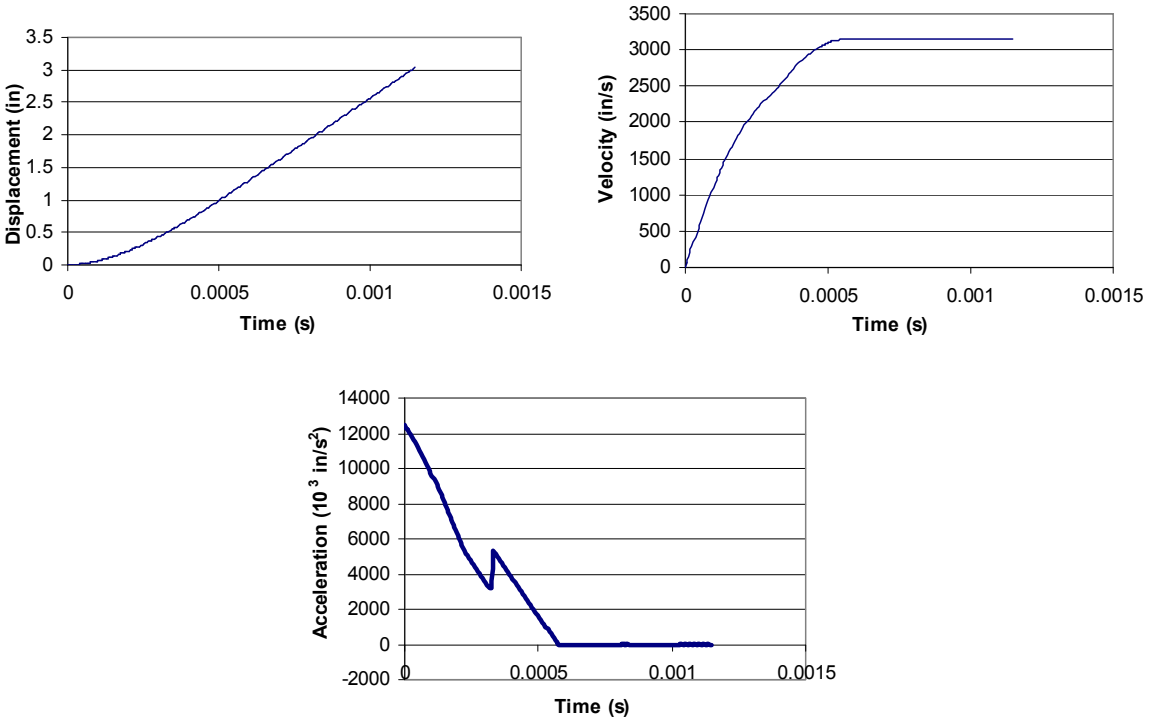

Figure 4.17: Case 1 dynamic response curves for AS carbon

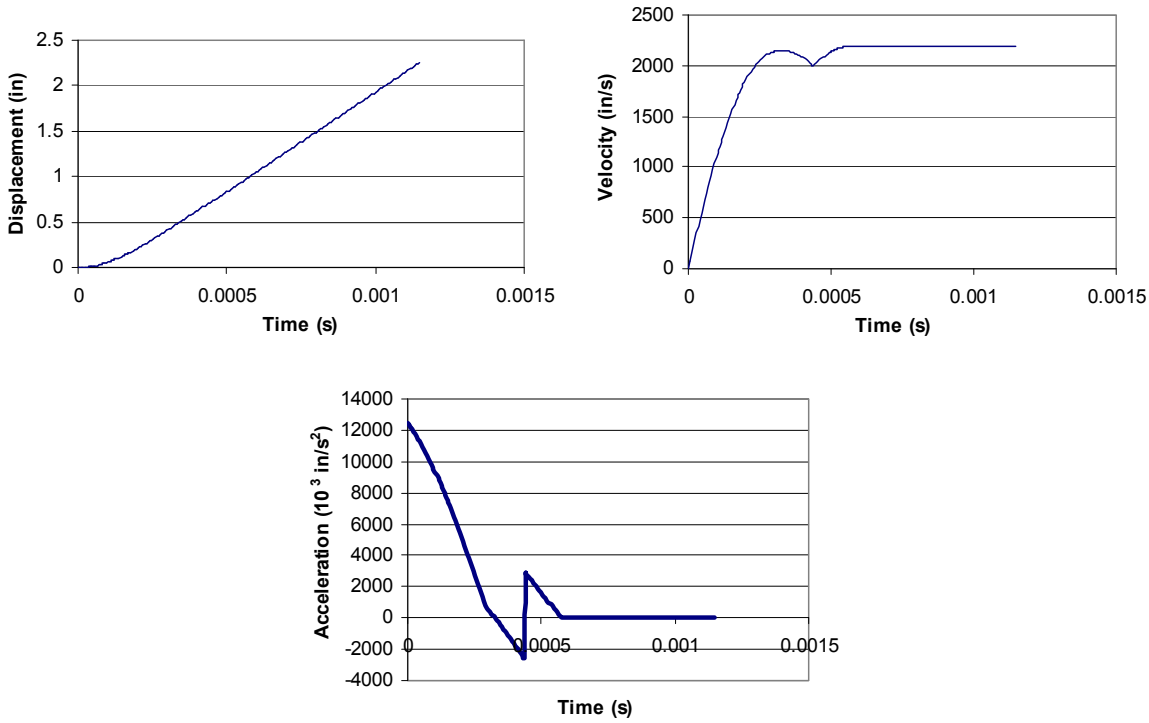

Figure 4.18: Case 1 dynamic response curves for IM6 carbon

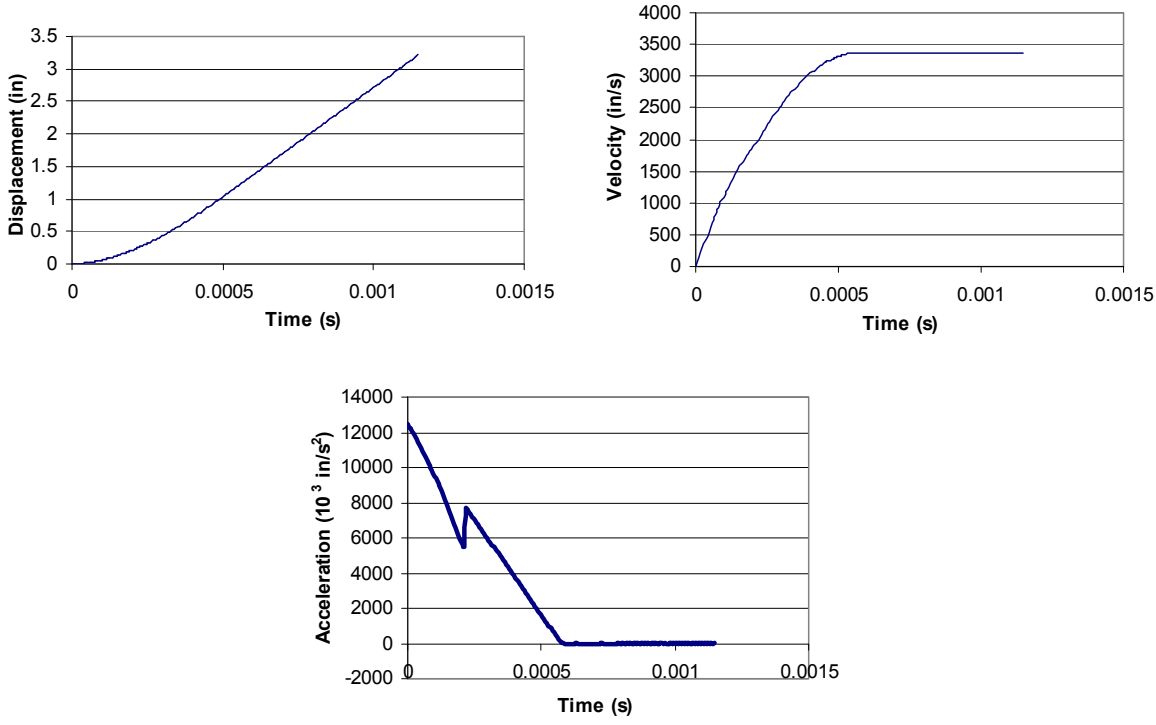

Figure 4.19: Case 1 dynamic response curves for T300 carbon

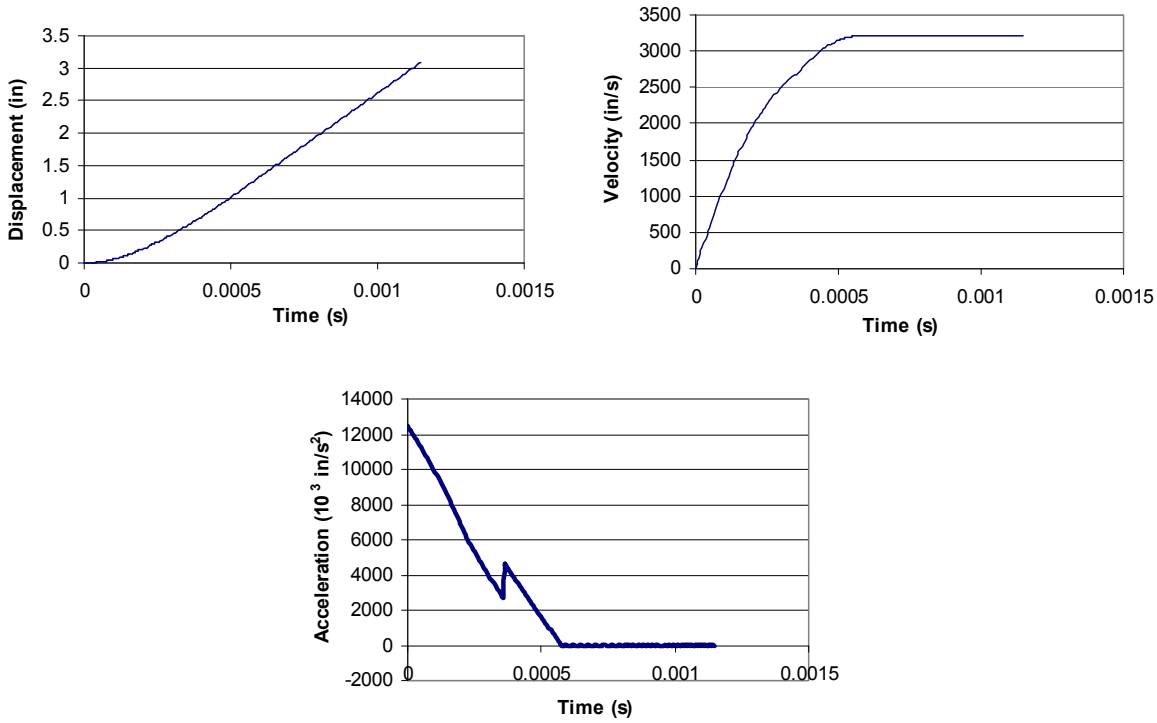

Figure 4.20: Case 1 dynamic response curves for Kevlar 49

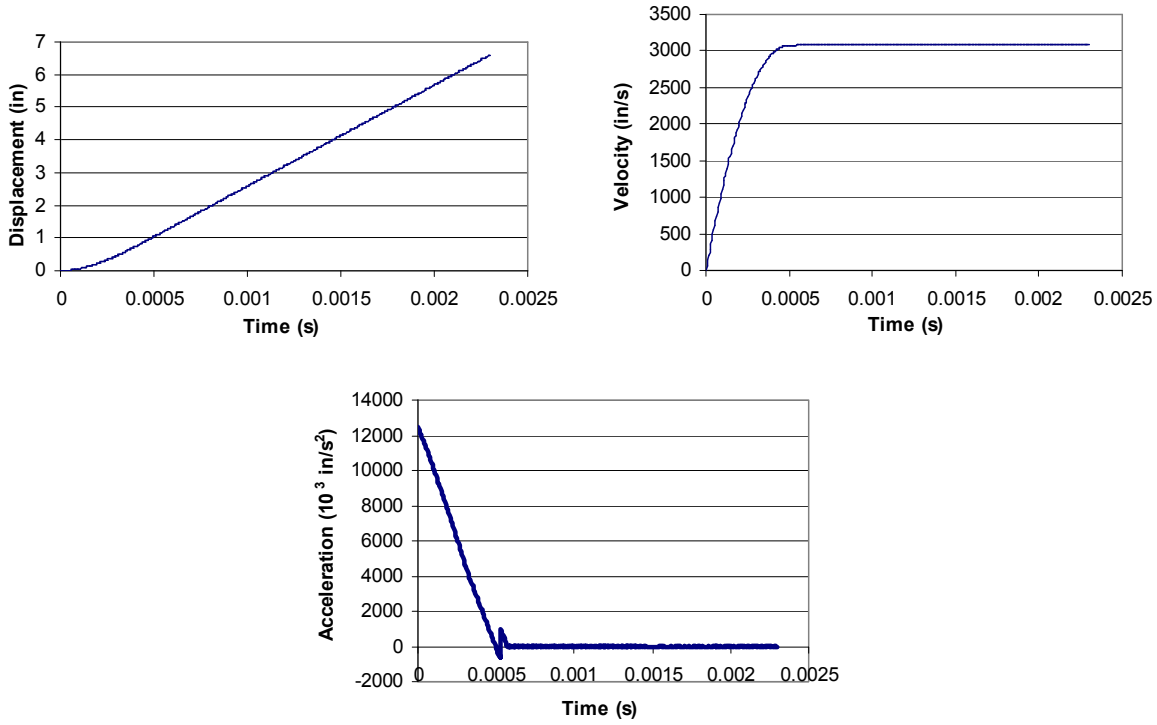

Figure 4.21: Case 2 dynamic response curves for [0/90/0]° stacking sequence

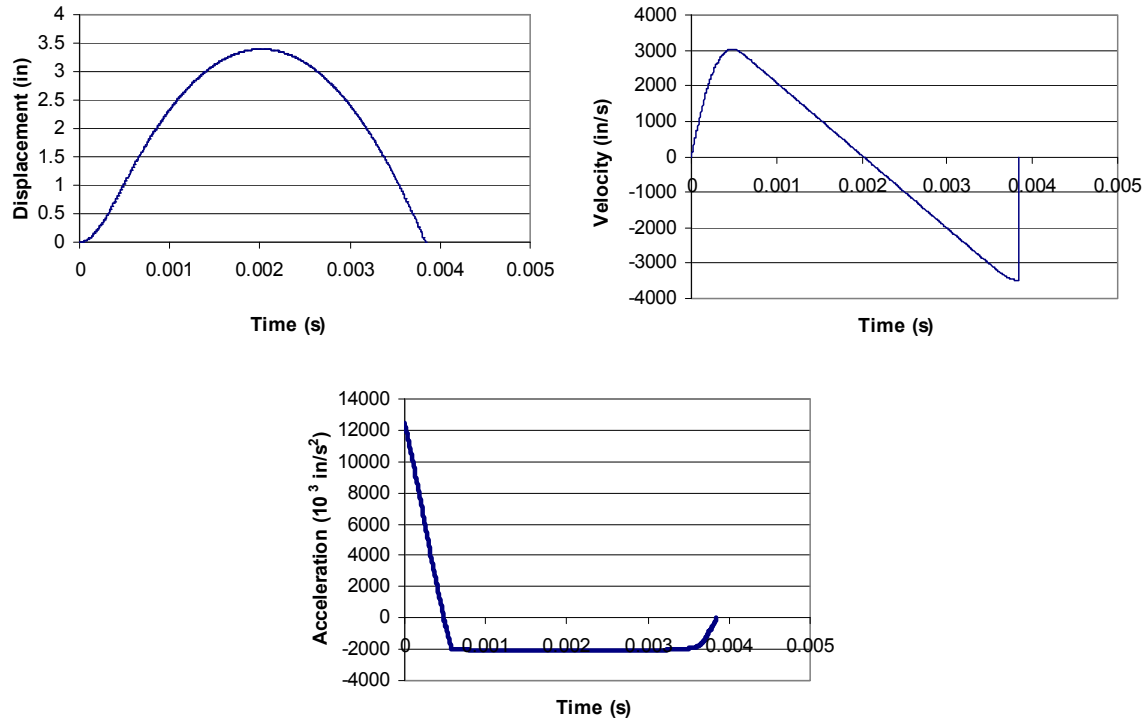

Figure 4.22: Case 2 dynamic response curves for [0/45/90]° stacking sequence

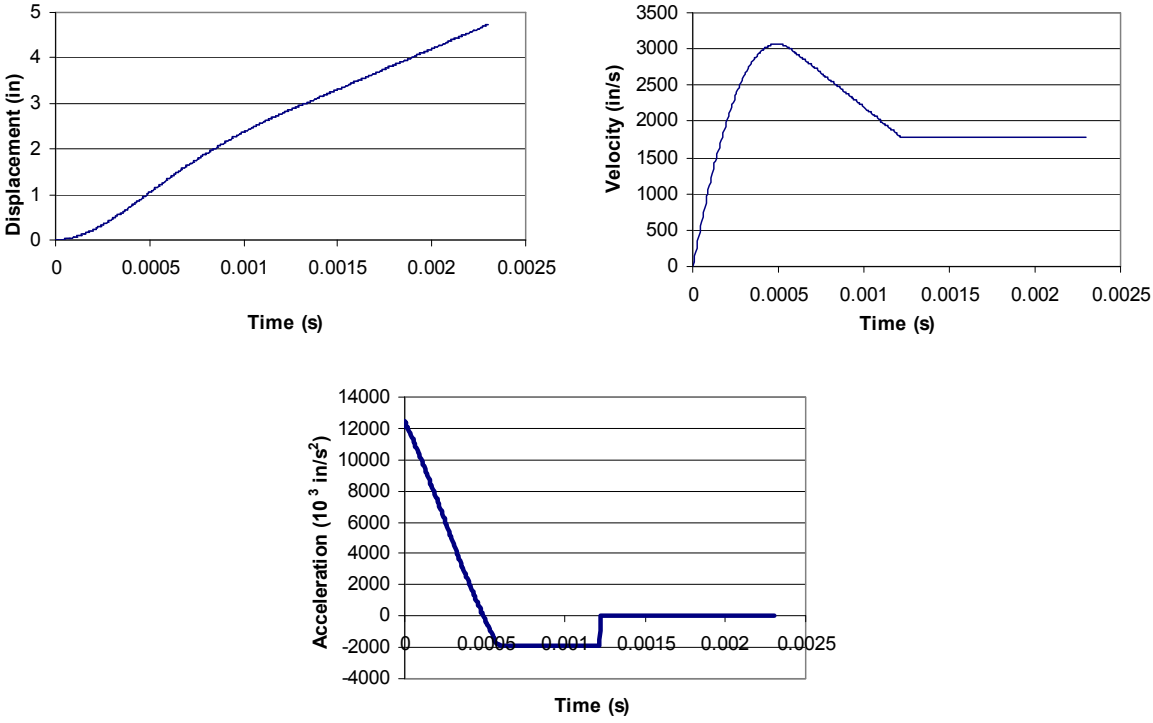

Figure 4.23: Case 2 dynamic response curves for [0/30/60/90]° stacking sequence

For the Case 1 SDOF models, the response curves are very similar for all fiber types except IM6 carbon. IM6 carbon shows the most resistance, showing a displacement of only approximately 2.25 inches and a peak velocity of approximately 2200 in/s. The other fibers show higher displacements, at just over 3 inches, as well as higher peak velocities, between approximately 3000 and 3500 in/s. Thus, it appears that the IM6 carbon fiber provides the best reinforcement for the composite pipe. Recalling the results from Chapter 3, this is understandable since IM6 carbon showed the highest toughness modulus among the same fiber types.

Theoretically, had the loading curve continued at 0 psi, the displacement curve would continue to increase to infinity, the velocity would stay at its constant value, and the acceleration would remain at 0 in/s^2 for each model in Case 1. However, the loading curve was cut at an arbitrary amount of time after decreasing to 0 psi (Figure 4.14), just long enough to show the velocity curve reaching a constant value; thus, the highest point shown on each displacement curve does not represent the actual *peak* displacement. In fact, the highest displacement values shown in the graphs are so small because the loading was only extended for 200 time steps, resulting in a total duration of just 1.15 ms. Obviously, then, had the loading been extended much longer, the displacement would be much higher.

This type of response behavior indicates that the composite material failed, as the explosive material was theoretically powerful enough to breach through the pipe and soil. The displacement of the system exceeded the maximum displacement on the resistance curve, so the resistance suddenly dropped to 0 lbs (the point where the acceleration curve "jumps"). Additionally, no gravity effects were taken into account within the SDOF

model, so no other resistance returns the mass of the system to its original position, and the displacement curve thus continuously increases. Finally, the acceleration reaches 0 in/s^2, at which point the velocity remains at a constant value.

This pattern of response behavior is repeated for several other SDOF models. Thus, for those models, only the velocity and acceleration can be read as true peak values. Furthermore, since there is zero damping in all the models, the initial acceleration only depends on the initial loading and the mass of the system (Equation 4-25, recalling that initial resistance is always zero). Therefore, when these parameters are constant, the initial acceleration is always the same value, so it is not necessary to compare these peak accelerations. (The peak accelerations are all the same, at just over 12,000,000 in/s^2, for each model in Case 1 and Case 2.)

For the Case 2 SDOF models, the [0/90/0]° and [0/30/60/90]° stacking sequences show dynamic response behaviors similar to the Case 1 models, with displacements of approximately 6.5 inches and 8 inches, respectively, and peak velocities of approximately 3090 in/s and 3070 in/s, respectively. For the [0/45/90]° stacking sequence, though, the dynamic response graphs show that the composite pipe completely resists the loading, theoretically representing total containment of the internal blast, rather than breaching of the pipe and soil. This is indicated by the displacement reaching an actual *peak* value before dropping to 0 inches, its original position. The [0/45/90]° stacking sequence ultimately shows the most resistance among the stacking sequences, having a peak displacement of just under 3.5 inches.

4.5.2 Geometric Effects

The next sets of SDOF models were generated in order to analyze how the geometry of the composite pipe affects the dynamic response of the system. The geometric parameters under consideration are the pipe thickness and its outer diameter. Again, the nonlinear resistance curves will vary depending on which composite pipe is being used. For comparison of the pipe thicknesses, classified as Case 3, the loading will be the same HE-14 impulsive loading used in the previous section (Figure 4.14). However, for diameter comparisons, classified as Case 4, although the same weight of explosive loading will be used, the loading history will differ depending on which diameter is being used.

The Case 3 SDOF models compare 1/4-inch, 1/2-inch, 3/4-inch, and 1-inch pipe thicknesses. The following parameters were held constant for all models: composite material of S-glass/epoxy, ply stacking sequence of [0/45/90]°, pipe diameter of 48 inches, soil cover depth of 12 inches, soil density of 120 pcf, cohesion angle of 45°, vehicle weight of 2600 lbs, and impulsive loading from the HE-14. Figures 4.24 through 4.27 illustrate the dynamic response curves generated for each of the Case 3 SDOF models.

The Case 4 SDOF models compare pipe diameters of 36, 48, and 60 inches. Much the same as Case 3, the following parameters were held constant: composite material of S-glass/epoxy, ply stacking sequence of [0/45/90]°, pipe thickness of 1 inch, soil cover depth of 12 inches, soil density of 120 pcf, cohesion angle of 45°, and vehicle weight of 2600 lbs. Also, an equivalent weight of loading was used; this corresponds to the HE-5, HE-14, and HE-15 loadings for the 36-inch, 48-inch, and 60-inch diameters, respectively.

Figures 4.28 through 4.30 illustrate the dynamic response curves generated for each of the Case 4 SDOF models.

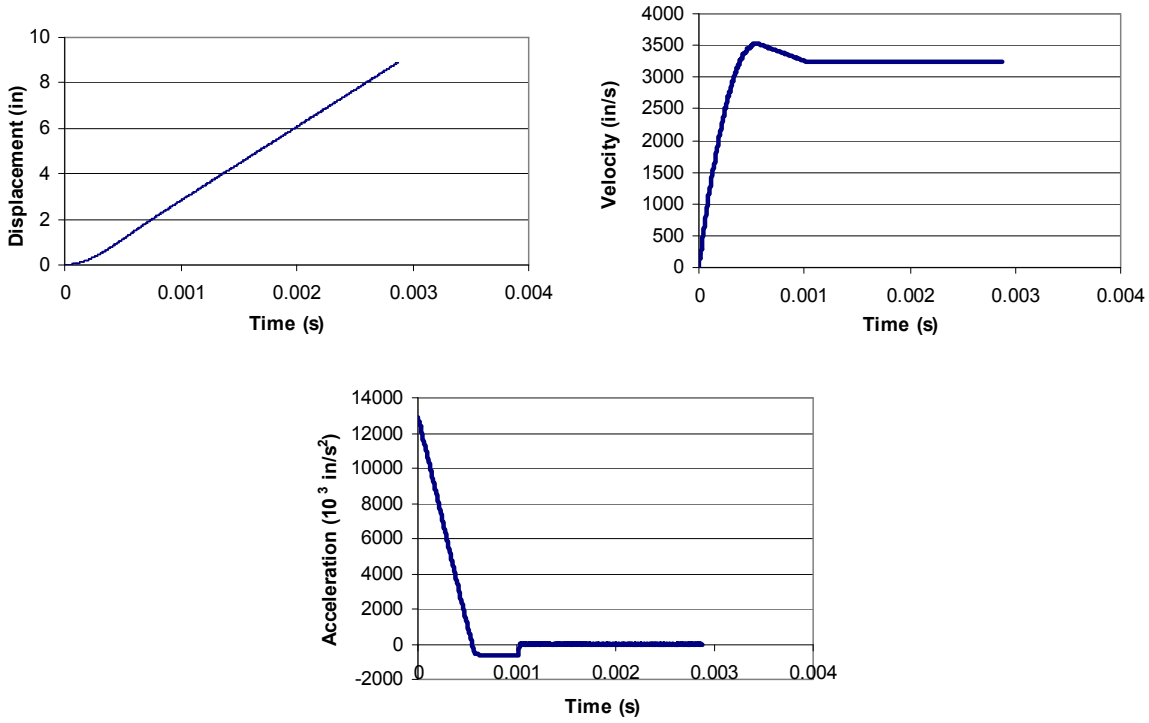

Figure 4.24: Case 3 dynamic response curves for 1/4-inch thickness

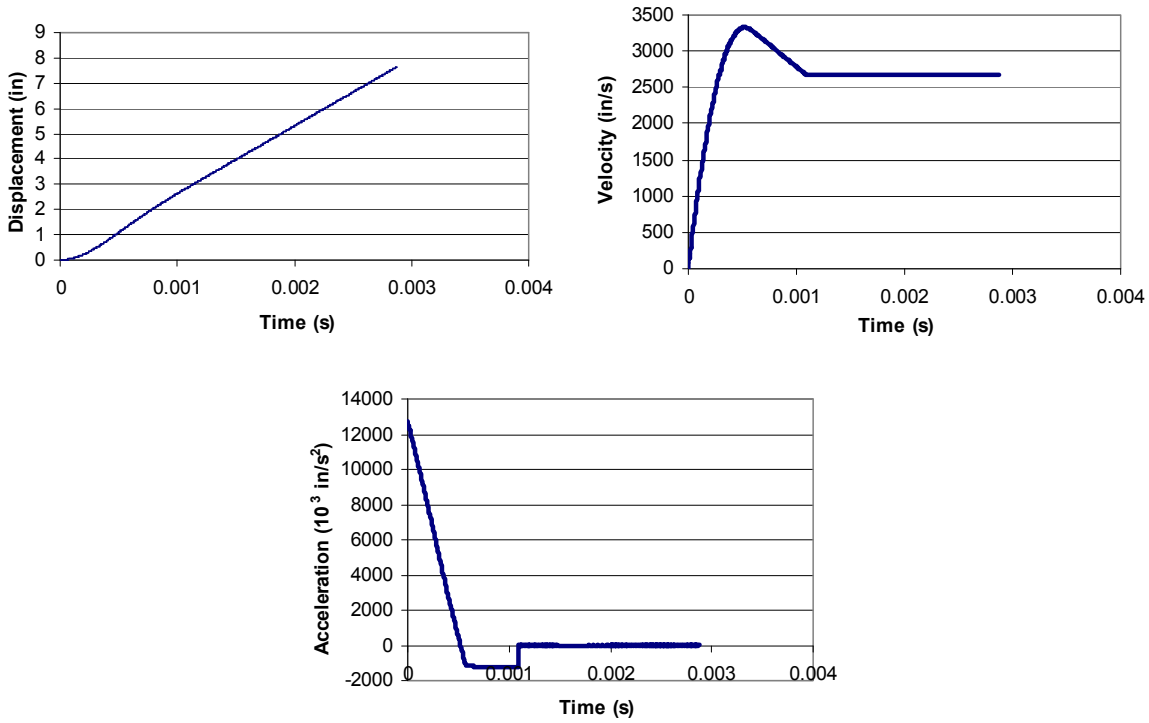

Figure 4.25: Case 3 dynamic response curves for 1/2-inch thickness

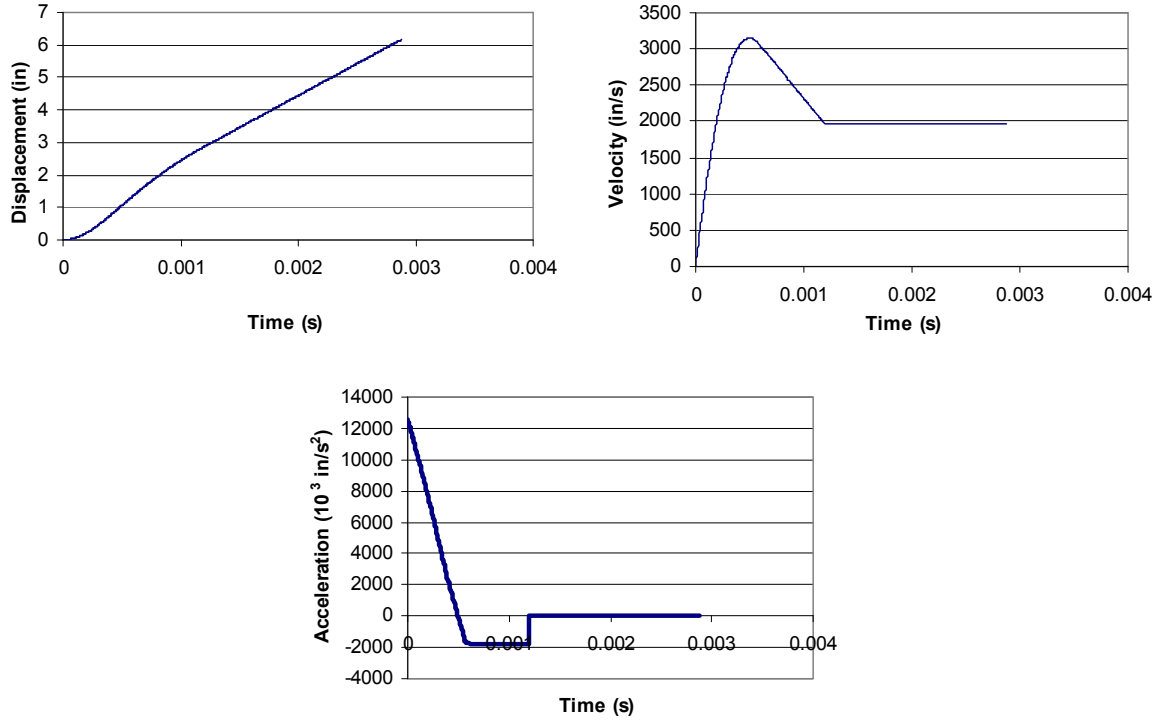

Figure 4.26: Case 3 dynamic response curves for 3/4-inch thickness

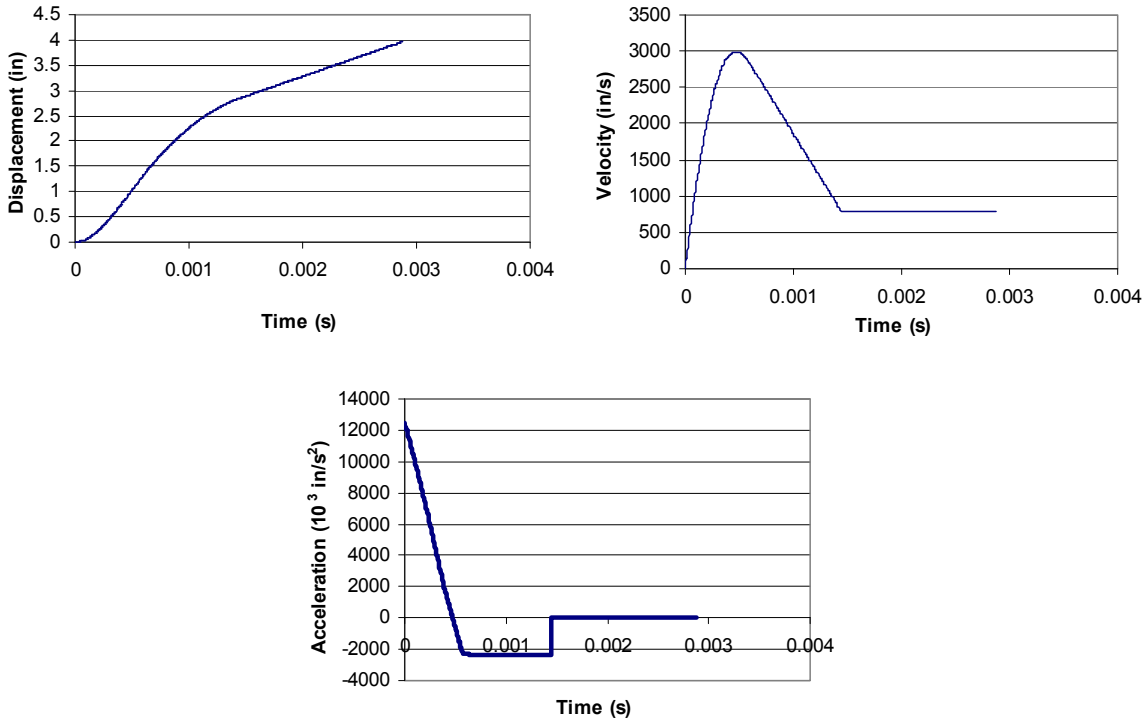

Figure 4.27: Case 3 dynamic response curves for 1-inch thickness

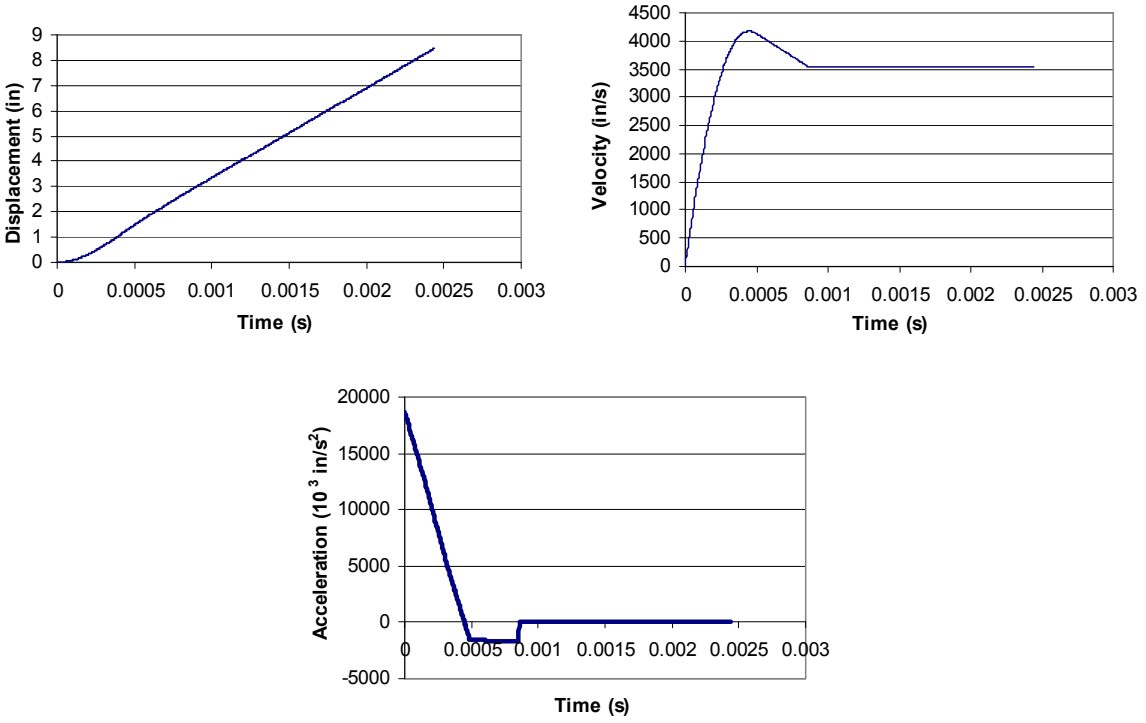

Figure 4.28: Case 4 dynamic response curves for 36-inch diameter

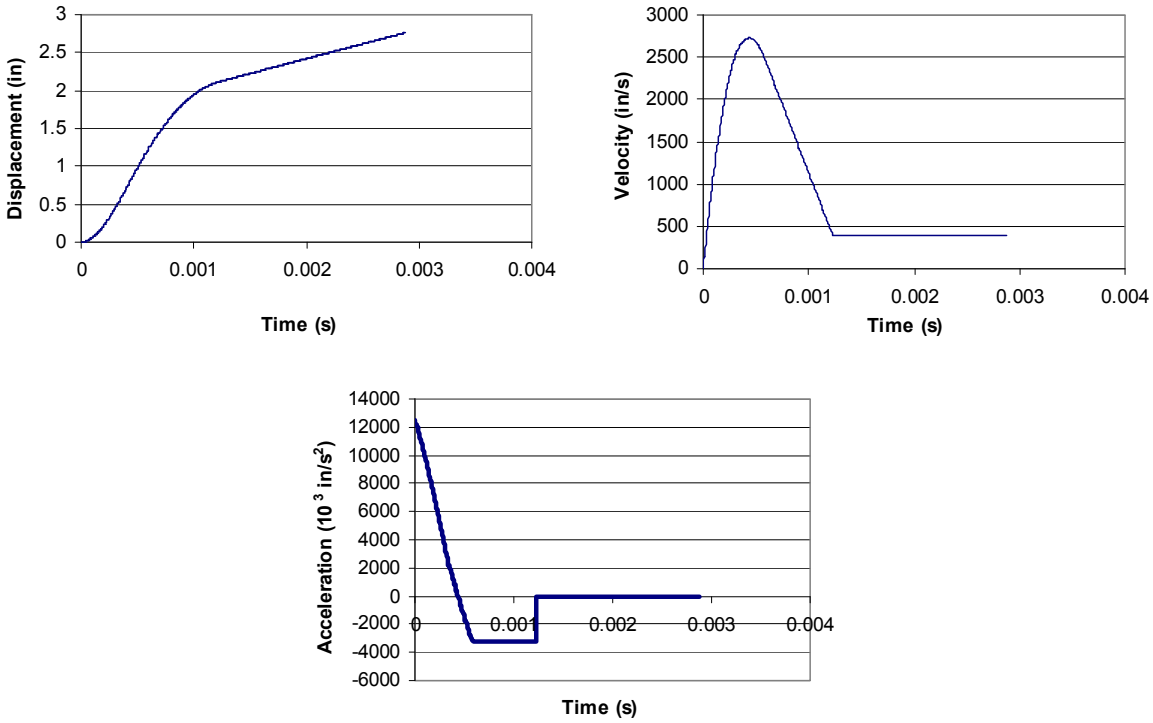

Figure 4.29: Case 4 dynamic response curves for 48-inch diameter

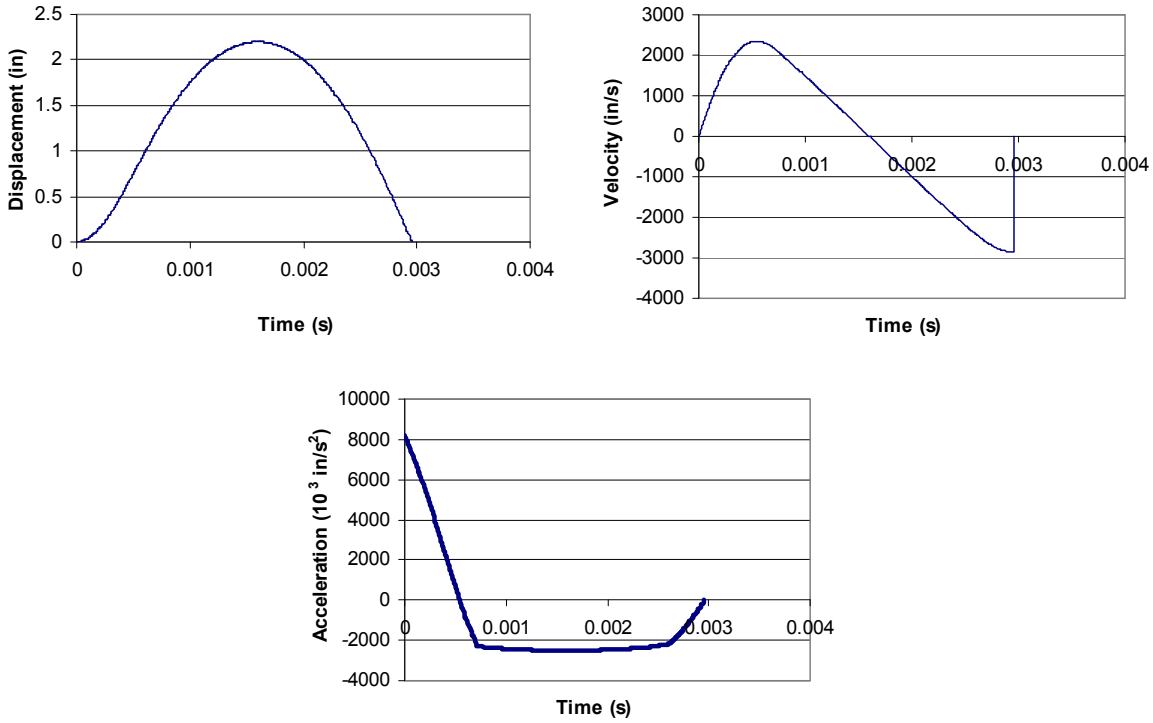

Figure 4.30: Case 4 dynamic response curves for 60-inch diameter

Looking at the SDOF models of Case 3, it is evident that there is a trend of decreasing displacement, velocity, and acceleration as the thickness increases, which is understandable since the resistance increases with larger thickness. The composite pipe theoretically failed and was breached by the explosion in all of the models. The pipe having a 1-inch thickness, though, showed the most resistance, reaching a displacement of approximately 4 inches in just 2.87 ms, a peak velocity of approximately 3000 in/s, and a peak acceleration of approximately 12,000,000 in/s^2 (the same as all the models in Cases 1 through 3).

For the SDOF models of Case 4, the 36-inch and 48-inch diameter pipes failed and were theoretically breached, but the 60-inch diameter pipe showed complete containment of the internal blast. The 60-inch diameter pipe showed a peak displacement of approximately 2.2 inches, a peak velocity of approximately 2800 in/s, and a peak acceleration of approximately 8,000,000 in/s^2. Comparing the 36-inch and 48-inch diameter pipes, the displacement, velocity, and acceleration values decrease with a larger diameter.

4.5.3 Soil Effects

Three important parameters involved with the mass of the system—soil type (Case 5), cover depth (Case 6), and soil cohesion angle (Case 7)—will be studied in order to determine how they affect the dynamic response of the underground composite pipe system. The other major component of mass, the vehicle, will be analyzed in the next section.

Various types of soil may exist above underground composite pipes. Typically, soil is classified as gravel, sand, silt, or clay, and any combination of these soil types may be present. They each differ in density, in the following order from least dense to most dense: clay, silt, sand, and gravel. The density of clay and silt generally ranges from 90 to 110 pcf, and the density of sand and gravel generally ranges from 120 to 140 pcf (MDOT 2007).

The Case 5 SDOF models compare the soil types by varying the densities as follows: 90 pcf for clay, 110 pcf for silt, 120 pcf for sand, and 140 pcf for gravel. The remaining system parameters are held constant as follows: composite material of E-glass/epoxy, ply stacking sequence of [0/90/0]°, pipe thickness of 1 inch, pipe diameter of 48 inches, cover depth of 12 inches, cohesion angle of 45°, vehicle weight of 2600 lbs, and impulsive loading HE-14. Figures 4.31 through 4.34 show the dynamic response curves generated for each of the Case 5 SDOF models.

The Case 6 SDOF models compare the following cover depths: 12, 24, 36, 60, 96, and 120 inches, while the remaining system parameters are held constant as follows: composite material of E-glass/epoxy, ply stacking sequence of [0/90/0]°, pipe thickness of 1 inch, pipe diameter of 48 inches, soil density of 120 pcf, cohesion angle of 45°, vehicle weight of 2600 lbs, and impulsive loading HE-14. Figures 4.35 through 4.40 show the dynamic response curves generated for each of the Case 6 SDOF models.

The Case 7 SDOF models compare the following cohesion angles: 15°, 30°, 45°, 60°, and 75°, while the remaining system parameters are held constant as follows: composite material of E-glass/epoxy, ply stacking sequence of [0/90/0]°, pipe thickness of 1 inch, pipe diameter of 48 inches, cover depth of 12 inches, soil density of 120 pcf,

vehicle weight of 2600 lbs, and impulsive loading HE-14. Figures 4.41 through 4.45 show the dynamic response curves generated for each of the Case 7 SDOF models.

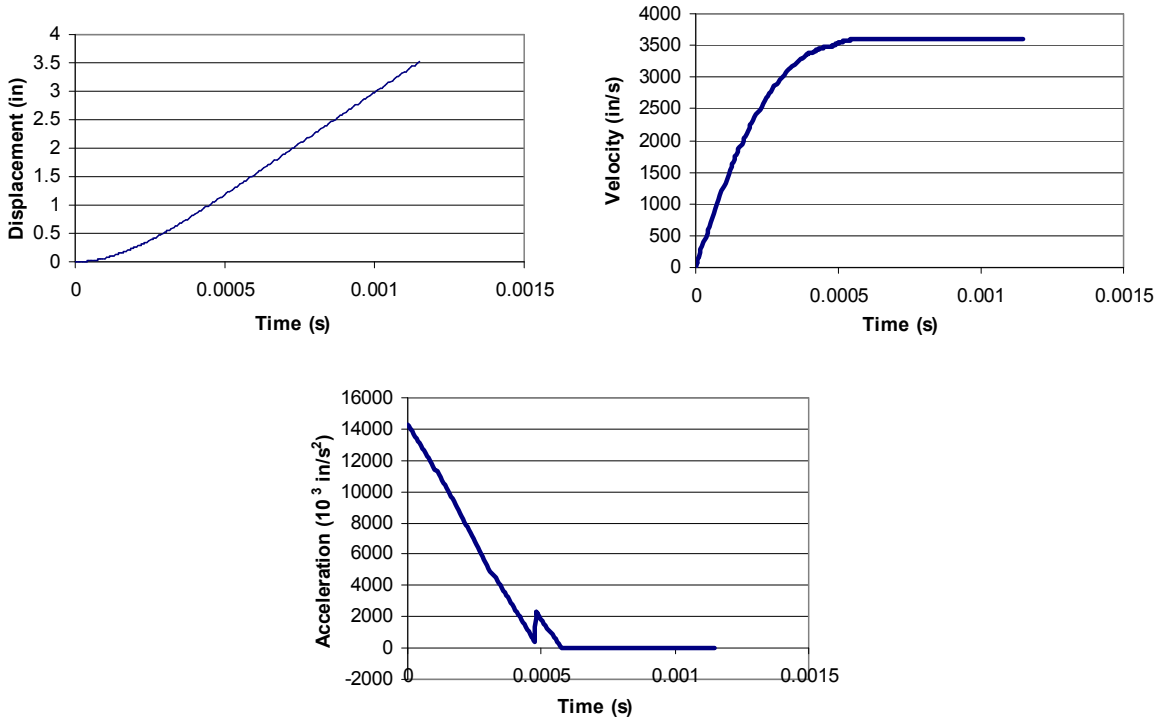

Figure 4.31: Case 5 dynamic response curves for clay

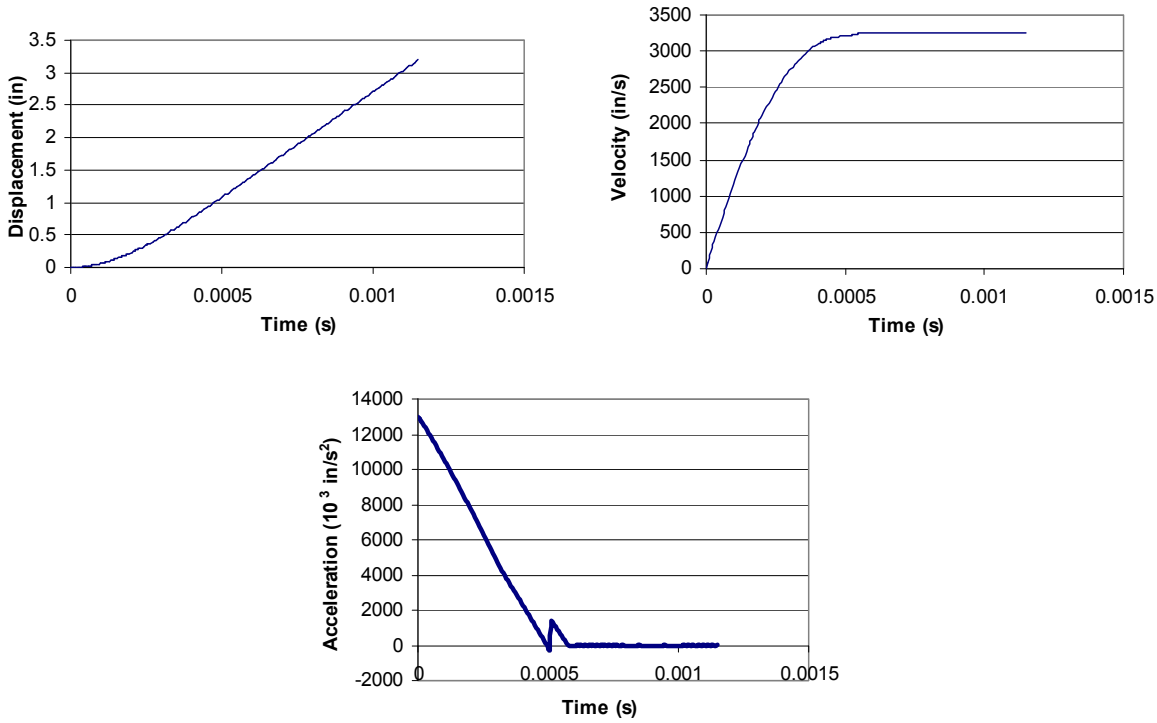

Figure 4.32: Case 5 dynamic response curves for silt

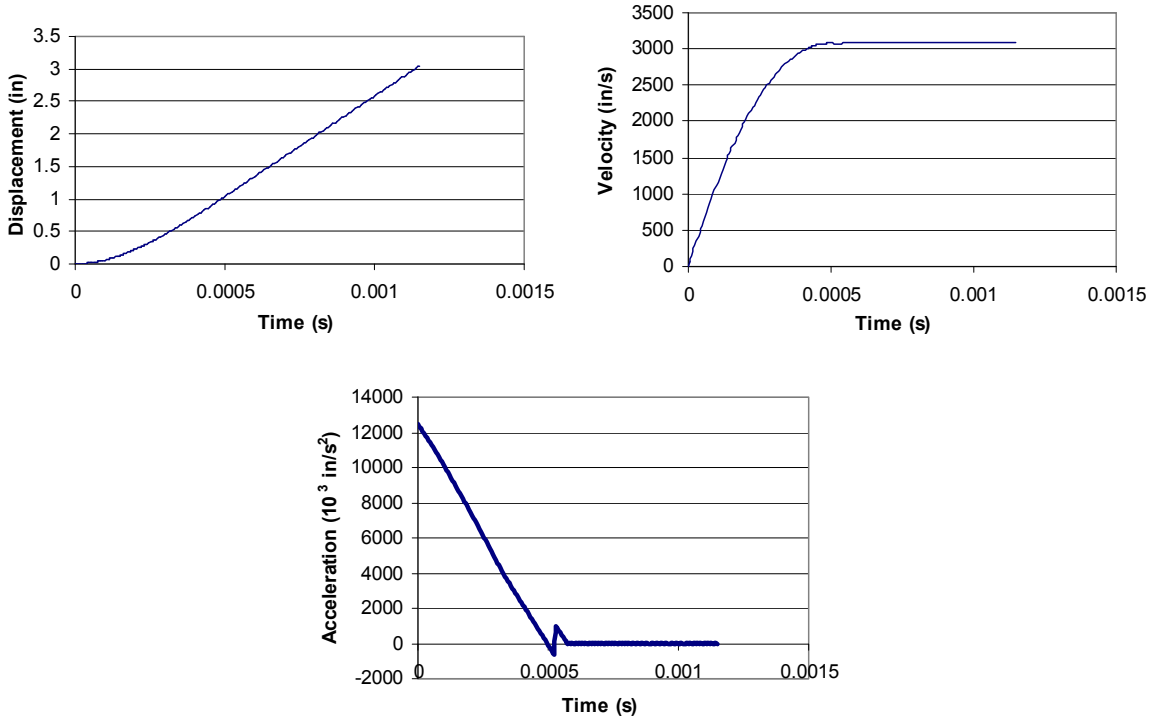

Figure 4.33: Case 5 dynamic response curves for sand

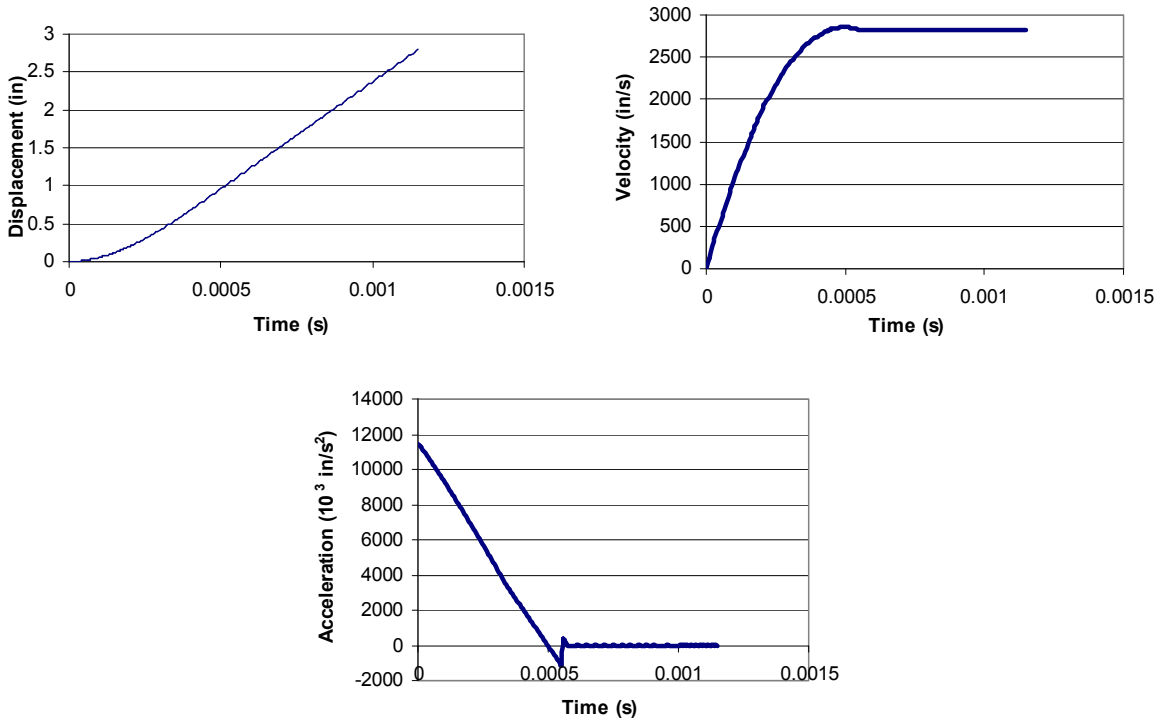

Figure 4.34: Case 5 dynamic response curves for gravel

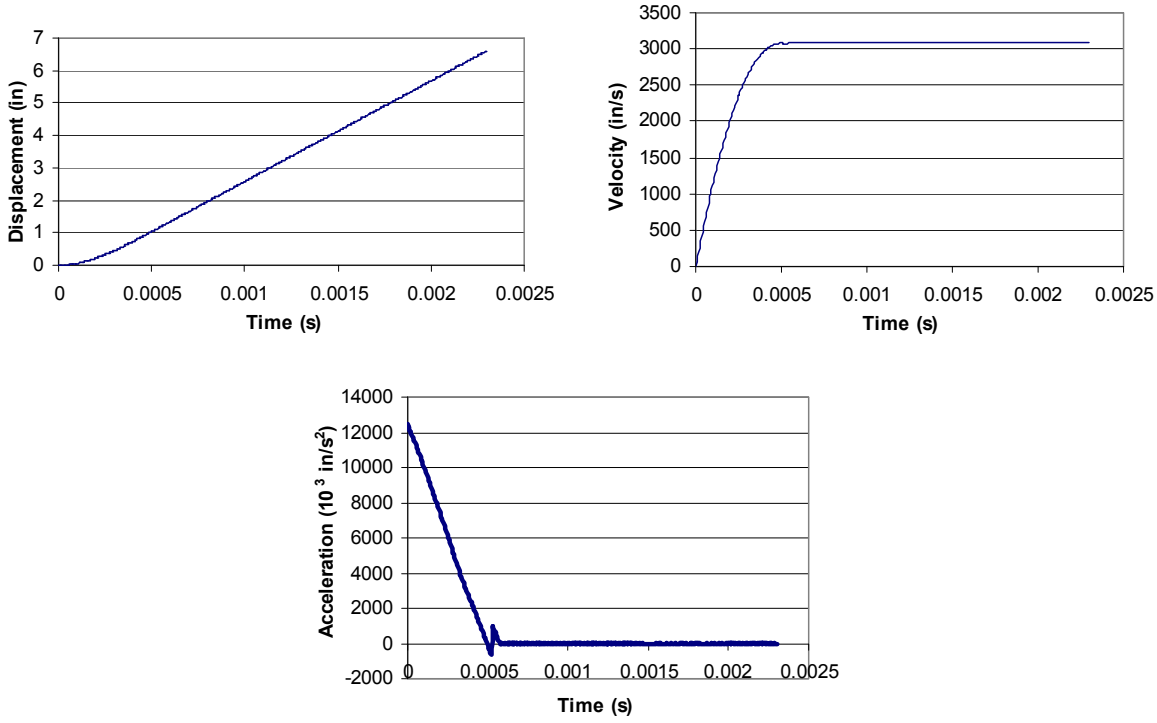

Figure 4.35: Case 6 dynamic response curves for 12-inch cover depth

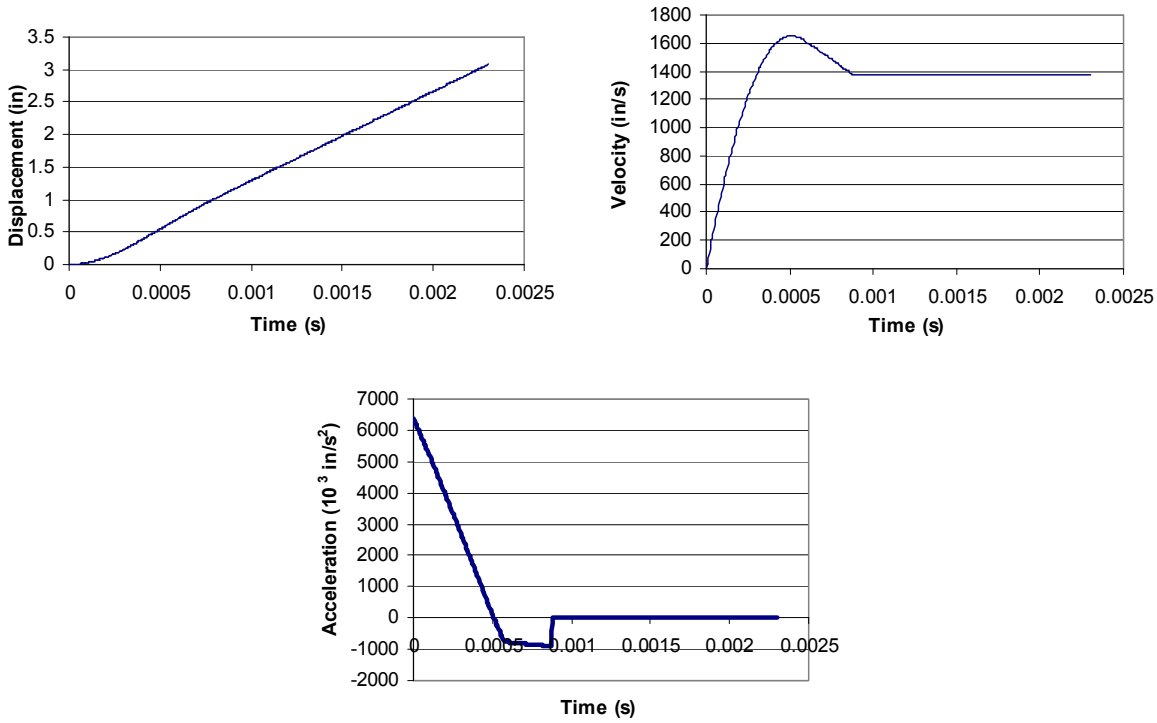

Figure 4.36: Case 6 dynamic response curves for 24-inch cover depth

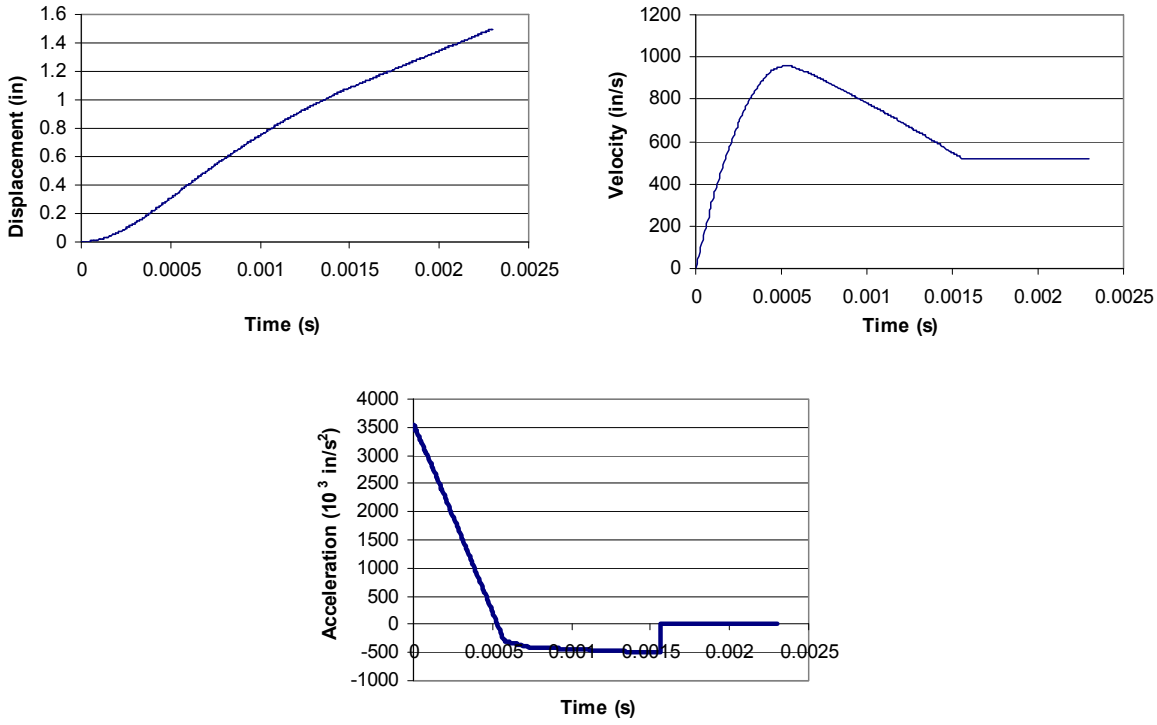

Figure 4.37: Case 6 dynamic response curves for 36-inch cover depth

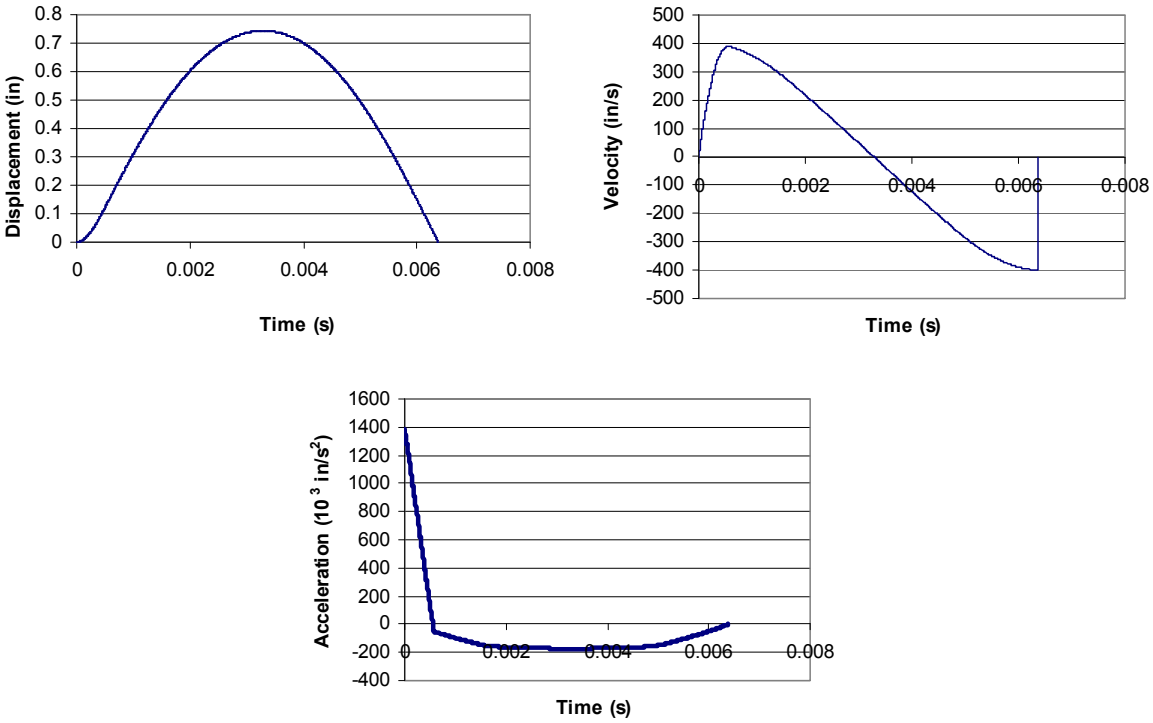

Figure 4.38: Case 6 dynamic response curves for 60-inch cover depth

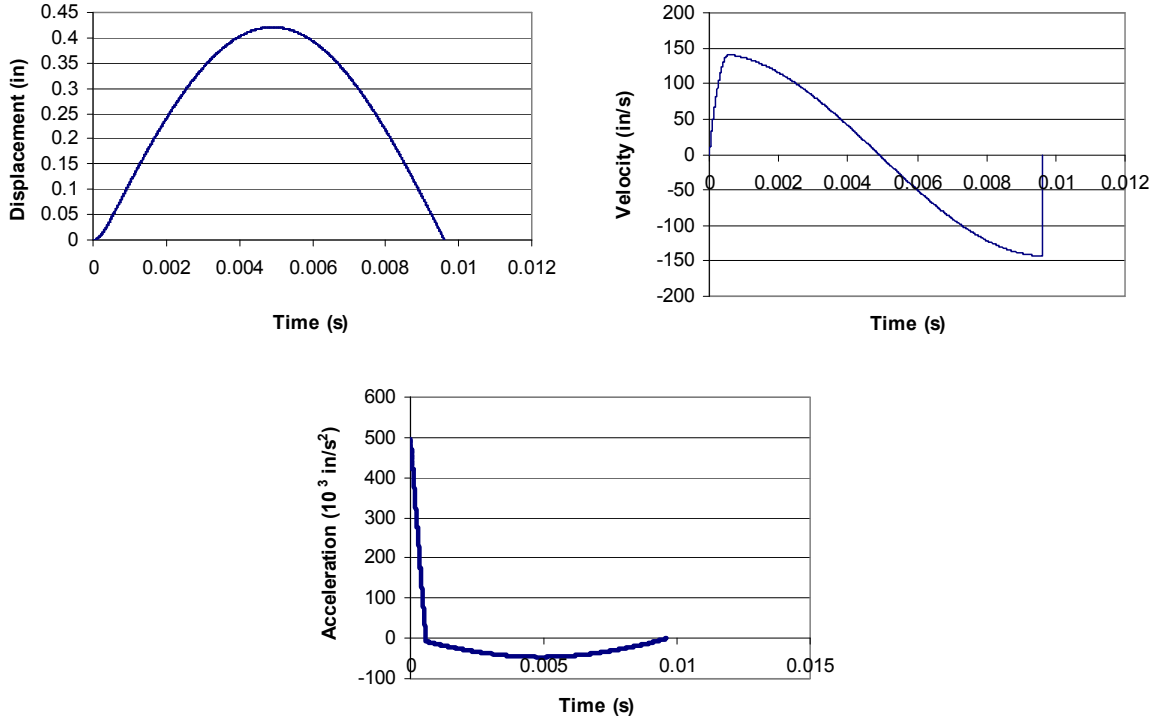

Figure 4.39: Case 6 dynamic response curves for 96-inch cover depth

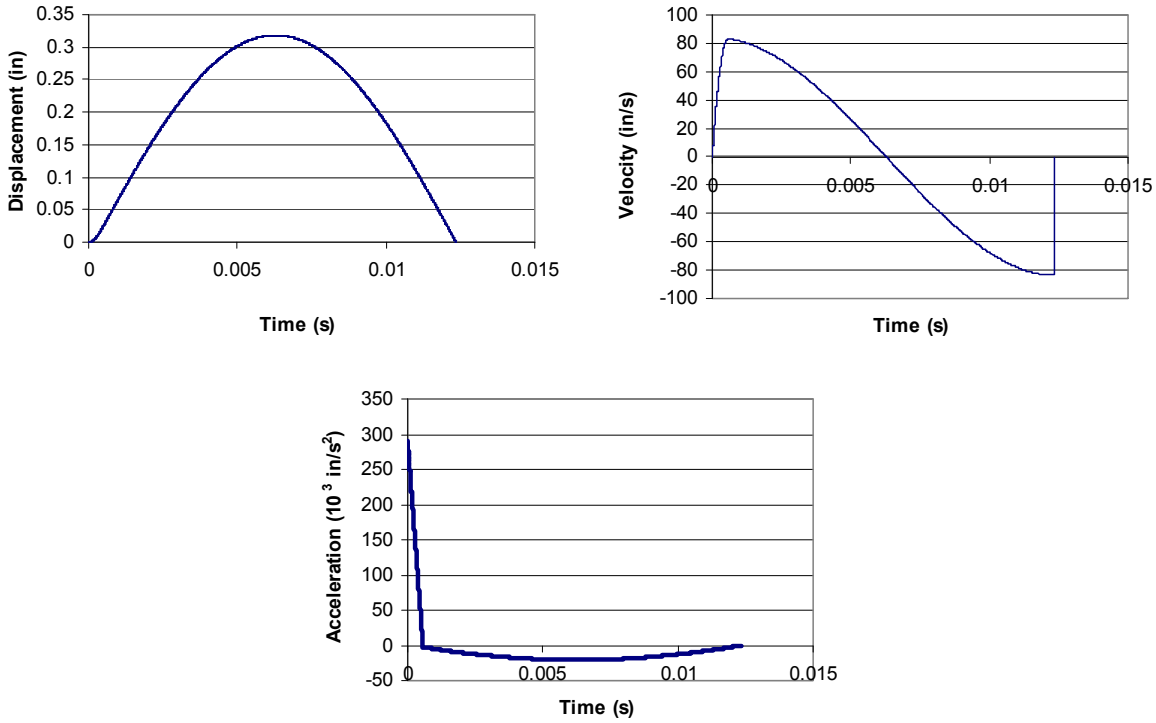

Figure 4.40: Case 6 dynamic response curves for 120-inch cover depth

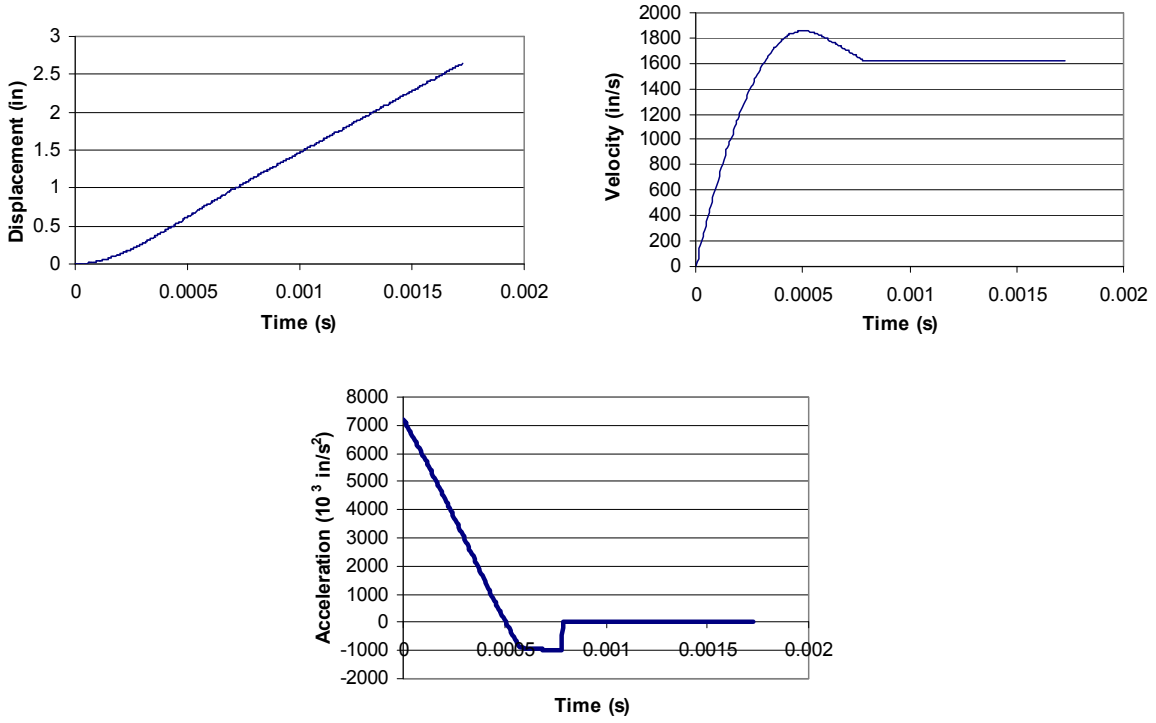

Figure 4.41: Case 7 dynamic response curves for 15° cohesion angle

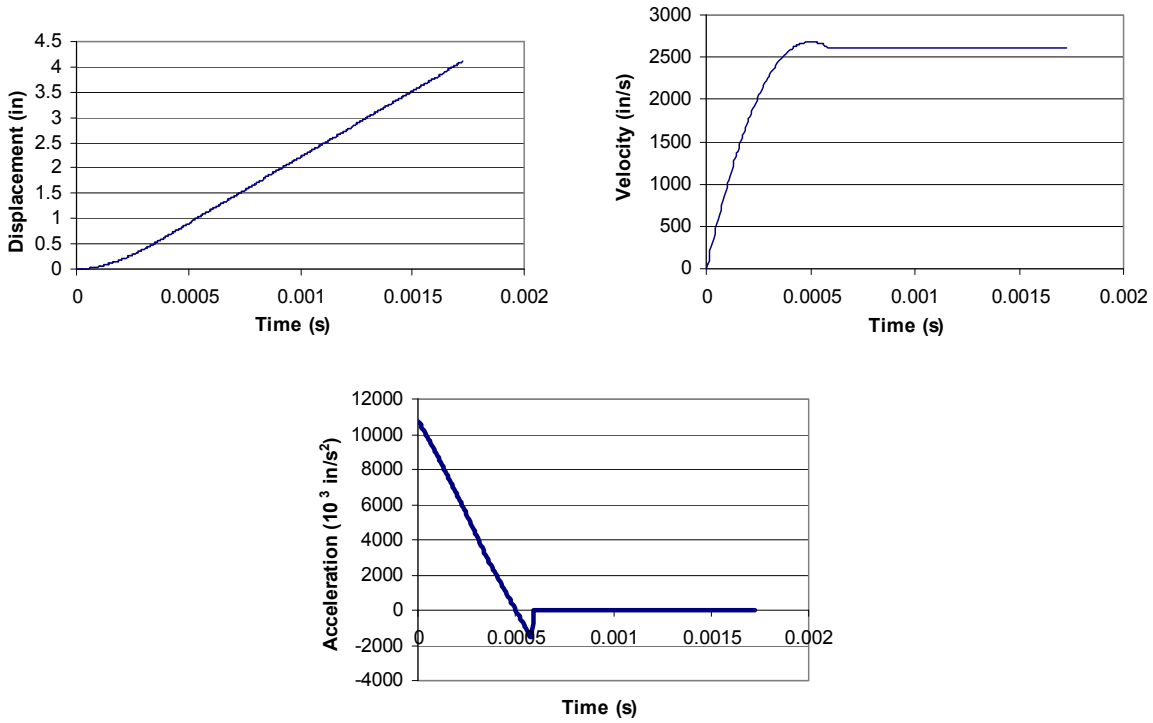

Figure 4.42: Case 7 dynamic response curves for 30° cohesion angle

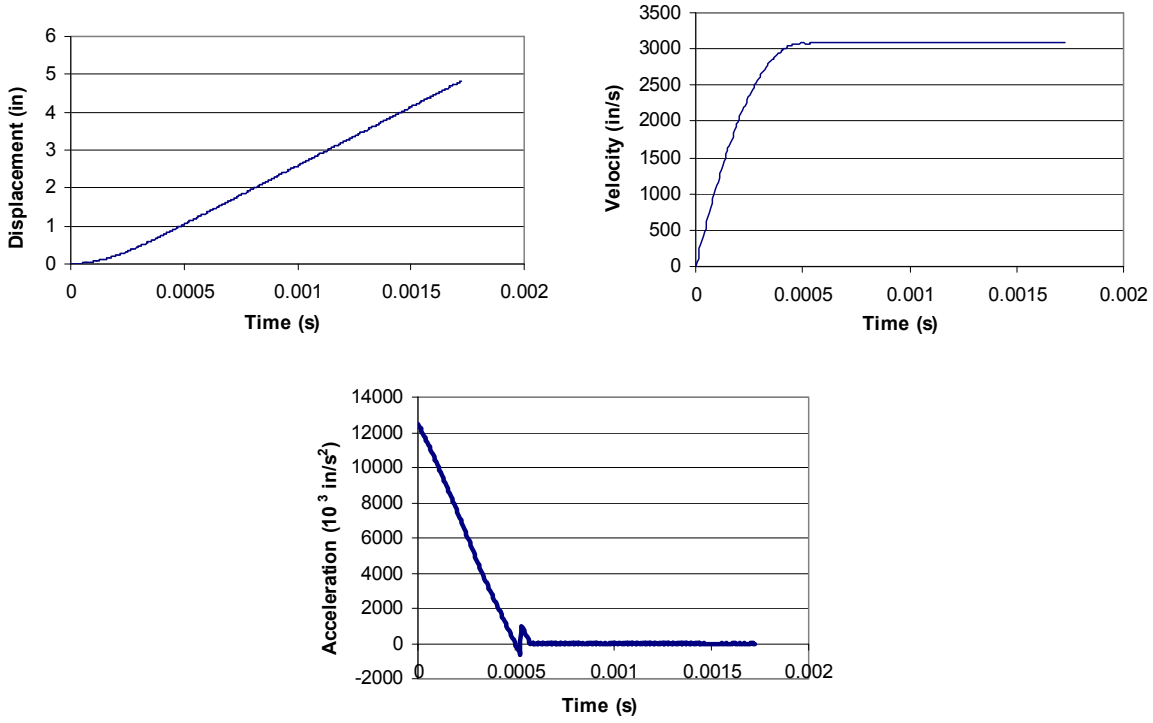

Figure 4.43: Case 7 dynamic response curves for 45° cohesion angle

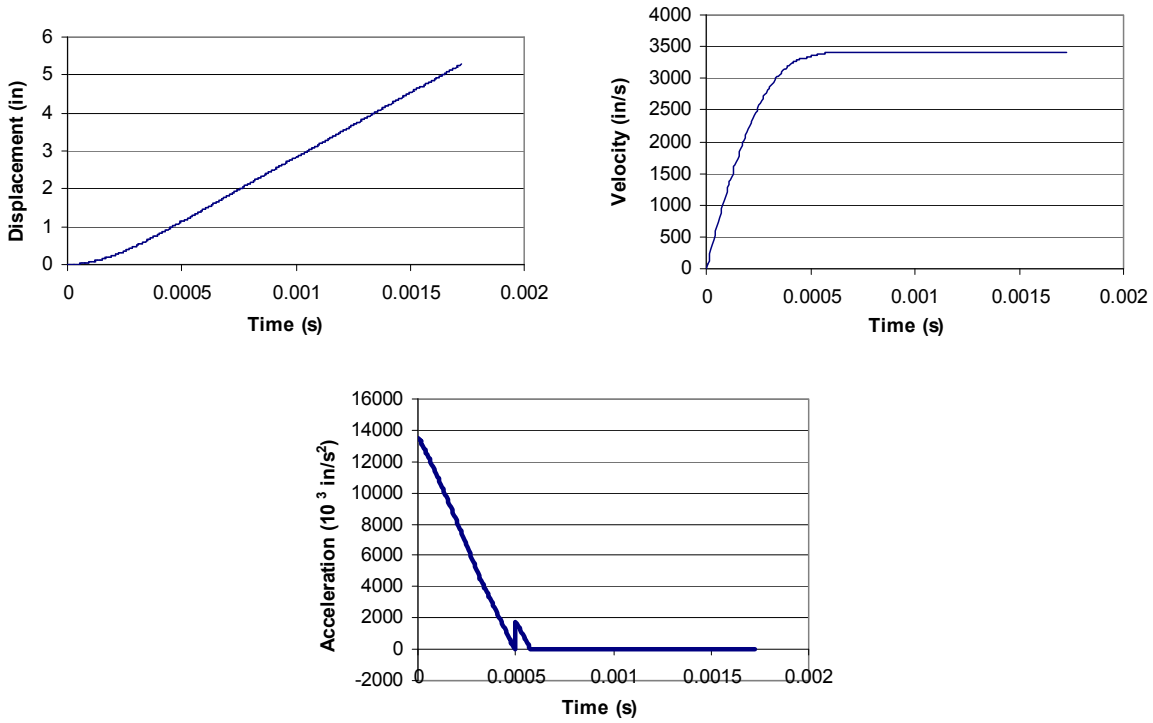

Figure 4.44: Case 7 dynamic response curves for 60° cohesion angle

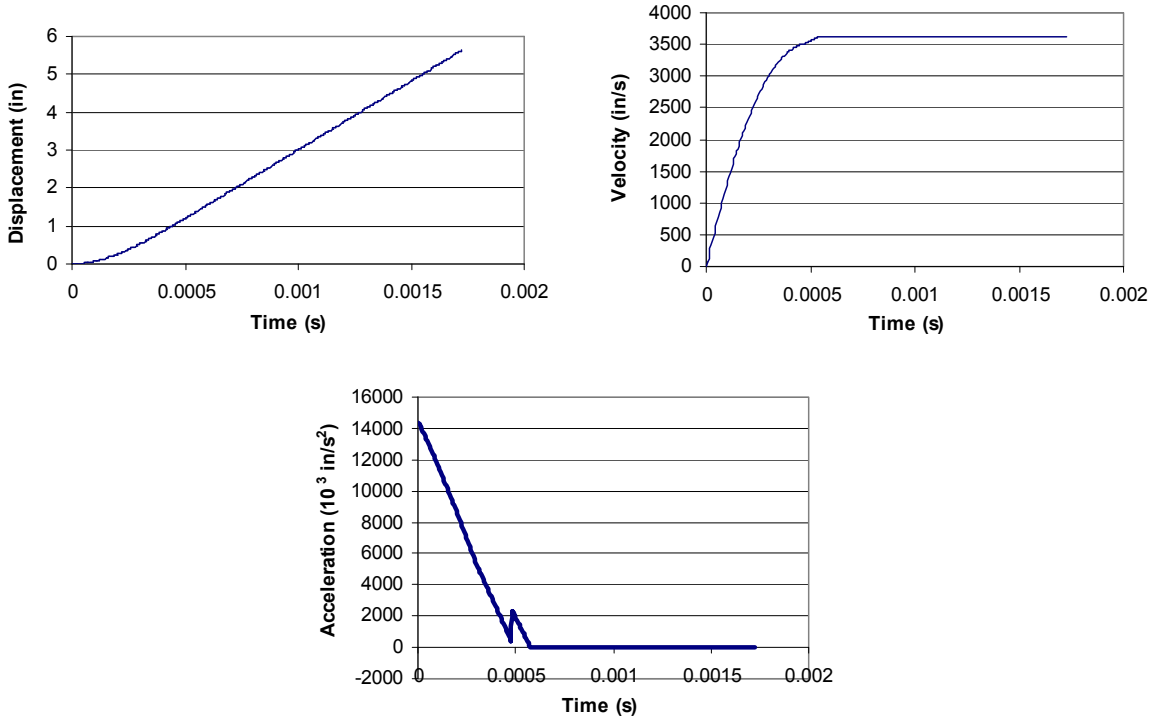

Figure 4.45: Case 7 dynamic response curves for 75° cohesion angle

Looking at the results in Case 5, it appears that as the soil density increases, the displacement, velocity, and acceleration all decrease significantly. Over a time of only 1.15 ms, the displacement ranges from approximately 3.5 inches for clay to approximately 2.8 inches for gravel. Again, because the composite pipe was theoretically breached by the explosion in each model, these displacements would continuously increase at a constant rate over additional time as the velocities remain at their constant peak values. The peak velocities range from just over 3500 in/s for clay to approximately 2800 in/s for gravel, and the peak accelerations range from approximately 14,000,000 in/s^2 for clay to approximately 11,000,000 in/s^2 for gravel. Thus, these SDOF models ultimately indicate that a gravel soil type is best at mitigating damage from the explosion.

Reviewing the Case 6 results, it is clear that as the soil cover depth increases, the displacement, velocity, and acceleration all significantly decrease. Theoretically, the results show that the pipes with 12 inches, 24 inches, and 36 inches of soil cover are breached by the blast, but the pipes at a depth of 60 inches and greater completely withstand the blast pressure without failing.

Although the composite pipe is theoretically breached for the depths of 12 inches to 36 inches, as the diameter increases the displacement decreases significantly from approximately 6.5 inches to approximately 1.5 inches over a time of just 2.3 ms; the peak velocity decreases from approximately 3100 in/s to approximately 950 in/s; and the peak acceleration decreases from approximately 12,000,000 in/s^2 to approximately 3,500,000 in/s^2. These results show that increasing the cover depth by just one more foot in the SDOF model theoretically shows a significant increase in mitigation of damage from the explosion.

These trends continue for the cover depths of 60 inches and greater, which show a great amount of resistance to the blast. Completely containing the blast in each of these models, as the cover depth increases, the displacement decreases from approximately 0.75 inches to approximately 0.32 inches, the velocity decreases from approximately 400 in/s to just over 80 in/s, and the acceleration decreases from approximately 1,400,000 in/s^2 to approximately 300,000 in/s^2. Thus, it is ultimately shown that cover depths of 60 inches and greater work well at mitigating damage from a vehicle passing aboveground and over the pipe.

Looking at the results in Case 7, it appears that as the cohesion angle increases, the displacement, velocity, and acceleration all increase significantly. This is understandable since the mass of soil decreases with a higher cohesion angle. Over a time of just 1.72 ms, the displacement increases from approximately 2.6 inches at 15° to over twice that much, approximately 5.5 inches, at 75°. Again, because the composite pipe was theoretically breached by the explosion in each model, these displacements would continuously increase at a constant rate over additional time as the velocities remain at their constant peak values. The peak velocities increase from approximately 1850 in/s at 15° to approximately 3700 in/s at 75°, and the peak accelerations increase from approximately 7,000,000 in/s^2 at 15° to approximately 14,000,000 in/s^2 at 75°. (Like the displacement, the velocity and acceleration roughly double in magnitude from 15° to 75°.) Thus, it is ultimately shown from these SDOF models that a higher cohesion angle is better at mitigating damage from the explosion.

4.5.4 Additional Mass Effects

As mentioned in Section 4.4.2, a Humvee has been selected as the vehicle type for the additional mass above the soil, and the contributing weight of two of its wheels, 2600 lbs, has generally been used as a more conservative approach. The results from this weight will now be compared to the results using the total weight of all four wheels, 5200 lbs. And finally, a model will be created using only the weight of a 200-lb human as the additional source of mass. This class of comparisons is designated as Case 8.

Varying the weights as just explained, the other following parameters were held constant as follows: composite material of E-glass/epoxy, ply stacking sequence of [0/90/0]°, pipe thickness of 1 inch, pipe diameter of 48 inches, cover depth of 12 inches, soil density of 120 pcf, cohesion angle of 45°, and impulsive loading HE-14. Figures 4.46 through 4.48 show the dynamic response curves for each of the Case 8 SDOF models.

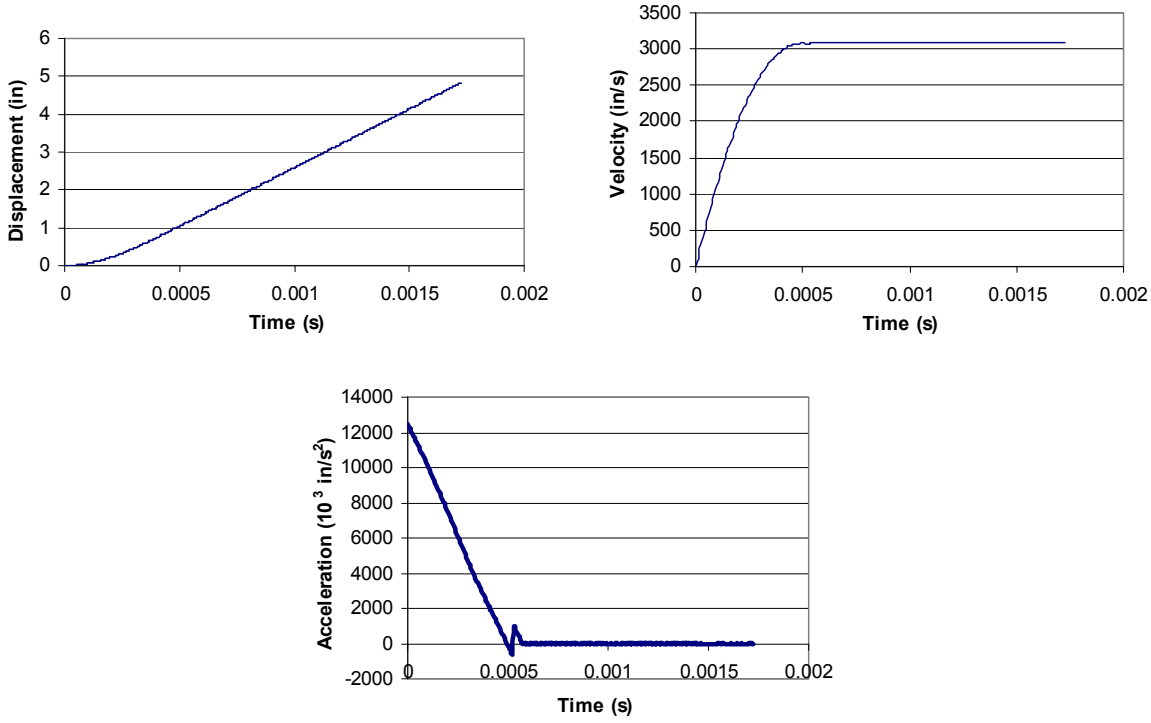

Figure 4.46: Case 8 dynamic response curves for a 2-wheeled Humvee

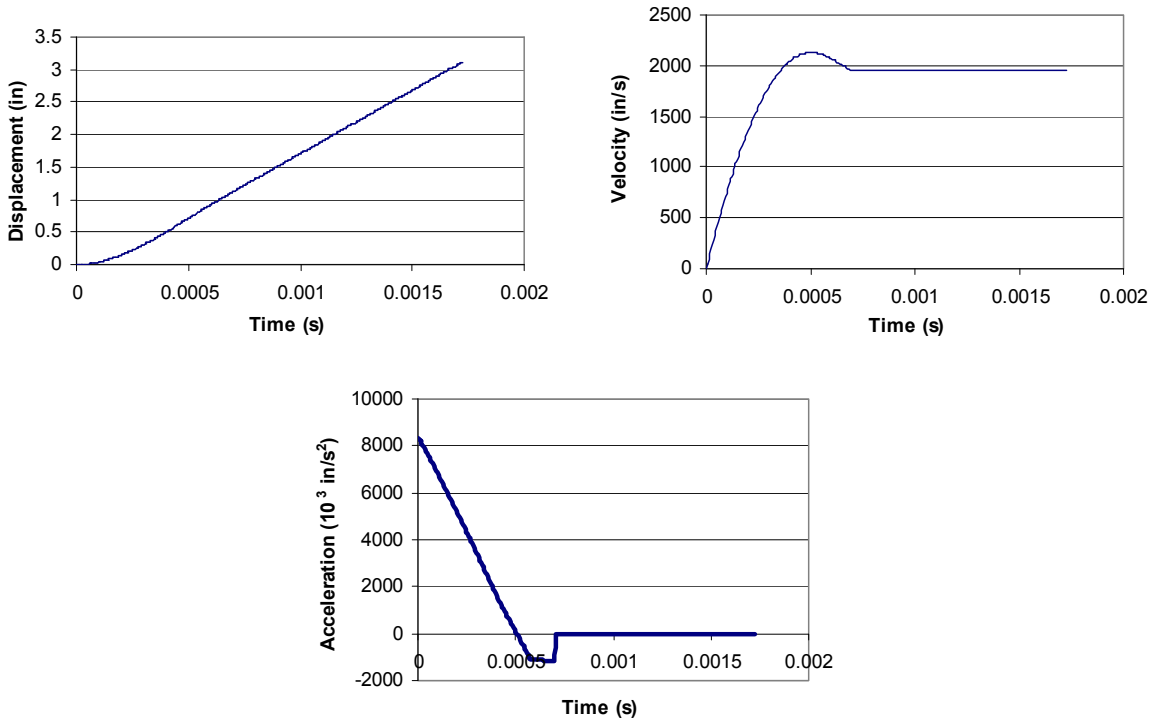

Figure 4.47: Case 8 dynamic response curves for a 4-wheeled Humvee

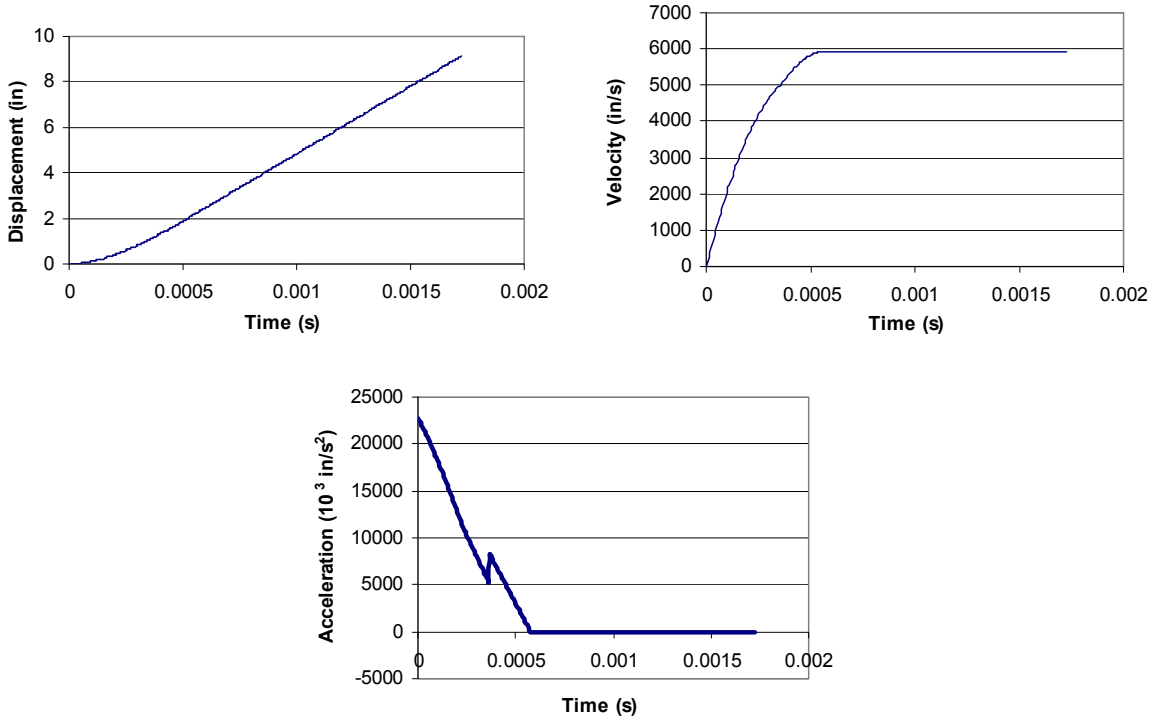

Figure 4.48: Case 8 dynamic response curves for a 200-lb human

From the results in Case 8, it is apparent that, as the weight decreases, the displacement, velocity, and acceleration responses increase. The composite pipe theoretically failed in each model, so the displacements shown should continue to increase over more time at a constant slope. Comparing them over just 1.72 ms, though, the displacement is much smaller when the weight of four wheels is used; its displacement is just over 3 inches, compared to just under 5 inches when using the weight of two wheels. Furthermore, the velocity and acceleration both significantly decrease when accounting for all four wheels. The peak velocity decreases from approximately 3000 in/s with two wheels to approximately 2100 in/s with all four wheels, and the peak acceleration decreases from approximately 12,000,000 in/s^2 with two wheels to approximately 8,000,000 in/s^2 with all four wheels.

Now looking at the results from the SDOF model using just the 200-lb human, the displacement, velocity, and acceleration responses are tremendously higher. Over only 1.72 ms, the displacement reaches approximately 9 inches. Moreover, the peak velocity and acceleration values reach as high as approximately 6000 in/s and 22,000,000 in/s^2, respectively.

Thus, it is ultimately shown from the Class 8 SDOF models that less damage will occur to a vehicle passing when all four of its wheels are over the pipe rather than just its front two or back two wheels, and a much higher response occurs when only a 200-lb human is walking over the pipe.

4.5.5 Loading Effects

The next set of SDOF models, Case 9, were generated to analyze the effects of different loadings—i.e., different amounts of explosive material—on the dynamic response of underground composite pipe systems, keeping all other system parameters the same.

As mentioned in Section 4.4.5, an loading weight was determined based on the density of loading material and the volume of a sphere having a diameter equivalent to one-fourth, and one having a diameter equivalent to half, the diameter of the composite pipe. These loadings will simply be referred to as the 1/4-diameter and 1/2-diameter loadings, respectively. Using this approach, the dynamic response values of the 1/4-diameter and 1/2-diameter loadings were calculated for each pipe diameter. Thus, referring to Table 4.2, the loadings used are HE-1 through HE-10.

Varying the loading weights and diameters as just mentioned, the rest of the system parameters were held constant as follows: composite material of E-glass/epoxy, ply stacking sequence of [0/90/0]°, pipe thickness of 1 inch, cover depth of 12 inches, soil density of 120 pcf, cohesion angle of 45°, and vehicle weight of 2600 lbs. Figures 4.49 through 4.58 show the dynamic response curves for each of the Case 9 SDOF models.

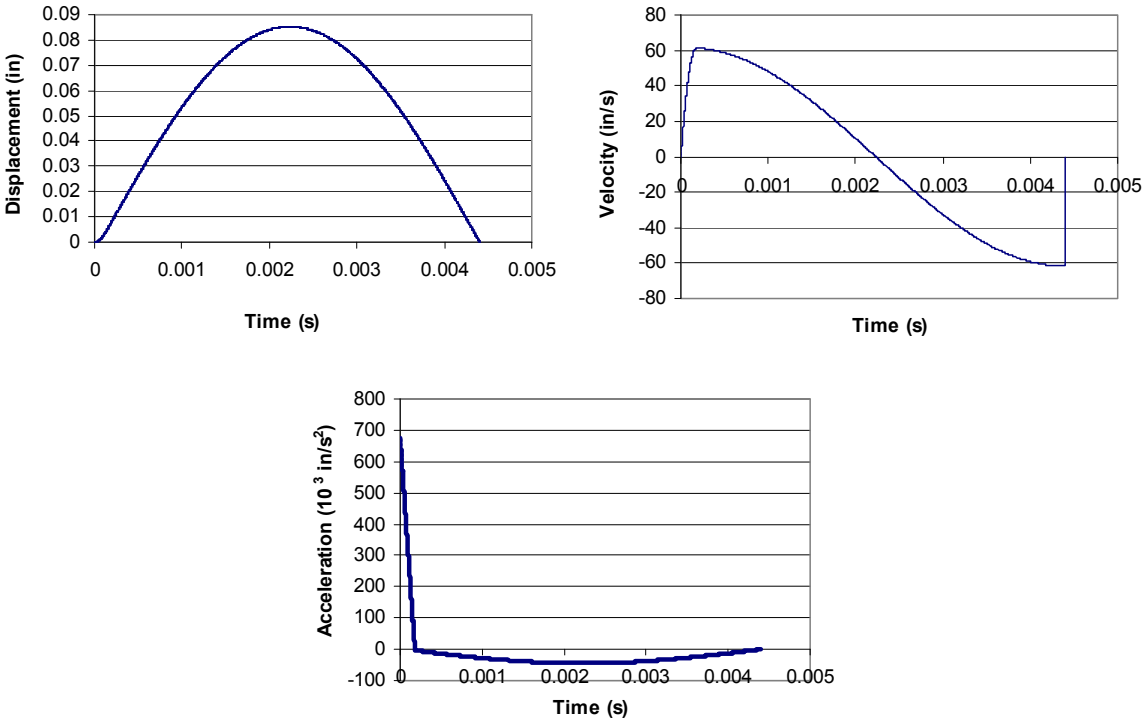

Figure 4.49: Case 9 dynamic response curves for HE-2 (16-inch diameter pipe)

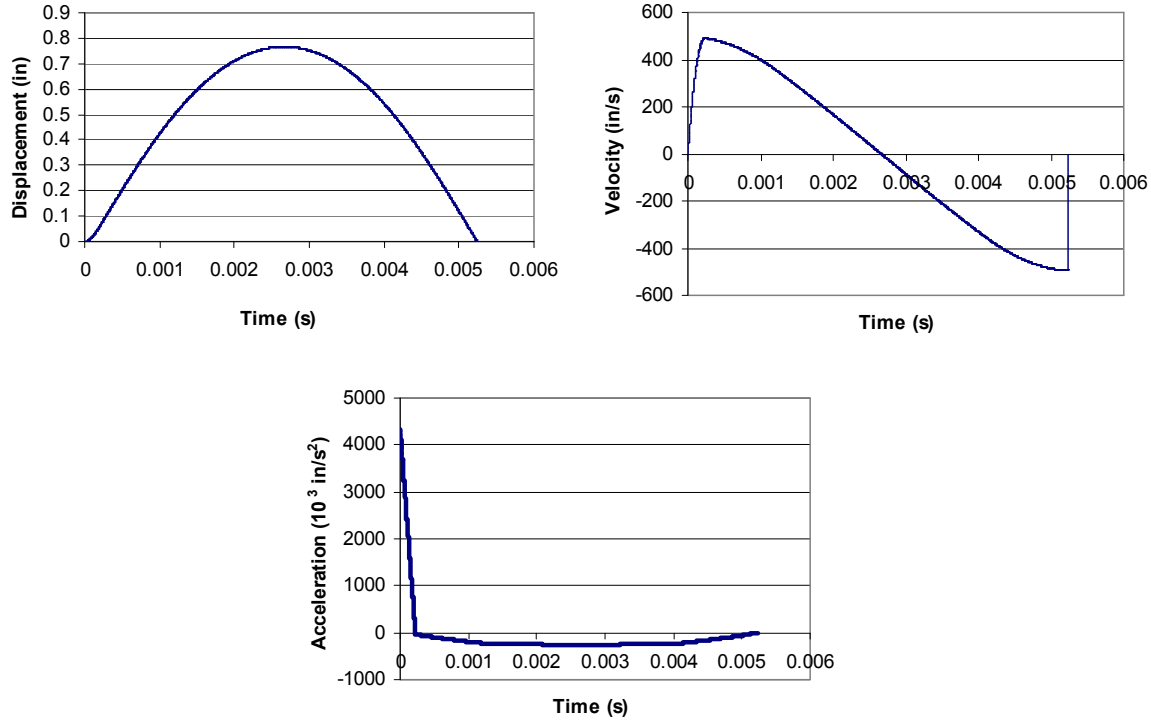

Figure 4.50: Case 9 dynamic response curves for HE-1 (16-inch diameter pipe)

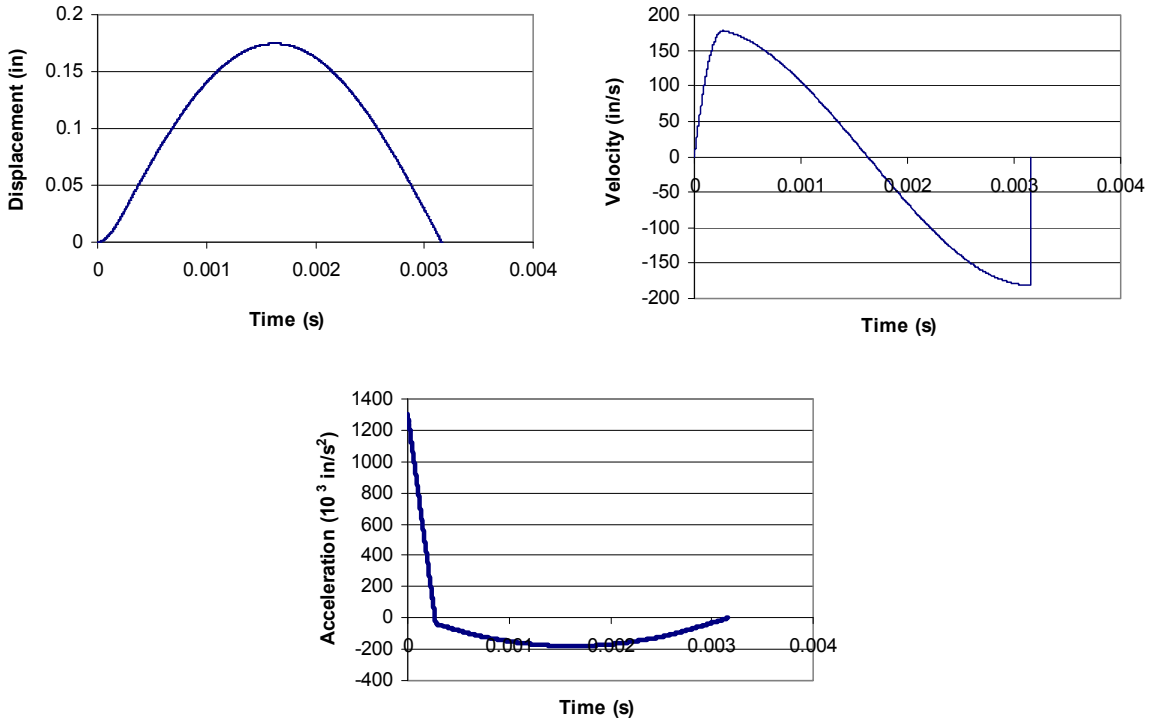

Figure 4.51: Case 9 dynamic response curves for HE-4 (24-inch diameter pipe)

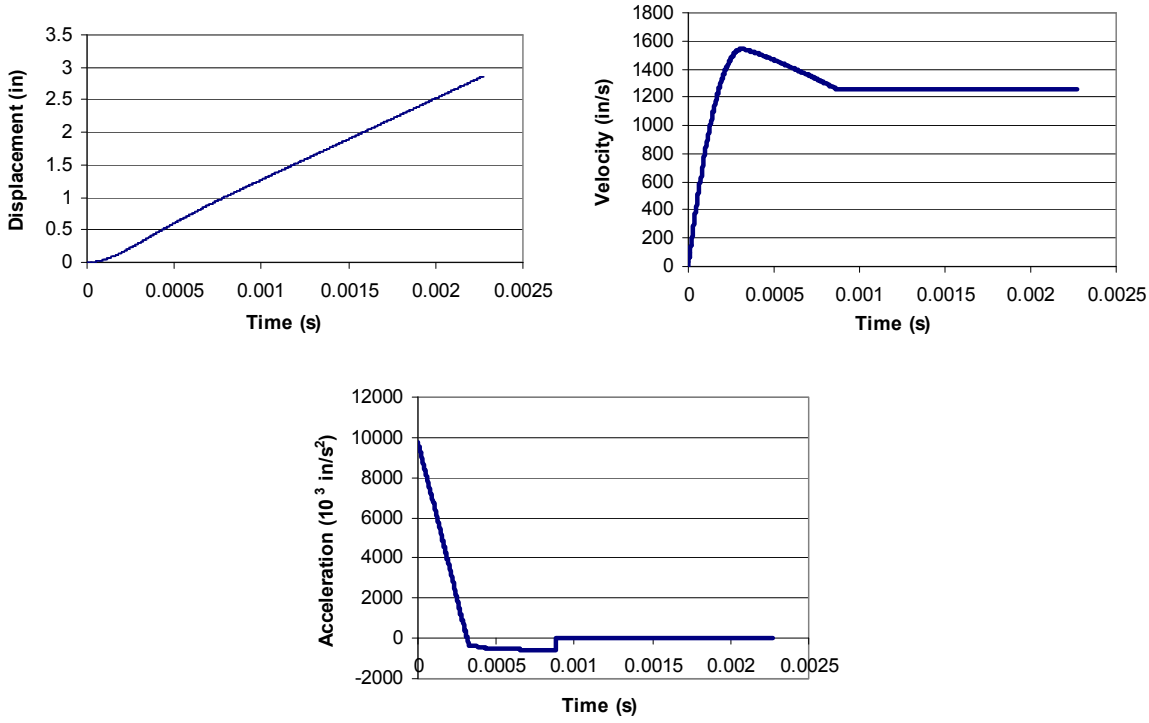

Figure 4.52: Case 9 dynamic response curves for HE-3 (24-inch diameter pipe)

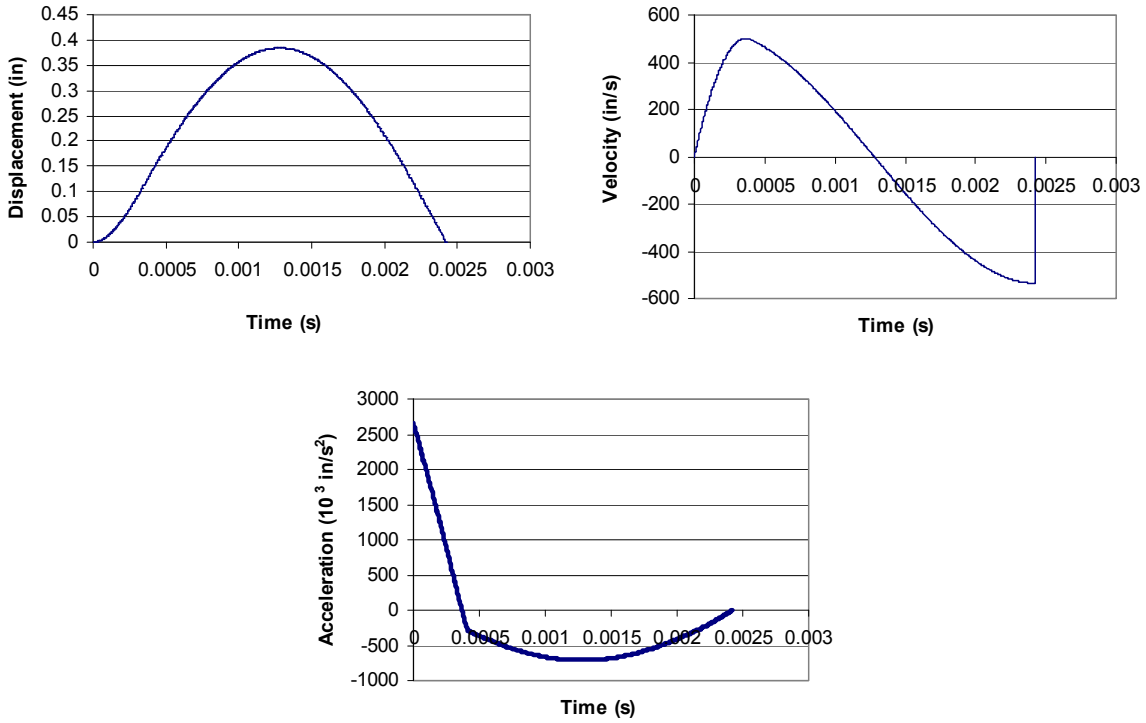

Figure 4.53: Case 9 dynamic response curves for HE-6 (36-inch diameter pipe)

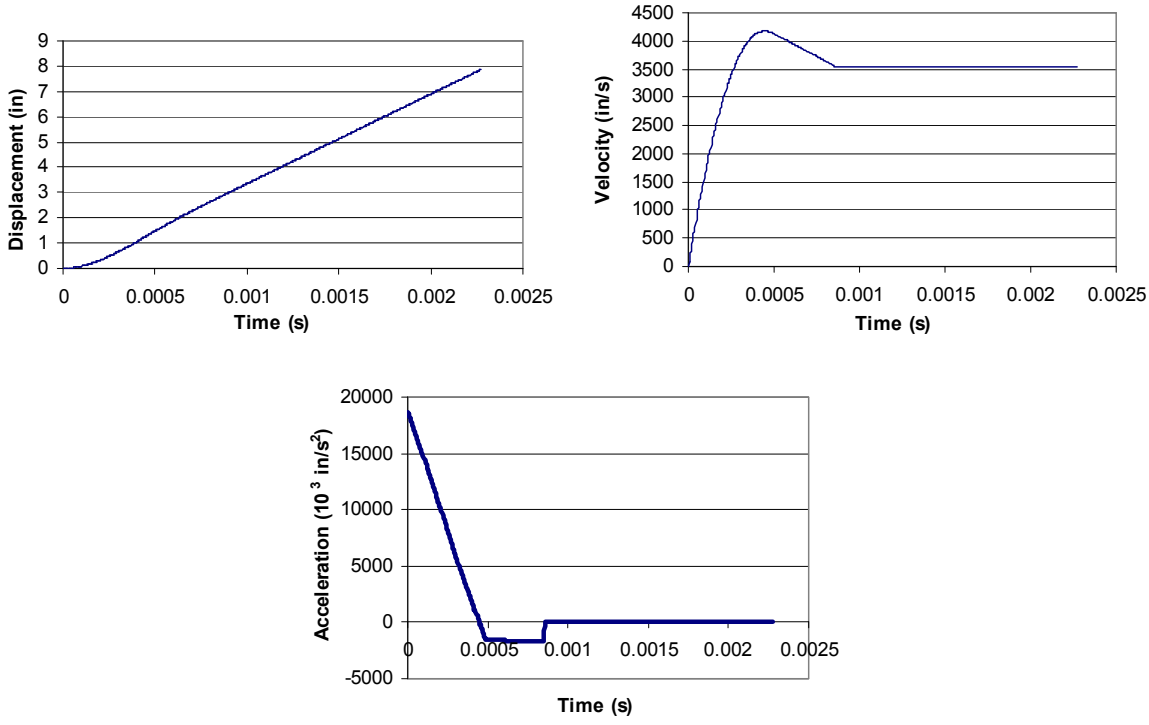

Figure 4.54: Case 9 dynamic response curves for HE-5 (36-inch diameter pipe)

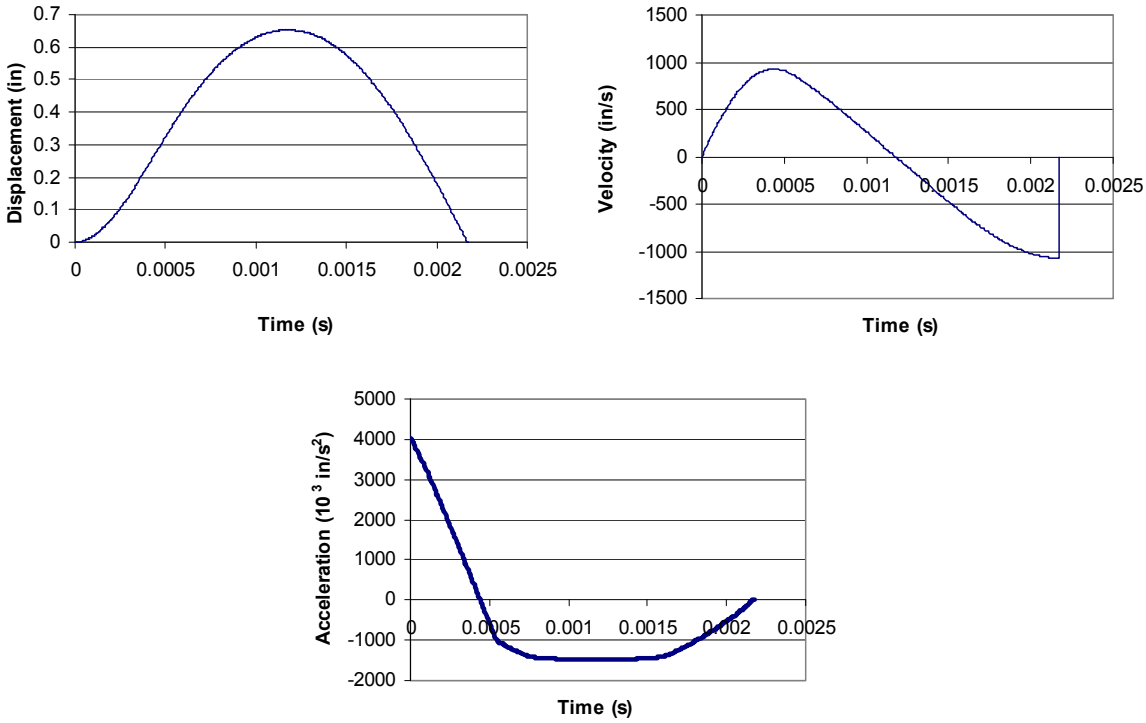

Figure 4.55: Case 9 dynamic response curves for HE-8 (48-inch diameter pipe)

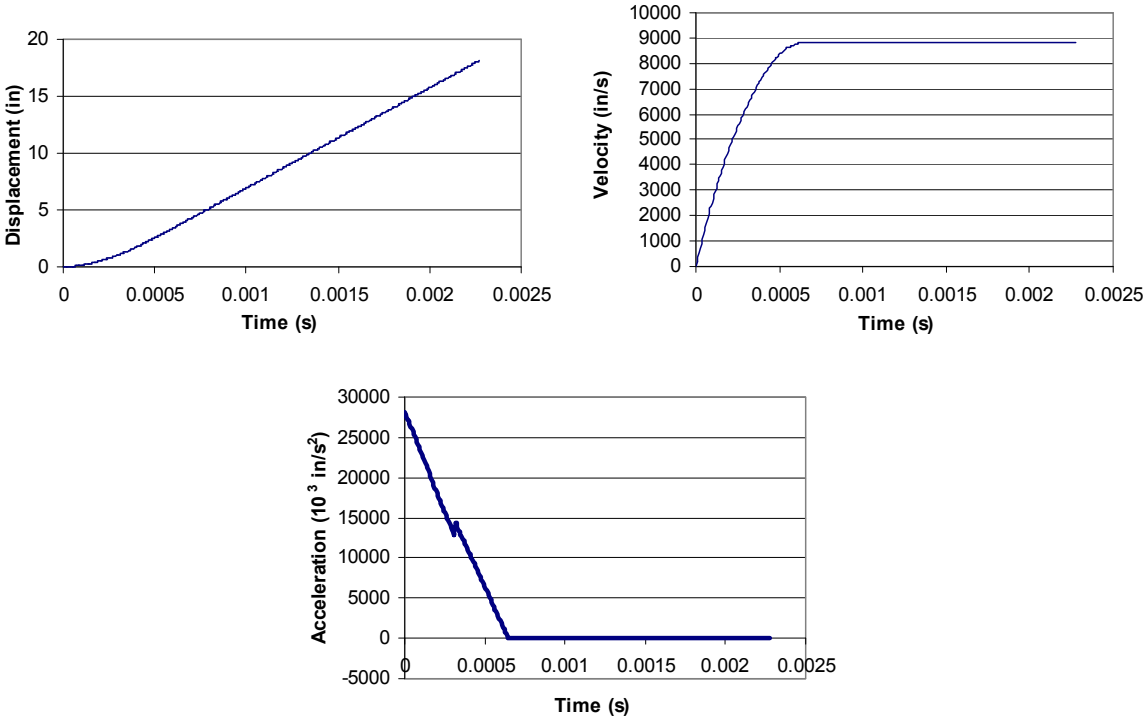

Figure 4.56: Case 9 dynamic response curves for HE-7 (48-inch diameter pipe)

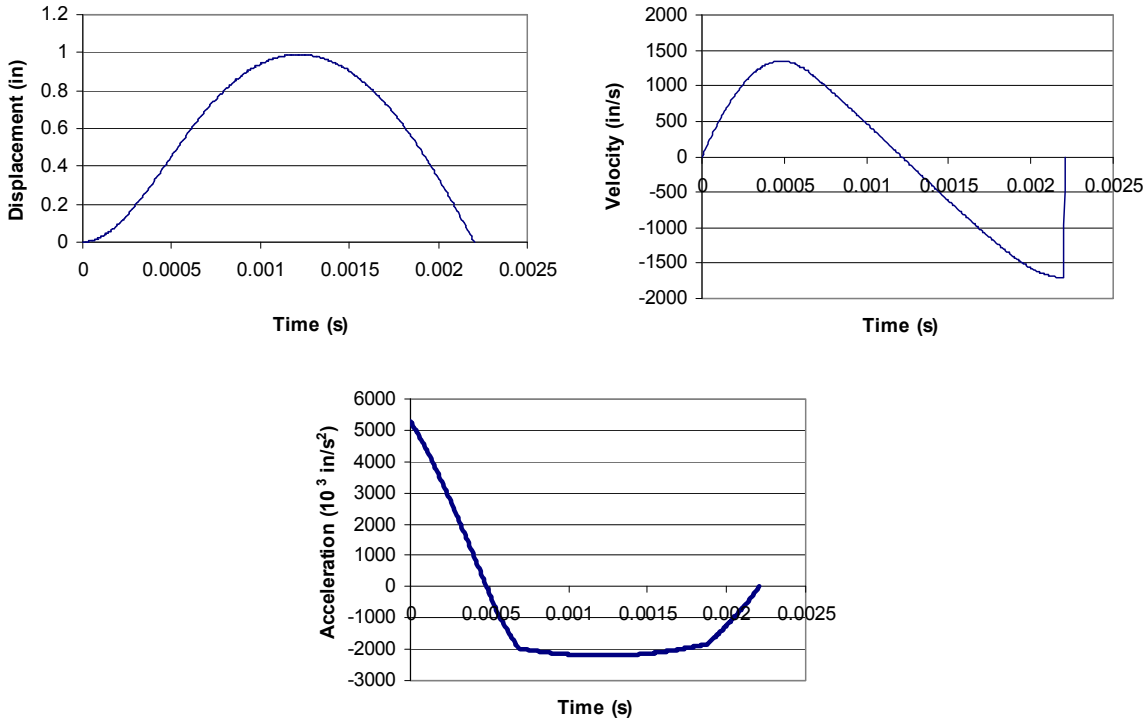

Figure 4.57: Case 9 dynamic response curves for HE-10 (60-inch diameter pipe)

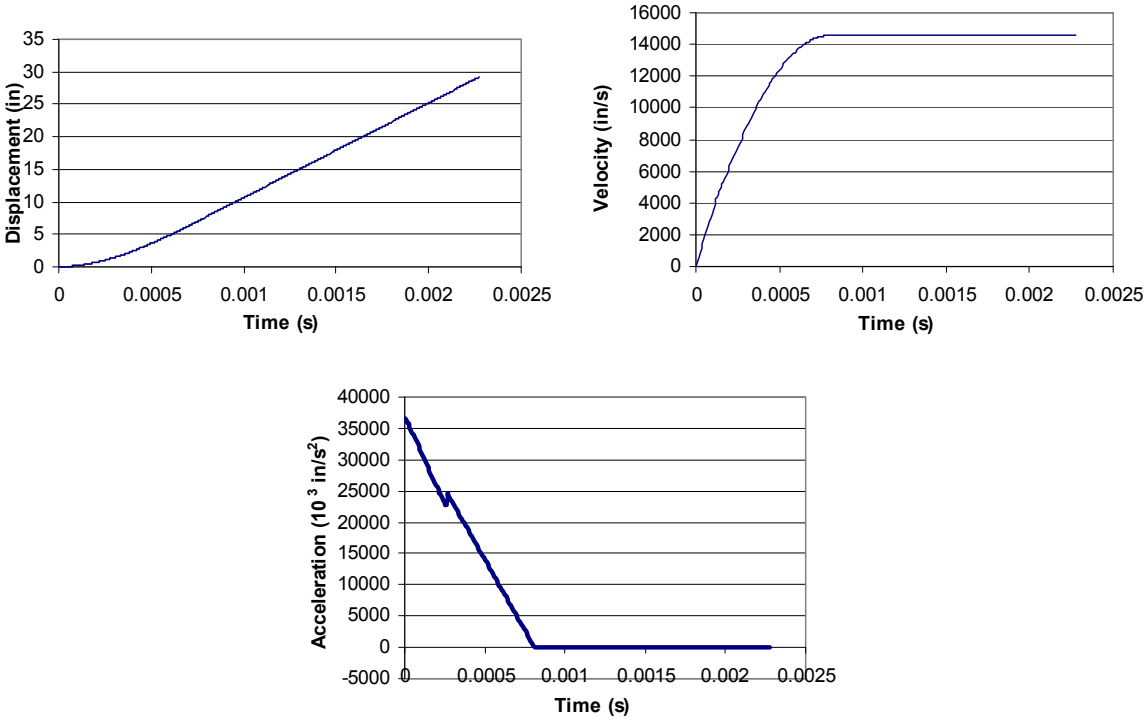

Figure 4.58: Case 9 dynamic response curves for HE-9 (60-inch diameter pipe)

Reviewing the results from the Case 9 models, for each diameter tested, the dynamic response values are significantly higher for the 1/2-diameter loadings than the 1/4-diameter loadings. For all models except the 16-inch diameter ones, the results theoretically indicate that the system completely withstands the pressure from the 1/4-diameter loading without failing, but it fails as the blast breaches through the pipe and soil from the 1/2-diameter loading.

Comparing the results of the models with 1/4-diameter loadings and pipe diameters from 24 inches to 60 inches, the response values increase as the diameter increases, with the 24-inch diameter pipe showing the most resistance, having a peak displacement of approximately 0.17 inches, a peak velocity of approximately 180 in/s, and a peak acceleration of approximately 1,300,000 in/s^2.

Comparing the results of the models with 1/2-diameter loadings and pipe diameters from 24 to 60 inches, the response values also increase as the diameter increases, with the 24-inch diameter pipe again showing the most resistance, having a displacement of approximately 2.8 inches in just 2.27 ms, a peak velocity of just under 1600 in/s, and a peak acceleration of approximately 10,000,000 in/s^2. The results are tremendously higher for the 60-inch diameter pipe, which shows a displacement of just under 30 inches in just 2.27 ms, a peak velocity of over 14,000 in/s, and a peak acceleration of over 35,000,000 in/s^2.

For the two models with 16-inch diameter pipes, both show complete containment of the blast, but the one subjected to the HE-2 loading shows the lowest response values, having a peak displacement of only approximately 0.085 inches, a peak velocity of just

over 60 in/s, and a peak acceleration of approximately 700,000 in/s^2. Overall, among all the Case 9 models, this is the one that shows the lowest response values.

4.5.6 Final Observations of Results

Reviewing the results of Cases 1 through 9, the following observations were made:

- Among the various types of fibers tested, IM6 carbon shows the most resistance, with significantly lower displacement and peak velocity than the other fiber types.
- The [0/45/90]° fiber stacking sequence shows complete containment of internal pressure loading, whereas the [0/90/0]° and [0/30/60/90]° stacking sequences show breaching of the pipe and soil.
- Dynamic response values decrease as the composite pipe thickness increases and as the diameter increases. The pipe diameter of 60 inches shows complete containment of the internal dynamic pressure.
- As the soil density increases (e.g., from clay to sand), the dynamic response values significantly decrease. Since its density is the highest, the gravel soil type shows the most resistance.
- As the soil cover depth increases, the dynamic response values significantly decrease. Cover depths of 60 inches and greater show complete containment of the internal dynamic pressure.

- As the soil cohesion angle increases, the dynamic response values increase. The angle of 15° shows the lowest displacement, velocity, and acceleration among the cohesion angles tested.
- Dynamic response values decrease when accounting for all four wheels of the Humvee, rather than just two, and the values are significantly greater when only accounting for a 200-lb human.
- With more explosive weight, the dynamic response values increase. With exception of the 16-inch diameter pipe, which shows complete containment of the pressure from both explosive weights, the weights associated with the 1/4-diameter loadings show complete containment for each pipe diameter, but the internal pressure theoretically breaches the pipe and soil when using the 1/2-diameter loadings.

The overall objectives of the dynamic analysis performed on the underground composite pipe system was to develop and utilize a *framework* algorithm that could compute dynamic response values of a source of mass positioned over a buried composite pipe, subjected to various system parameters associated with the composite reinforcing material, the pipe geometry, the mass (i.e., soil and additional mass), and the internal dynamic loading, as well as to illustrate trends that show the effects of changing these parameters.

The tool created was essentially a spreadsheet acting as the *SDOF model*, which consists of various formulas developed based on single-degree-of-freedom numerical evaluation (i.e., central difference methodology), as mentioned earlier in the chapter. The

dynamic response values were computed incrementally over time, and the trends associated with changing system parameters were summarized in the previous sections.

Finally, a couple of examples will be illustrated to show how the model can be implemented for design scenarios. It will also be noted how the SDOF tool can be further refined to calculate dynamic response values more accurately, and how the results can be used to address, most importantly, the concern of vehicle occupant safety. These issues will be discussed further in the following sections.

4.5.7 Implementation of SDOF Model for Design Scenarios

Now, it will be illustrated how the SDOF model works for a couple of scenarios that could actually be encountered in the field. First, in Example 1, a composite pipe exists consisting of S-glass fibers and epoxy resin, with the fibers stacked in a [0/90/0]° layup pattern. The composite pipe is 48 inches in diameter and has a 1/2-inch wall thickness. There is about 24 inches of sandy soil above the buried pipe, at a cohesion angle of about 45°. Suppose an engineer needs to know how the system responds to an internal dynamic pressure from the HE-8 loading. To be conservative, the additional mass used will be equivalent to two wheels of a Humvee, or 2600 lbs. Figure 4.59 shows the dynamic response predictions for this example.

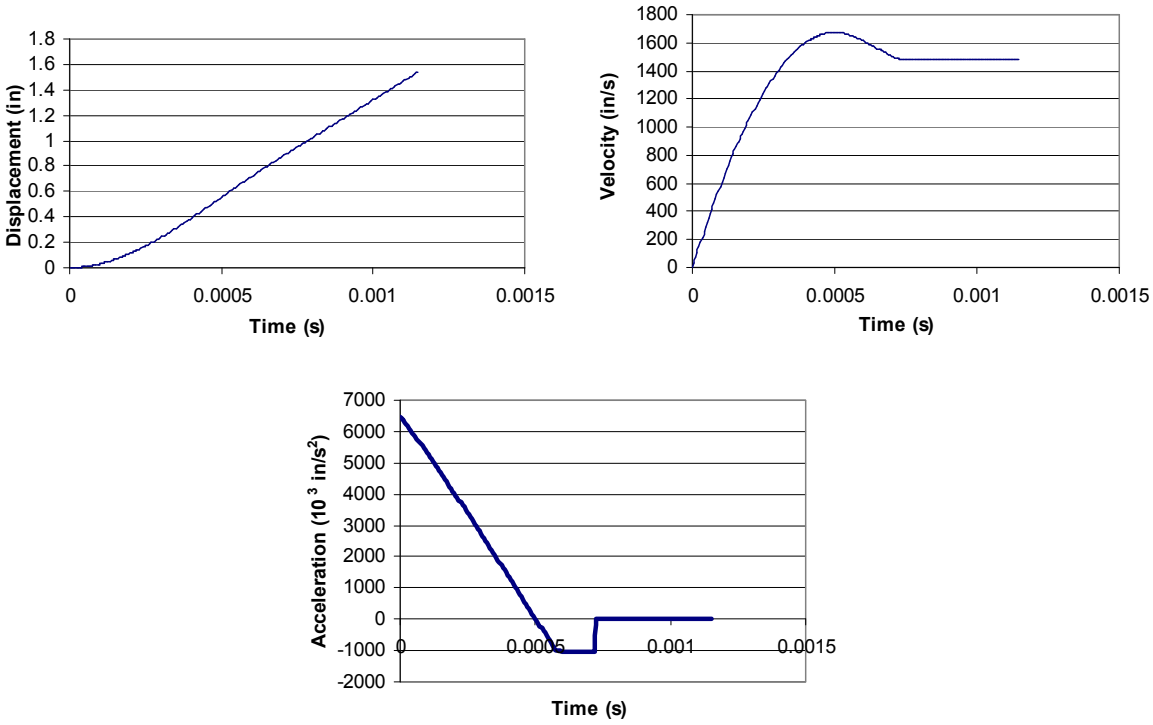

Figure 4.59: Dynamic response curves for Example 1

As shown by the results, the SDOF model indicates that the composite pipe would rupture and breaching would occur. The system's displacement continuously increases, and its velocity reaches a peak value of approximately 1670 in/s and a peak acceleration of approximately 6,500,000 in/s^2.

Since breaching occurred in Example 1, the engineer could make modifications to the system to attempt containment of the internal pressure. These modifications are accounted for in Example 2. In this example, the fiber type is changed to E-glass, and the fibers are stacked in a [0/45/90]° layup pattern. Also, 3 more feet (36") of additional sandy soil is added above the 48-inch diameter pipe, and a 1-inch wall thickness is used. Again, the engineer wants to know how the system responds to an internal dynamic pressure from the HE-8 loading, and the additional mass used will be equivalent to two

wheels of a Humvee, or 2600 lbs. Figure 4.60 shows the dynamic response predictions for this example.

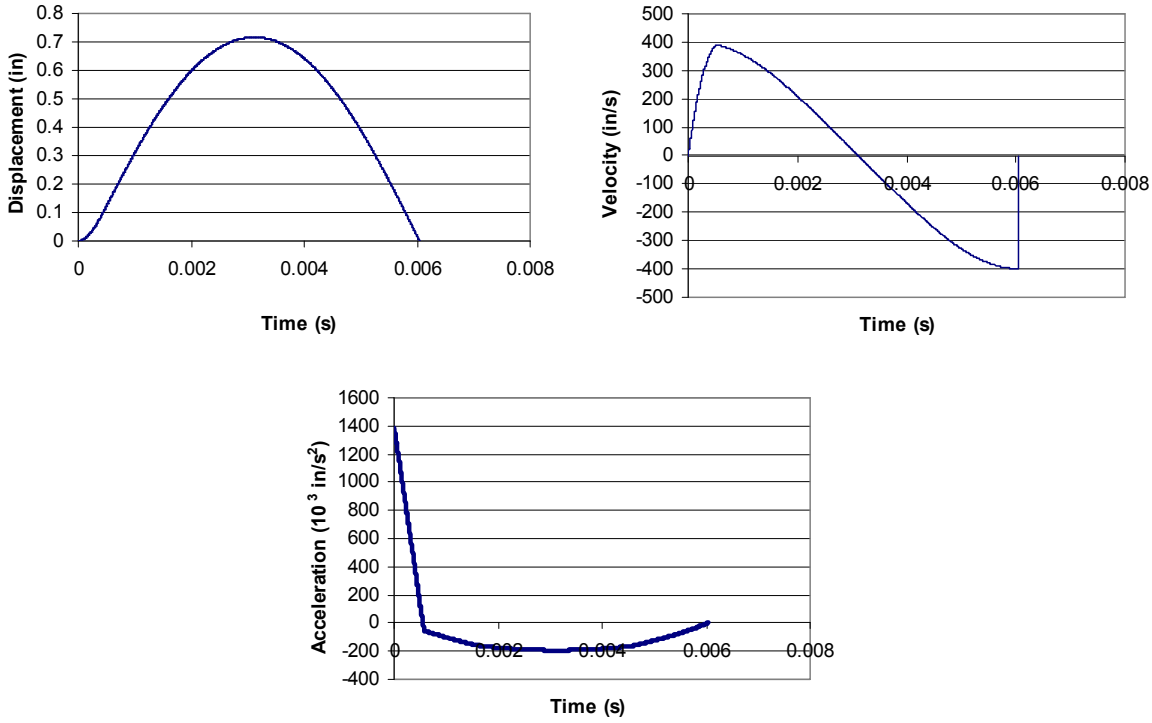

Figure 4.60: Dynamic response curves for Example 2

As shown by the results, the system modifications were successful since the SDOF model indicates that the composite pipe would completely withstand the internal pressure in this example. The system's displacement reaches a peak value of only approximately 0.7 inches, and its velocity reaches a peak value of only approximately 400 in/s and a peak acceleration of only approximately 1,400,000 in/s^2.

4.6 Further Refinement of SDOF Model

The SDOF analytical tool developed in this chapter is simply a framework algorithm for determining the dynamic response of the system subjected to blast loading. Although the overall approach is justifiable in terms of single-degree-of-freedom methodology, only a foundation was laid for correctly implementing the primary system parameters—that is, the mass, resistance, and loading components. Thus, further steps should be taken to account for such factors as a more accurate representation of nonlinear resistance and high strain-rate effects. These issues will be discussed briefly in the following subsections.

4.6.1 Nonlinear Resistance

According to Chopra (2007), the nonlinear force-displacement relationship for an inelastic structure depends not only on the history of displacements, but also on whether the displacements are increasing or decreasing. Thus, the nonlinear resistance function f_S should actually be a function of both displacement u and velocity $\dot{u}$:

$$f_S = f_S(u, \dot{u}) \tag{4-35}$$

This approach was beyond the scope of this research, however, since a static analysis was performed to determine the resistance curve, neglecting the effects of velocity as the pipe expands.

As mentioned in Section 4.3.2, in addition to material and geometric nonlinearity, contact problems are another type of nonlinearity also present in the underground composite pipe system. They involve boundary conditions that change with the motion of

the structural system. As one structural component comes in contact with another, the resistance of the system changes (Tedesco et al. 1999).

When the static analysis was performed on the composite pipe to determine its nonlinear resistance, the soil was not taken into account. As the composite pipe comes in contact with the soil throughout the motion of the system, though, the resistance actually changes. Thus, in reality, this form of nonlinearity exists in the underground composite pipe system, but the complexity involved in establishing equilibrium under this condition is beyond the scope of this research.

4.6.2 High Strain-Rate Effects

As mentioned in Chapter 2, fiber-reinforced composites show an increase in yield strength as the strain rate increases. However, information on strain-rate data for composites is limited and remains an ongoing research study. Ultimately, though, once more research and experimentation have been performed to yield reliable strain-rate data, the resistance of the composite pipe can be adjusted appropriately, resulting in more accurate nonlinear resistance functions for the SDOF model.

4.7 Vehicle Occupant Safety

At the heart of the matter dealing with blast mitigation of the underground composite pipe is the safety and survivability of individuals occupying a vehicle as it crosses over the roadway. Unlike most cases of structural analysis, failure of the structure is usually expected for structural systems subjected to blast loading. So rather than

focusing on methods to entirely sustain the loading, attention is primarily devoted to developing techniques to mitigate damage to the surrounding environment and people.

In many structures subjected to explosions, such as buildings, injuries and fatalities occur due to fragmentation of structural debris at extremely high accelerations. In this case, however, more attention should be paid simply to the acceleration of the vehicle as it is impacted by the blast. It will be assumed that the acceleration of the vehicle occupant is the same as that of the vehicle.

Human tolerance of acceleration is determined according to how much "g-force" one can withstand. Rather than a measurement of actual force, the g-force is a measurement of acceleration, expressed as a factor of the acceleration due to gravity *g*. For example, 50 g is equivalent to 19,320 in/s^2 since 50 × 386.4 in/s^2 = 19,320 in/s^2.

The g-force limit for a human depends on various factors, such as the magnitude of the acceleration, the duration it is applied, its direction and location on the body, and the position of the body (eNotes 2011). Many studies have been performed on determining g-force limits, and these limits are typically divided into vertical axis and horizontal axis limits. Horizontal axis limits are used in car crash studies, for example. For the purpose of this research, though, focus will only be paid to the limit associated with the vertical axis since the blast propagates upwardly from directly beneath the vehicle.

According to the Department of the Army's *Occupant Crash Protection Handbook for Tactical Ground Vehicles*, published in 2000, the vertical axis limit for an accelerative force acting upwardly is about 15 g, which is equivalent to 5796 in/s^2 (Tabiei and Nilakantan 2007). Reviewing all the peak accelerations calculated in Section 4.5,

unfortunately all of them exceed this limit, with the lowest being approximately 300,000 in/s^2 (Case 6 model with 120-inch cover depth). Thus, theoretically, fatality of the vehicle occupant occurs in each model run. However, due to this SDOF algorithm being developed only as an initial framework, with much further refinement necessary in order to determine accurate results (as explained in Section 4.6), this safety assessment is not very valid. Ultimately, only when the SDOF algorithm is further refined and then validated by testing in the field can the issue of vehicle occupant safety and survivability be accurately analyzed.

Chapter 5

Conclusions and Recommendations

5.1 Conclusions

Buried pipes are used for various industrial applications, but their serviceability is often jeopardized by internal explosions, such as gas line ruptures or detonation of IEDs. Composite pipes and liners have the potential to help contain the energy from an internal detonation. Thus, an engineering methodology was developed to analyze underground composite pipes subjected to short duration internal dynamic pressure loads and to demonstrate its applicability.

Finite element models of composite pipes were developed, and static analyses were performed using fundamental pipe mechanics theory to determine their resistances to internal pressure loading. A static analytical tool was created that could take the effective stress-strain data computed from the finite element analysis and output a pressure-displacement relationship. Using this pressure-displacement data, a SDOF model was developed using numerical central difference methodology, in order to determine dynamic response predictions for a source of mass overlaying a buried composite pipe that is subjected to internal blast loading. Blast loading data was calculated, and several runs were then generated by varying system components related to its mass, resistance, and loading.

From the static analyses, a few observations were made. First, it became evident that, regarding the composite pipe wall, the total thickness is the parameter that primarily affects the pipe's resistance, regardless of the density of plies within the wall. Second, the [0/45/90]° orientation and the IM6 carbon fiber were the most effective in terms of strength and strain energy capacity. Third, regarding the pipe radius and thickness, the bursting pressure follows a linearly increasing relationship with respect to an increasing thickness-to-radius ratio of the pipe.

From the SDOF model runs, more conclusions were drawn based on the calculated dynamic response results. The analyses either showed complete containment of the blast pressure, as shown by the displacement reaching a peak value before decreasing to its original position, or the runs showed the blast pressure completely breaching through the pipe and soil, as shown by the displacement continuously increasing to infinity as the velocity reached a constant magnitude.

First, the IM6 carbon fiber and the [0/45/90]° stacking sequence showed the most resistance among all tested fiber types and stacking sequences, respectively. Second, smaller dynamic response values were calculated with increasing pipe diameters and thicknesses. Third, as the soil density increased, the cohesion angle decreased, and the cover depth increased, smaller dynamic response values resulted. Fourth, dynamic response values decreased with more vehicle weight. Fifth, as a higher weight of explosive material was used within a pipe of a certain diameter, the dynamic response values increased.

Finally, the dynamic response values calculated by those runs provided insight into the techniques that would be most effective in terms of increasing the resistance of

the underground composite pipe system and, in turn, mitigating damage to structures outside of the pipe. However, since the model must be refined to account for factors such as high strain-rate effects and validated against field test results, only the trends observed can be accepted. Nonetheless, a methodology framework was successfully developed for performing an engineering analysis on buried composite pipes subjected to internal dynamic loading.

5.2 Recommendations

In regard to treating the system as a single degree of freedom, refinement to the SDOF model is necessary, as previously explained in Chapter 4, in order to obtain accurate dynamic response predictions. Additionally, the model must be validated by comparing its results with those from field testing of composite pipes under dynamic loading.

High strain-rate testing of fiber-reinforced composites specifically used for pipes and liners should be conducted. Examples of such tests, including the Hopkinson pressure bar test, the expanding ring test, and the flyer plate test, were discussed in Chapter 2.

It is recommended to investigate analytical approaches outside the concept of single-degree-of-freedom methodology. This includes performing a numerical dynamic evaluation with two or more degrees of freedom, or considering the energy of the system as the primary focus. A two-degree-of-freedom approach would involve analyzing the system with two resistances and two masses. In addition to resistance from the composite pipe, the soil would act as a separate resistance; instead of combining the soil and additional source of mass (such as a vehicle) as one mass, they would act as two separate

masses. Thus, the resistance of the composite pipe would be linked to the mass of the soil, and the resistance of the soil would link the mass of the soil to the additional source of mass.

With the soil having its own resistance, shock wave effects should then be considered to properly take into account material and geometric nonlinearity. The soil particles adjacent to the blast waves are pushed away by the high pressure, and the soil exhibits a fluid-like behavior, "flowing" outwardly from the blast waves. Additionally, significant material nonlinearity exists as the soil is subjected to severe material damage and plastic deformations. These nonlinearities must be taken into account within nonlinear numerical evaluation (Lee 2006).

Last, taking an energy approach would involve determining whether the strain energy capacity of the system is exceeded by the kinetic energy of the internal blast. The strain energy capacity is given by the toughness modulus, calculated as explained in Chapter 3, and the internal blast energy would be computed based on the mass of explosive material and its projecting velocity.

References

About.com (2011). "A brief history of Kevlar." *About.com: composites/plastics*, <http://composite.about.com/od/aboutcompositesplastics/l/aa050597.htm> (May 17, 2011).

About.com (2011). "Composite materials properties database." *About.com: composites/plastics*, <http://composite.about.com/cs/databases/l/bldata.htm> (June 17, 2011).

Advanced Pipe Inspection (API) (2010). "Cured in place pipe (CIPP) lining." *Advanced Pipe Inspection, Inc.*, <http://advancedpipe.com/pipe_lining.html> (May 17, 2011).

Agrawal, J.P., and Hodgson, R.D. (2007). *Organic chemistry of explosives*, John Wiley and Sons, Ltd., West Sussex, England, Chapter 4, 172.

Alkhrdaji, T. (2006). "Blast mitigation of concrete structures." *The Construction Specifier*, 59(3), 38-47.

Al-Sulaiman, F., Khan, Z., Merah, N., Kounain, M.A., and Mehdi, M. (2010). "Effects of weathering on failure pressure of filament-wound GFRP thermoset pipes." *Journal of composite materials*, 45(6), 645-655.

AM General LLC (2011). "Features and design." *AM General LLC – mobility solutions for the 21st century*, <http://www.amgeneral.com/vehicles/hmmwv/features.php> (Feb. 17, 2011).

Ashhab, M.S. (2004). "Lecture #5." *Control systems lecture notes*, <http://homepage.mac.com/sami_ashhab/courses/control/lectures/lecture_notes.htm> (June 17, 2011).

Ashley, S. (2007). "Body armor fiber and fabric." *Officer.com*, <http://www.officer.com/article/10249489/body-armor-fiber-and-fabric> (May 17, 2011).

Askeland, D.R., and Phule, P.P. (2003). *The science and engineering of materials, 4th ed.*, Thompson Brooks/Cole, Pacific Grove, CA.

Austin, M.A. (1996). "Library of finite elements." *The Institute for Systems Research, Clark School of Engineering, University of Maryland*, <http://www.isr.umd.edu/~austin/aladdin.d/fe-library.html> (June 17, 2011).

Baltic Yachts Americas (2006). "Philosophy." *Baltic Yachts Americas – worldwide yacht brokers*, <http://www.balticyachts.com/philosophy.html> (May 17, 2011).

Baton Rouge City-Parrish Department of Public Works (DPW) (2010). "Section 809, cured-in-place pipe (CIPP) laterals." *Baton Rouge City-Parrish DPW projects website*, <http://brprojects.com> (Feb. 10, 2011).

Biggs, J.M. (1964). *Introduction to structural dynamics*, McGraw-Hill Book Company, New York, NY.

Bolcof Plastic Materials (BPM) (2010). "Ultra-high-molecular-weight polyethylene, UHMWPE, UHMW." *BPM products*, <http://www.bolcofplastic.com/products/uhmwpe-uhmw.html> (May 17, 2011).

Boresi, A.P., and Schmidt, R.J. (2003). *Advanced mechanics of materials, 6th ed.*, John Wiley and Sons, Inc., Hoboken, NJ, Chapter 4, 104-107.

Chaturvedi, S.K., and Sierakowski, R.L. (1997). *Dynamic loading and characterization of fiber-reinforced composites*, John Wiley and Sons, Inc., New York, NY, Chapter 2, 80-90.

Chen, W.F. (1997). *Handbook of structural engineering*, CRC Press LLC, Boca Raton, FL.

Chen, W.F., and Han, D.J. (1988). *Plasticity for structural engineers*, Springer-Verlag New York, Inc., New York, NY, Chapter 4, 197-204.

Chopra, A.K. (2007). *Dynamics of structures, 3rd ed.*, Pearson Education, Inc., Upper Saddle River, NJ.

CIPP Corporation (2011). "Our resins." *CIPP Corporation*, <http://www.cippcorp.com/our-resins.php> (May 17, 2011).

City of Huntsville, AL (COH) (2011). "Storm water features gallery." *HuntsvilleAL.gov*, <http://www.hsvcity.com/Gis/projects/storm_gallery.htm> (May 17, 2011).

Composites One (2005). "Basics." *Composites One*, <http://www.compositesone.com/basics.htm> (May 17, 2011).

Composites World (2002). "Fiber types." *The online magazine of high performance composites and composites technology: Composites World*, <http://www.compositesworld.com/articles/fiber-types> (May 17, 2011).

Composites World (2002). “Pre-cured sleeves for high-pressure pipes.” *The online magazine of high performance composites and composites technology: Composites World*, <http://www.compositesworld.com/articles/pre-cured-sleeves-for-high-pressure-pipes> (Sep. 5, 2011).

Deshpande, A.B. (2006). “Characterization of CFRP and GFRP composite materials at high strain rate tensile loading.” M.S. thesis, Wichita St. Univ., Wichita, KS.

DuPont (2011). “Kevlar fiber and filament.” *DuPont. The miracles of science*, <http://www2.dupont.com/Kevlar/en_US/products/fibers/fiber.html> (May 17, 2011).

eFunda (2011). “Thin-walled pressure vessels.” *eFunda*, <http://www.efunda.com/formulae/solid_mechanics/mat_mechanics/pressure_vessel.cfm> (June 17, 2011).

eNotes (2011). “G-force.” *eNotes*, <http://www.enotes.com/topic/G-force> (Aug. 16, 2011).

Gilgwang Greentech (2004). “GRP pipe.” *GD Ecotech*, <http://www.gdecotech.com/english/frp/grp01.html> (May 17, 2011).

Hamouda, A.M.S., and Hashmi, M.S.J. (1998). “Testing of composite materials at high rates of strain: advances and challenges.” *Journal of Materials Processing Technology*, 77, 327-336.

Hoeffel, J., Hennessy-Fiske, M., and Goffard, C. (2010). ”San Bruno explosion death toll climbs to seven; six are missing.” *Los Angeles Times*, <http://articles.latimes.com/2010/sep/12/local/la-me-0912-san-bruno-explosion-20100912> (Aug. 30, 2011).

Hu, Y., Xia, Z., and Ellyin, F. (2006). “The failure behavior of an epoxy resin subjected to multiaxial loading.” *National Research Council Canada*, 1.

Insituform (2011). “Insituform CIPP.” *Insituform, global pipeline protection*, <http://www.insituform.com/mm/files/Insituform%20CIPP%20Brochure.pdf> (May 17, 2011).

International Insitute for FRP in Construction (IIFC) (2005). *FRP International*, 2(3), 8.

KAYA Archery (2011). “K7 professional risers.” *2011 KAYA Archery products catalog*, <http://archery-shop.jp/catalog/kaya_2011catalog.pdf> (May 17, 2011).

Laney, P. (2002). *Use of composite pipe materials in the transportation of natural gas*, Chapter 4, 5.

Lee, W.Y. (2006). "Numerical modeling of blast-induced liquefaction." Ph.D. thesis, Brigham Young Univ., Provo, UT.

Longinow, A. (2003). "Blast basics." *Proc., Steel Building Symposium: Blast and Progressive Collapse Resistance*, AISC, New York, NY, 13-19.

Minnesota Department of Transportation (MDOT) (2007). *Pavement design manual*, Section 3-2, 19.

National Program on Technology Enhanced Learning (NPTEL) (2006). *Composite materials – civil engineering*, <http://nptel.iitm.ac.in/courses/Webcourse-contents/IISc-BANG/Composite%20Materials/New_index1.html> (May 17, 2011).

Nova Scotia Department of Education (DOE) (2011). "Mathematics 8: focus on understanding, Diagrams for use in Chapter 9: Geometry II." *Nova Scotia Department of Education - Learning Resources and Technology*, <http://lrt.ednet.ns.ca/PD/geometry8ch9/index.shtml> (June 17, 2011).

North American Society for Trenchless Technology (NASTT) (2005). "Cured in place pipe." *North American Society for Trenchless Technology*, <http://www.nastt.org/pdf/PowerPoint/CIPP.pdf> (May 17, 2011).

Olarewaju, A.J., Kameswara Rao, N.S.V., and Mannan, M.A. (2011). "Dimensionless response of underground pipes due to blast loads using finite element method." *Electronic Journal of Geotechnical Engineering*, 16(E), 563.

Onder, A., Sayman, O., Dogan, T., and Tarakcioglu, N. (2008). "Burst failure load of composite pressure vessels." *Composite Structures*, 89, 159-166.

Oppel, R.A. (2009). "9 soldiers killed in Afghanistan." *The New York Times*, <http://www.nytimes.com/2009/08/03/world/asia/03afghan.html> (Sep. 14, 2011).

Otterman, S. (2009). "4 U.S. soldiers killed in Afghanistan." *The New York Times*, <http://www.nytimes.com/2009/10/17/world/asia/17afghan.html> (Sep. 14, 2011).

Plastics Pipe Institute, Inc. (PPI) (2011). "Culvert and highway drainage." *Plastics Pipe Institute*, <http://www.plasticpipe.org/drainage/culverts_highways.html> (May 17, 2011).

Rose, A.J. (2010). "San Bruno explosion: photos of the fire's aftermath paint a bigger picture." *HuffPost Los Angeles*, <http://www.huffingtonpost.com/2010/09/12/san-bruno-explosion-photos_n_713976.html#137507> (Aug. 30, 2011).

PurePipe Composite Manufacturing (2011). "Why Composite?" *PurePipe Composite Manufacturing*, <http://www.purepipe.co.uk/pages/index.asp?title=High_Pressure_Water_Pipes_-_PurePipe_Composite_Manufacturing_Why_Composite> (Sep. 5, 2011).

Sierakowski, R.L. (1997). "Strain rate behavior of metals and composites." *IGF Conference*, Cassino (FR), Italy, 10-15.

SIMULIA (2009). *Abaqus standard user's manual, version 6.9*, Hibbit, Karlsson & Sorensen, Inc., Pawtucket, RI.

SP Systems (2010). "The advantages of epoxy resin versus polyester in marine composite structures." *C&C Yachts*. <http://www.c-cyachts.com/images/company_assets/512F1C7F-0D64-4A5E-9D91-785DC064755F/16cf4_Adv_of_Epoxy_v_Poly.pdf> (May 17, 2011).

Tabiei, A., and Nilakantan, G. (2007). "Reduction of acceleration induced injuries from mine blasts under infantry vehicles." *6th European LS-DYNA Users Conference*, Gothenburg, Sweden, 3.

Tedesco, J.W., McDougal, W.G., and Ross, C.A. (1999). *Structural dynamics*, Addison Wesley Longman, Inc., Menlo Park, CA.

Ugural, A.C., and Fenster, S.K. (1981). *Advanced strength and applied elasticity*, Elsevier North Holland, Inc., New York, NY, Chapter 8, 235-238.

United States Army Corps of Engineers Protective Design Center (USACE PDC) (2008). *Methodology manual for the single-degree-of-freedom blast effects design spreadsheets (SBEDS)*.

Whitman, Z., and Saponara, V.L. (2007). "Bistable structures for energy absorption, II. Composite structures under tension." *Journal of Mechanics of Materials and Structures*, 2(2), 361.

Appendix A

Composite Material Properties for Finite Element Models

Table A.1: Composite data format and units (adapted from About.com 2011b)

E_{11}	E_{22}	G_{12}	ν_{12}
Msi	Msi	Msi	

F_{1t}	F_{1c}	F_{2t}	F_{2c}	F_6
ksi	ksi	ksi	ksi	ksi

Variables:

- E_{11} = longitudinal modulus
- E_{22} = transverse modulus
- G_{12} = in-plane shear modulus
- ν_{12} = major Poisson's ratio
- F_{1t} = longitudinal tensile strength
- F_{1c} = longitudinal compressive strength
- F_{2t} = transverse tensile strength
- F_{2c} = transverse compressive strength
- F_6 = in-plane shear strength

Table A.2: AS/3501 carbon/epoxy unidirectional prepreg properties (adapted from About.com 2011b)

E_{11}	E_{22}	G_{12}	ν_{12}
20.0	1.30	1.03	0.30

F_{1t}	F_{1c}	F_{2t}	F_{2c}	F_6
210	209.9	7.5	29.9	13.5

Table A.3: Generic IM6 carbon/epoxy unidirectional prepreg properties (adapted from About.com 2011b)

E_{11}	E_{22}	G_{12}	ν_{12}
29.4	1.62	1.22	0.32

F_{1t}	F_{1c}	F_{2t}	F_{2c}	F_6
508	223.4	8.1	21.8	14.2

Table A.4: T300/5208 carbon/epoxy unidirectional prepreg properties (adapted from About.com 2011b)

E_{11}	E_{22}	G_{12}	ν_{12}
26.3	1.49	1.04	0.28

F_{1t}	F_{1c}	F_{2t}	F_{2c}	F_6
218	217.6	5.8	35.7	9.9

Table A.5: Generic E-glass/epoxy unidirectional prepreg properties (adapted from About.com 2011b)

E_{11}	E_{22}	G_{12}	ν_{12}
5.7	1.25	0.55	0.28

F_{1t}	F_{1c}	F_{2t}	F_{2c}	F_6
157	89.9	5.7	18.6	12.9

Table A.6: Generic S-glass/epoxy unidirectional prepreg properties (adapted from About.com 2011b)

E_{11}	E_{22}	G_{12}	ν_{12}
6.2	1.29	0.65	0.27

F_{1t}	F_{1c}	F_{2t}	F_{2c}	F_6
186	100.1	7.1	22.9	10.0

Table A.7: Generic Kevlar 49/epoxy unidirectional prepreg properties (adapted from About.com 2011b)

E_{11}	E_{22}	G_{12}	ν_{12}
12.6	0.80	0.32	0.34

F_{1t}	F_{1c}	F_{2t}	F_{2c}	F_6
186	48.6	4.4	22.9	7.1

Appendix B

Pipe Model and Pressure-Impulse Graphs

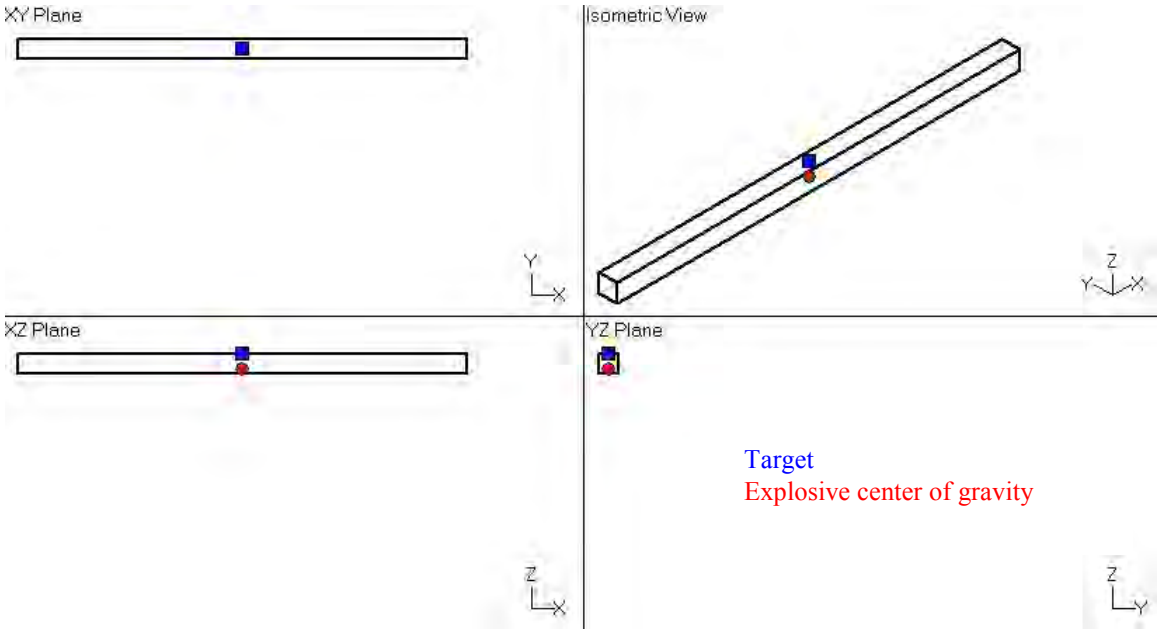

Figure B.1: Pipe model used to generate pressure-impulse histories

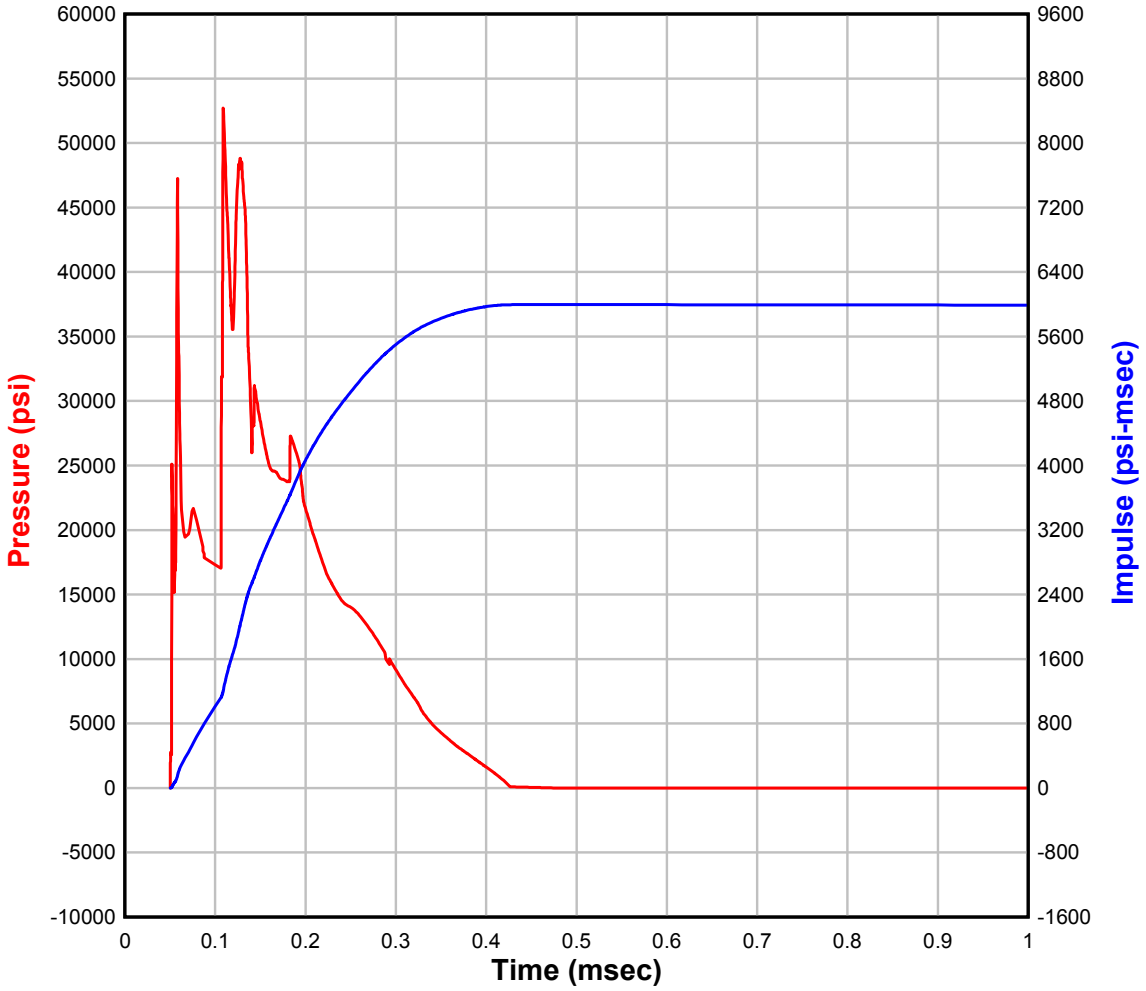

Figure B.2: Pressure-impulse graph for HE-1

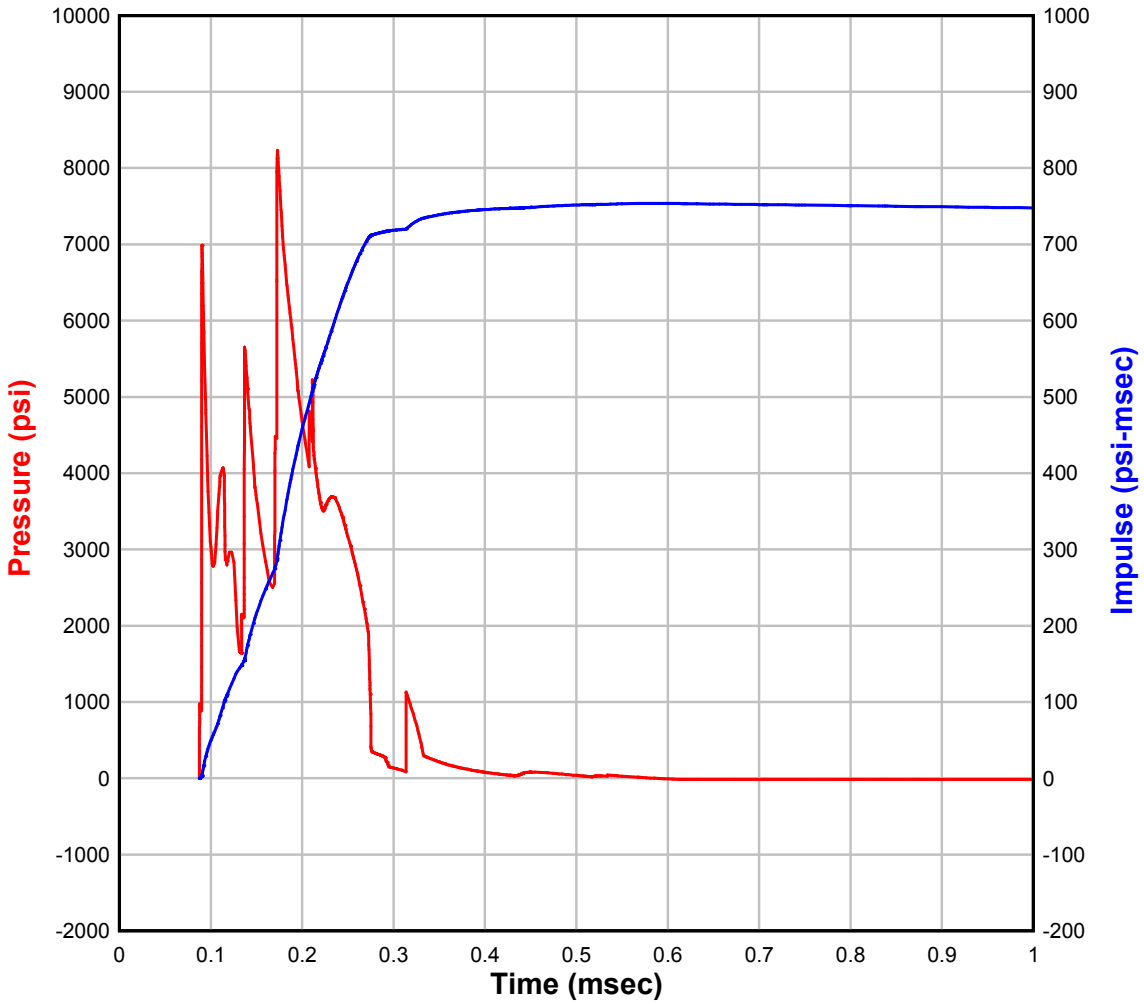

Figure B.3: Pressure-impulse graph for HE-2

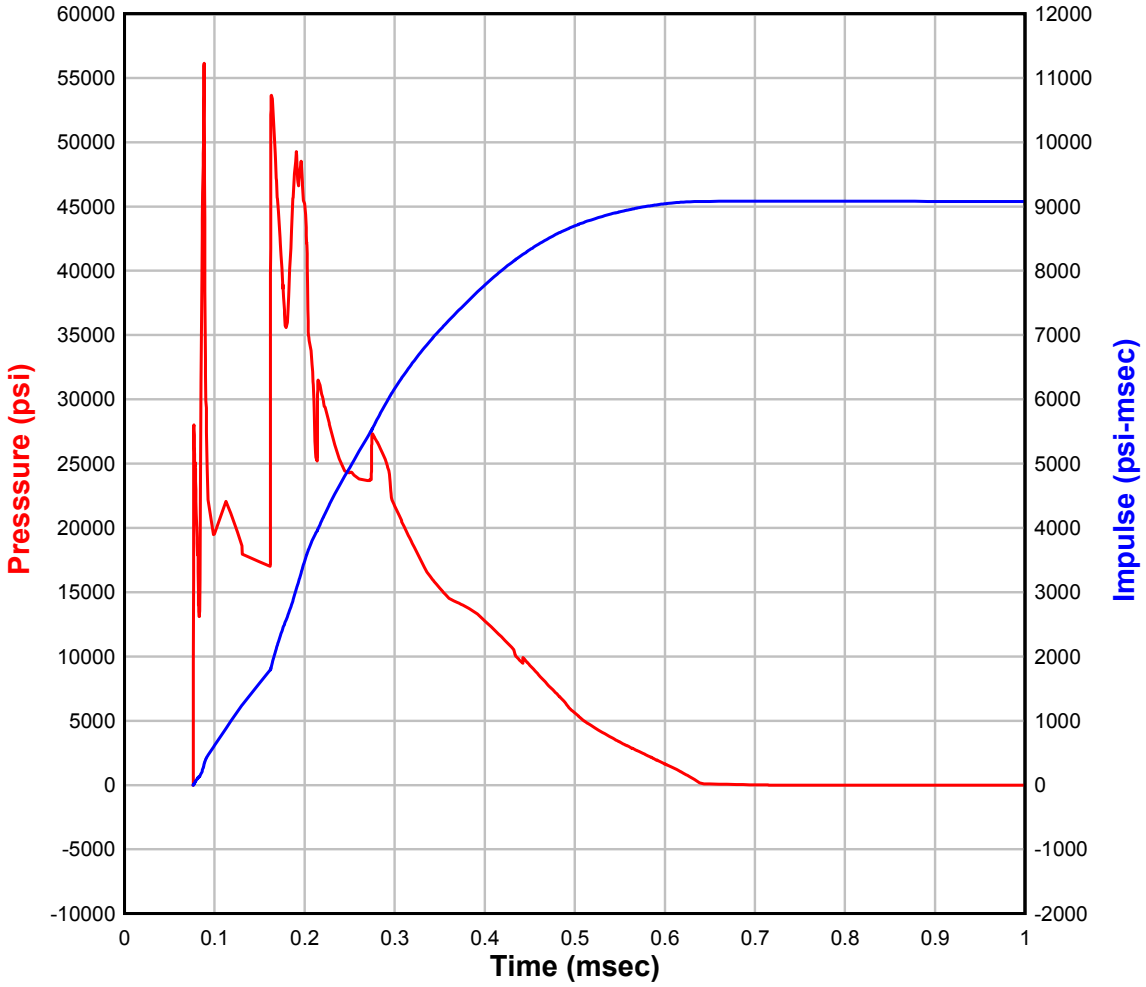

Figure B.4: Pressure-impulse graph for HE-3

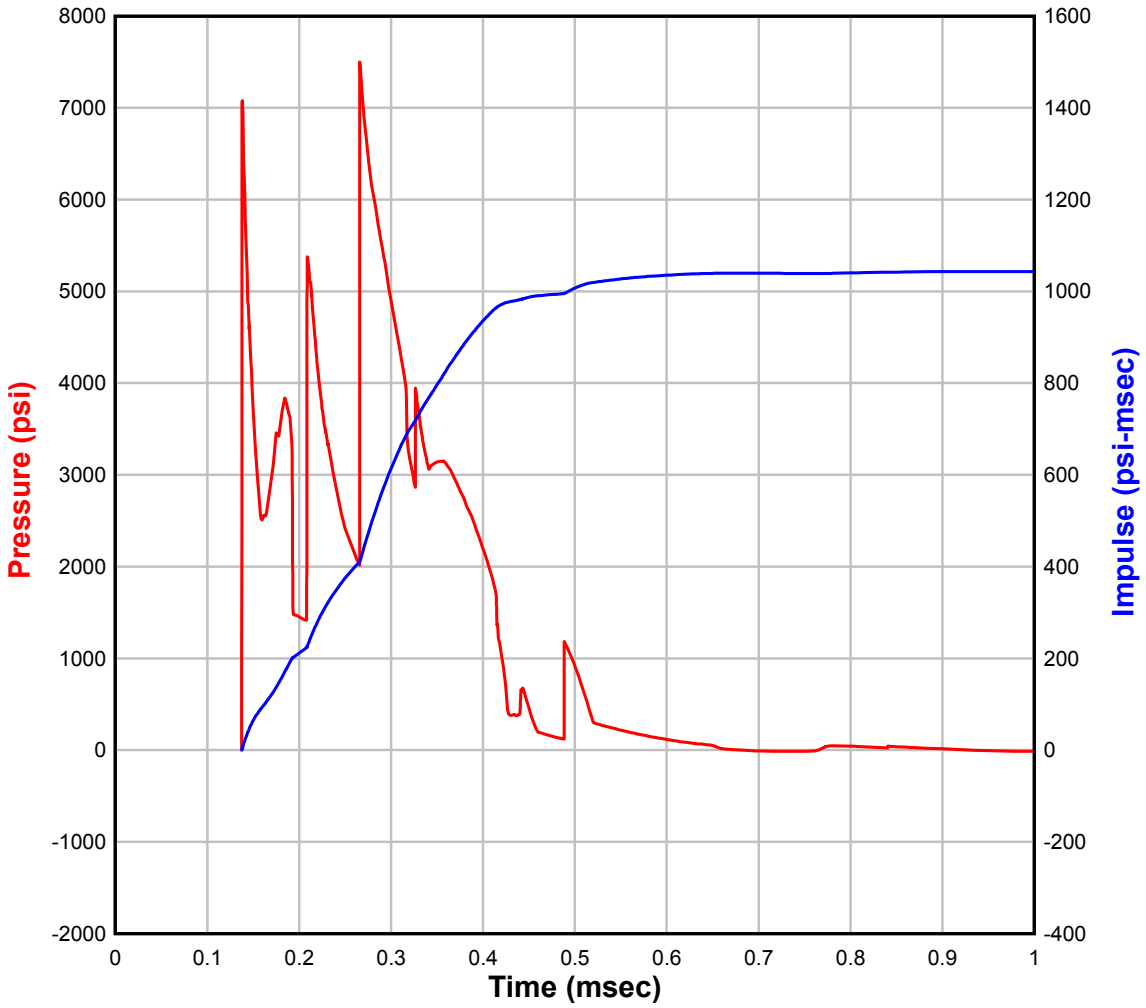

Figure B.5: Pressure-impulse graph for HE-4

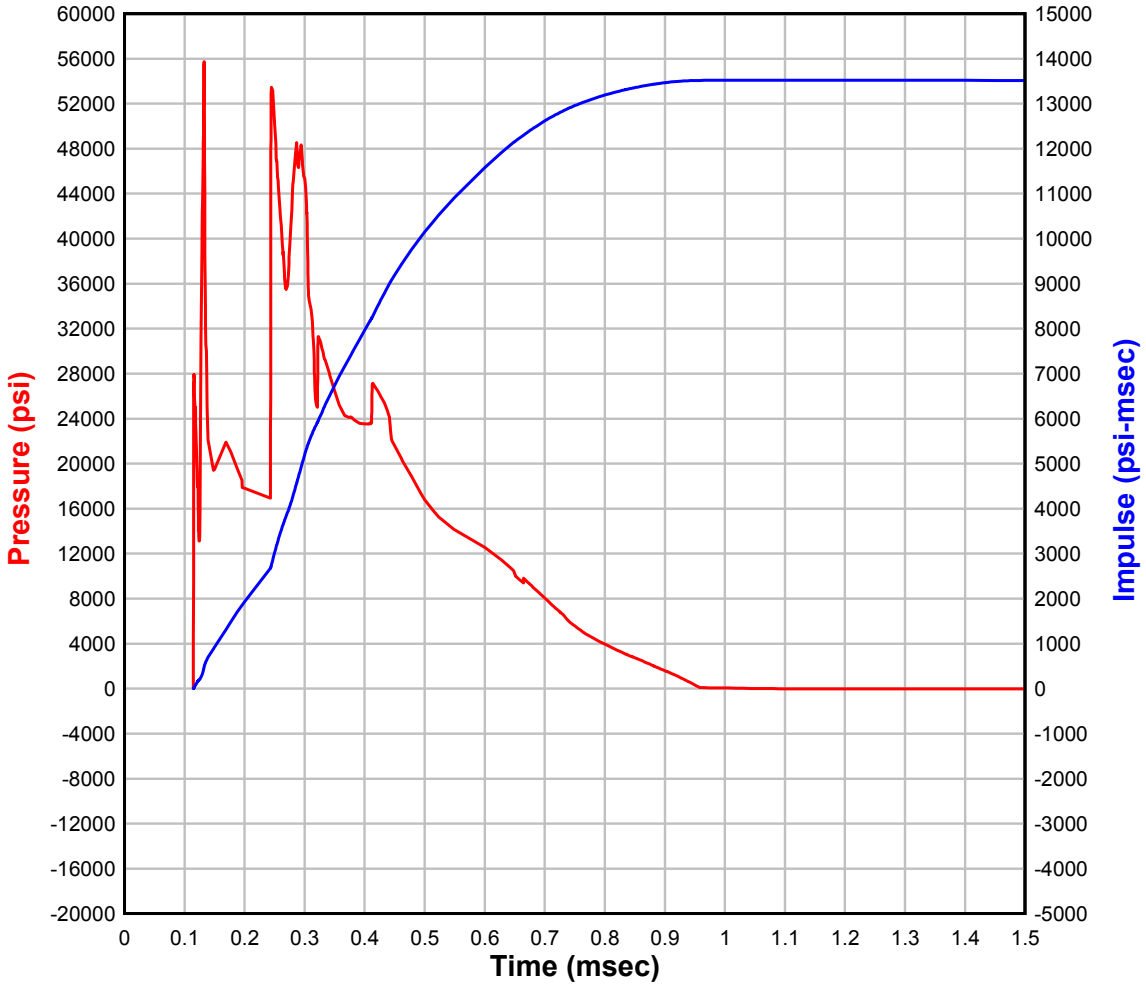

Figure B.6: Pressure-impulse graph for HE-5

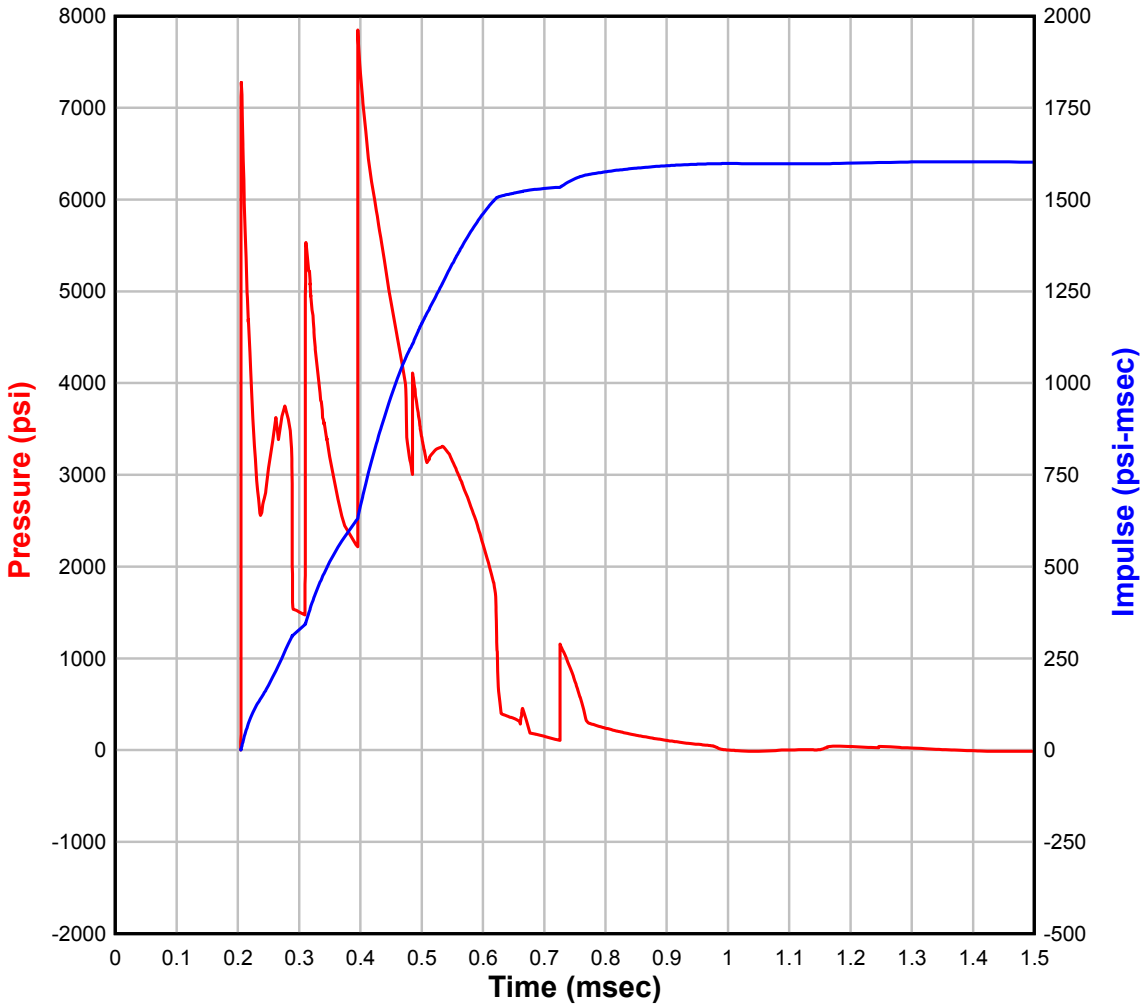

Figure B.7: Pressure-impulse graph for HE-6

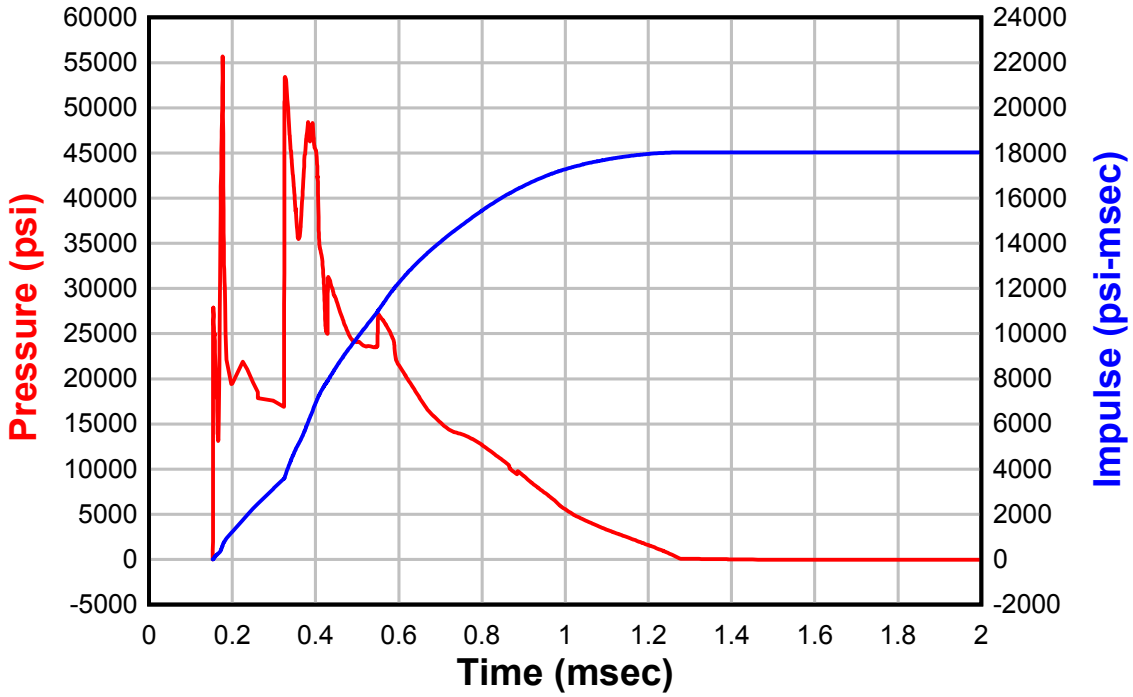

Figure B.8: Pressure-impulse graph for HE-7

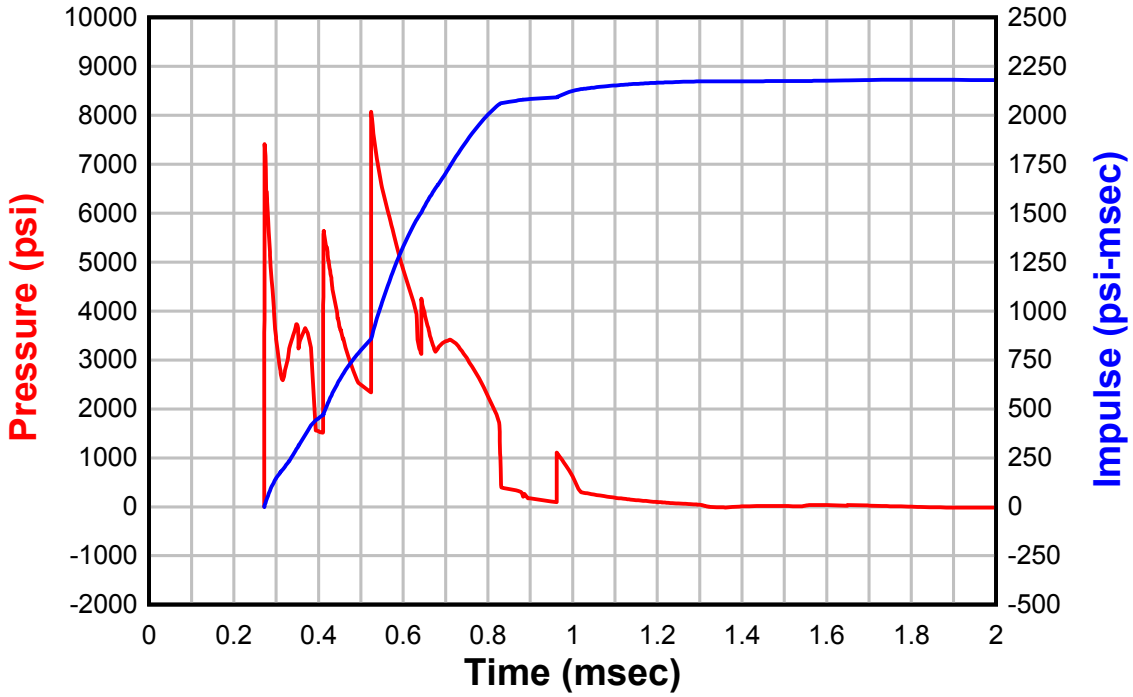

Figure B.9: Pressure-impulse graph for HE-8

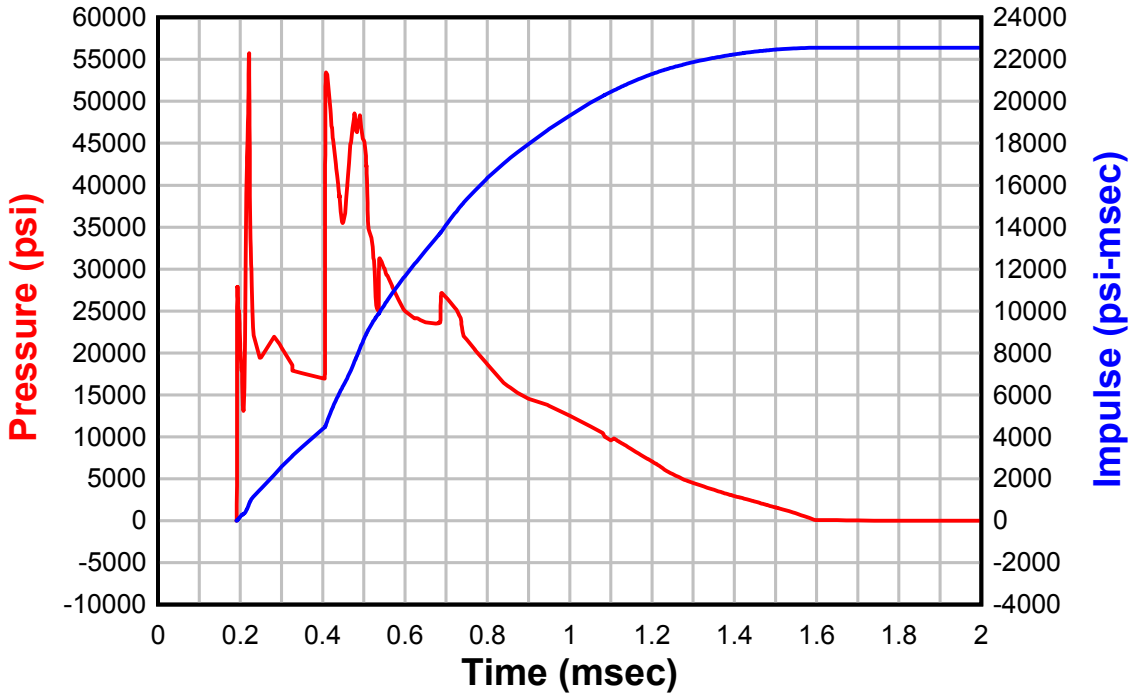

Figure B.10: Pressure-impulse graph for HE-9

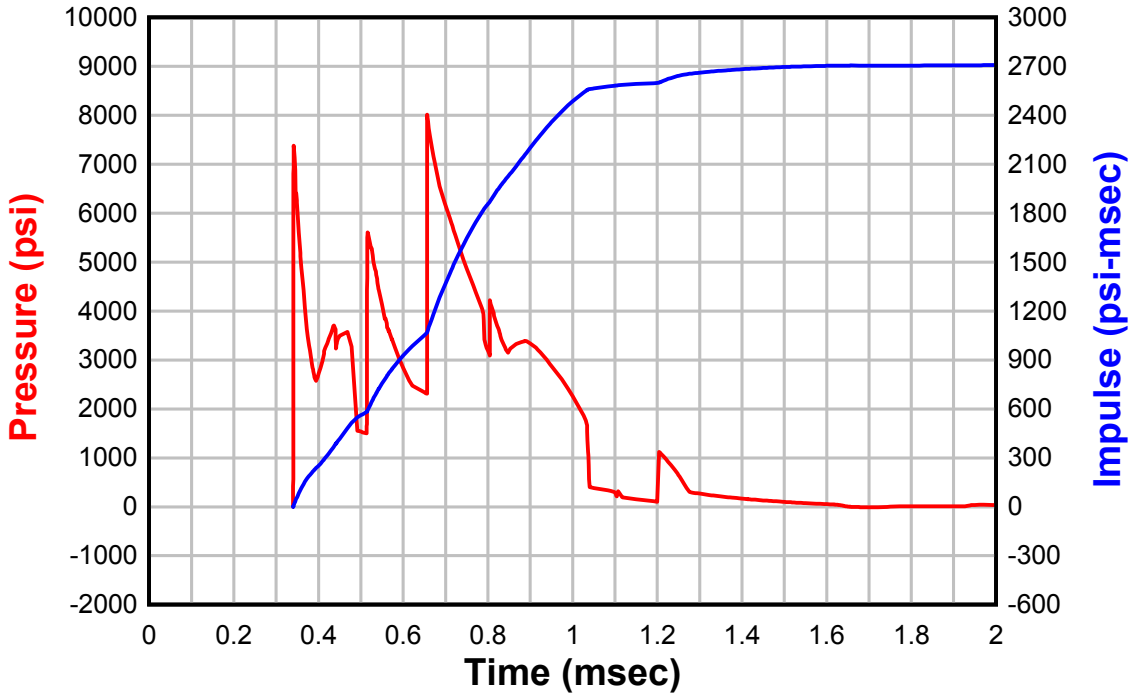

Figure B.11: Pressure-impulse graph for HE-10

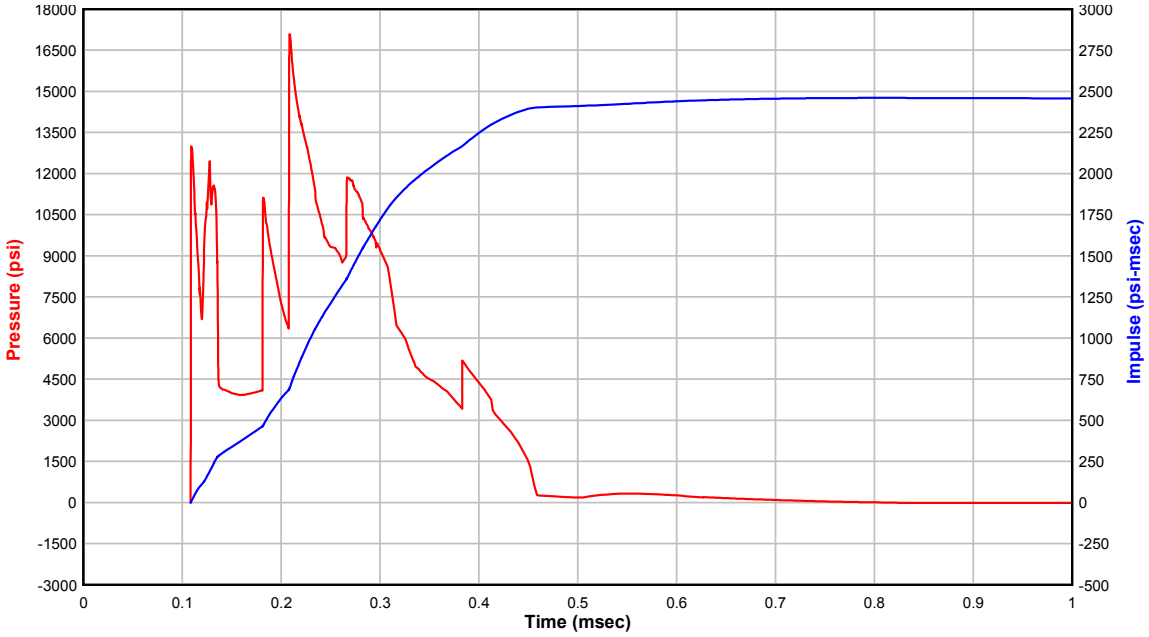

Figure B.12: Pressure-impulse graph for HE-11

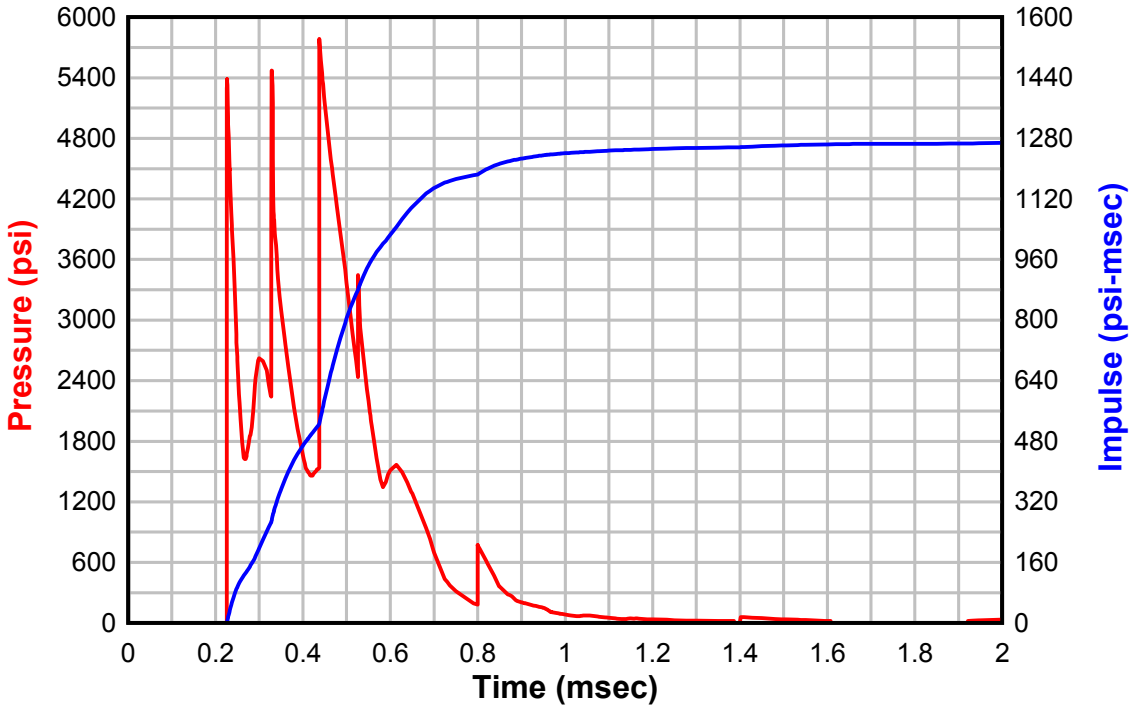

Figure B.13: Pressure-impulse graph for HE-12

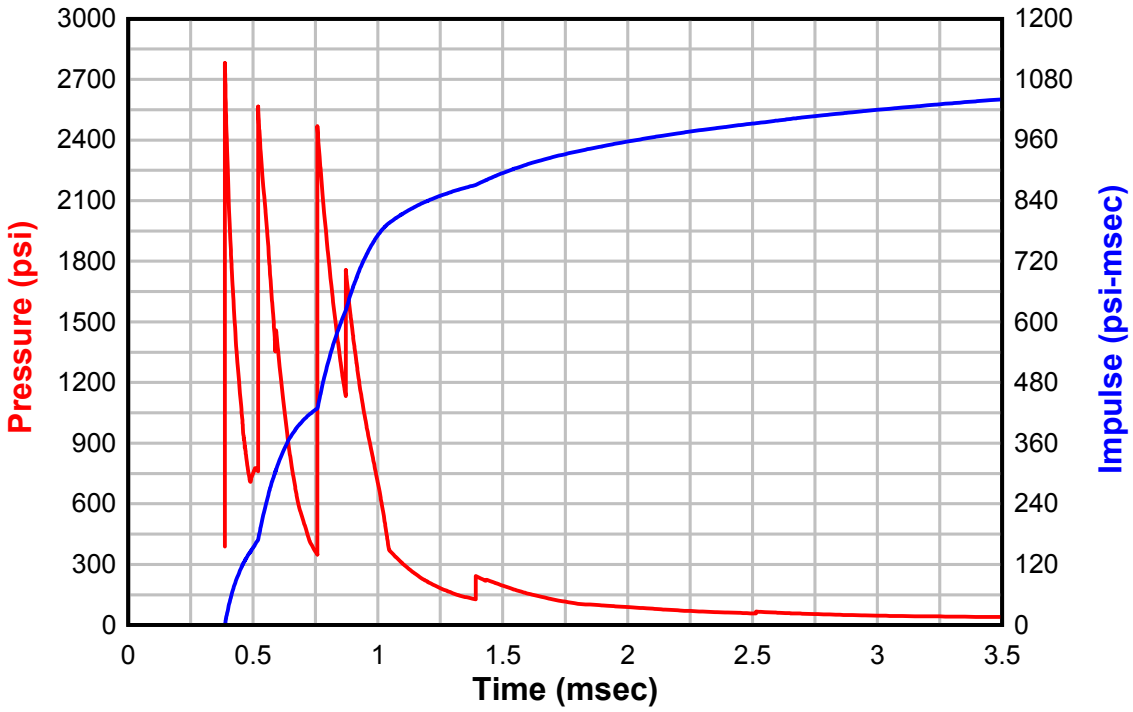

Figure B.14: Pressure-impulse graph for HE-13

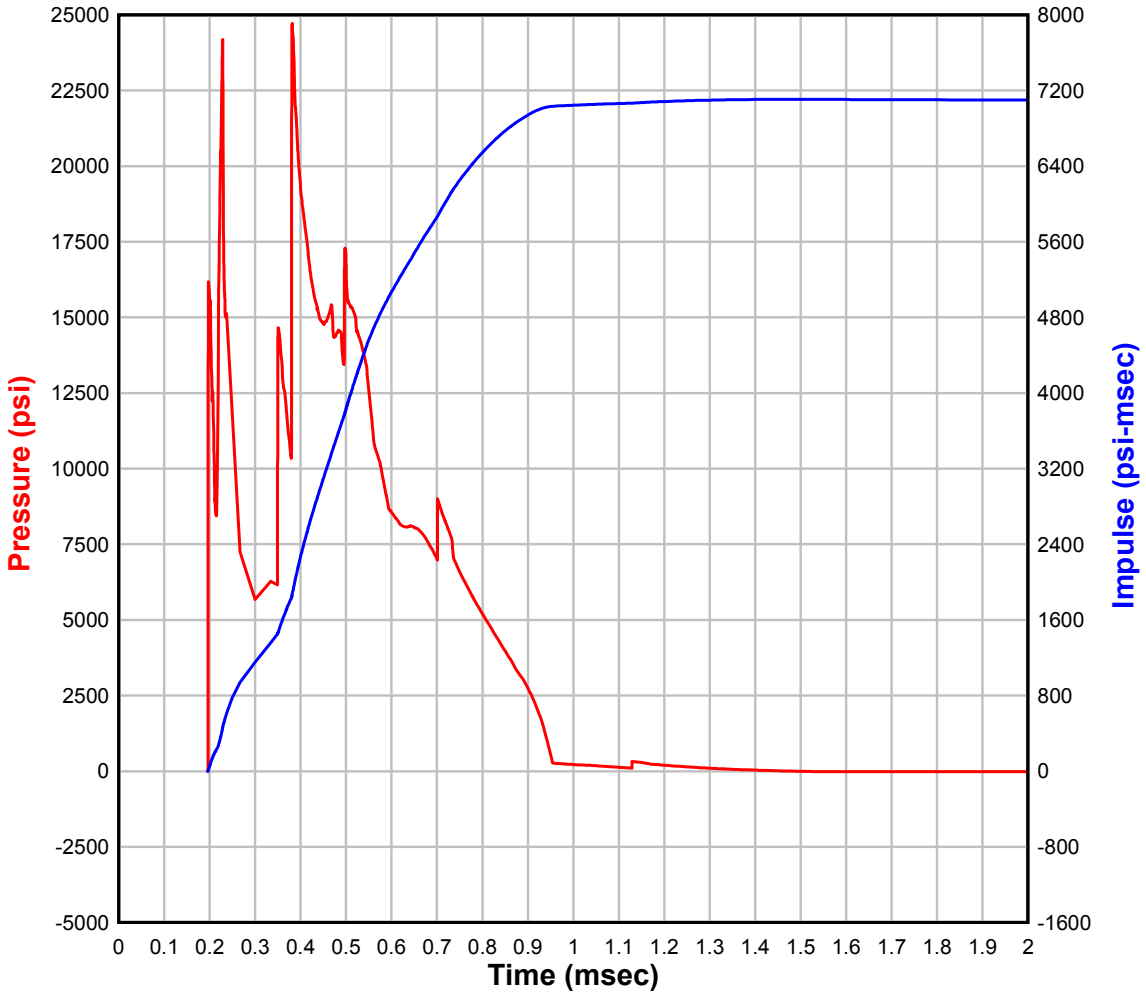

Figure B.15: Pressure-impulse graph for HE-14

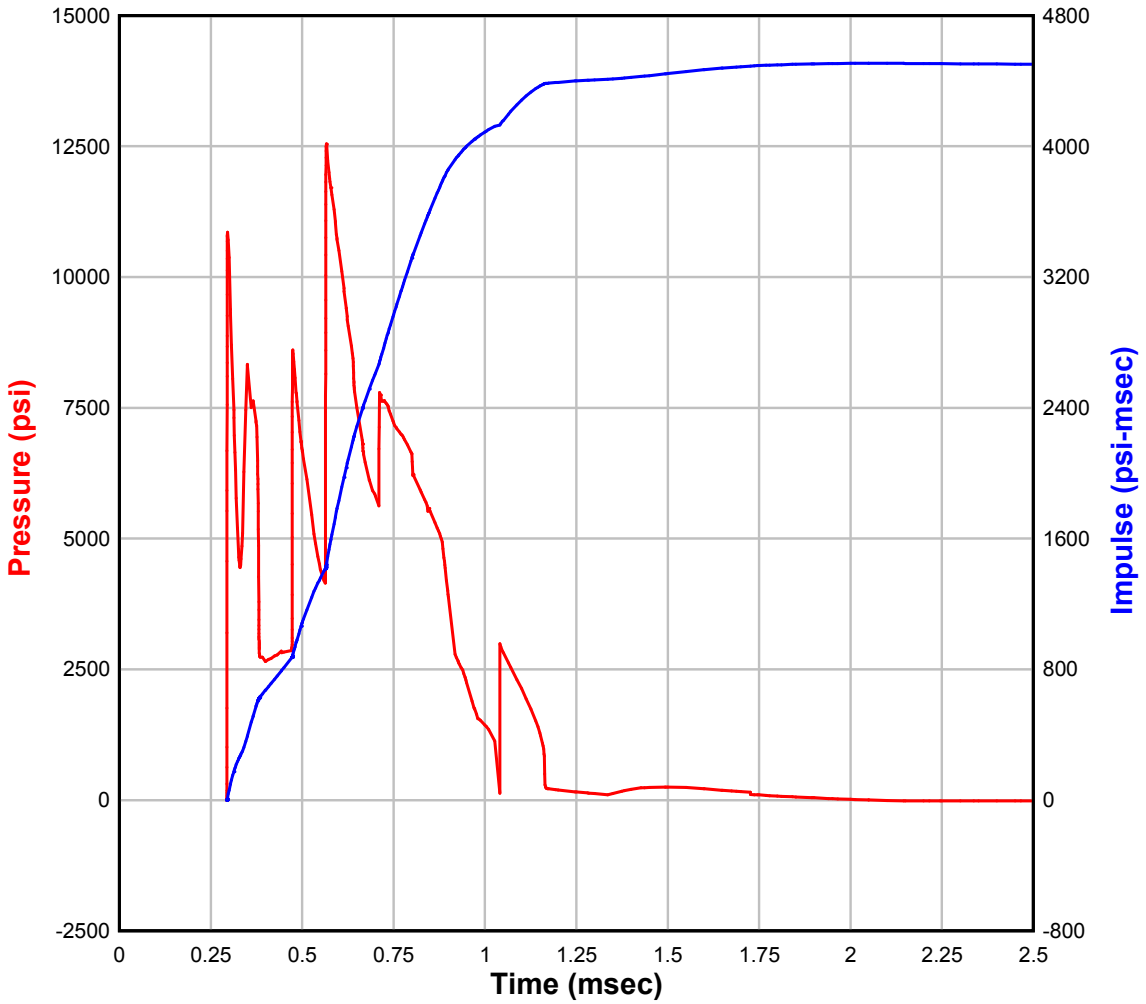

Figure B.16: Pressure-impulse graph for HE-15

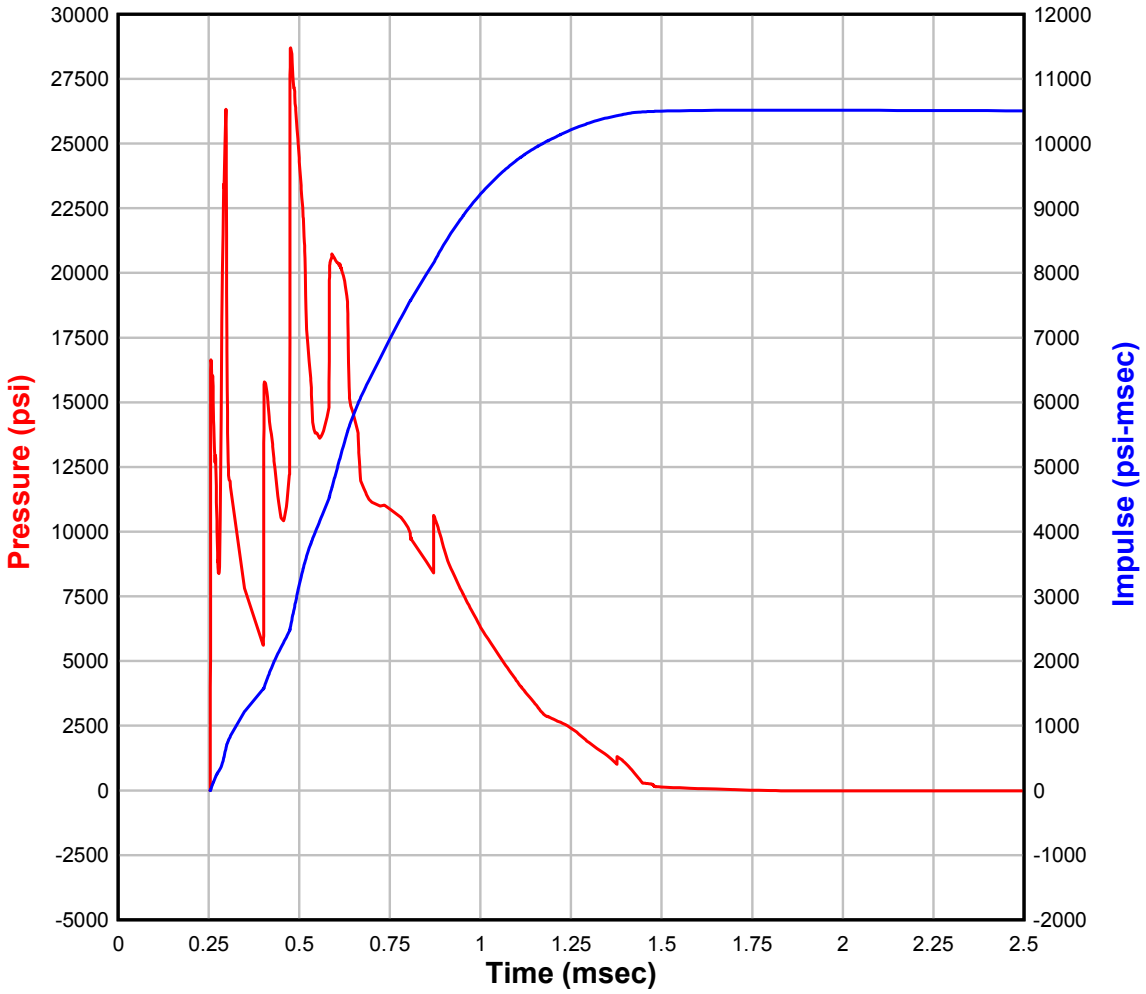

Figure B.17: Pressure-impulse graph for HE-16